

# Hot Particle Dosimetry Using a Wall-Less Tissue Equivalent Proportional Counter

by

Craige BOYD

A thesis submitted in partial fulfillment  
of the requirements for the degree of:

Doctor of Philosophy

in

Nuclear Engineering

The Faculty of Engineering and Applied Science

University of Ontario Institute of Technology(Ontario Tech  
University)

Oshawa, Ontario, Canada

May 2023

Copyright © Craige BOYD, 2023

# Hot Particle Dosimetry Using a Wall-Less Tissue Equivalent Proportional Counter

Submitted by Craig BOYD

Doctor of Philosophy in Nuclear Engineering

An oral defense of this thesis took place on April 05, 2023 in front of the following examining committee:

## Supervisory Committee

---

Chair of Examining Committee	Dr. Jennifer Mckellar, Ontario Tech University
Supervisor	Dr. Glenn Harvel, Ontario Tech University
Research Supervisor	Dr. Anthony Waker, Ontario Tech University
Committee Member	Dr. Edward Waller, Ontario Tech University
Committee Member	Dr. Markus Piro, Ontario Tech University
University Examiner	Dr. Paul Yelder, FHS, Ontario Tech University
External Examiner	Dr. John Kildea, McGill University

---

The above committee determined that the thesis is acceptable in form and content and that a satisfactory knowledge of the field covered by the thesis was demonstrated by the candidate during an oral examination. A signed copy of the Certificate of Approval is available from the School of Graduate and Postdoctoral Studies.

# Abstract

Highly radioactive specks of irradiated nuclear fuel or activated material, colloquially known as ‘hot particles’, can enter the workplace or external environment from nuclear power plant operations such as refurbishment and decommissioning or from a severe nuclear accident. If deposited on the skin, ingested or inhaled, hot particles can pose a significant radiological hazard. Typically, hot particles are beta particle or alpha particle emitters and deposit their energy over very small distances in tissue making dose determinations through measurement or computation to the target tissues at risk such as epithelial cells in lung and gut and basal cells in skin difficult. Furthermore, current methods fail to determine changes that might occur in radiation quality as the charged particles lose energy and their stopping power increases with depth of penetration providing challenges in assessing the biological outcome of an exposure.

In this work, an apparatus that is not commercially available was constructed so absorbed dose and quantities that can be used to quantify radiation quality could be measured as a function of tissue depth. The apparatus consisted of a custom fabricated wall-less tissue equivalent proportional counter and a mechanism for increasing the beta or alpha particle source to counter distance by distances equivalent to tens of micrometers of unit density tissue. Monte Carlo computational models of the experimental apparatus were also made using the electron transport code PENELOPE for several beta particle emitting sources acting as a proxy for hot particles.

Results from both experiments and Monte Carlo simulations for low energy beta emitters showed steep dose gradients as dose rates decreased to almost zero over

tissue-like distances of a few tens of microns depending on the energy spectrum of the beta particles. An increase in dose-mean lineal energy indicative of increased biological effectiveness was also observed, experimentally and computationally, as source to target tissue distances increased.

Taken together, the experimental and computational methods described in this work have proved the principle of using microdosimetric methods for the direct determination of hot particle dose and potential biological effectiveness and concludes with recommendations for further research to promote the development of equipment suitable for nuclear power plant field deployment.

**Keywords:** Absorbed Dose; Depth in Tissue; Experimental Microdosimetry; Hot Particles; Monte-Carlo simulations; Radiation Quality; Biological Effectiveness; Wall-less Tissue Equivalent Proportional Counter

# Declaration of Authorship

- I hereby declare that this thesis consists of original work of which I have authored. This is a true copy of the thesis, including any required final revisions, as accepted by my examiners.
- I authorize the University of Ontario Institute of Technology (Ontario Tech University) to lend this thesis to other institutions or individuals for the purpose of scholarly research. I further authorize University of Ontario Institute of Technology (Ontario Tech University) to reproduce this thesis by photocopying or by other means, in total or in part, at the request of other institutions or individuals for the purpose of scholarly research. I understand that my thesis will be made electronically available to the public.

## Statement of Contributions

I hereby certify that I am the sole author of this thesis and that no part of this thesis has been published or submitted for publication. I have used standard referencing practices to acknowledge ideas, research techniques, or other materials that belong to others. Furthermore, I hereby certify that I, along with Dr. Anthony Waker, am the source of the creative works and/or inventive knowledge described in this thesis.

I performed majority of the measurements and investigations using the apparatus described along with computational modelling of the various experiments to produce this thesis. The new knowledge contributed by this work addresses the radiation science and health physics complexities of hot particle dosimetry.

Dedicated to Wilfred Wallace  
(1902-1992)

*“When I heard the learn’d astronomer,  
When the proofs, the figures, were ranged in columns before me,  
When I was shown the charts and diagrams, to add, divide, and measure them,  
When I sitting heard the astronomer where he lectured with much applause in the  
lecture-room,  
How soon unaccountable I became tired and sick,  
Till rising and gliding out I wander’d off by myself,  
In the mystical moist night-air, and from time to time,  
Look’d up in perfect silence at the stars.”*

Walt Whitman (1867)



# Acknowledgements

I would like to recognize my co-supervisor Dr. Glenn Harvel, the University's Chair, and my supervisory committee members for their efforts towards the submission and fulfillment of this work. This endeavor would not have been possible however without my research supervisor Dr. Anthony John Waker. I would like to express my deepest gratitude to him for allowing me the opportunity to participate in this work and for making my experience in this research program a satisfying one. The advice, direction, feedback and tremendous effort provided has been indispensable to the body and quality of work presented. Special thanks also to my research teammates, the individual and team discussions and research interests instigated an environment for a high caliber of work. I am very grateful for the discussions especially with Mr. Adam Caly, whose mutual interest in nuclear instrumentation design and Monte Carlo modeling inspired me. Special thanks to the University Network of Excellence in Nuclear Engineering (UNENE) and the Natural Sciences and Engineering Research Council (NSERC) of Canada for generously supporting this work. Thanks should also go to the faculty's lab technicians and the university's librarians for all their efforts. Lastly, I would be remiss in not mentioning my family and friends. Their belief in me fueled and motivated me especially during the challenging times. Thank you for the periodic requests for project updates, and for offering support.

# Contents

<b>Abstract</b>	<b>iii</b>
<b>Declaration of Authorship</b>	<b>v</b>
<b>Statement of Contributions</b>	<b>vi</b>
<b>Acknowledgements</b>	<b>ix</b>
<b>1 Introduction</b>	<b>1</b>
1.1 Hot Particles . . . . .	1
1.2 Relevance of Beta Emitters in Radiation Science Studies . . . . .	9
1.2.1 Medical Relevance . . . . .	11
1.2.2 Industrial Relevance . . . . .	13
1.3 Motivation for Thesis . . . . .	15
1.4 Objectives of Thesis . . . . .	16
1.4.1 Approach . . . . .	17
1.5 Outline of Thesis . . . . .	17
<b>2 Radiation Dosimetry and Radiation Quality</b>	<b>19</b>
2.1 Interaction of Beta Particles and Photons with Tissue . . . . .	19
2.2 Absorbed Dose Concept and Measurement . . . . .	24
2.2.1 Definition of Absorbed Dose . . . . .	24
2.2.2 Measurement Using Gas-Ionization . . . . .	25
2.2.3 Measurement Using Ion Chambers . . . . .	26
2.2.4 Measurement Using Proportional Counters . . . . .	27
2.3 Radiation Quality . . . . .	29
2.3.1 Experimental RBE . . . . .	30

2.3.2	Linear Energy Transfer . . . . .	35
2.3.3	Radiation Protection and Radiation Wiegthing Factors . . .	35
2.3.4	Measurement of Quality . . . . .	36
	LET (L) and Quality Factors, ( $Q$ ) . . . . .	36
2.4	Experimental Microdosimetry and Radiation Quality . . . . .	38
2.4.1	Microdosimetric Quantities . . . . .	38
2.4.2	Measurement of Dose . . . . .	42
2.4.3	Tissue Equivalent Proportional Counters . . . . .	42
2.4.4	"Wall-less" TEPC . . . . .	44
<b>3</b>	<b>Literature Review</b>	<b>47</b>
3.1	Methods of Hot Particle Dosimetry . . . . .	47
3.1.1	Software Based Tools -"VARSKIN" and "DETEC" . . . . .	47
3.1.2	Expedient Field Method(EFM) with G-M Pancake Probe . .	50
3.1.3	Hot Particle Dosimetry System (HPDS) . . . . .	51
3.1.4	The Extrapolation Chamber . . . . .	53
3.2	Monte Carlo Methods of Computational Dosimetry and Micro- dosimetry . . . . .	54
3.2.1	Electron-Photon Transport with PENELOPE . . . . .	55
3.2.2	Subroutine Package PENGEOM for Quadric Geometries . .	58
3.2.3	Structure and Operation of the PENELOPE Code . . . . .	63
<b>4</b>	<b>Methodology</b>	<b>64</b>
4.1	Experimental Design and Set Up of the Apparatus . . . . .	65
4.1.1	Detector Design and Construction . . . . .	71
4.1.2	Determining the Gas Gain . . . . .	72
	Counter and Vacuum Chamber Assembly Parts . . . . .	74
4.2	Operation of the WTEPC Architecture . . . . .	77
4.2.1	Anti-Coincidence Mode . . . . .	78
4.2.2	Coincidence Mode . . . . .	82
4.2.3	Far West Technology Single Wire Counter Alpha Experiment	89
4.2.4	Alpha Source Experiment and Calibration of the Wall-less TEPC . . . . .	92

4.2.5	Beta Source Experiments . . . . .	97
4.3	Experimental Determination of Lineal Energy and Dose Mean Lineal Energy . . . . .	99
4.3.1	Plotting the Microdosimetric Event-Size Spectra from Experiments . . . . .	100
4.3.2	Normalization . . . . .	102
4.3.3	Experimental Determination of Dose and Dose Rate . . . . .	103
4.3.4	Determination of the Uncertainties in Experimental Microdosimetry . . . . .	103
4.4	Simulation and Modeling of Experiments with Monte Carlo Code PENELOPE . . . . .	106
4.4.1	Defining Geometry and Input Files . . . . .	106
4.4.2	PENELOPE Output . . . . .	113
4.4.3	Determination of Lineal Energy, $y$ , through Monte Carlo Simulations . . . . .	115
4.4.4	Determination of the Dose Mean Lineal Energy, $\bar{y}_D$ , Normalization and Dose Rate from Monte Carlo simulations . . . . .	117
4.5	A Low Energy Photon Irradiation Benchmark Simulation . . . . .	117
<b>5</b>	<b>Results and Discussion</b>	<b>123</b>
5.1	Experimental Investigation . . . . .	123
5.2	Experimental Study of the Wall-less TEPC Response to Short Ranged Alpha and Beta particles . . . . .	125
5.2.1	WTEPC's Response to $^{241}\text{Am}$ Alpha particles . . . . .	125
5.2.2	WTEPC's Response to $^{63}\text{Ni}$ Beta particles . . . . .	130
5.2.3	WTEPC's Response to $^{14}\text{C}$ Beta particles . . . . .	139
5.3	Monte-Carlo simulations of Photon Irradiations in a Wall-less TEPC. Results of the Transport Code PENELOPE for Kliauga and Dvorak's Benchmark Study. . . . .	144
5.4	Monte Carlo Modeling for HP Dosimetry . . . . .	149
5.4.1	Monte Carlo Determination of $\bar{y}_D$ and RBE Values when Modeling the Wall-less TEPC with PENELOPE . . . . .	153

5.5	A Comparison of Experimental Measurements with Monte Carlo simulations . . . . .	169
5.5.1	$^{63}\text{Ni}$ and $^{14}\text{C}$ Experimental Results compared with PENE-LOPE Calculations . . . . .	169
<b>6</b>	<b>Conclusions and Future Work</b>	<b>174</b>
6.1	Summary of Research Contributions . . . . .	175
6.2	Recommendations for Future Work . . . . .	177
<b>A</b>	<b>Penelope</b>	<b>179</b>
A.1	PenGeomJar . . . . .	179
A.2	Input Files for PENELOPE . . . . .	182
A.3	PENMAIN(*.dat) output files . . . . .	195
<b>B</b>	<b>Experimental Wall-less TEPC</b>	<b>207</b>
B.1	Detector parts . . . . .	207
B.2	Radioactive Sources used in Experiments . . . . .	208
B.2.1	$^{241}\text{Am}$ . . . . .	208
B.2.2	$^{63}\text{Ni}$ . . . . .	209
B.2.3	$^{14}\text{C}$ . . . . .	210
B.2.4	3D Printed Source Collimator . . . . .	211
B.2.5	3D Printed Source Holder . . . . .	211
B.3	Sample of Matlab Code . . . . .	212
B.4	Matlab Programme: <i>LogplotMCA16383</i> for Alpha particles . . . . .	213
B.5	Matlab Programme: <i>BetaLogplotMCA16383</i> for Beta particles . . . . .	213
B.6	Matlab Code Interface . . . . .	215
	<b>Bibliography</b>	<b>216</b>

# List of Figures

1.1	HPs from Weapons Test . . . . .	3
1.2	Fukushima HPs in dust . . . . .	5
1.3	Layers of the skin associated with a thumb and the dimensions involved in depth of tissue . . . . .	8
1.4	Hot Particles . . . . .	10
2.1	Electron Tracks . . . . .	21
2.2	Compton Scattering . . . . .	22
2.3	Pair Production . . . . .	23
2.4	Ion Chamber . . . . .	27
2.5	Electron avalanche . . . . .	28
2.6	Variation of RBE with LET . . . . .	31
2.7	Cell Survival and LET 1 . . . . .	32
2.8	Cell Survival and LET 2 . . . . .	34
2.9	Lineal Energy Distribution of Three Different Radiation Qualities .	40
2.10	Single-event lineal energy dose distributions for different photon energies. . . . .	41
2.11	Typical Rossi Counter. . . . .	43
2.12	Pulse height Detection using a TEPC. . . . .	44
2.13	Wall Effects . . . . .	46
3.1	VARSKIN4.0 . . . . .	49
3.2	Activity Calculator . . . . .	50
3.3	Hot Particle Dosimetry System . . . . .	52
3.4	Electrons and Positrons Interaction . . . . .	56
3.5	Quadric Surfaces . . . . .	60

3.6	Quadric Surfaces 2D viewer . . . . .	61
3.7	Quadric Surfaces 3D viewer . . . . .	62
4.1	Cross-section of a cylindrical Wall-less TEPC . . . . .	65
4.2	Schematic of a cylindrical Wall-less TEPC . . . . .	66
4.3	Flow Diagram of the basic operation of a TEPC . . . . .	67
4.4	Cross-sectional schematic view of the counter components . . . . .	68
4.5	Wall-less Counter Internal Components . . . . .	69
4.6	Experimental set up used to measure pulse heights . . . . .	70
4.7	Gas gain calculations for a cylindrical type Wall-less TEPC . . . . .	73
4.8	Assembly parts for the Wall-less counter and chamber . . . . .	75
4.9	Relative Gain Test . . . . .	77
4.10	Anode potential tubes uninstalled . . . . .	78
4.11	Anti-Coincidence Mode ADC Settings Collection set up for the 'MCARD' . . . . .	79
4.12	Anti-Coincidence Mode with Anode Potential Tubes installed . . . . .	80
4.13	Anti-Coincidence Mode with Anode Potential Tubes Uninstalled . . . . .	81
4.14	Surface Barrier Detector . . . . .	82
4.15	Surface Barrier Detector . . . . .	83
4.16	Circuit Diagram with Surface Barrier Detector Intalled . . . . .	84
4.17	Oscilloscope Displays the overlap between the signals on the SBD and the WTEPC . . . . .	85
4.18	Coincidence Mode with Anode Potential Tubes installed . . . . .	86
4.19	Coincidence Mode with Anode Potential Tubes Uninstalled . . . . .	87
4.20	Coincidence Mode with Anode Potential Tubes Uninstalled with an Extended Counting Period . . . . .	88
4.21	Experimental Set up of WTEPC and Electronics to Investigate Measurements in Coincidence Mode . . . . .	89
4.22	Far West Technology (F.W.T.) Commercial TEPC . . . . .	91
4.23	A measured Far West Technology (F.W.T.) $^{244}\text{Cm}$ Alpha spectrum . . . . .	92
4.24	$^{241}\text{Am}$ Alpha spectrum . . . . .	93
4.25	Alpha Particle Range in Propane TE-Gas . . . . .	95
4.26	Background spectrum . . . . .	97

4.27	$^{63}\text{Ni}$ Beta Spectrum 0 mm Source-Counter Distance . . . . .	98
4.28	Logarithmic Redistribution Technique for 50 Equal Logarithmic Bins per Decade of Lineal Energy, $y$ . . . . .	101
4.29	PenGeomJar Geometry Editing Tool in PENELOPE . . . . .	107
4.30	2D View of the Geometry Designed in PenGeomJar . . . . .	108
4.31	3D View of the Geometry Designed in PenGeomJar . . . . .	109
4.32	Simulating Beta particles with mean energy of 17.42 keV and end point energy of 66.95 keV with PENELOPE . . . . .	111
4.33	PENELOPE Subroutine Package "SHOWER.exe" Displaying 50 Electron Showers . . . . .	113
4.34	Plot of PENELOPE's <i>PENMAIN</i> Output File . . . . .	114
4.35	Principle of scoring of lineal energy values for a single incident electron . . . . .	116
4.36	Kliauga and Dvorak (1978) Benchmark Experiment . . . . .	118
4.37	2D View of the Kliauga and Dvorak Geometry Designed in PenGe- omJar . . . . .	119
4.38	3D View of the Kliauga and Dvorak Geometry Designed in PenGe- omJar . . . . .	120
4.39	Simulating 323keV photons with PENELOPE . . . . .	122
5.1	Alpha Dose Rate varied with Simulated Tissue Distances . . . . .	127
5.2	Microdosimetric Weighted Dose distribution for an Alpha Source at Four Simulated Tissue Distances ( $\mu\text{m}$ ) away from the WTEPC sensitive site . . . . .	128
5.3	$^{63}\text{Ni}$ Beta Spectrum . . . . .	131
5.4	Dose Rate from a $^{63}\text{Ni}$ Pure Beta Minus Emitter, varied against a Range of Simulated Tissue Distances . . . . .	135
5.5	RBE Values for Selected Beta Emitting Radionuclides . . . . .	136
5.6	Weighted Dose distribution for a $^{63}\text{Ni}$ Beta Source at Five Simu- lated Tissue Distances ( $\mu\text{m}$ ) away from the WTEPC . . . . .	138
5.7	$^{14}\text{C}$ Beta Spectrum . . . . .	139
5.8	$^{14}\text{C}$ Beta Emitter Dose Rate varied with Simulated Tissue Distances	141



5.9	Weighted Dose distribution for a $^{14}\text{C}$ Beta Source at Five Simulated Tissue Distances ( $\mu\text{m}$ ) away from the WTEPC . . . . .	143
5.10	Results for 1250 keV $^{60}\text{Co}$ Photon Irradiation Benchmark Experiment by Kliauga and Dvorak, 1978 . . . . .	145
5.11	PENELOPE Results for the Distribution $yd(y)$ as a Function of $y$ ( $\text{keV}/\mu\text{m}$ ) . . . . .	148
5.12	The Microdosimetric Distribution $yd(y)$ Plotted as a Function of $y$ on a logarithmic scale for five HP radionuclides Simulated by PENELOPE . . . . .	150
5.13	Schematic of the Source to Counter Simulated Tissue Distances for a $2\mu\text{m}$ diameter simulated cavity size and the beam angle along the negative $Z$ -axis . . . . .	152
5.14	Dose Rates in nano-Grays per electron Shower per Second are modeled as a Variation of the Simulated Source to Counter Tissue distances for $^3\text{H}$ and $^{63}\text{Ni}$ in a $2\mu\text{m}$ diameter tissue cavity for simulation parameters with a step length of 0.02 and a cut off energy of 250eV for 20 million electron showers. . . . .	156
5.15	Same as Figure 5.14 but for $^{14}\text{C}$ and $^{60}\text{Co}$ in a $2\mu\text{m}$ diameter tissue cavity for simulation parameters with a step length of 0.02 and a cut off energy of 250 eV for 20 million electron showers . . . . .	158
5.16	Same as Figure 5.14 but for $^{177}\text{Lu}$ and $^{90}\text{Sr}$ in a $2\mu\text{m}$ diameter tissue cavity for simulation parameters with a step length of 0.02 and a cut off energy of 250 eV for 20 million electron showers. . . . .	160
5.17	Microdosimetric dose distributions $yd(y)$ as a function of lineal energy, $y$ , calculated by PENELOPE for non-monoenergetic beta particles of $^3\text{H}$ entering a simulated $2\mu\text{m}$ cavity site. Simulation parameters were set for a cut off energy of 250 eV for $2 \times 10^7$ electron showers. . . . .	162

5.18	Microdosimetric dose distributions $yd(y)$ as a function of lineal energy, $y$ , calculated by PENELOPE for non-monoenergetic beta particles of $^{63}\text{Ni}$ entering a simulated $2\ \mu\text{m}$ cavity site. Simulation parameters were set for a cut off energy of 250 eV for $2 \times 10^7$ electron showers. . . . .	163
5.19	Microdosimetric dose distributions $yd(y)$ as a function of lineal energy, $y$ calculated by PENELOPE for non-monoenergetic beta particles of $^{14}\text{C}$ entering a simulated $2\ \mu\text{m}$ cavity site. Simulation parameters were set for a cut off energy of 250 eV for $2 \times 10^7$ electron showers. . . . .	164
5.20	Microdosimetric dose distributions $yd(y)$ as a function of lineal energy, $y$ calculated by PENELOPE for non-monoenergetic beta particles of $^{60}\text{Co}$ entering a simulated $2\ \mu\text{m}$ cavity site. Simulation parameters were set for a cut off energy of 250eV for $2 \times 10^7$ electron showers. . . . .	165
5.21	Microdosimetric dose distributions $yd(y)$ as a function of lineal energy, $y$ calculated by PENELOPE for non-monoenergetic beta particles of $^{177}\text{Lu}$ entering a simulated $2\ \mu\text{m}$ cavity site. Simulation parameters were set for a cut off energy of 250 eV for $2 \times 10^7$ electron showers. . . . .	166
5.22	Microdosimetric dose distributions $yd(y)$ as a function of lineal energy, $y$ calculated by PENELOPE for non-monoenergetic beta particles of $^{90}\text{Sr}$ entering a simulated $2\ \mu\text{m}$ cavity site. Simulation parameters were set for a cut off energy of 250 eV for $2 \times 10^7$ electron showers. . . . .	167
5.23	$^{63}\text{Ni}$ Comparisons of the Monte Carlo Simulation with the WTEPC Experiment . . . . .	171
5.24	$^{14}\text{C}$ Comparisons of the Monte Carlo Simulation with the WTEPC Experiment . . . . .	172

(The figures in colour are available in the electronic version)

# List of Tables

1.1	Beta Particles in Medicine . . . . .	12
3.1	Quadric surfaces used in PENGEOM . . . . .	59
4.1	An Estimate of the Experimental Uncertainties for Measurements taken by the Wall-less TEPC . . . . .	105
5.1	Beta Particles used in Monte Carlo Calculations and Experiments .	124
5.2	$^{241}\text{Am}$ Alpha Particle Measurements . . . . .	126
5.3	$^{63}\text{Ni}$ Beta Particle Measurements . . . . .	133
5.4	$^{14}\text{C}$ Beta Particle Measurements . . . . .	140
5.5	Comparisons of the Dose mean lineal Energies, $\bar{y}_D$ , from Kliuaga and Dvorak Experimental Results versus PENELOPE Simulations at $2\ \mu\text{m}$ Tissue Site Size . . . . .	146
5.6	Microdosimetric values calculated by PENELOPE simulating isotropic sources emitting electrons at various tissue distances away from a $2\ \mu\text{m}$ diameter simulated target size model of the wall-less counter. The mean energy-range relationship for beta particles emitted from each radionuclide are in parentheses. . . . .	154

# List of Abbreviations

<b>TEPC</b>	Tissue Equivalent Proportional Counter
<b>NEW</b>	Nuclear Energy Worker
<b>HP</b>	Hot Particle
<b>PPE</b>	Personal Protective Equipment
<b>IAEA</b>	International Atomic Energy Agency
<b>CANDU</b>	Canada Deuterium Uranium
<b>ICRP</b>	International Commission on Radiological Protection
<b>CNSC</b>	Canadian Nuclear Safety Commission
<b>RNT</b>	Radionuclide Therapy
<b>ICRU</b>	International Commission on Radiation Units and Measurements
<b>IPS</b>	Isotope Production System
<b>LET</b>	Linear Energy Transfer
<b>RBE</b>	Relative Biological Effectiveness
<b>LNT</b>	Linear No-Threshold
<b>IC</b>	Ionization Chamber
<b>PC</b>	Proportional Counter
<b>TDRA</b>	Theory of Dual Radiation Action
<b>TE</b>	Tissue Equivalent
<b>EFM</b>	Expedient Field Method
<b>HPDS</b>	Hot Particle Dosimetry System
<b>PENELOPE</b>	PENetration and Energy LOSS of Positrons and Electrons
<b>ORNL</b>	Oak Ridge National Laboratory
<b>WTEPC</b>	Wall-less type TEPC
<b>MCA</b>	Multi-Channel Analyzer
<b>SHV</b>	Safe High Voltage

<b>CSDA</b>	Continuous Slowing Down Approximation
<b>LLD</b>	Lower Level Discriminator
<b>ULD</b>	Upper Level Discriminator
<b>GD</b>	Gate and Delay generator
<b>SBD</b>	Surface Barrier Detector
<b>FWT</b>	Far West Technology
<b>FET</b>	Field Effect Transistor

# List of Symbols

$\mu m$	Micrometer
$Bq$	Becquerel
$H_p(0.07)$	The shallow dose equivalent limit
$Sv$	Sievert
$MeV$	Mega Electron Volt
$\beta$	Beta
$\gamma$	Gamma-ray or Photon
$H_p(10)$	Deep personal dose equivalence
$Ci$	Curie
$\theta$	Angle
$\phi$	Angle
$h$	Plank's Constant
$\nu$	Frequency
$c$	speed of light
$\bar{\epsilon}$	mean energy
$m$	Mass
$Gy$	Gray
$J$	Joule
$W$	W-value- Ion Pairs
$\alpha$	Townsend coefficient
$r$	Radius
$\infty$	Infinity
$\bar{Q}$	Quality Factor
$\bar{y}_D$	Dose Mean Lineal Energy
$\bar{y}_F$	Frequency Mean Lineal Energy

$y$	Lineal Energy
$\bar{l}$	Mean Chord Length
$\varepsilon_s$	Single Energy Deposition
$\rho$	Density
$\lambda$	Mean free path

# Chapter 1

## Introduction

### 1.1 Hot Particles

The Nuclear Energy Worker (NEW) and the environment surrounding a nuclear power plant, are vulnerable to "Hot Particle"(HP) hazards in the form of beta and beta/gamma emitting radioisotopes. A NEW may be at risk from contamination events arising from regular plant operations or during the controlled decommissioning or refurbishment at a nuclear installation. The relative risk to a NEW is quantified by occupational exposures to ionizing radiation that may result in disease such as cancer. Other exposures epidemiologically prevalent among NEWs globally are the risk of developing eye lens opacification through cataractogenesis. The surrounding environment and the public are also open to any pollutant that could potentially be expelled in the event of a severe nuclear plant accident, and there is a growing awareness that protection limits supporting people may not be sufficient to protect the diversity within the natural biota. HPs are defined by several authors [1], [2], [3] and [4], as very small, ranging from 1 mm down to 100  $\mu m$ . They are barely visible particulates of radioactive materials, with high specific activity and are often electrically charged. HPs tend to cling to the skin or onto Personal Protective Equipment (PPE) and pose a risk of external and internal exposure. They are capable of delivering shallow doses at a rate that could cause the shallow dose equivalent limit to be exceeded within a few hours or sometimes less. According to Charles and Harrison (2007), the term "hot particle" was conceived some 50 years ago as a result of the irregular dose patterns occurring from distinct beta particle sources found in the lungs



---

following a "radioactive fallout on a nuclear battle field" [2]. HPs from nuclear fuel are usually called fuel fragments, but are also referred to as "fleas" [2] due to their small size and mobility. The "hot" in "hot particles" indicate that the fragment is radioactive and potentially highly contaminating. HPs of focus in the nuclear industry are typically beta or beta-gamma emitting radionuclides. It is believed HPs originate predominately from degraded fuel and from neutron activated corrosion and wear products such as stellite (cobalt-chromium alloys) [5]. Figure 1.1 shows a magnified ( $100\ \mu\text{m}$ ) image of Plutonium and Strontium HPs examined by a X-ray micro-tomography spectrometer, after being separated from the surface of a coral atoll sediment in Mururoa, French Polynesia [6], an indication that HPs remain in the environment long after a nuclear weapons tests. The characterization of radioactive particles originating from fallout at weapons test sites were comprehensively covered by an International Atomic Energy Agency's (IAEA) report, 2011, for radioactive particles in the environment [6]. The report publishes the characterization of HPs from severe nuclear reactor accidents and dumped nuclear wastes incidents occurring up to August of 2011.

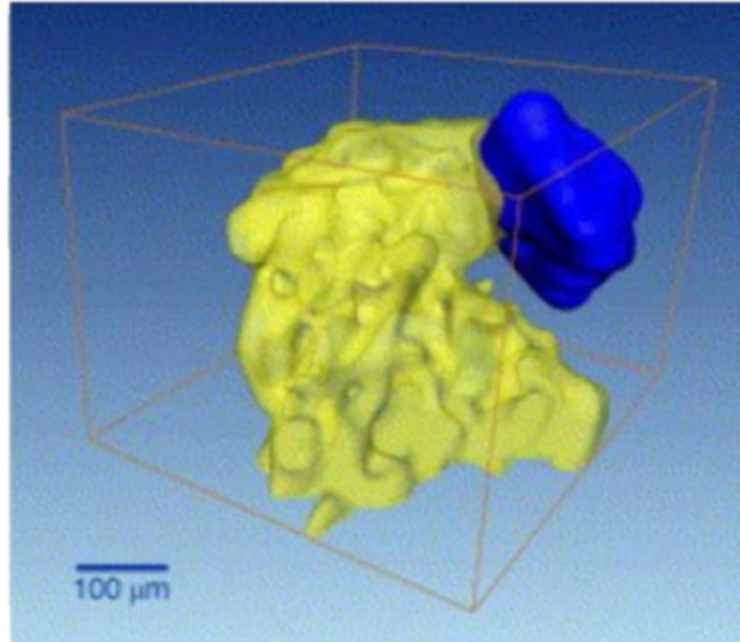


FIGURE 1.1: HPs from the Maruroa Atoll showing the distribution of Sr (larger, yellow mass) and Pu (smaller, blue mass) merging after a nuclear explosion

[6]

The nuclear accident on March 11, 2011 at the Fukushima Daiichi power plant in Ōkuma, Fukushima Prefecture, Japan, has been the latest nuclear accident. According to the International Atomic Energy Agency report (2015), on the radiological consequences of the Fukushima Daiichi accident, radioactive material was released into the environment, both to the atmosphere and into the ocean. Statistical analysis using Bayesian techniques suggests that the mean activity for  $^{131}\text{I}$  in the atmosphere was between 140 and 200 PBq [7]. For  $^{137}\text{Cs}$ , the mean activity released to the atmosphere was estimated to be between 12 and 16 PBq [7]. The IAEA report (2015), indicated that the total measured release

of  $^{131}\text{I}$  was estimated to have been 20% of the release from the Chernobyl accident, while the total measured release of  $^{137}\text{Cs}$  was estimated to have been 35% of the release from the Chernobyl accident [7]. Unlike the Chernobyl accident, the Fukushima Daiichi accident is estimated to have led to only negligible releases of radionuclides such as  $^{90}\text{Sr}$  and  $^{239}\text{Pu}$  [7]. Release of  $^{137}\text{Cs}$  in the ocean were estimated in the range of 1-6 PBq and release of  $^{131}\text{I}$  were measured in the range of 10 to 20 PBq. The maximum recorded activity concentrations of  $^{131}\text{I}$  in air was  $1600\text{ Bq/m}^3$ , and for  $^{134}\text{Cs}$  and  $^{137}\text{Cs}$   $180\text{ Bq/m}^3$  and  $190\text{ Bq/m}^3$  respectively, within the same sampling period. It was also reported that restrictions on drinking water consumption was put in place for several areas with levels of  $^{131}\text{I}$  exceeding  $100\text{ Bq/kg}$  around the time of the accident. The maximum recorded activity concentration measured in drinking water came from the Fukushima Prefecture at  $965\text{Bq/kg}$ , restrictions to consume drinking water (not bottled water) were lifted on April 1st, 2011 in that area [7]. Radionuclide measurements of  $^{131}\text{I}$ ,  $^{134}\text{Cs}$  and  $^{137}\text{Cs}$  were found in terrestrial and aquatic foods at levels requiring restrictions on the sale and distribution of these food items. The average activity concentration on  $^{131}\text{I}$  in leafy vegetables was measured at around  $1954\text{ Bq/kg}$ . Radio-cesium in agricultural products such as rice are well documented in [7]. Cultivation of rice a staple food in Japan was restricted in soil if radio-cesium concentrations exceeded  $5000\text{ Bq/kg}$ . A very high percentage of samples for raw milk, eggs and meat predominately had activity concentrations of radio-cesium below  $50\text{ Bq/kg}$ . Relatively high concentrations were measured in alternative food sources (country foods) such as in wild boar, wild mushrooms, and wild berries. The activity concentrations of all food items are well documented in [7] and other IAEA technical documents. It was recommended that groundwater surveillance continues as groundwater still enters the damaged buildings and contributes to an increase in the amount of water containing radionuclides that needs to be treated, stored, or discharged.

Isolated particles from samples collected in 2016 at Nagoya, 433 km away from the Fukushima Daiichi accident location, were analyzed by scanning electron microscopy and energy dispersive X-ray spectroscopy. Individual HPs were identified by auto-radiography [8], and reaffirmed the persistence of these materials,

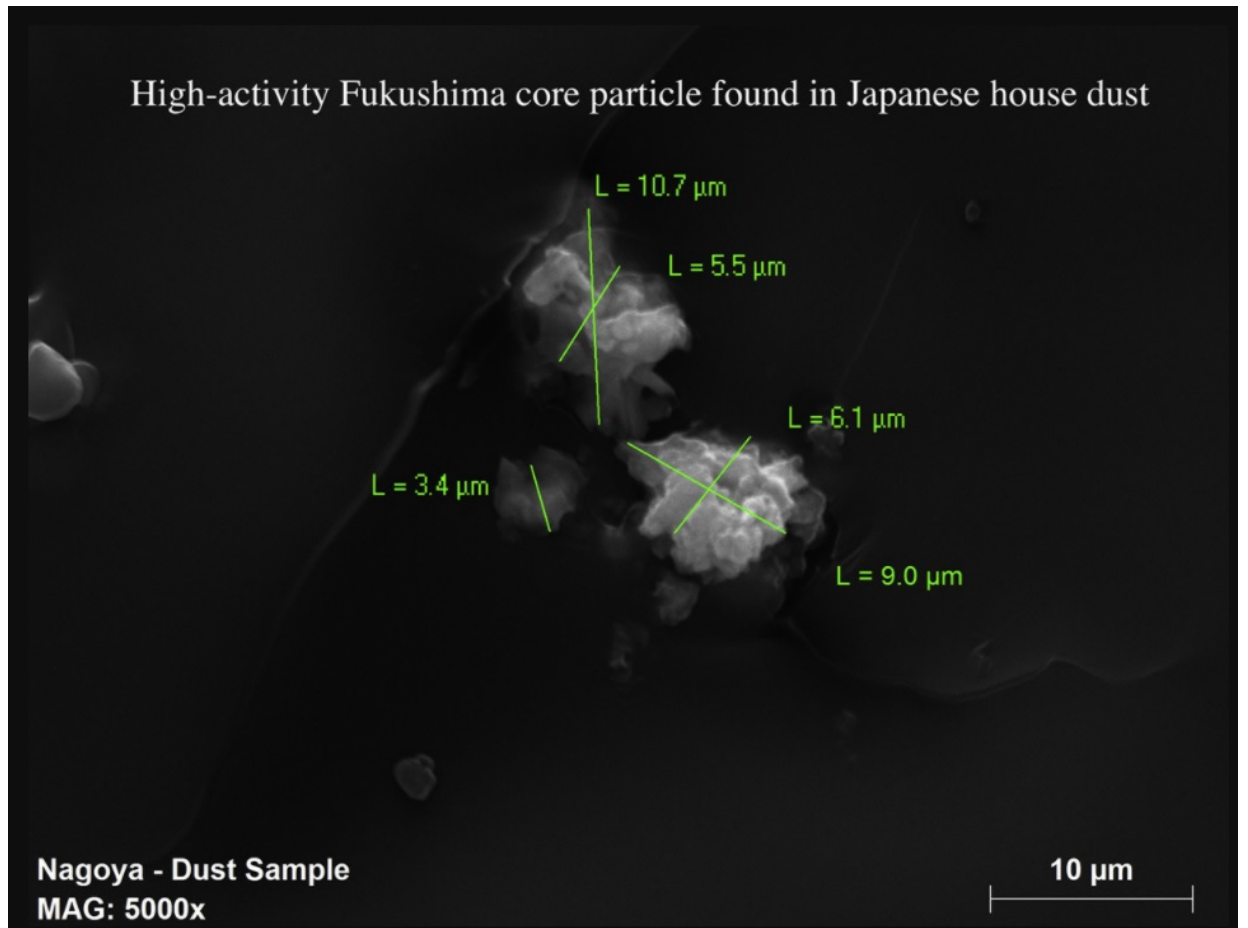


FIGURE 1.2: HPs from the Fukushima core found in Nagoya (433 km from Fukushima Daiichi) particle ranging in size from 3.4  $\mu\text{m}$  to 10.7  $\mu\text{m}$ . The activity of the HPs measured 324 Bq by gamma spectroscopy and 285 Bq by beta-counting, using a Ludlum Model 3030 beta ratemeter [8].

remaining in the environment roughly 5 years later. The fuel particulate materials identified from the emissions were  $^{134}\text{Cs}$  and  $^{137}\text{Cs}$ , and were characterized as having high specific activities [8]. Figure 1.2 illustrates a sample taken from dust and soil particulates. The samples recorded a gamma and beta particle signature and ranged in size from  $3.4\ \mu\text{m}$  to  $10.7\ \mu\text{m}$ . The authors of this study concluded that accurate radiation risk assessments required data for HP exposure, as individuals in this region may have received inhalation and ingestion doses higher than the mean dose calculated from average environmental data. Similarly in a contamination event or accident at a CANDU nuclear facility, occupationally exposed NEWs are potentially open to inhalation and ingestion events resulting from micron-sized volumes of radioactive HPs. In this thesis an alternative method to those currently being used in the industry for measurement and quantification of dose rate and the potential change in radiation quality as a function of depth in tissue from hot particles is posed and investigated.

The International Commission on Radiological Protection (ICRP) is an established international body responsible for improving protection against ionizing radiation. The body recommends administrative controls for localized skin exposures to HPs, specifically skin dose contamination limits [9] [10]. The maximum permissible exposure to the extremity of an occupationally exposed worker recommended by the ICRP is 0.5 Sv per year at a depth of  $70\ \mu\text{m}$  over an area of  $1\text{cm}^2$  also called  $H_p(0.07)$ , the shallow dose equivalent limit. The dose limit recommendation for general public exposure is an order of magnitude lower at 0.05 Sv [2]. The ICRP publishes guidelines on how to protect against the risks associated with ionizing radiation from radioactive sources used in medicine, general industry and nuclear facilities. These high-level guidelines are intended to instruct regulators and operators in demonstrating compliance with existing and future legislation. The local Canadian Nuclear Safety Commission (CNSC) is the federal regulator for nuclear power and materials in Canada, and has taken significant steps to incorporate and amend where necessary the guidance and advice from the ICRP. For Canadian licensees, the expectation for immediate reporting to the CNSC for skin contamination is 50 mSv for a NEW and 5 mSv for a non-NEW [11]. Notwithstanding these protection limits, the practical challenges

of HP dosimetry still exists. One major challenge is determining absorbed dose and the risks from internal exposures to HP radionuclides and the assessment of the potential adverse biological response. Estimating the likelihood of non-stochastic effects developing as a result of exceeding these dose limits set by the ICRP is another significant challenge faced. Equal to the task is the difficulty in dose measurements over thin layers, such as the basal cells at the bottom of the epidermis of the skin [1]. Figure 1.3 illustrates the units, scale and sizes of measured components and parts associated with various depths in tissue. From an external contamination point of view the images show a progression from a thumb, to skin, to skin cells and sub-cellular components and the dimension of the associated molecular structures of cells. For this thesis the reader should also bare in mind that contamination can be internal, via ingestion, there is a risk to the cells in the gastrointestinal tract and the stem cells in the crypt of the villi usually range in size from 8 to 20  $\mu m$ . From an inhalation event the cells in the lungs or on flattened surfaces typically have sizes around 10  $\mu m$ . The HP problem to the NEW, indicates just some of the challenges that require further investigation. In managing the risk to the NEW, it is important to consider all potential elevated effectiveness from HP radiation in an effort to improve the quality of radiation protection. The development of methodologies for advanced dosimetry mechanisms are believed to be a potential solution to these challenges [1]. In the sections to follow further rational for investigating beta particles or HPs having a beta/gamma signature are reviewed.

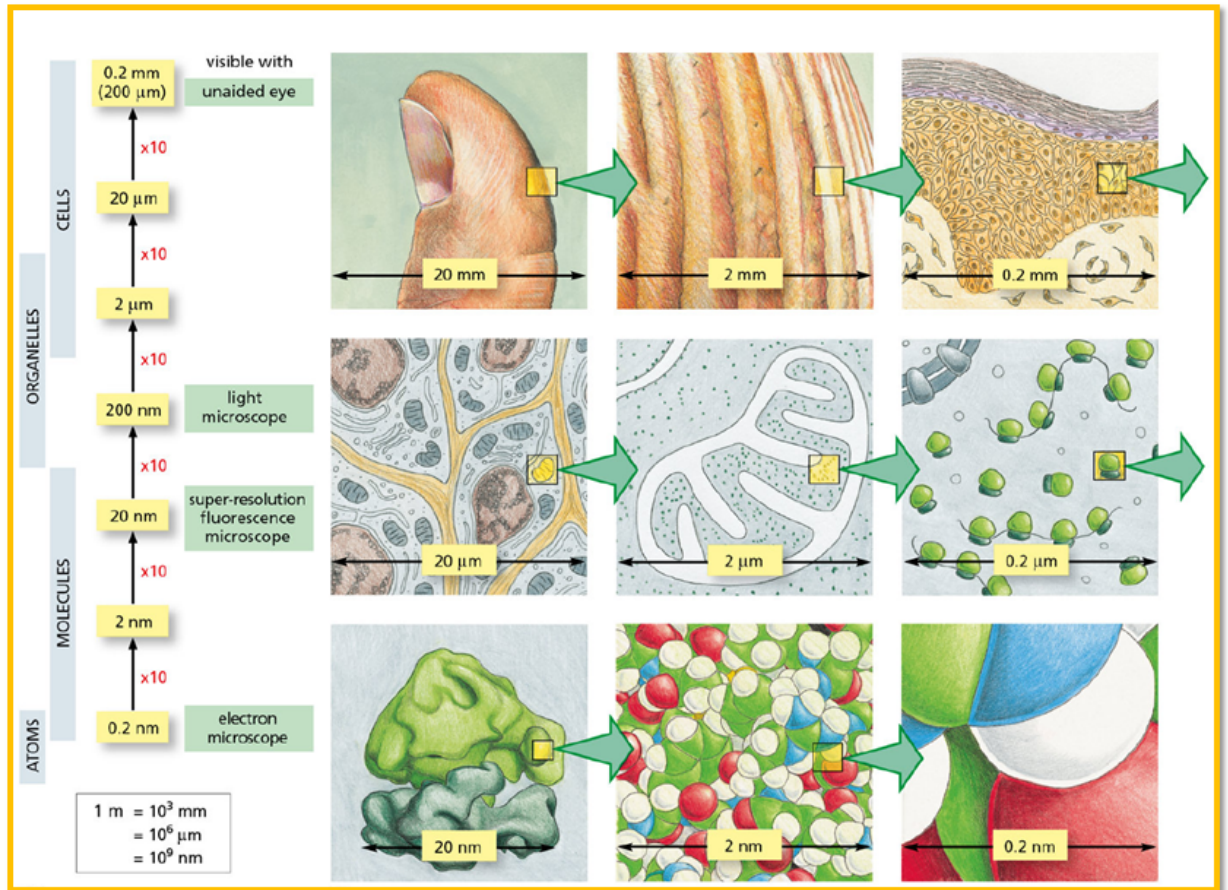


FIGURE 1.3: The sizes of cells and the internal dimensions of their component parts progressing from a thumb, to skin, to skin cells and to sub-cellular molecular components. A  $2 \mu\text{m}$  dimension for a flattened surface cell is a convenient and conservative match for sub-cellular geometries modelled in this thesis [12].

## 1.2 Relevance of Beta Emitters in Radiation Science Studies

Radionuclides characterizing HPs emit beta and gamma radiation. The sections to follow will continue the discussion on HPs, further highlighting their relevance in industry and comparative issues found in medicine.

As discussed earlier in Section 1.1, HPs can be fuel fragments, and many fission products emit beta radiation [6]. In medicine radioactive particles used for treatment also decay by emission of beta particles and are produced in nuclear reactors or from charged particle accelerators. Fission products are neutron-rich and may undergo decay releasing energy in the form of beta particles, anti-neutrino and gamma rays. In this work one focus will be on measuring the energy deposited in tissue by beta particles emanating from  $^{63}\text{Ni}$  and  $^{14}\text{C}$  sources representing a hot particle exposure. Figure 1.4 shows HPs discovered at different reactor installations in the United Kingdom, displaying very small sizes (ranging from  $100\ \mu\text{m}$  to  $1\ \text{mm}$ ) with high specific activities. The "AGR mixed fission product particle", in particular, shows a magnified image of a HP at  $100\ \mu\text{m}$ , which is virtually undetectable with the naked eye, but having a skin dose rate of a few Grays per hour. Over a regulated depth of 70 microns and an area the size of  $1\ \text{cm}^2$  a skin contamination event from this particle is likely to exceed the regulated limit and could be deadly if ingested or inhaled. A clear indicator of the severity of potential exposure to a NEW and the surrounding work environment.



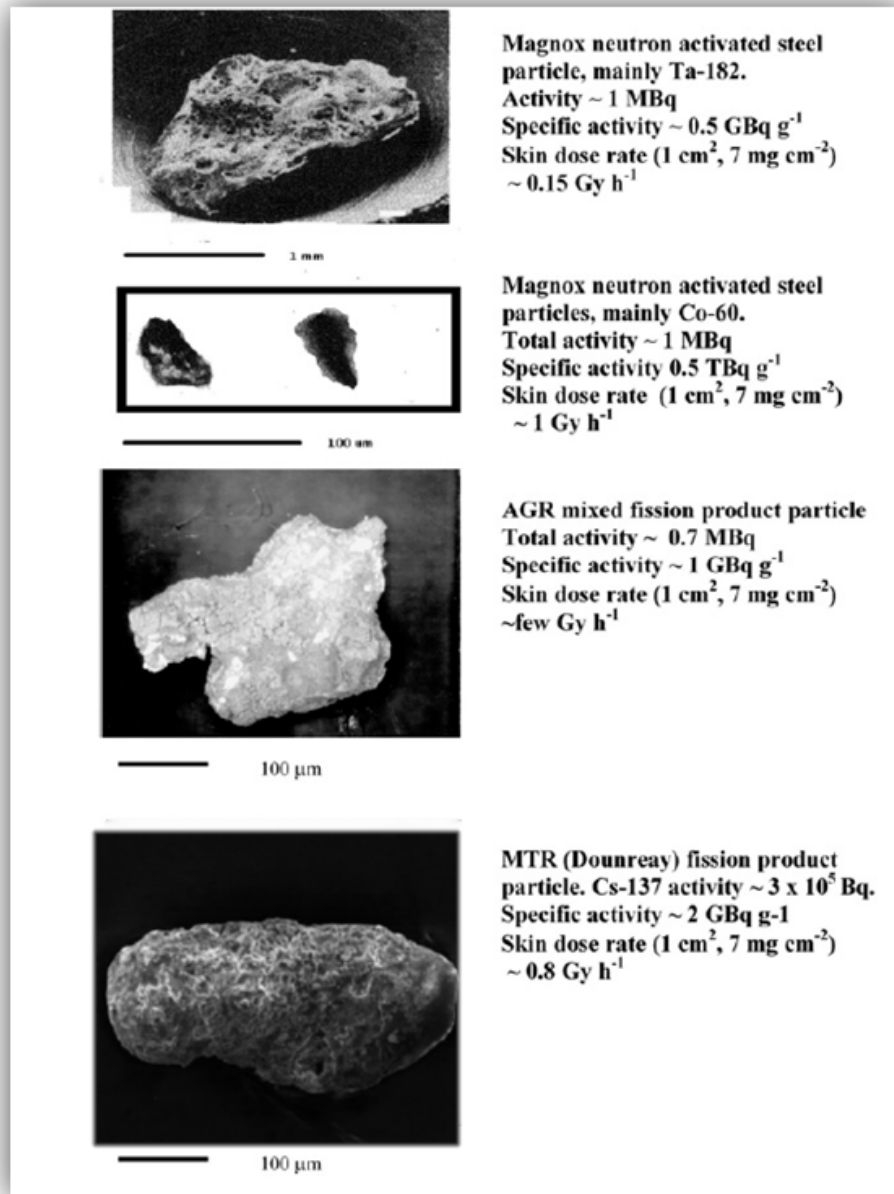


FIGURE 1.4: Examples of the relative size, activity and skin dose rates found in HPs at UK power reactor sites [2]

### 1.2.1 Medical Relevance

Beta particle sources play a significant role in the treatment of certain medical conditions. Ionizing radiation fields in the form of beta particle emitting sources have been designed in such a way to deliver a precise dose to a specific disease site in the body. Minimizing exposure to patients and medical workers while administering comprehensive treatment for medical conditions such as cancer is an essential task in the advancement of dosimetry. Table 1.1 shows a list of radionuclides potentially administered in the treatment mechanism for malignant diseases. Some of these radionuclides are produced in nuclear installations (for example:  $^{32}P$ ,  $^{105}Rh$  and  $^{131}I$  etc.), others are generated in charged particle accelerators (for example:  $^{177}Lu$ ,  $^{47}Sc$ ,  $^{64}Cu$  and  $^{67}Cu$ ) [13]. Omitted from Table 1.1 is  $^{125}I$ , an important gamma ray emitter (0.035 MeV), used in biological assays, nuclear medicine imaging and in radiation therapy as brachytherapy to treat several medical conditions.

TABLE 1.1: Radionuclides emitting Beta particles potentially used in treating medical conditions, particularly cancer [13]. The isotopes are listed along with their half life in days, the end point energies of their beta particles and associated gamma ray energies given in MeV.

Radionuclide	$t_{\frac{1}{2}}$ (Days)	$E_{\beta}$ max (MeV)	$\gamma$ -ray energy (MeV)
$^{32}P$	14.3	1.71	0.159
$^{47}Sc$	3.4	0.6	0.511
$^{64}Cu$	0.5	0.57	0.184
$^{67}Cu$	2.6	0.57	0.092
$^{89}Sr$	50.5	1.46	0.319
$^{90}Y$	2.7	2.27	0.306
$^{105}Rh$	1.5	0.57	0.342
$^{111}Ag$	7.5	1.05	0.158
$^{117m}Sn$	13.6	0.13	0.364
$^{131}I$	8.0	0.81	0.286
$^{149}Pm$	2.2	1.07	0.103
$^{153}Sm$	1.9	0.8	0.81
$^{166}Ho$	1.1	1.6	0.113
$^{177}Lu$	6.7	0.5	0.208
$^{186}Re$	3.8	1.07	0.137
$^{188}Re$	0.7	2.11	0.155

The interest in this work associated with medical applications, is the mechanism of radioactive materials emitting beta particles towards a target tissue which is comparable to the mechanism of HPs contaminating the skin or internal organs of a NEW. Sealed and unsealed sources of ionizing radiation are used in therapeutic applications to treat cancerous diseases. Unsealed source radionuclide therapy (RNT) or molecular radiotherapy, uses HPs in the form of radiopharmaceuticals. Sealed source RNT is referred to as brachytherapy and are seeds or capsules of these radiopharmaceutical (such as  $^{125}I$ ) that are physically implanted into an area precisely defined by the medical practitioner in treatment

planning. Matching the size of the tumor and the energy and range of the isotope is crucial to the success of the treatment [13]. It is possible for smaller tumors treated with high energy beta particles to have reduced deposition inside the tumor due to most of the energy absorption occurring outside of the tumor volume. In contrast for larger tumors, total absorption of the beta particle energy may occur inside the tumor volume, reducing the escape of energy to untargeted tissues. The physical characteristics of beta particles having a short range which results in a high dose gradient or steep dose fall off with distance provides this advantage in treatment. According to the International Commission on Radiation Units and Measurements (ICRU) [14] the useful range in treatment is up to 3 mm for beta rays and for low energy photons up to 10 mm. Absorbed dose in micron-sized tissue volume depends strongly on the source to measurement distance at close distances for seed-sources delivering beta particles and photons [15]. The variation in distance of the dose rate is directly related to the inverse square law, attenuation, and build up in the treatment volume. However, at very close distances the inverse square becomes the main factor resulting in high dose rate gradients [15]. This highlights the importance to this work, as measurements of the absorbed dose distribution in close proximity to a beta source (or photon source) is not a trivial task. There are other areas of interest such as accident and interface dosimetry (e.g. bone and tissue interface), and operational eye dosimetry (occupational exposure to the lens of the eye) where accurately determining the absorbed dose distribution to the sensitive volume has been difficult.

## 1.2.2 Industrial Relevance

Canada is committed to the peaceful uses of clean, low-carbon nuclear energy systems and radioactive materials. This is evident in the Province of Ontario which has eighteen (18) CANDU commercial nuclear power generating units. There is one (1) nuclear installation in New Brunswick, and ten (10) CANDU nuclear installations in operation outside of Canada. These reactors are all governed under the same Canadian nuclear non-proliferation policy for the peaceful use of Canadian Uranium. In 2015, power reactors supplied 16.6% of Canada's

total electric energy generation. In the Province of Ontario, nuclear power supplied 60% of the energy demand in 2015. Risk analysis predictions indicate that a severe accident can be expected once or twice every 100 years due to the number of nuclear reactors and radioactive materials active in industries across the world, and the frequency of accidents occurring thus far. Historically, the frequency of a severe accident at a nuclear installations is one event every 25 years. Decommissioning, refurbishment or plant maintenance activities is another avenue for the release of HPs. Lastly, nuclear weapons testing even though less frequent now, has added to the burden of HPs released into the environment. Realistically the potential for a large scale accident to occur in Ontario and therefore Canada exists along with potential accidents related to the use of radioactive materials. In order to minimize the potential effects significant research must continue in nuclear engineering and radiation-health physics disciplines, to contribute up to date information and methods to the public, users, regulators and safety stakeholders.

In recent publications of industrial relevance [16] [17], the authors addressed the ICRP's 2012 recommendation for lowering the annual dose limit to the lens of the eye from 150 mSv to 50 mSv. The steam generators around CANDU facilities were identified as a high risk location with high beta fluence rates expected for CANDU nuclear power plant workers. The joint investigation across the plants (OPG: Darlington and Pickering, and Bruce Power A) assessed the operational dosimetric quantities deep and shallow personal dose equivalence  $H_p(10)$  and  $H_p(0.07)$  respectively. With one study concluding that skin dose or  $H_p(0.07)$  can be used as a conservative surrogate for eye lens dose [17].

Also of interest to this work is the installation of an Isotope Production System (IPS) in 2021, at Bruce Power's nuclear generating station, with support from Isogen ("partnership between Kinetrics and Framtome") for the production of Lutetium -177 ( $^{177}\text{Lu}$ ). This isotope is a radiolanthanide with a short range in soft tissue of approximately 0.6mm ( $E_{ave} = 133\text{keV}$ ). In the production of  $^{177}\text{Lu}$ , natural or enriched  $^{176}\text{Lu}$  is irradiated directly with thermal neutrons from a reactor:  $^{176}\text{Lu}(n, \gamma)^{177}\text{Lu}$ . Indirectly,  $^{177}\text{Lu}$  is also produced by neutron irradiation of natural or enriched  $^{176}\text{Yb}$  producing short lived  $^{177}\text{Yb}$  ( $T_{1/2} = 1.9\text{h}$ ), which

decays to the desired  $^{177}\text{Lu}$ :  $^{176}\text{Yb}(n, \gamma)^{177}\text{Lu} \rightarrow ^{177}\text{Lu}$ .

It is important to note that security clearance providing access to HP accident reports, and contamination events that have occurred in Canada's nuclear installation or radioactive facilities could not be obtained by the investigator to further support the relevance of HP dosimetry in industry, as presented in this thesis.

### 1.3 Motivation for Thesis

Understanding the impact of radioisotopes likely released into the environment by a severe accident from a nuclear power plant, during decommissioning, or refurbishment activities requires the quantification of absorbed doses as well as the appropriate radiation weighting factors. Achieving this will require using and developing advanced dosimetry and micro-dosimetry methods and analysis principles. Microdosimetric techniques provide a quantitative description of the stochastic nature of energy depositions in irradiated cell-nuclei sized micrometric targets. This measurement technique will provide a physical quantity that can be used to predict the potential biological damage of low-energy beta emitters likely to be released in the event a severe nuclear accident in Ontario.

This study contributes to advancing the fundamental understanding of beta particle dosimetry. The research program design is to assist nuclear industry partners in response to changing regulatory demands, and to provide fundamental data that can assist the formulation of new national regulations. This work intends to reduce uncertainties in science around the radiological impact of low energy radiation. As the province of Ontario continues its mandate of a low-carbon economy and the fight against climate change and its future electrical power demands progress, there is a need to optimize protection in all exposure situations and for all categories of exposure.

Interest in the study of hot particle dosimetry is stimulated by the fact that beta particles will have a finite range depending on the energy spectrum of the radionuclides associated with the HPs. Therefore, absorbed dose and dose gradients are likely to be steep. If an occupationally exposed worker ingests a HP, or a

HP gets onto the skin of the worker, knowing how the dose is changing with distance away from the HP is important. This will determine what it will irradiate, what it will affect, and ultimately what the dose imparted to that volume of tissue will be. There is a comparable problem in radiotherapy where very localized treatment is required by implanting a radioisotope with limited range beta particles, for example  $^{125}\text{I}$  used in prostate cancer treatment. There are also other modalities, where determining how the absorbed dose gradient varies could be important. However, for this study the aspect of operation or decommissioning or refurbishment in a nuclear plant, or during accidental releases or contamination resulting from a HP, is the primary focus and concern.

## 1.4 Objectives of Thesis

The objectives of this thesis are to determine how the absorbed dose-rate and radiation quality will change with distance in tissue from a low-energy beta particle source, thereby contributing to our understanding of the potential impacts of a HP contaminant. Beta sources emit beta particles (electrons) with a spectrum of energies including many low energy particles with limited ranges in tissue. This means that moving away from a HP like source, the dose-rate is expected to decrease based on the inverse square law, but also because of the range of the beta particles themselves. Thus, dose-rate gradients are likely to be steep, making measurements difficult with conventional radiation counters and chambers as well as increasing the uncertainty of determining the dose to a particular biological structure such as a layer of critical cells in skin or gut tissue. The situation is further complicated by a potential change in radiation quality as low energy electrons have a higher stopping power (higher Linear Energy Transfer or LET) than higher energy electrons. For a given beta spectrum, over a short distance, all the lower energy beta particles will be absorbed leaving the more energetic particles. Therefore, not only will dose-rate gradients be steep but the fact that the energy spectrum of beta particles is changing leads to the possibility of some variation of radiation quality with distance from a HP. The objective of the research recorded

in this thesis is to investigate through experimentation and Monte Carlo computation the possible changes in radiation quality, expressed in microdosimetric quantities as well as the absorbed dose-rate gradients for a selection of beta emitting radionuclides relevant to hot particle dosimetry and radiation biology.

### 1.4.1 Approach

To arrive at achieving these objectives:

- A wall-less proportional counter was designed and constructed and a series of experimental measurements conducted for dose rate determination and microdosimetric analysis as a function of tissue distance using a  $^{63}\text{Ni}$  ( $10.1\mu\text{Ci}$ ) and  $^{14}\text{C}$  ( $103.9\text{ nCi}$ ) beta particle source. An  $^{241}\text{Am}$  ( $0.1045\mu\text{Ci}$ ) alpha particle emitter was used to calibrate the counter.
- Monte Carlo simulations using the electron-positron transport code PENELOPE were carried out to provide computational results for various beta particle source scenarios. A reference experiment by Kliauga and Dvorak (1978) that measured the microdosimetric spectra for low energy photons with a wall-less counter [18] was used to benchmark the Monte Carlo simulations. The PENELOPE simulations included modeling the experimental measurements in order to compare results and draw final conclusions regarding the performance of both code and experimental apparatus.

## 1.5 Outline of Thesis

Chapter 1 presents the rationale for carrying out this study. The relevance of radionuclides decaying by emitting beta particles in industry and medicine were also reviewed. The significant problems HP poses to NEWs and the environment were also discussed. Finally, to complete this chapter, the motivation and objectives highlighting the need for added research in this area of hot particle dosimetry were considered. In Chapter 2, further discussions on the theoretical background to radiation dosimetry and interactions of ionizing radiation with matter



are given. Different dosimetry principles that currently exist are reviewed, and the concept of microdosimetry and its potential to provide measurements toward the objectives of this study are presented. The properties of proportional counters will be discussed and the rationale for choosing to design and construct a wall-less type counter are given. The relevant literature reviewed to determine the status of work being done in the area of hot particle dosimetry, Monte Carlo simulation and gaps in the knowledge from peer reviewed articles are covered in Chapter 3. Chapter 4 offers details about the design and operation the wall-less Tissue Equivalent Proportional Counter (TEPC). The procedures used to determine the relevant microdosimetric quantities are discussed along with the uncertainties in values determined. The chapter concludes by presenting the parameters used with PENELOPE for Monte Carlo simulations of the experiment. Chapter 5 provides the results and a comprehensive discussion on the findings of these investigations. Finally, Chapters 6 forms the conclusions of this study and offers some argument for future work towards improving the knowledge of hot particle dosimetry.

## Chapter 2

# Radiation Dosimetry and Radiation Quality

In Chapter 1, the relevance, motivation and objectives for this thesis were highlighted. There were also terminologies and conditions that may not have been clearly defined and require additional background knowledge and information. In this chapter the theoretical background and the stochastic nature of radiation interactions are reviewed. HP dosimetry and interactions for beta-gamma radiation with matter are discussed. The theory of dosimetry, radiation quality, techniques of experimental microdosimetry, and the properties, design and use of TEPCs are discussed in this chapter.

## 2.1 Interaction of Beta Particles and Photons with Tissue

According to Frank Herbert Attix a pioneer in this field of study, "radiation dosimetry (or simply 'dosimetry') deals with the measurement of *absorbed dose* or *dose rate* resulting from the interaction of ionizing radiation with *matter*" [19]. The important concept and measurement of absorbed dose is dealt with separately and in more details in the section 2.2 that follows. "Matter", within the context of this thesis refers to biological tissue, which primarily consists of

the fundamental elements Hydrogen, Carbon, Nitrogen and Oxygen. Hot particle (HP) interactions with matter or tissue occurs in two ways. Either by direct charged particle (electrons or alphas) interactions or by indirect neutrally charged particles (photons or neutrons) generating secondary electrons or other charged particles. The kinetic energies absorbed can disrupt biological systems made up of micron-sized organic molecules such as the cell nucleus and chromosomes containing the nano-scopic sized deoxyribonucleic acid (DNA) chains comprising of those four base elements mentioned. DNA can undergo mis-repaired damage which can result in a negative outcome such as cancerous disease formations. For a HP decaying by emitting beta radiation, fast streams of positrons or electrons (negatrons) directly deposit ionizing radiation in matter through coulomb or electrostatic forces of interaction. The interaction occurs between the beta particles and the orbital electrons within the atomic shells of elements within the absorbing medium. Close to all energy can be lost in a single collision with an electron of equal mass, leading to the beta particle or electron undergoing an abrupt change in direction. Figure 2.1 shows the behavior of ten (10) electron tracks in a slab of water, one electron track changes direction undergoing a back-scatter and escapes the slab. Non-monoenergetic beta particles are expected to emanate from HPs, and will have an attenuation in a given material that is determined by the equation:

$$I = I_o e^{-nt} \quad (2.1)$$

Where  $I$  is the counting rate with absorber,  $I_o$  is the counting rate without absorber,  $t$  is the absorber thickness ( $\frac{g}{cm^2}$ ); and  $n$  the absorption coefficient[20]. HPs also produce gamma-ray photons which indirectly deposit energy in matter through collisions with the orbital electrons or nucleus of an atom, resulting in the release of electrons or positrons. The photon interactions occur through three processes: the photoelectric effect, Compton scattering and pair production. The dominant process depends on the energy of the photon's emanating from the HPs and the material the photons interact with. For the photo-electric effect the photon dissipates by giving up all its energy to the ejected electron. An equation of the reaction is given by:

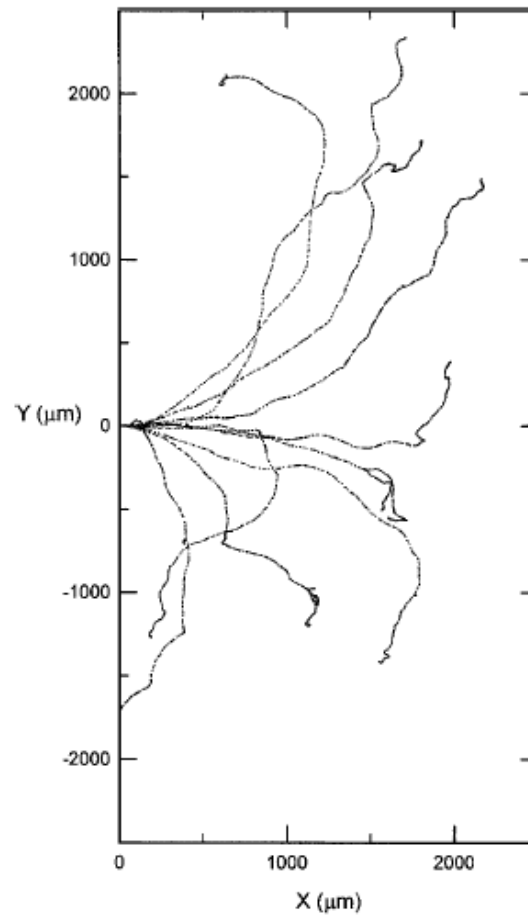


FIGURE 2.1: 740keV electrons in a water slab, showing one track back-scattered out of the slab to the origin along the XY-plane. Retrieved from: James Turner (1995), "Atoms, Radiation and Radiation Protection" [21].

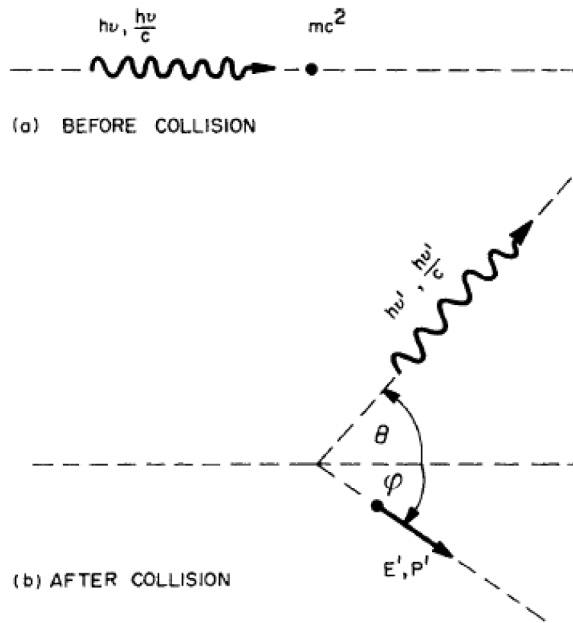


FIGURE 2.2: A photon with energy  $h\nu$  collides with an electron at rest in (a). Compton scattering occurs after the collision with the photon scattered at angle  $\theta$  and the electron at an angle  $\psi$  in (b). Retrieved from: Jamaes Turner (1995), "Atoms, Radiation and Radiation Protection"

[21]

$$E_k = h\nu - E_b \quad (2.2)$$

$E_k$  = Photoelectron's Energy,  $h\nu$  = Photon Energy, ( where,  $h$  is Plank's constant and;  $\nu$  is the frequency of the Photon)  $E_b$  = Binding Energy of Photoelectron shell [20]

In the Compton effect, photons are deflected from their incident angle by an electron in the reacting medium, a partial transfer of the photon's energy takes place with the recoiling electron. Figure 2.2 gives a visual of what occurs before and after a photon collides with an electron, causing it to scatter at an angle away

from the trajectory of the incident photon, which becomes deflected and undergoes an energy change. The liberated recoil electron energy can range from zero to a substantial fraction of the incident photon's energy. Therefore the effect on the incident photon energy is represented by the equation:

$$h\nu' = \frac{h\nu}{1 + \frac{h\nu}{m_0c^2}(1 - \cos\Theta)} \quad (2.3)$$

Pair production occurs when the incident photon energies are greater than 1.022 MeV and interacts with the nuclear field around the nucleus producing an electron-positron pair equally having a rest energy of 511 keV. At energies greater than 1.022 MeV, the electron-positron pair will share the excess energy as kinetic energy. Figure 2.3 shows the region where pair production is more likely to dominate, with each line of the curves indicating equal probability of the other photon interaction types dominating in a given medium of atomic number  $Z$ , with  $h\nu$  in MeV. If and only if the gamma-ray energy exceeds 1.02 MeV, can the process of pair production be expected.

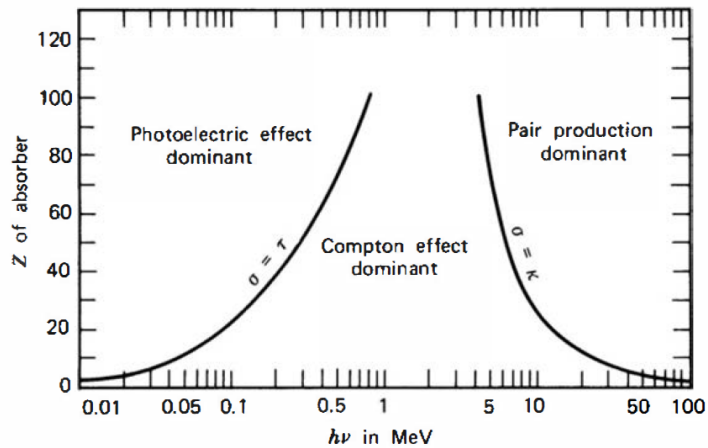


FIGURE 2.3: The three main types of gamma-ray interaction. Retrieved from: Glenn F. Knoll (2010), Radiation and Detection and Measurement, 4th edition" [20].

Taken together both beta particles and gamma liberate charged particles. The

energy transfer or absorbed dose we should expect from HPs is a result of the physical properties of the radiation fields they emanate and the subsequent interactions of their liberated charged particles.

## 2.2 Absorbed Dose Concept and Measurement

From absorbed dose data derived from the Japanese bomb survivors we have been able to determine the relative risks from exposure to ionizing radiation[22]. Currently, a simple linear model is accepted in radiation protection that extrapolates high risk from high absorbed dose in a proportional relationship, to a resulting low risk at low absorbed doses [22]. This model is called the linear no-threshold (LNT) model and suggests that the relative risk from exposure to a beta particle (or photons) is proportional to the dose absorbed. However, measuring the change in absorbed doses over very small dimensions as might be the case for HP dosimetry remains a challenge and constitutes the focus of this work. When charged particles get to the end of their range of interaction, their rate of ionization also increases. The energy absorbed from a spectrum of short ranged, low-energy charged particles may actually increase per unit distance with depth in the absorbing material. As will be discussed later, the properties of HPs could therefore lead to both a steep dose gradient and an increase in what is termed as the radiation's "quality".

### 2.2.1 Definition of Absorbed Dose

Absorbed dose,  $D$ , is defined as the quotient of the mean energy,  $d\bar{\epsilon}$ , imparted as a result of a beta-gamma interactions with matter of mass,  $dm$ , in some limited volume [23].

The equation is given by:

$$D = \frac{d\bar{\epsilon}}{dm} \quad (2.4)$$

The integral of all the energies entering the sensitive volume less all the energies leaving the volume is the total energy imparted. The energy imparted  $d\bar{\epsilon}$  is an averaged quantity (not specific), hence the absorbed dose becomes an average

or non stochastic quantity. One unit of absorbed dose is a Joule per kilogram (J/kg), and it has a special name called the Gray(Gy) [23].

## 2.2.2 Measurement Using Gas-Ionization

For a given volume of a gas, or a liquid and certain solids, the absorbed dose as a result of charged particle interactions, can be determined for a variety of ionizing radiations. For gases and liquids positive ions and electrons are generated. For some solids however, conduction electrons and corresponding holes are formed [24]. The focus of this study and this section deals with the energy imparted during charged particle interactions with gases to create two pairs of oppositely charged ions. The term "ion pair" refers to the pair of electrons and the corresponding heavier positive ions created simultaneously with each interaction. Some examples of common gases used for measurement include: *Ar*, *He*, *H<sub>2</sub>*, *N<sub>2</sub>*, *Air*, *O<sub>2</sub>*, *CH<sub>3</sub>* and *C<sub>2</sub>H<sub>4</sub>* (and other organic gases). In order to create an ion pair the minimum energy equaling the ionization energy of the gas molecule must be transferred. The mean energy imparted in a gas per ion pair created is determined by its *W*-value. The *W*-value is a quotient of the initial kinetic energy, *E*, the mean energy imparted in the gas, and the mean number of ion pairs formed, *N*. The equation is represented by the following:

$$W = \frac{E}{N} \quad (2.5)$$

Two methods for determining the mean number of ion pairs, *N* are by pulse height measurements and the measurement of total ionization current (or total charge). In the pulse height method a complex electronic amplification system is required and particles with energies above the electronic noise are accepted. For gas ionization chambers, energies above 30keV are preferred, however for proportional counters much lower energies can be used [24]. For the total ionization current method, charges are collected over a given time period and the number of incident particles are determined along with their energy [24]. The unique properties of two types of counters, ion chambers and proportional counters, are discussed separately in more details in the upcoming sections 2.2.3 and 2.2.4.



In order to determine the number of ion pairs created in a gas by a HP decaying by beta particle emissions, the absolute average energy,  $W_\beta$  required to form an ion pair in the gas is measured. For instance, the absolute average energy from a  $^{35}\text{S}$  beta particle beam to produce an ion pair was determined by Jesse and Sadauskis (1956) for different gases. The  $W_\beta$  values for  $\text{N}_2$ ,  $\text{C}_2\text{H}_4$ , and  $\text{C}_2\text{H}_6$  were measured to be 35.3, 26.2, and 24.7 eV/ion-pair respectively. However, in air  $W_\beta$  values of 34.1 eV/ion-pair were reported and corresponded well with other values of  $W_\beta$  determined experimentally in other gases [25].

### 2.2.3 Measurement Using Ion Chambers

Gas filled detectors are the oldest and most widely used radiation detectors. They are based on the resulting effects of a charged particle passing through a gas and forming electron-ion pairs. They detect the direct ionization created by the passage of the radiation. An ionization chamber (I.C.) is the simplest type of these gas filled detectors. The basic components of the I.C. are illustrated in Figure 2.4. A gas enclosure houses a known volume of gas with an external voltage applying an electric field across the positive (anode) and negative electrodes (cathode). The electric field strength across the electrodes is optimized for maximum electron-ion pair collection. The ionization current becomes a measure of the ion pairs created in the gas volume, as a result of the radiation interactions taking place. Ion pairs can undergo processes such as recombination, diffusion, thermal motion, electron attachment, or charge transfer to surrounding neutral gas molecules, all are capable of limiting the ionization intensity [20]. These conditions can significantly reduce the probability of accurately measuring the ionization current in the chamber and hence require optimization to determine the true signal.

Based on the Bragg-Gray principle the energy absorbed (or dose) from a HP decaying by beta emission or photon emission per mass of interacting gas can be determined by equation 2.6. It is important to note however, that a walled proportional counter would not be able to measure beta dose unless the beta emitter was introduced into the chamber gas.

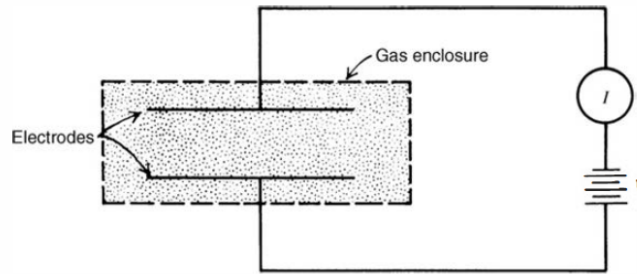


FIGURE 2.4: Basic components of the Ion Chamber. Retrieved from: Glenn F. Knoll (2010), Radiation and Detection and Measurement, 4th edition page 196"

[20]

$$D_w = D_g = WS_mP \quad (2.6)$$

The Bragg-Gray principle posits that for a small cavity made of the equivalent wall and gas material, the dose to the wall  $D_w$  will be equivalent to the dose to gas,  $D_g$ , for any kind of radiation. Where  $W$ , is the mean energy loss per ion pair formed.  $S_m$  is the relative mass stopping power of the wall material making up the the chamber relative to the fill gas enclosed in the finite volume.  $P$  indicates the amount of ion pairs per mass formed in the gas. If the material of the gas and wall are equal, such as a wall-less chamber which will be discussed in more details later on in this chapter, then  $S_m = 1$ .

### 2.2.4 Measurement Using Proportional Counters

Another useful tool in measuring absorbed dose with accurate and reproducible results is the Proportional Counter (PC). In a PC multiplication of free electrons occur by increasing the electric field resulting in an amplified pulse. The pulse amplitude is proportional to the number of original ion pairs created by the incident radiation and the resulting charge collected. This gas multiplication process takes the form of a cascade known as the Townsend avalanche [20], and ends when all the free electrons are collected on the positive electrode. The increase in

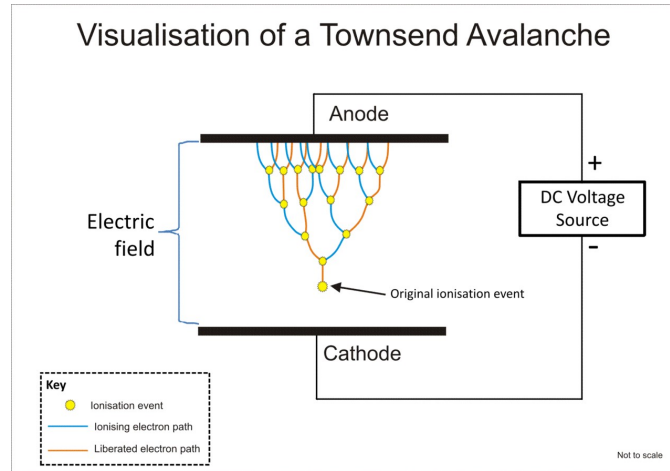


FIGURE 2.5: Illustrates the Townsend avalanche effect in a PC and the gradient of electrons maintained, eventually cascading unto the anode electrode. Retrieved from: Dougsim (2012), This file is licensed under the Creative Commons Attribution-Share Alike 3.0 unported license.

the number of electrons per unit path length is described by the Townsend equation:

$$\frac{d(n)}{n} = \alpha d(x) \quad (2.7)$$

Where  $n$  is the number of free electrons within the gas,  $\alpha$  is the Townsend coefficient for the gas enclosed and  $x$  the path length. Figure 2.5 demonstrates the creation of avalanches in a PC, and the path of the liberated and ionized electrons. If the right conditions are met the amount of secondary, tertiary, quaternary, etc., ionization events generated will be proportional to the the amount of primary ions pairs formed.

A cylindrical geometry is the most common form of a PC. It is advantageous when designing a PC since it allows for a large electric field near the anode. To determine the appropriate electric field strength  $\varepsilon(r)$  for a cylindrical geometry, the equation is applied:

$$\varepsilon(r) = \frac{V}{r \ln(\frac{b}{a})} \quad (2.8)$$

The variable  $r$  denotes the radial distance from the anode, and  $V$  the applied voltage between the cathode and the anode. The radius of the cathode and anode are represented by the values for  $b$  and  $a$  respectively. The fill gas is usually chosen for its minimum electron attachment coefficient to maintain electrons being free within the gas.

From these measurements with proportional counters we can determine the absorbed dose created in the counter's volume from the energies imparted. The proportional counters can also be operated in the experimental microdosimetric mode to determine the quality of the incident radiation. The section to follow will look at radiation quality as another measurement mechanism used to predict or estimate the relative biological effectiveness of different radiation.

## 2.3 Radiation Quality

This study also seeks to investigate whether there is a significant change in radiation quality as a result of the changing absorbed doses over microscopic distances. However, in order to arrive at these measurements the absorbed dose alone is not sufficient to quantify the radiation effect, it also requires the determination of the radiation quality factor.

The history of radiation quality was briefly reviewed by Lindborg and Waker (2017), who mentioned the "Haut erythema dose (HED)" as an initial method used to quantify radiation treatment [23]. A physical dose distribution method was also separately developed and provided a unit called the R-unit to measure exposures. The two methods were harmonized for comparison of the treatment doses which at that time were being delivered predominately by low energy X-rays (300 keV) and also by high energy photons such as 662 keV  $^{137}\text{Cs}$  and 1250 keV  $^{60}\text{Co}$ . Investigations of the biological outcome from each treatment dose revealed that for high energy photons to have the same impact as X-rays under standardized conditions they had to increase the high energy photon dose. It was

determined that the high energy photon doses needed to be increased by about 25% [23], this factor was declared as the radiation quality factor. A correction factor that would be introduced with the dose absorbed to determine the radiobiological effect in treatment. Currently, other uncharged (neutrons) and charged (protons and Ions) particles are now being used in treatment, and require their unique quality factors or radiation weighting factors to determine biological responses and treatment outcomes [26].

The first to report the significance of "microscopic energy depositions for effectiveness of ionizing radiation" was Douglas Lea (1946) [27]. A decade later R. E. Zirkle proposed that "linear energy transfer (LET)" was a convenient way to describe radiation quality. This was based on his finding on the relative effectiveness of various types of radiation. Zirkle [27], recognized from his measurements that the effect of bringing about a biological response was due to the variations in the ionization density in their particle tracks. Investigations on the relationship between Relative Biological Effectiveness (RBE) and LET to determine the biological effects on mammalian cells was subsequently carried out by Barendsen (1968) [27]. Figure 2.6 shows this relationship for survival curves at different absorbed doses. For all the survival curves the RBE increased to a maximum at  $100\text{keV}\mu\text{m}^{-1}$  and then decreases.

### 2.3.1 Experimental RBE

The term RBE is an experimentally measured quantity defined as the quotient of absorbed dose for a reference radiation,  $D_R$ , (such as 250 kVp X-rays or 1250 keV  $^{60}\text{Co}$  photons), to the absorbed dose  $D_\beta$  of the radiation being investigated such as beta particles in this case, and depends on the biological system used (for instance HeLa cells) and the survival or end point being investigated (such as 80% survival depicted in curve 1, Figure 2.6). The shape of the curve in the RBE against LET relationship, Figure 2.6, is usually explained by the DNA double stranded breaks occurring within the molecules having a nanoscopic size of approximately  $2\text{nm}$ . The ionization density (LET) rises to a maximum point and

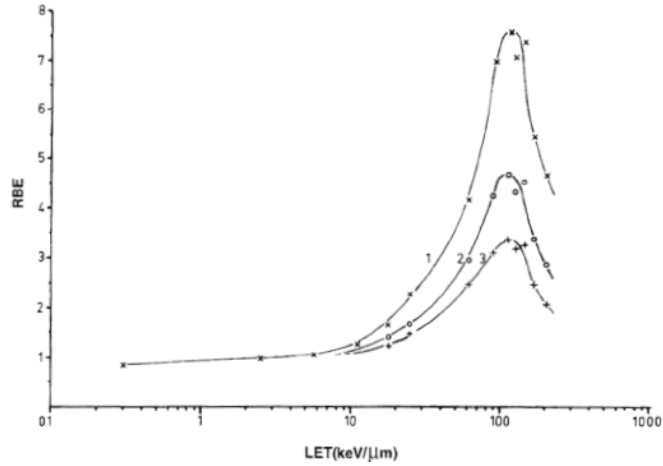


FIGURE 2.6: Variations of RBE with LET for survival of mammalian cell. Curves identified by 1, 2 and 3 with levels of survival at 80% 10% and 1% respectively for mammalian cells. Retrieved from G. W. Barendsen (1968). Responses of cultured cells, tumors and normal tissues to radiations of different linear energy transfer. *Current Topics in Radiation Research Quarterly* 4:293-356 [27].

then becomes less efficient at creating lethal damage. At this point the cell damage is experiencing "overkill" [23] or damage saturation. RBE is represented by the simple equation:

$$RBE = \frac{D_R}{D_\beta}; \{\text{For the same biological end-point}\} \quad (2.9)$$

When mammalian cells of human origin such as HeLa cells (or cells from other complex biological systems) are exposed to ionizing radiation, there is a probability they will not survive and the likelihood of survival decreases with increasing absorbed dose. The relationship of the surviving fraction is given by Lindborg and Waker (2017) as,

$$S(D) = S(0)e^{-(\alpha D + \beta D^2)} \quad (2.10)$$

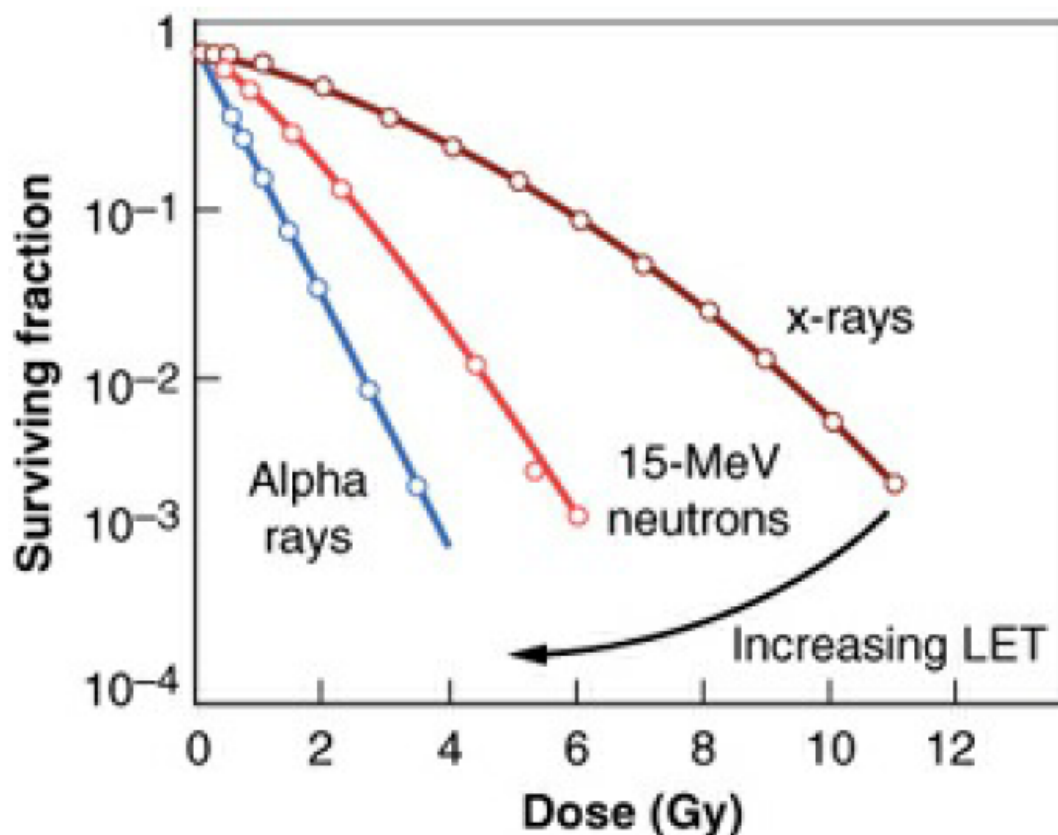


FIGURE 2.7: Survival curves for cultured cells of human origin exposed to 250 kVp x-rays, 15 MeV neutrons, and 4 MeV  $\alpha$  particles. Adopted from Eric J. Hall and Amato J. Giaccia: *Radiobiology for the Radiologist*(2019), page 205.

Where  $\alpha$  and  $\beta$  are the linear and quadratic cell survival parameters.  $S(D)$  is the fraction or surviving cells after absorbed dose  $D$ , and  $S(0)$  is the survival expected at zero dose. Hall and Giaccia (2019), in the latest edition of the book "Radiobiology for the Radiologist", discuss in detail the dependence of the fraction surviving the dose based on the radiation quality. For survival curves of cultured cells of human origin, as the linear energy transfer (LET) of the radiation increases, the slope of the survival curves gets steeper and the size of the initial shoulder gets smaller Figure 2.7 [28]. The figure also illustrates that for a given

endpoint RBE for mammalian cells will increase with increasing ionization density (LET). Lindborg and Waker (2017) with a modified version from the ICRP publication 103 (2007) [23], Figure 2.8 illustrates the comparison between different end points at 10% and 1%. For high and low LET radiation the RBE values at their respective end points are different at 5.7 compared to 4.7, and also indicate that the RBE becomes higher for lower doses. The term LET has been used to describe ionization density at cell like dimensions in this section, and has been helpful in looking at the concept of RBE which varies with radiation quality. To further the discussion the LET or the changing radiation quality will be looked at closer in the section that follows.



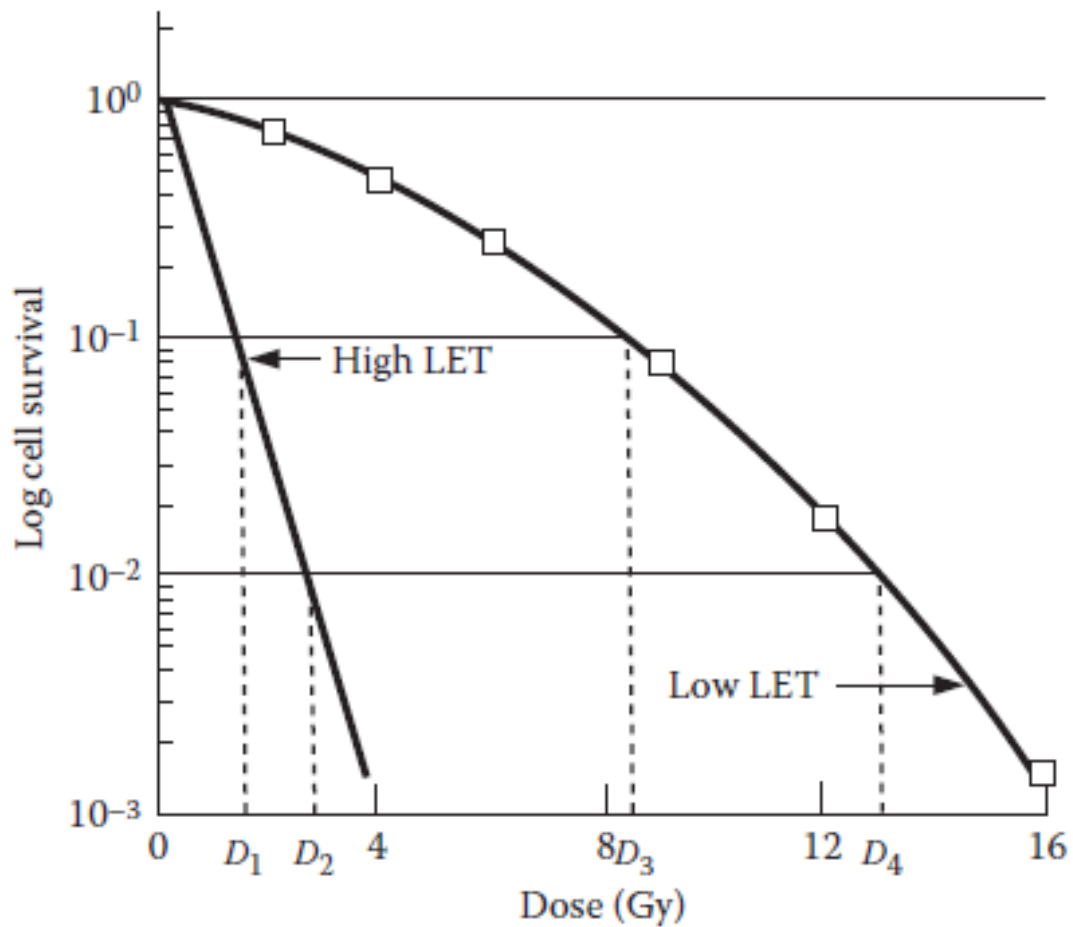


FIGURE 2.8: "Relative cell survival as function of the absorbed dose (Gy) to the cells. The dose values for 10% and 1% cell survival are marked in the figure as  $D_1$  and  $D_3$  and  $D_2$  and  $D_4$  respectively. RBE for the two levels of survival becomes  $(D_3/D_1) = (8.5/1.5) = 5.7$  and  $(D_4/D_2) = (13/2.75) = 4.7$ ". This indicates that that RBE is dependent on the endpoint chosen. Here RBE for 10% survival is larger (5.7) than that for 1% survival (4.7). Retrieved from Lindborg and Waker (2017); A modified version from the 2007 recommendations of the International Commission on Radiological Protection; Publication 103. Annals of the ICRP 37 (2-4)[23].

### 2.3.2 Linear Energy Transfer

LET is a benchmark quantity of ionization density or radiation quality and can help to explain why a beta particle may differ from a gamma ray, a neutron or an alpha particle in biological effect. LET is the average rate of energy loss per unit distance traveled in  $keV(\mu m)^{-1}$ , along a charged particle track passing through a given material such as tissue. The restricted stopping power or  $LET_{\Delta}$  according to the ICRU report 16 (1970) is given by:

$$LET_{\Delta} = \left(\frac{dE}{dx}\right)_{\Delta}; \quad (2.11)$$

and represents the 'local' deposition of energy.

The  $\Delta$  symbol indicates there is a range restriction of the delta rays along the primary charged particle track, and  $dE$  is the mean energy locally imparted as a result of collisions. The value  $dx$  is the distance traversed. Taken together, the LET is an average and macroscopic quantity that does not account for the random or stochastic behavior of the energy losses along charged particle tracks. Important to this investigation is measuring the changing absorbed dose and LET in biological systems at the microscopic scale while moving away from an HP. Hence, as previously stated the concept of microdosimetry allows for the comprehensive determination of the energy depositions, the LET distribution and the track length distribution, the energy loss straggling of charged particles and delta ray energies traversing a simulated microscopic volume [27]. As a result of the quality of different types of radiation the biological effects observed from the same energy deposition can differ and in radiation protection this concept has implications for the health of the NEW, the public and the environment. As such the quality of the radiation requires a factor to equate the energy deposited in the volume of interest and is given the special name *Dose Equivalent*.

### 2.3.3 Radiation Protection and Radiation Wighting Factors

For the purpose of protecting the NEW, the ICRP and ICRU have jointly reviewed studies that indicate exposures will result in some small relative risk of

cell death, mutations or carcinogenesis above 100 milliSieverts(mSv) averaged over five years. A Sievert is the SI unit for measurement of dose equivalence, a biological response from exposure to ionizing radiation. Radiation weighting factors,  $W_r$  ( where  $r$ -value usually assumes the symbol of the radiation of interest) are assigned to the four types of ionizing radiation of interest in the nuclear industry. However in this work the conversion factors for beta particles and photons will be the focus. The equivalent dose delivered to a tissue volume irradiated by a HP is the accumulation of both radiations and their unique quality factors, calculated by the equation:

$$H = D_{\beta}W_{\beta} + D_{\gamma}W_{\gamma} \quad (2.12)$$

Where:  $H \equiv$  equivalent dose delivered to the volume of interest (unit: Sievert)

$D_{\beta} \equiv$  absorbed dose delivered to the volume by beta particles (unit: Gray)

$D_{\gamma} \equiv$  absorbed dose delivered to the volume by gamma rays (unit: Gray)

$W_{\beta} \equiv$  radiation weighting factor for beta particles (dimensionless)

$W_{\gamma} \equiv$  radiation weighting factor for gamma rays (dimensionless)

In radiation protection there is the relationship between quality factors and radiation weighting factors. For radiation protection the weighting factor or quality factor for photons and beta particles is 1 by definition [22]. In radiation protection the focus is mainly lowering the risk of carcinogenesis, however, for HPs the concern is for direct tissue damage. As discussed earlier by the example given in Section 2.3 there is evidence that RBE measured for cell survival and tissue responses is not the same for low energy x-rays or beta particles, as for high energy particles [23] [26].

### 2.3.4 Measurement of Quality

#### LET (L) and Quality Factors, ( $Q$ )

The mean quality factor  $\bar{Q}$  is calculated in the following manner:

$$\bar{Q} = \frac{\int_0^{\infty} Q(L)d(L)dL}{\int_0^{\infty} d(L)dL} \quad (2.13)$$

And are governed by the following conditions according to the ICRP publication 60.

$$Q(L) = \{1, \text{assuming } L < 10 \text{keV}(\mu\text{m})^{-1}\}$$

$$Q(L) = \{0.32L - 2.2, \text{assuming } 10 \leq L \leq 100 \text{keV}(\mu\text{m})^{-1}\}$$

$$Q(L) = \left\{ \frac{300}{\sqrt{L}}, \text{assuming } L > 100 \text{keV}(\mu\text{m})^{-1} \right\}$$

Assume lineal energy,  $y$  equates to linear energy transfer (LET) represented by  $L$  [29], in equation 2.13 then;

$$\bar{Q} = \frac{\sum Q(y_i) \times y_i f(y_i)}{\sum y f(y)} \quad (2.14)$$

The dose equivalence,  $H_{TEPC}$ , for a tissue equivalent proportional counter operated in the microdosimetric mode is determined by the equation:

$$H_{TEPC} = D_{TEPC} \times \bar{Q} \quad (2.15)$$

By definition,  $\bar{Q}$ , the tissue weighting factor, will always be equal to 1 for photons and beta particle type radiation, and does not provide a measure of the suspected changing radiation quality. In this work the dose mean lineal energy,  $\bar{y}_D$ , will be a more useful measure of radiation quality and the potential for biological damage over micron sized distances. The concept of this microdosimetric quantity will be defined in more details in Section 2.4

The Theory of Dual Radiation Action (TDRA) was presented in original work published by authors [30] and [31]. In the most recent publication on the topic Lindborg and Waker (2017) discussed that at very small absorbed dose values RBE becomes equal to the ratio of dose mean lineal energies for the two radiation qualities at different positions along the experimental test sites [23]. In this study the reference dose mean lineal energy would be analyzed at the physical position of the anode wire at 2.5 mm, and a simulated distance of 2  $\mu\text{m}$ . The test  $\bar{y}_D$  values will be investigated at various positions ( $z$  mm) away from a reference site at  $x$  mm.

$$RBE = \frac{D_R}{D_\beta} \approx \frac{\bar{y}_{D,x,H}}{\bar{y}_{D,z,L}} \quad (2.16)$$

Where,  $\bar{y}_{D,x,H}$  is the dose mean lineal energy in a single energy deposition event at reference position  $x$  with a dose for high LET radiation and  $\bar{y}_{D,z,L}$  is the dose mean lineal energy in a single energy deposition event at reference position  $z$ . The  $z$  position varies in a range from 1 to 41  $\mu m$  of simulated tissue equivalent material.

## 2.4 Experimental Microdosimetry and Radiation Quality

In previous sections the discussion surrounded the measurement of absorbed dose by various methods of gas ionization and secondary charged particle multiplication supported by electronics to determine the physical effect of the incident radiation. However, as a quantity of measurement the absorbed dose alone was not enough to determine the biological effect or endpoint of the ionizing radiation absorbed. For the same biological endpoint (e.g. a 20% chance for a mammalian cell to survive irradiation) the concept of RBE was introduced as a ratio of the absorbed dose, and determined the change occurring from one radiation quality to another. Consequently, it can be expected that for the same end point, as the quality (LET) of the radiation increased the RBE will also increase. For defining radiation protection limits for humans and specifically occupationally exposed workers the absorbed dose is used as a product of these radiation weighting factors to produce a special quantity called the equivalent dose. In this section experimental microdosimetry provides another way to measure the quality of the radiation. The technique results in a microdosimetric spectra that gives a comprehensive description of the microscopic pattern of energy depositions and not just the average LET.

### 2.4.1 Microdosimetric Quantities

LET and lineal energy are both quantities that allow for the characterization of charged particle tracks. Using the technique of microdosimetry however, allows

for the measurement of radiation quality in the form of lineal energy,  $y$ . As discussed, the LET is useful in determining the quality of the radiation, where as the quantity lineal energy, referred to as the microdosimetric stochastic analog of LET, is used when characterizing the radiation quality in small microscopic volumes [23].

The stochastic quantity lineal energy,  $y$  is the quotient of the energy imparted  $\varepsilon_s$  from a single energy deposition event and the mean chord length  $\bar{l}$  traversed in the defined microscopic volume of interest.

$$y = \frac{\varepsilon_s}{\bar{l}} \quad (2.17)$$

One *event* is defined as one single deposition of kinetic energy in the site traversed by one charged particle plus all its associated secondary tracks. Lineal energy,  $y$ , is a stochastic quantity and is given in units of Joule per meter ( $Jm^{-1}$ ) or more typically as  $keV\mu m^{-1}$  [23][27]. The energy  $\varepsilon_s$ , is imparted into the volume by one single deposition event and  $\bar{l}$  is the mean chord length in that volume. To determine the mean chord length in a volume the average length of randomly oriented chords are taken and can be expressed using Cauchy's theorem:

$$\bar{l} = 4\left(\frac{V}{a}\right) \quad (2.18)$$

Where  $V$  is the volume of the microscopic tissue site and  $a$  is the surface area of this site [32].

The frequency of lineal energies,  $y$  is the function  $f(y)$  and has a distribution of individual stochastic energy depositions depending on where the radiation interaction occurs. The other two important quantities are the *frequency mean lineal energy*,  $\bar{y}_F$  and the *dose mean lineal energy*,  $\bar{y}_D$ , and are both non-stochastic quantities. A detailed derivation of each quantity is expertly given in ICRU report 36 (1983) and most recently by Lindborg and Waker (2017). The frequency mean lineal energy with frequency function  $f(y)$  and dose mean lineal energy with dose distribution function given by  $d(y)$  are both independent of the absorbed dose or dose rate but are dependent on the size and shape of the microscopic volume that the energies impart. The relationship between  $d(y)$  and  $f(y)$ ,

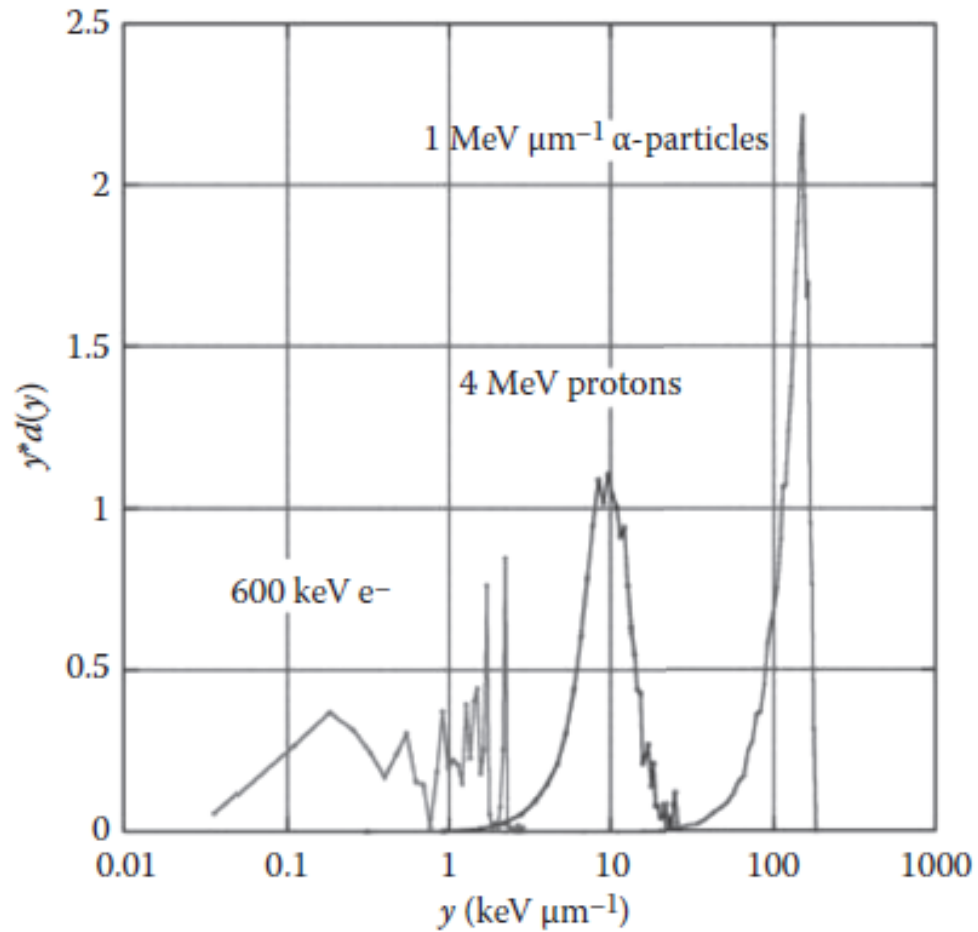


FIGURE 2.9: Lineal energy dose distribution for three different radiation qualities: 600 keV electrons, 4 MeV protons and 1 MeV alpha particles in a sphere of diameter  $1\mu\text{m}$ . Adopted from Lindborg and Waker (2017). Microdosimetry, Experimental methods and applications.[23].

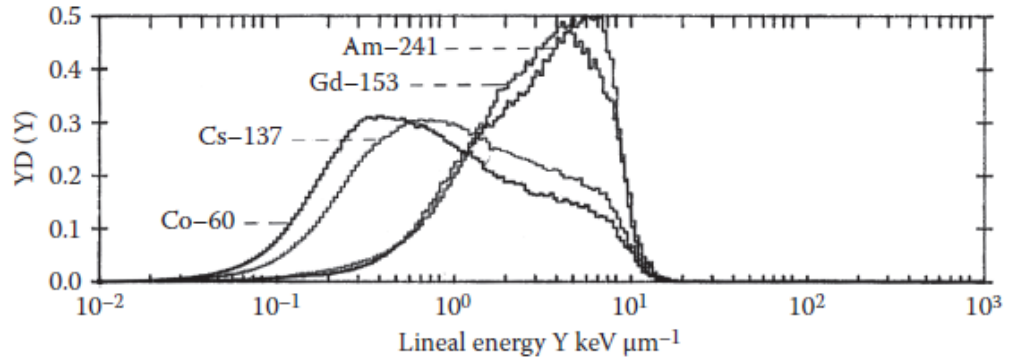


FIGURE 2.10: Single-event  $yd(y)$  dose distributions for different photon energies measured with a Far West Technology 1.27 cm Rossi counter simulating a  $2 \mu\text{m}$  tissue sphere. Adopted from Lindborg and Waker (2017). Microdosimetry, Experimental methods and applications [23].

and between  $\bar{y}_D$  and  $\bar{y}_F$  [32] [23] can be represented by the equation:

$$\bar{y}_D = \frac{1}{y_F} \int_0^{\infty} y^2 f(y) dy \quad (2.19)$$

Examples of a single event spectra are illustrated in Figure 2.9, which visually depicts the distribution of lineal energies among electrons, protons and alpha particles of varied radiation qualities in a microscopic volume. The technique also allows for distinguishing the differences in radiation quality for one type of radiation having different energies. The spectra of photons in Figure 2.10, for different energies shift towards the right and the radiation quality measured in lineal energy,  $y$  increases on a log scale as the photon energies decrease. The spectra gives visual support for the argument that as the energy of the particles decrease their radiation quality or ionization densities will increase. Typical  $\bar{y}_D$  values for the spectra of  $^{60}\text{Co}$  and Am-241 are  $1.47 \text{ keV}(\mu\text{m})^{-1}$  and  $3.96 \text{ keV}(\mu\text{m})^{-1}$  [33] respectively. Knowledge of this concept is exploited by Tissue equivalent proportional Counters (TEPC) which are designed to measure dose and radiation quality in microscopic volumes simulating biological systems.



### 2.4.2 Measurement of Dose

With the experimental microdosimetric method the total absorbed dose,  $D$  is calculated from the following equation:

$$D[Gy] = \frac{\sum(y_i)(f_i)[keV/\mu m] \times \bar{l}[\mu m]}{m[kg]} \times 1.602 \times 10^{-16}[J/keV] \quad (2.20)$$

The absorbed dose to the gas cavity of a TEPC can be determined by measuring the single event spectra provided the dose rate of the measurement is low enough that one single event occurs during the TEPC pulse processing time [23].

### 2.4.3 Tissue Equivalent Proportional Counters

As discussed above, the dual nature of the technique of experimental microdosimetry, provides the advantages of being both an 'LET' spectrometer and a dosimeter [34]. In section 2.2.4, the discussion looked at the principle of measuring absorbed dose from the energy deposited in a gas creating ion pairs, in the so called proportional region. For very low energy particles an increased voltage results in the multiplication of primary electrons to secondary electrons further generating a cascade of electrons towards the collecting electrode. Detectors operating in this region are called proportional counters (PC) as the total number of ion pairs created is proportional to the inchoate energy.

To simulate microscopic dimensions of cells in tissue or muscle with a PC, tissue equivalent (TE) or muscle equivalent gas is used and manipulated at low pressures. The International Commission on Radiation Units and Measurements (ICRU) [1983 and 1989] suggests that ICRU tissue has the elemental composition in percent by weight: 10.1% H, 11.1% C, 2.6% N, 76.2% O [23]. The composition of TE fill gases, TE plastic (A-150), and the partial pressure components and densities typically used when designing TEPC are listed in tables given by Lindborg and Waker (2017). The dosimetric properties of the TEPC comes from its tissue equivalence and forms a Bragg-Gray cavity device. The Bragg-Gray cavity theory is discussed in literature [35] [34] and considers that Bragg-Gray conditions are met when the gas cavity and wall are tissue-equivalent with an homogeneous atomic compositions throughout the chamber. These chambers are

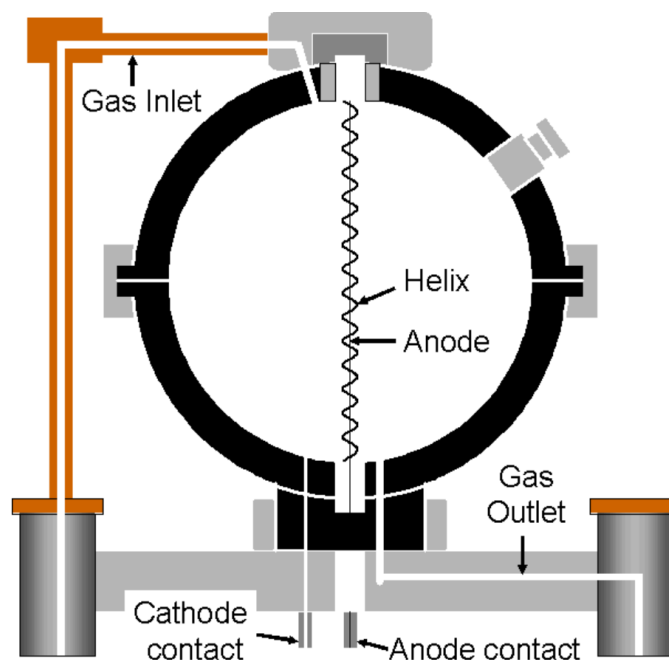


FIGURE 2.11: Early 1960 design of a "Rossi Counter" [27].

referred to as tissue equivalent proportional counters (TEPC) and the measurable quantities they provide are dose and radiation quality in biological systems via the microdosimetric technique.

A typical TEPC is a "Rossi Counter" developed at Columbia University in 1960 and is shown in Figure 2.11. The counter employs a spherical chamber with tissue-equivalent walls, and a tissue equivalent fill gas. The chamber in this design is spherical in shape so that it would be angularly independent of the direction of the radiation [36]. Cylindrical designed detectors have also been developed and possess the advantage of a uniform electric field along the anode wire which allows for a uniform gas gain [23]. According to Lindborg and Waker (2017) in order to overcome the non-uniformity in spherically designed detectors a helix is used around the central electrode which was the addition by Harold Rossi in the initial design of spherical TEPC. Since then, several types of TEPC have been designed and constructed. The effort into optimizing the design and managing the electric field and gas gain in the counters have been discussed in literature

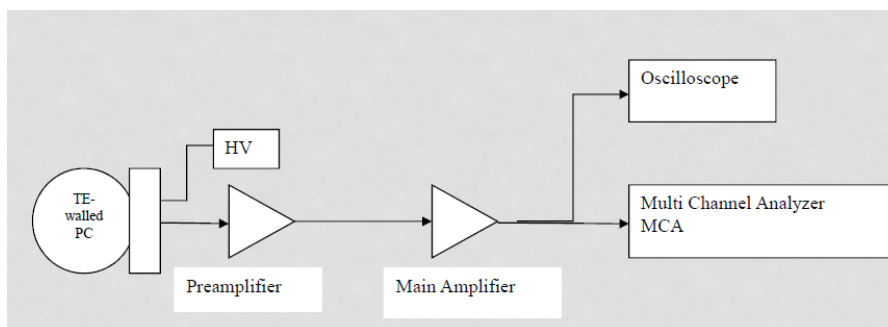


FIGURE 2.12: A simple electronic arrangement for collecting the pulse height spectrum from a tissue-equivalent proportional counter. Modified from Waker A.J., Principles of Experimental Microdosimetry, Radiation Protection Dosimetry, vol.61, No.4, pg. 299.

[37] [34] [23]. For the spherical design in Figure 2.11, the sphere consists of conductive TE material which acts as the cathode, and the thin wire surrounded by the helix is the anode; TE gas at low pressure will engulf the chamber from the gas inlet valve. Incident radiation interacts with the TE wall of the chamber which "knock" charged particles across the TE gas that fills the chamber. The size of the pulse reflects the ionization produced in the gas by the particle. As such, the pulse size also reflects the absorbed dose to the gas per particle. A simple electronic set up of the microdosimetric circuitry can be found in Figure 2.12. By measuring the size of each pulse, the absorbed dose  $D$  per particle in the gas can be measured. The dose equivalent  $H$  per particle is calculated from the mean quality factor  $\bar{Q}$ .

#### 2.4.4 "Wall-less" TEPC

The energy deposition spectra for short ranged charged particle beams expected from HPs, and the extent of their delta ray influence can be investigated only with a "wall-less" TEPC. A "wall-less" proportional counter with nearly all gas components, is a device which collects ionization from a small central region of a large gas volume by utilizing a minimum amount of structural material [38]. In

a normal TEPC, Bragg-Gray conditions are met in the chamber when the secondary charged particle distribution measured by the counter are the same in the tissue equivalent gas cavity comprised of homogeneous material. The phenomenon known as "wall effects" [38] is known to occur as a result of the interruption created by the solid wall which produces distortions in the measured spectrum. In discussions on designing a TEPC, Kliagua, Waker and Barthe (1995) indicated that these wall effects are as a consequence of the "angular relations not being preserved in the branches and curves of charged particle tracks when they pass through a boundary between gas and solid wall". The wall-less counter in this study is designed to avoid these wall effects. For a normal TEPC, low energy beta particles would not be able to penetrate the wall and enter the gas cavity, hence a wall-less counter has to be used. Figure 2.13 illustrates four different situations which can possibly occur from wall effects. Important to this investigation on HP dosimetry is the aspect of radionuclides decaying by beta particles emission. The re-entry effect indicated in Figure 2.13(b) is important only for electrons scattering back into the cavity due to their curled tracks. However given there are no density differences the possibility of re-entry is not likely to occur [23]. The other three effects are reviewed in literature in much more details [23][38].

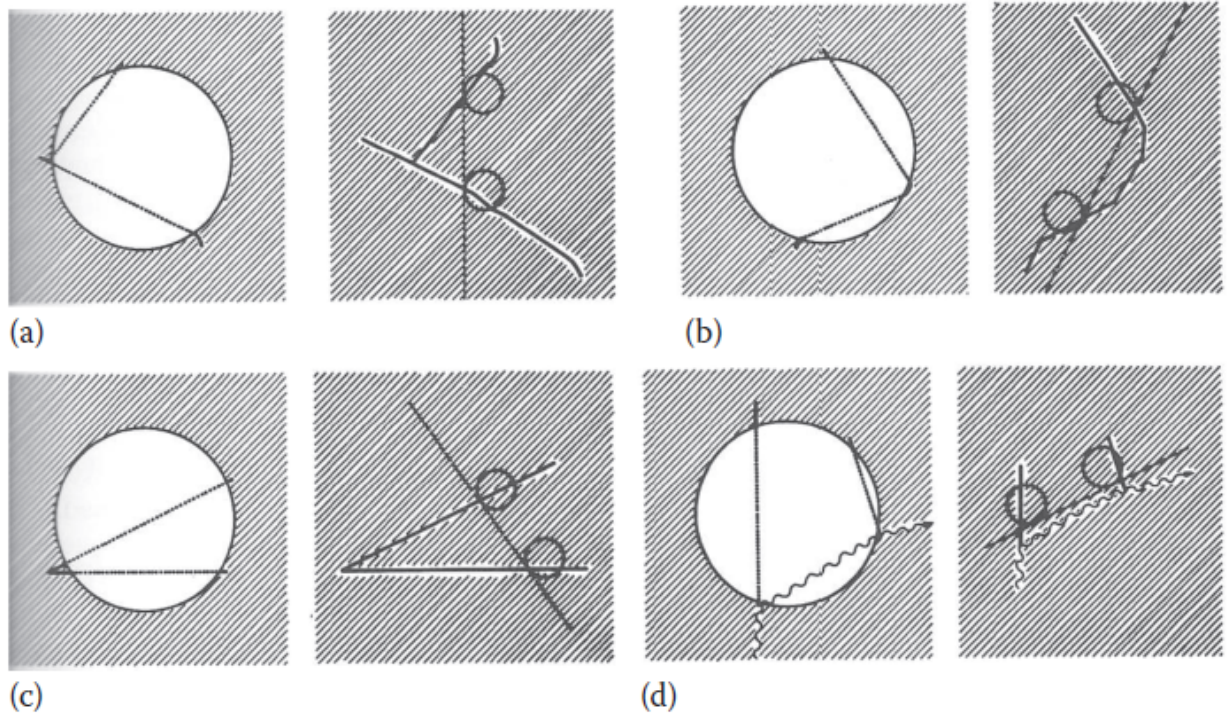


FIGURE 2.13: Classification of the four wall effects (a) Delta-ray effect, most important for heavy charged particles (b) Re-entry effect, important for electrons. (c) V-effect, important for highly energetic charged particles (nuclear fragmentation) and (d) scattering effect, important to uncharged particle interactions. Adopted from Lindborg and Waker (2017). *Microdosimetry, Experimental methods and applications*.

## Chapter 3

# Literature Review

### 3.1 Methods of Hot Particle Dosimetry

The argument was made by Charles and Harrison (2007) in their work [2], that conventional methods available for evaluating dose and determining the radiobiological effects from HPs are currently unsuitable. To accurately measure surface dose is important, and measuring dose at shallow depths as discussed earlier [1] is considered in literature a difficult process [39]. Discrepancies between measured and calculated doses were observed among inter-comparisons of theoretical methods for HP dosimetry [1]. As a consequence, Aydarous et. al.(2007) [1] in their work to develop a intensified charge coupled device (ICCD) scintillator system declared that there is a need for exploring and developing alternate experimental microdosimetric techniques. In this section we review the current literature and highlight some computing codes and methods that are currently being employed, or have been used in the past to measure the changing dose over small distances and the subsequent or potential change in radiation quality moving away from a HP. This section does not intend to compare the results of each method or code, only to introduce the concept of each technique and the approach applied to their function.

#### 3.1.1 Software Based Tools -"VARSKIN" and "DETEC"

VARSKIN, is a computer code for skin contamination dosimetry, and has the ability to provide both gamma ray and beta particle components of the dose.

Skin dose calculations are computed based on the point kernel method addressed by several authors [40][41] [42]. The code allows for selection of five source geometries: point source, disk source (infinitely thin), cylindrical source (thick), spherical source and slab source (rectangular). It also supports multiple attenuating layers for clothing and air gaps. The code functions by calculating the dose to water for a single radionuclide or for a mixture of sources of contamination over circular areas selected by the user for depth in water as an estimate of the penetrating distance or depth in tissue. VARKIN's growing success relates to the many versions of the code such as version 4.0 for photon skin dosimetry and the most recent in literature version 5.35.3 for skin doses exposed to beta particles. The codes are typically compared to Monte Carlo particle transport simulations to determine their accuracy or deviation in the skin dose predictions. A recent peer reviewed article on "beta skin dose calculations" compared VARSKIN 5.35.3 with Monte Carlo code, MCNP5, the authors concluded that VARSKIN 5.3 was very credible in the rapid assessment of skin dose following a contamination incident, however when compared to MCNP5 it appeared to underestimate the dose when there was an air gap between skin and protective clothing [43]. Figure 3.1 gives a snapshot of VARSKIN 4.0 in operation, and illustrates its characteristic user interface window and its claim for rapid performance in reporting skin doses. The literature does not have any indication of this model being able to evaluate the variations in radiation quality for skin doses based on depth in tissue nor the potentially elevated effectiveness of the contamination under investigation.

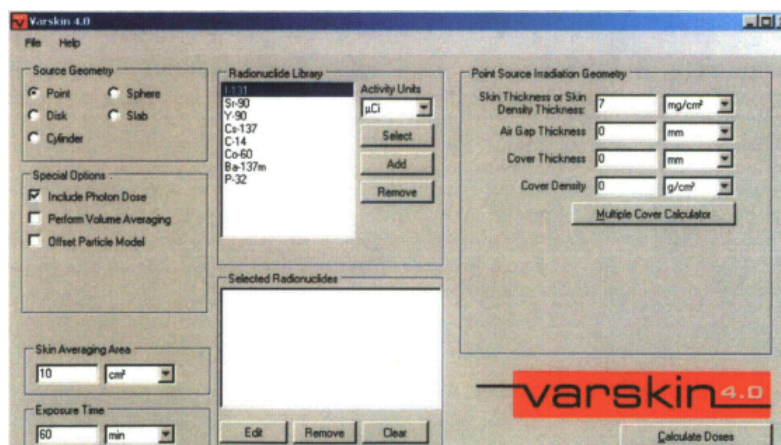


FIGURE 3.1: Snapshot of VARSKIN version 4.0 in operation. Adopted from the U.S. Nuclear Regulatory Commission. VARSKIN 4: A computer code for skin contamination dosimetry. NUREG/CR-6918, Rev 1 (2011) [40]

The other software based skin dose calculator developed by Canadian Nuclear Laboratories (CNL) and "DETEC" is called the "Activity Calculator" [42]. The user friendly GUI operating terminal is shown in Figure 3.2. The value of the code is its ability to quickly and accurately calculate the absolute activity of mixed radionuclide sources implicated in a contamination event by using a database (library of 1252 radionuclides) of pre-calculated counting efficiency for photons and electrons. The code requires raw counting rate data measured in the field at distance from the source in the range 0.5 to 10 cm. Relative fraction of radionuclide contained in the contamination are deduced directly or indirectly from gamma spectroscopy, presumably by a health physics personnel. Back-scatter from the interacting mediums like air, polyethylene, aluminum or steel are accounted for in the code which applies the gamma and beta emissions data for radionuclides [42]. There were no published data from "Detec" in literature up to writing this thesis, hence it was difficult to determine how the Activity Calculator compared with other well established codes for skin dose measurements.



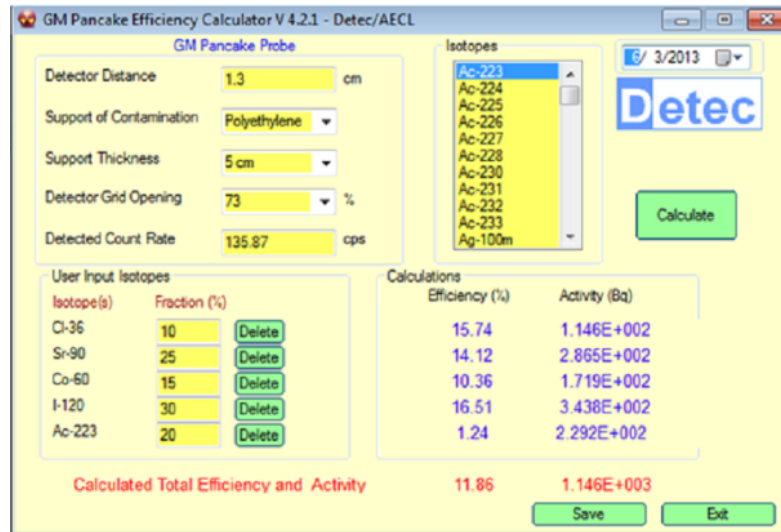


FIGURE 3.2: Screenshot of the "Activity Calculator" from **Detec**, to determine the dose delivered from unknown sources of radioactive contamination. Adopted from "**Detec**" [44]

### 3.1.2 Expedient Field Method(EFM) with G-M Pancake Probe

The Expedient Field Method(EFM) provides another technique in estimating skin dose rates, by simply using the measurements taken by a surveyor with a Geiger-Muller (G-M) pancake probe at a known distance. The method is also effective when radionuclide identification is not required or the contamination is lost before a laboratory analysis can be conducted [42]. The methodology is based on measuring random mixtures of radionuclides decaying by emitting beta particles of a wide variety of end point energies (for instance low energy  $^{85}\text{Nb}$  with an energy of 1670 keV and high energy  $^{106}\text{Rh}$  with an end point energy of 3.54 MeV). Dubeau et. al. (2016), suggests that a simulated ratio of the skin dose rate (Gy/h) to the G-M probe counting rate (in CPS) will strongly peak at a certain value in the distribution of cases of skin contamination for various mixtures of beta emitting radionuclides. For more complex exposure geometries however the accuracy of the method decreases, and the narrow peak simulated

distribution broadens in width. Overestimation of skin dose is therefore a possibility, however when using the EFM for low energy beta particles counts are generated with the G-M probe on contact, but on clothing a radionuclide such as  $^{85}\text{Nb}$  would contribute very little skin dose [42]. The EFM, similar to the other methods presented in this section, is purely an absorbed dose measurement tool that can not quantify radiation quality.

### 3.1.3 Hot Particle Dosimetry System (HPDS)

The Hot Particle Dosimetry System (HPDS) is current instrumentation being developed by Canadian Nuclear Laboratories (CNL) that measures skin dose rate from a measured count rate of a recovered HP. The HPDS measures the count rate from HPs without the need for radionuclide identification. When compared to a TEPC containing tissue like gases and materials of homogeneous atomic composition, the HPDS in contrast uses an air-water interacting interface. According to the principle, for a parallel beam incident on an air-water interface, the beta particles flux at a depth of  $70\ \mu\text{m}$  in water is approximately proportional to the skin dose over an area of  $1\ \text{cm}^2$  from a point source in contact with the skin, and independent of the beta end point energy [42].

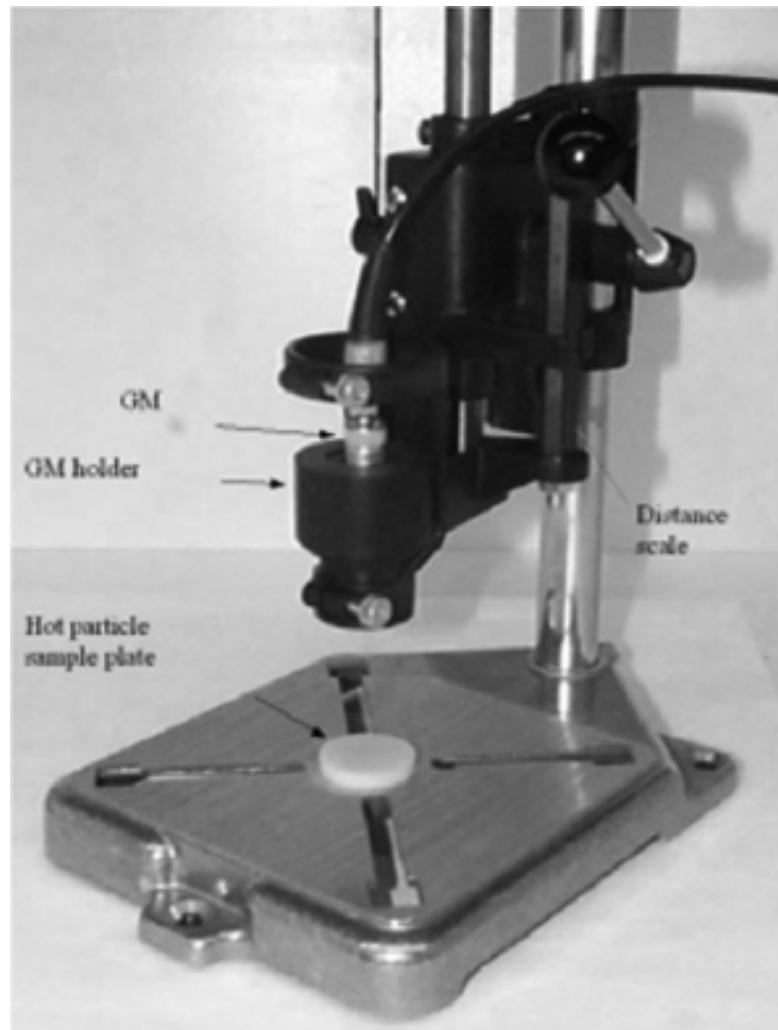


FIGURE 3.3: Hot Particle Dosimetry System developed by CNL  
[42]

The HPDS is described as a fast, accurate, on site measurement device for skin dose, usable in a variety of contamination scenarios. Details of the mechanisms behind its instrumentation are briefly provided in literature [42], Figure 3.3 provides an image of the device. The method has the disadvantage of requiring the complete recovery of the hot particle for quantification. The HPDS also can not measure radiation quality.

### 3.1.4 The Extrapolation Chamber

As discussed previously measurement of surface dose for HP dosimetry is important, however determination of dose at such shallow depths is a challenging issue [39][45][46][47]. The Extrapolation Chamber (EC) is a device which precisely and accurately measures absolute absorbed dose rate for beta particles and photons at the surface and within the buildup region [46]. As previously introduced, the internationally recommended absorbed dose rate in tissue at a depth of  $70\mu\text{m}$  is the standard quantity related to beta particles. The EC is a specially designed IC with parallel plate electrodes in which the mass of the gas in the chamber's sensitive volume can be varied. The mass of the gas is varied by adjusting the opening between electrodes and registering the resulting changes in ionization current, which can be extrapolated back towards a zero chamber depth [46]. The ionization current is rarely registered based on varying the area of the electrodes or the density of the gas, these and other features of the EC are discussed in details in literature [39][45][46][47]. In the absence of EC, a good alternative is a fixed separation plane parallel IC or a Markus chamber, due to its thin entrance window [39]. However, a limitation of the Markus chamber is its over response caused by the secondary electrons produced by scattering within the walls of the chamber. This over response is accounted for by correction factors associated with the specific chamber properties: volume, plate separation, and guard size. Finally, the measuring apparatuses and software based tools presented in this chapter are all capable of determining absorbed doses at the regulated surface layers of  $70\mu\text{m}$ , with acceptable correction factors to adjust for the best results therapeutically and for contamination events in industry. However, none have the ability to determine the changes in radiation quality over microscopic distances. Chapter 4 to follow, features a proposed apparatus that was designed and constructed to be capable of delivering both measurements. The progress in the design and construction of the apparatus and counter is presented.

## 3.2 Monte Carlo Methods of Computational Dosimetry and Microdosimetry

The Monte Carlo method is a statistical technique which provides the ability to simulate a mathematical or physical experiment. The ability to simulate the tortuous path of short ranged particles from electron and photon beams emanating from HPs is applicable to the objectives of this study. Monte Carlo codes up until the 1990s mainly allowed for benchmarking studies for scientists and engineers, but more recently have become a primary tool for performing particle transport simulations for a variety of investigations [48]. An attribute of the Monte Carlo code is sampling the probability density functions associated with particle interactions of matter or tissue in the case of this study. Simulating complex problems using Monte Carlo methods for random processes with known or assumed probability density functions are discussed comprehensively in literature by Haghghat (2016). Monte Carlo (MC) codes such as OREC, MOCA and PITS are considered the preferred choice when computing distributions of event-by-event microdosimetric quantities [49]. However, the code PENELOPE, an acronym for PENetration and Energy LOSS of Positrons and Electrons, provides the advantage of simulating coupled electron-photon transport in the range of 100eV to 1GeV [50], which agrees with the demands of this investigation for short ranged charged particle interactions. It should be noted immediately that the cross sections and physics below about 500 eV however, will be more uncertain than those at higher energies [49]. This study requires a MC code to aid in the design of the apparatus and interpreting the results associated with energies from HPs. Stewart et. al., (2002) designed a intercomparison study to test the applicability of the MC code system PENELOPE for microdosimetry applications. The study concluded that for sites comparable in size to a mammalian cell or cell nucleus, and for single-event distributions there was reasonable agreement with predicted event-by-event Monte Carlo simulations. The findings from that study highlighted that PENELOPE is more applicable to radiation transport through materials other than water, which suites this proposed investigation of TE gas particle interactions. Considering the work of Stewart et al (2002) we can justify

the choice of PENELOPE to fulfill this task. Further confirmations were reached by Stewart et al (2002), in their work "Microdosimetric properties of ionizing electrons in water: at test of the PENELOPE code system" investigation. Inter-comparison results for PENELOPE and other codes operating in the condensed history mode suggests PENELOPE can be used for microdosimetric applications [49].

### 3.2.1 Electron-Photon Transport with PENELOPE

The distinct advantage of PENELOPE is its ability to track the transport of electrons and positrons in an arbitrary medium, down to energies as low as 100 eV whereas other Monte Carlo codes: EGS4, ETRAN, ITS3 and MCNP are limited to electron-positron kinetic energies above 1 to 20 keV [49]. PENELOPE implements a mixed simulation algorithm, 'hard' electron and positron events are simulated in detail with condensed simulation of 'soft' events using multiple scattering theory [50] [49]. This code offers the event by event physics models for hard collisions along with the simulation efficiency of histories of condensed Monte Carlo system.

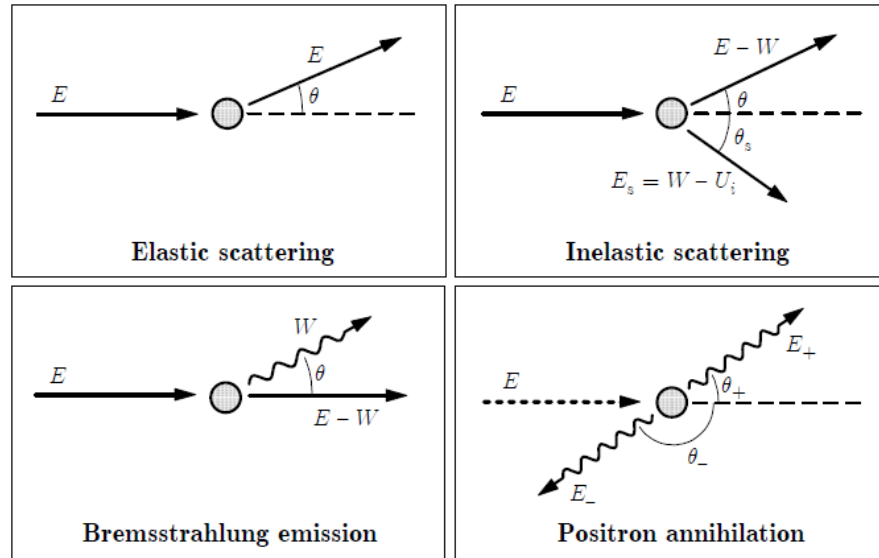


FIGURE 3.4: Basic interactions of electrons and positrons with matter. Adopted from F. Salvat (2015). PENELOPE-2014, A Code System for Monte Carlo Simulation of Electron and Photon Transport. Workshop Barcelona, Spain, 29th June - 3rd July 2015 pg. 101.

As discussed earlier in section 2.1, interaction of photons were also reviewed by Salvat (2015), highlighting the photoelectric absorption, incoherent Compton scattering, pair production, and also coherent Rayleigh scattering as the dominant interaction processes in the energy range 50 eV to  $10^9$  eV for atoms of atomic number  $Z$ . Electron and positron interaction probabilities in the same energy range are also discussed and are considered to undergo elastic scattering, inelastic scattering, Bremsstrahlung emissions and positron annihilation [50]. The Figure 3.4, illustrates possible interactions of electrons and positrons with the medium and assumes the particles are moving in a single-element medium of atomic number  $Z$  and density,  $\rho$ , with  $N$  atoms per unit volume.

As stated initially the simulation of electron and positron tracks are performed by means of a mixed (class II) algorithm. Individual hard elastic collisions, hard inelastic interactions and hard bremsstrahlung emission are simulated in detail. The cut off angle  $\theta_c$  is determined by the two user defined parameters,  $C_1$  and

$C_2$  according to equation 3.1 [50] for the mean free path  $\lambda^{(h)}$  for some particle of energy, (E).  $C_1$  and  $C_2$  specifies the displacement between hard elastic collisions and is also an indication of computer processing unit (CPU) time needed to simulate each track. When  $C_1 = 0$ , PENELOPE is forced to use a detailed analog model for elastic scattering interactions.  $C_2$  parameter has a maximum allowed value of 0.1 where as  $C_{1,max}$  is 0.2.

$$\lambda^{(h)}(E) = \max \left\{ \lambda_{el}(E), \min \left[ C_1 \lambda_{(el,1)}(E), C_2 \frac{E}{S(E)} \right] \right\} \quad (3.1)$$

For hard energy loss events the user defines the cutoff energies  $W_{cc}$  and  $W_{cr}$  in accordance with the required energy resolution, where  $E_0$  is the initial kinetic energy of the primary electron or positron.  $W_{cc}$  is the cut off energy for hard inelastic collisions and  $W_{cr}$  determines the cut off energy for hard radiative transfer events [49]. According to Stewart et al (2002), the recommended parameters to operate PENELOPE for microdosimetric investigations are  $0 \leq C_1 \leq 0.02, 0 < C_2 \leq 0.02, 100eV \leq W_{cc} \leq 500eV$  and  $100eV \leq W_{cr} \leq 500eV$ . The track of a particle between successive hard interactions, or between a hard interaction and the crossing of an interface is generated as a series of steps of limited length. The parameter,  $S_{max}$ , sets the a limit to the step length to account for the variation of energy along the step, and for consistency of the simulation of soft events. The electron positron transport mechanics for simulation of soft interactions follows the "random hinge method"[50]. The soft interactions in a step  $S$  between a pair of hard interactions is simulated as a single event, a "hinge". The angular deflection and the energy loss at the hinge are sampled from approximate distributions having the correct first and second moments. The role or effect of the simulation parameters for step length control (for each material), energy-straggling control(for each material), reasonable "blind" choices and geometrical constraints are discussed in detail by Francesc Salvat (2015) in the PENELOPE-2014 operating manual.

In the section to follow the subroutine package PENGEOM will be examined for transport electrons and positrons in complex geometries.



### 3.2.2 Subroutine Package PENGEOm for Quadric Geometries

PENELOPE is a general purpose Monte Carlo simulation code system with efficient tools for tracking particles through complex geometries defined by constructive quadric geometry (i.e. material systems consisting of homogeneous bodies limited by quadric surfaces). Physics subroutines determine the distance that particles would travel in an infinite medium whereas geometry subroutines move the particle and stop it when the trajectory intersects an interface. "PENGEOm" is the geometry subroutine package of PENELOPE with this responsibility [50] and its purpose is to:

1. Track particles within material systems consisting of homogeneous bodies limited by quadric surfaces
2. Move particles along straight trajectory segments
3. Find intersections with the surfaces that limit the body
4. Identify the body and material behind the interface

Any quadric or quadratic surface after appropriate translation, rotation, and scaling can be reduced to the form

$$\phi(x, y, z) = I_1x^2 + I_2y^2 + I_3z^2 + I_4z + I_5 = 0 \quad (3.2)$$

Where the indices  $I_i$  takes the values 0, +1, or -1.

TABLE 3.1: Reduced Quadrics [50]

Reduced form	Indices	Quadric
$z - 1 = 0$	0 0 0 1 -1	plane
$z^2 - 1 = 0$	0 0 1 0 -1	pair of parallel planes
$x^2 + y^2 + z^2 - 1 = 0$	1 1 1 0 -1	sphere
$x^2 + y^2 - 1 = 0$	1 1 0 0 -1	cylinder
$x^2 - y^2 - 1 = 0$	1 -1 0 0 -1	hyperbolic cylinder
$x^2 + y^2 - z^2 = 0$	1 1 -1 0 0	cone
$x^2 + y^2 - z^2 - 1 = 0$	1 1 -1 0 -1	one sheet hyperboloid
$x^2 + y^2 - z^2 + 1 = 0$	1 1 -1 0 1	two sheet hyperboloid
$x^2 + y^2 - z = 0$	1 1 0 -1 0	paraboloid
$x^2 - z = 0$	1 0 0 -1 0	parabolic cylinder
$x^2 - y^2 - z = 0$	1 -1 0 -1 0	hyperbolic paraboloid

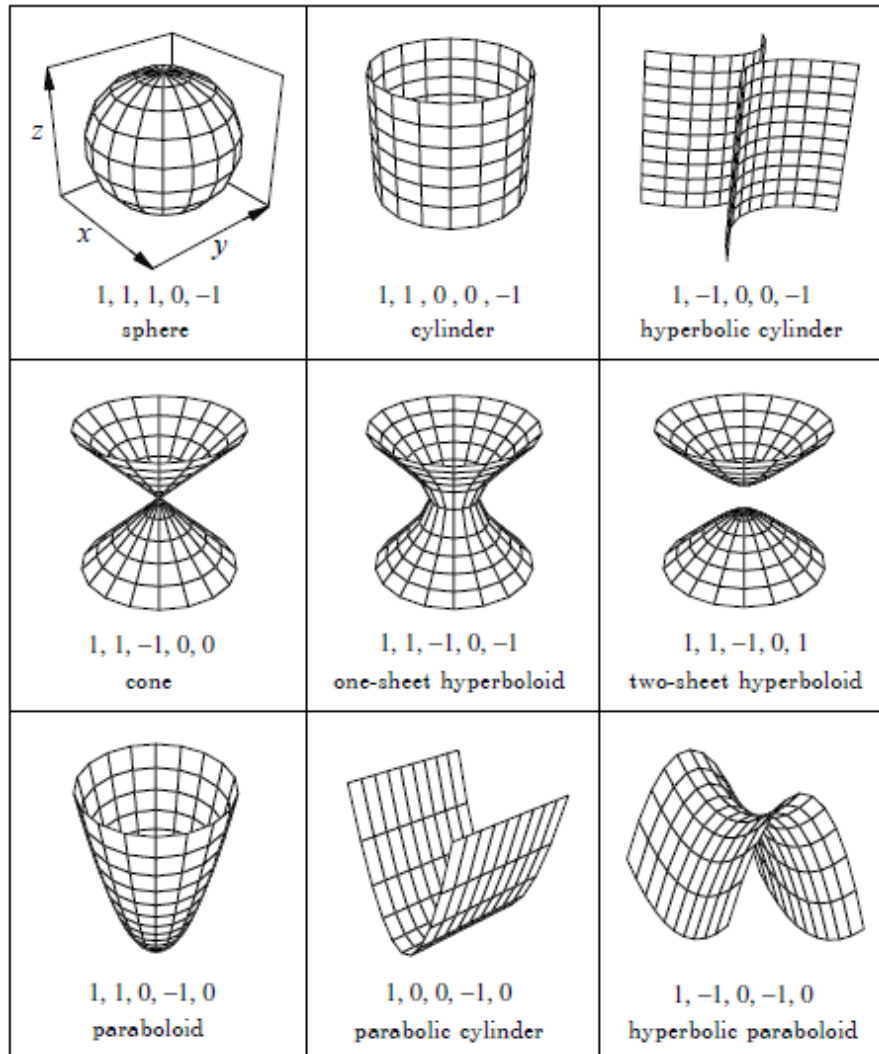


FIGURE 3.5: Non-planar reduced Quadric Surfaces and their Indices. Adopted from F. Salvat (2015). PENELOPE-2014, A Code System for Monte Carlo Simulation of Electron and Photon Transport. Workshop Barcelona, Spain, 29th June - 3rd July 2015 pg. 101.

To make the tracking code efficient, the complexity of the surface functions are limited by using quadric surfaces of the types listed in Table 3.1. A 'Body' is defined by their limiting surfaces, Figure 3.5 illustrates the different types of surfaces and their associated indices. For instance, a sphere (with indices: 1, 1, 1, 0,

-1) of radius  $R$ , is reduced by the equation:

$$\phi(R) = x^2 + y^2 + z^2 - R^2 = 0 \quad (3.3)$$

Quadric surfaces are versatile enough to design many real objects. There are two geometry viewers providing two and three dimensional images, as shown in Figures 3.6 and 3.7 respectively. Geometry definition files can be edited and debugged by using the Java GUI "PenGeomJar".

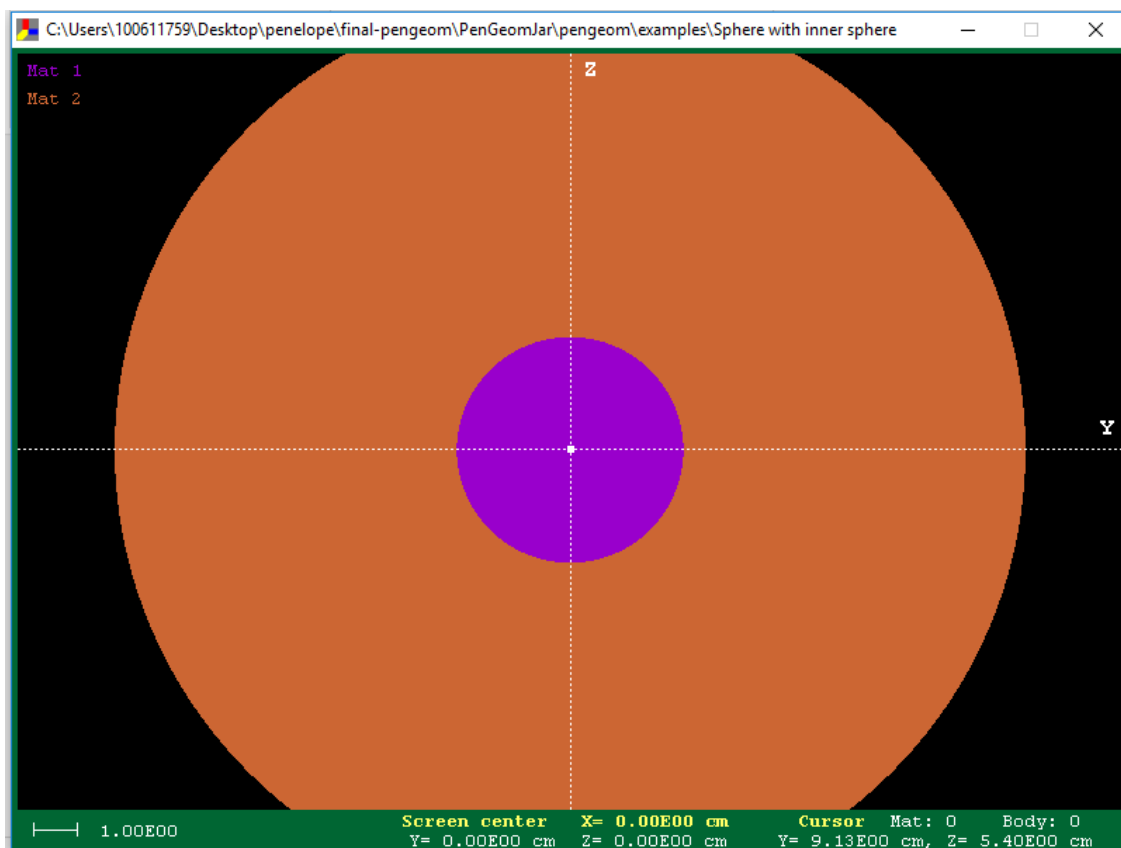


FIGURE 3.6: 2D view simulating the experimental set up used by Kliauga and Dvorak (1978), MAT1: 2.54cm diameter grid wall-less counter, surrounded by MAT2: a 10.2cm spherical shell [18]



FIGURE 3.7: 3D view simulating the experimental set up used by Kliauga and Dvorak (1978), MAT1: 2.54cm diameter grid wall-less counter, surrounded by MAT2: a 10.2cm spherical shell. The wedged out portion exposes MAT2 [18]

This versatile subroutine package allow for particles to be tracked through the complex geometries and materials used when designing and constructing the Wall-less type TEPC.

### 3.2.3 Structure and Operation of the PENELOPE Code

The structure of the PENELOPE code system incorporates the subroutine package *penelope.f*, which defines the interaction properties of materials and executes the simulation of interactions [50]. As discussed previously the complex geometry and material combinations of the wall-less TEPC will be simulated using the geometry package *pengeom.f*, and the 2D and 3D viewers (*gview2d.exe* and *gview3d.exe*) for the exhibition. The most recent addition of the "Java GUI" *PenGeomJar* (AppendixA.1) which allows geometry definition files to be edited and debugged is a very useful extension to the geometry subroutine package. Variance reduction routines *penvared.f* will offer particle splitting, Russian roulette, interaction forcing, and delta scattering of photons. The *database: 995 ascii* files with interaction cross sections and other properties of the elements Hydrogen to Einsteinium comprehensively accounts for the materials in the chamber. The two main programs *pencyl.f* and *penmain.f* for cylindrical and quadric geometries respectively, simulates a variety of radiation sources allowing scoring of different transport properties. For tracking charged particles in static electromagnetic fields, the subroutine *penfield.f* is available [50]. For displaying plots of energy-dependent interactions, program *tables.f* provides results numerically and graphically. To displaying electron-photon showers in material slabs, *shower.exe* [50] application is available.

In documentation provided from the manual and tutorial by Salavat (2014), the source codes are written in FORTRAN and requires an operating system with a FORTRAN compiler. The geometry viewers *gview2d.exe* and *gview3d.exe* and the shower program all work on Microsoft windows OS platforms. The output of the simulation programs and *tables.f* is formatted for visualization with the plotting program *GNUplot*, available for Windows. A license from the Oak Ridge National Laboratory's (ORNL) Radiation Safety Information Computational Center (RSICC) was obtained to activate the use of PENELOPE.

## Chapter 4

# Methodology

This chapter introduces the apparatus, including conditions that went into the design and construction of the counter and vacuum chamber assemblies. The wall-less design of the TEPC allows for the detection of low-energy particles that would otherwise be absorbed by the walls of a traditional proportional counter. By using a gas mixture that simulates the ionization characteristics of tissue, the wall-less TEPC accurately measures the dose and quality of radiation that would be absorbed by biological tissue. Three radioactive sources available in the laboratory with direct significance to this work were utilized. An  $^{241}\text{Am}$  alpha emitter was used to determine a calibration factor for the counter, and  $^{63}\text{Ni}$  a pure beta emitter, and  $^{14}\text{C}$ , another beta particle emitter allowed for comparative investigations. Experimental investigations of the measured dose gradient at specific measurement positions and the microdosimetric quantity the dose mean lineal energy,  $\bar{y}_D$ , were varied at distances away from a source simulating an HP within a Wall-less type TEPC (WTEPC). In addition, Monte Carlo simulations with the code PENELOPE provided a model of these possibilities for similar experimental conditions for different types of HPs. Also presented in this chapter are the various computational arrangements for PENELOPE as the modelling tool used in this study, and the procedure used to arrive at data calculated for a benchmark experiment in microdosimetry (Kliauga and Dvorak, 1978), [18] as a means of gauging the potential output data from these Monte Carlo simulations.

## 4.1 Experimental Design and Set Up of the Apparatus

In sections 2.4.3 and 2.4.4 a brief description and purpose of a TEPC and a wall-less TEPC respectively was introduced. Counters operating in the proportional region are called proportional counters (PC) as the total number of ion pairs created is proportional to the incident energy. The specific operation of the wall-less counter allows for investigations of short ranged charged particle beams. The wall-less designed counter is composed of a cylindrical A150 tissue equivalent plastic body, Delrin insulators and 50  $\mu\text{m}$  gold plated tungsten anode wire. Figure 4.1 illustrates a 2D sketch of the cylindrical counter  $\approx 23$  mm in length with a outer diameter of  $\approx 9$  mm. The hollow internal cylinder measures 5 mm in diameter, with a 5 mm cavity at the centre. Figure 4.2 gives a schematic of the counter assembled inside the vacuum chamber apparatus. The source collimator and holder are 3D printed from Polyactic Acid (PLA) material (Appendix B.2.4 and B.2.4), and can be fitted interchangeably with an alpha source  $0.1 \mu\text{Ci } ^{241}\text{Am}$  or two beta sources a  $10.2 \mu\text{Ci } ^{63}\text{Ni}$  source and a  $103.9 \text{ nCi } ^{14}\text{C}$  source.

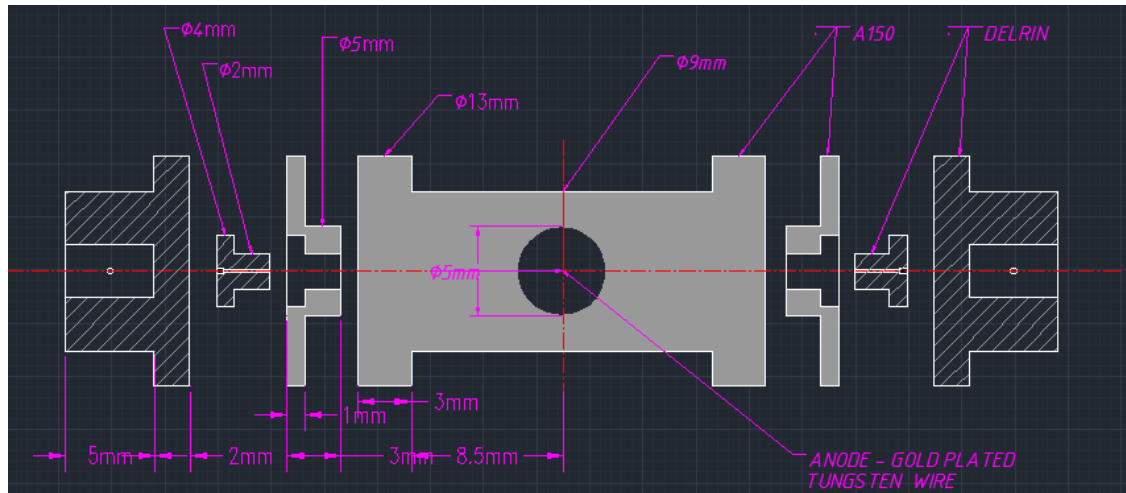


FIGURE 4.1: Cross-section of a cylindrical Wall-less TEPC. The anode wire runs centrally through a 5 mm cavity.



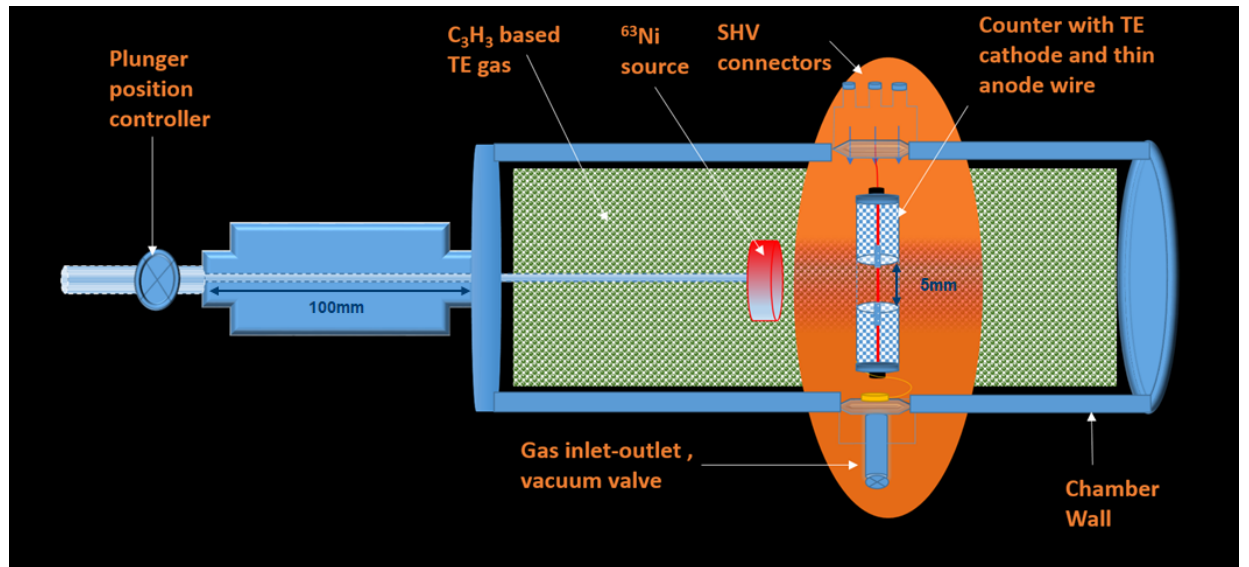


FIGURE 4.2: Annotated schematic of a cylindrical type Wall-less TEPC currently constructed: with a low energy (max  $E_{\beta} 0.07 \text{ MeV}$ )  $^{63}\text{Ni}$  source, in propane based TE gas, used for simulating a distance from the counter to the maximum range of beta particles ( $41 \mu\text{m}$ )

Figure 4.3, is a flowchart illustrating three phases of operation used in this work for investigating these short ranged alpha and beta particles. The aim of a wall-less TEPC is to provide a radiation detector that can accurately measure the dose and quality of radiation that penetrates biological tissue. The TEPC is designed to mimic the response of human tissue to ionizing radiation and is made of materials that have similar atomic and density properties to human tissue.

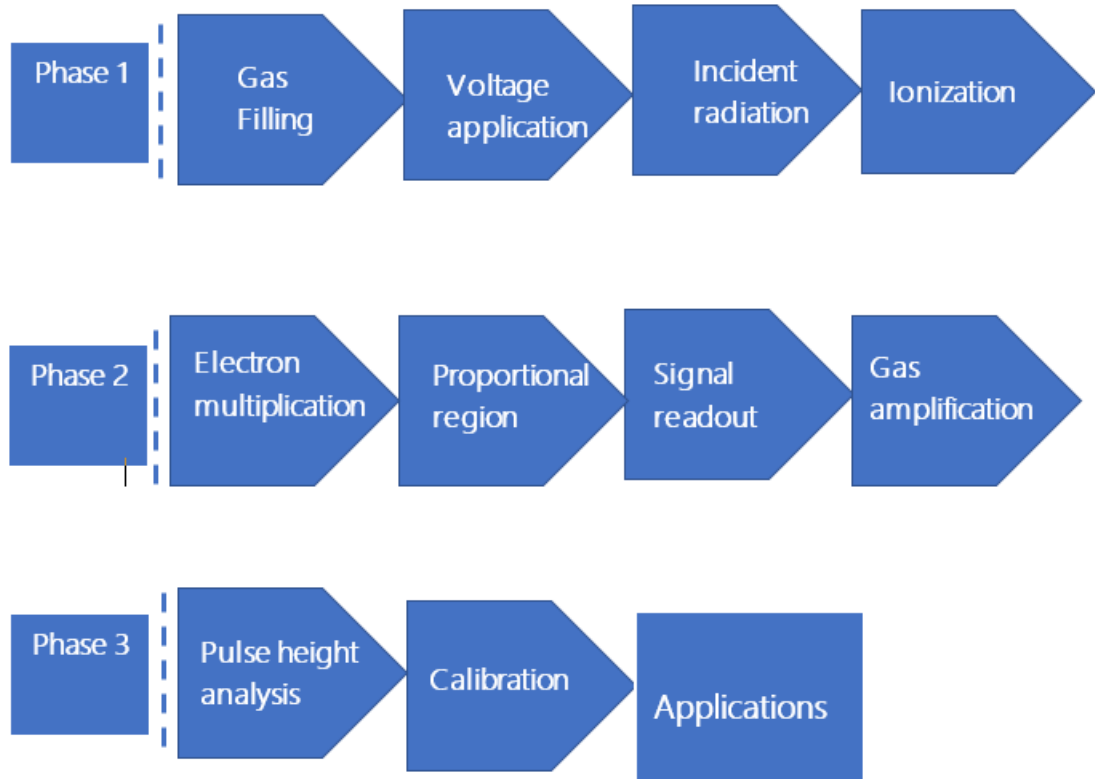


FIGURE 4.3: Flow Diagram of three operating phases of a Wall-less TEPC

Phase 1 of the detector or counter's operation is described as the source and ionization phase. For instance a source of beta particles installed into the apparatus mimics a hot particle that decays by beta emission. A source of short ranged charged alpha particles mimics a HP that decays by alpha emission. The short ranged charged particles pass through the high transparency copper mesh cathode to interact with the counter's sensitive volume simulating a 2 micron unit density tissue site. Figure 4.4 illustrates a cross-sectional schematic view of the wall-less design components, with the aluminum anode potential tubes installed to essentially reduce ionization outside of the sensitive 5 mm cavity.

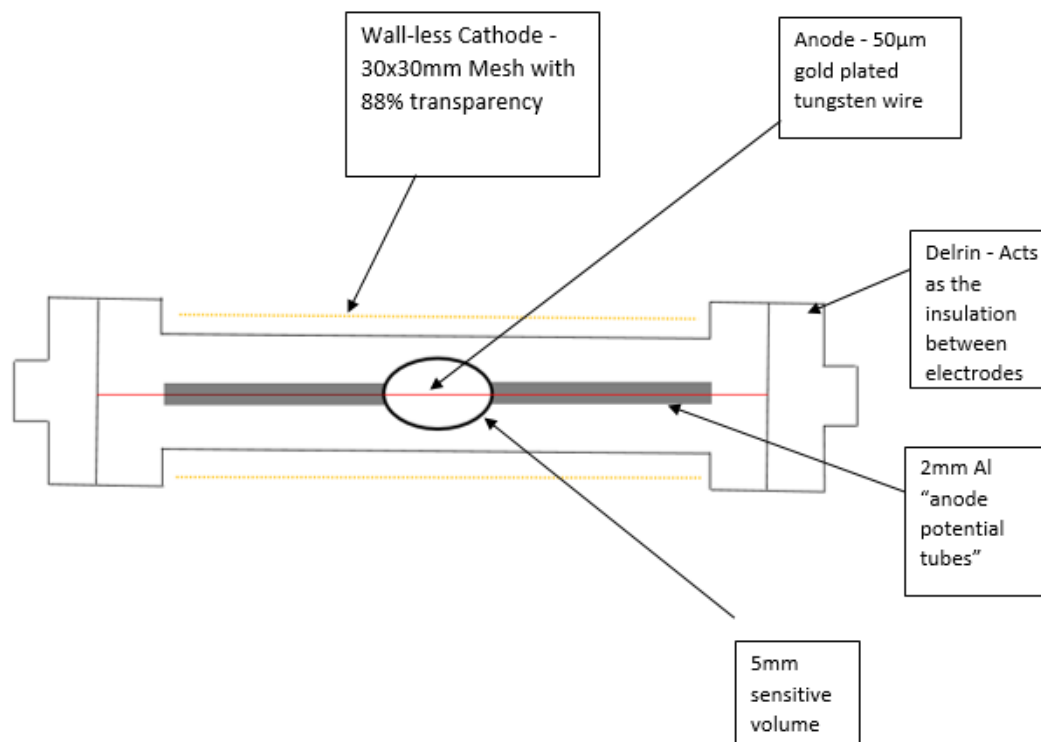


FIGURE 4.4: Cross-sectional schematic view of the Wall-less Counter Components with Anode Potential tubes installed just outside the 5 mm sensitive cavity

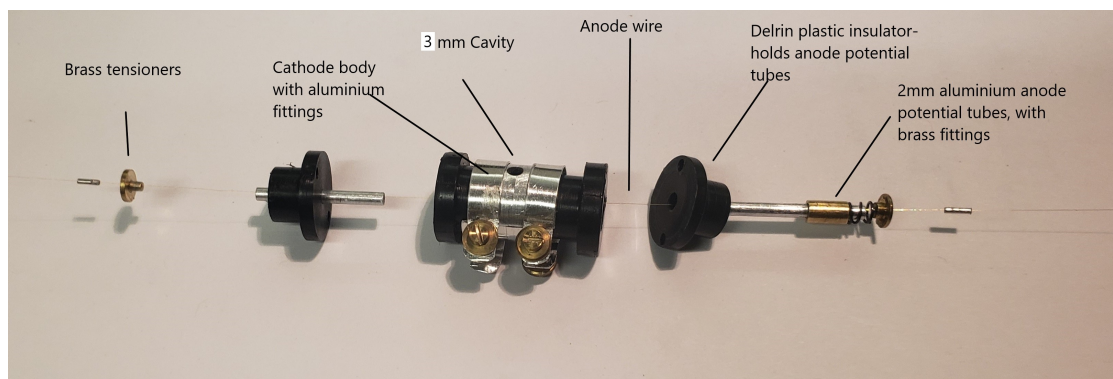


FIGURE 4.5: A view of one design version of the wall-less counter's internal components with the anode potential tubes installed. This design investigated the sensitivity of the counter with 100% transparency (Meaning no material between the beam and the gas inside the sensitive volume)

Phase 2 of the detector or counter's operation is described as the drift or multiplication region. For this wall-less designed TEPC the behavior of the electric field is based on the radius of the anode wire as described in Equation 2.8 in Section 2.2.4. Figure 4.5 is an annotated diagram of the counter before being fully assembled. This version of the counter was used to investigate the general beam alignment and sensitivity of the anode wire at various high voltages. As the radius of the wire gets smaller the strength of the electric field increases. It was also advantageous to use a thin wire of a very small radius ( $\mu\text{m}$  sized) to confine the multiplication region as close to the anode as possible. The voltage is adjusted and optimized so that the number of charge that gets to the anode is proportional to the amount of charge that was initially present, at this moment the detector or counter exists in the proportional region. The gas amplification factor is controlled by the voltage applied to the counter, which can be adjusted to change the sensitivity of the counter. In the Section 4.1.2 on determining gas gain, a deeper explanation and method of arriving at the appropriate anode wire size, and the anode potential tube size.

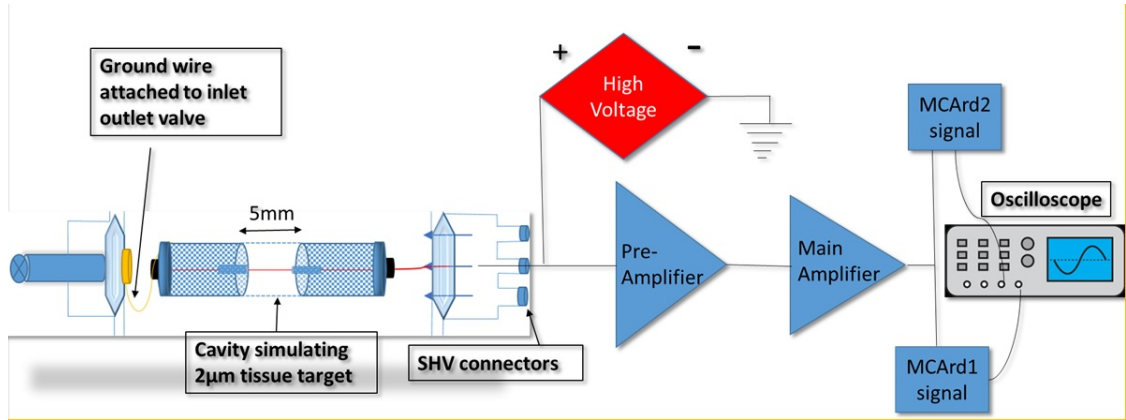


FIGURE 4.6: Experimental set up used to measure pulse heights. A build up of charge in the pre-amplifier is converted to a voltage pulse. Each single event creates a pulse at the amplifier which is proportional to the energy deposited. The cavity represents a 5mm diameter sphere of chord length  $1.33 \mu\text{m}$  conveniently simulating  $2 \mu\text{m}$  tissue dimensions matching sub-cellular geometries.

Phase 3 of the detector or counter's operation is described as the collection and analysis phase. Inevitably there is a build up of charge on the anode as a result of the initial charged interactions that were multiplied in the proportional region. A pre-amplifier which is a charge sensitive device converts the charge into voltage via the function  $Q = VC$ , where the charge,  $Q$  goes into an input capacitor  $C$  which stores the charge and converts it into a voltage pulse,  $V$ . Repeated increased build up of charges is discharged as a voltage pulse. The Voltage pulse goes into a main amplifier or a digital pulse processor that shapes the pulse for a trapezoidal or Gaussian display. Figure 4.6 displays all the electronic components of the experimental set up. Each event or ionization creates a pulse at the amplifier which is proportional or indicative of the energy deposition experienced in the tissue equivalent gas. The Multi-Channel Analyzer (MCA) is a voltmeter with a range of 3 V from 0 channel to 16383 channels, approximately 0.2 mV per channel. The MCA measures the height of each pulse and deposits each pulse into its respective bin appropriate to the height per channel per volt. The height of the pulse is a factor of the time the capacitor takes to discharge the voltage,

each discharge having a different height. The MCA based on the pulse heights and voltage per channel places the pulse into different bins producing a distribution of pulse sizes or single events. This becomes the imparted energy data for the lineal energy measurements with respect to a constant, the mean chord length  $\bar{l}$  of the sensitive volume. To determine the absorbed dose the counter is allowed to collect enough counts, which is indicative of the energy deposited into the gas. The more counts collected improves the counting statistics, and the energy per mass of the gas determines the absorbed dose. The uncertainty in the data was expected to be small after collecting for more than 15000 seconds. A proportional counter typically is calibrated using standard radiation sources to establish the relationship between the electrical signal and the energy of the incident radiation. This will be discussed further in and in more details in the upcoming sections.

### 4.1.1 Detector Design and Construction

Significant to accomplishing the objectives of this study were the design and construction of a 5mm cavity wall-less counter or detector in a vacuum chamber that is capable of measuring dose and a potential change in radiation quality. Accomplishing this objective required investigating the appropriate size for the anode wire needed in a 5 mm cavity mimicking a  $2 \mu m$  tissue target site, a convenient dimension that matches sub-cellular geometries. Also, the pressure (in torr) of the gas for a propane based (55.01%  $C_3H_8$ , 5.39%  $N_2$ , 39.6%  $CO_2$ ) TE gas mixture occupying the entire chamber had to be determined. The range of  $^{63}Ni$  pure beta emitter with an  $E_{max} \approx 3 \times 17.4$  keV was experimentally measured to be about 6.5 cm in air, equivalent to a range of 16.75 cm in this TE gas mixture [20]. Apriori, for a 12.7 mm counter simulating a  $2 \mu m$  site size, Ali et. al., determined that the pressure of the TE gas required to fill the chamber was 65 torr [51]. For the required 5 mm counter mimicking  $2 \mu m$  of tissue size, the calculated pressure of the TE gas needed for this apparatus is 165 torr. The next step in the design phase was reliant on understanding the prospective gas multiplication taking place around the positive electrode. In the immediate section that follows,

the iterative process in choosing the appropriate sized wire that would fulfill the requirements of the investigation is explained in more details.

### 4.1.2 Determining the Gas Gain

In order to determine the adequate gas multiplication in the proportional region needed at the anode for a  $2 \mu m$  simulated site volume, a range of voltages were analyzed against various radii of anode wires with the radius of the negative electrode fixed at 2.5 mm. Figure 4.7 illustrates the results for after investigating the gas gains at various calculated anode wire diameters ( $50 \mu m$ ,  $100 \mu m$ , 1 mm, 2 mm, 3 mm, and 4 mm) against different potentials ranging from 50 V to 1500 V. These results are introduced as part of the methodology section as they provided an important step in the development of the counter's design.

According to Lindborg and Waker (2017), an equation capable of estimating an appropriate gas gain [23] was as follows:

$$LnG = \frac{AV}{B \ln(\frac{c}{a})} \left[ \frac{c}{a} \right]^{-\frac{aBP}{V}} \quad (4.1)$$

Where  $c$  and  $a$  are the radii of the cathode and anode wires respectively, and  $V$  is the applied potential. In Equation 4.1  $A$  and  $B$  are gas specific constants, and for a cylindrical counter  $A$  was taken to be  $34 \text{ cm}^{-1} \text{ torr}^{-1}$ , and  $B$  was given as  $418 \text{ V cm}^{-1} \text{ torr}^{-1}$  by Waker (1982) [52]. The constant  $A$  is proportional to the reciprocal of the mean free path in the TE gas and the constant  $B$  relates to the ionization potential of the gas molecules [23].

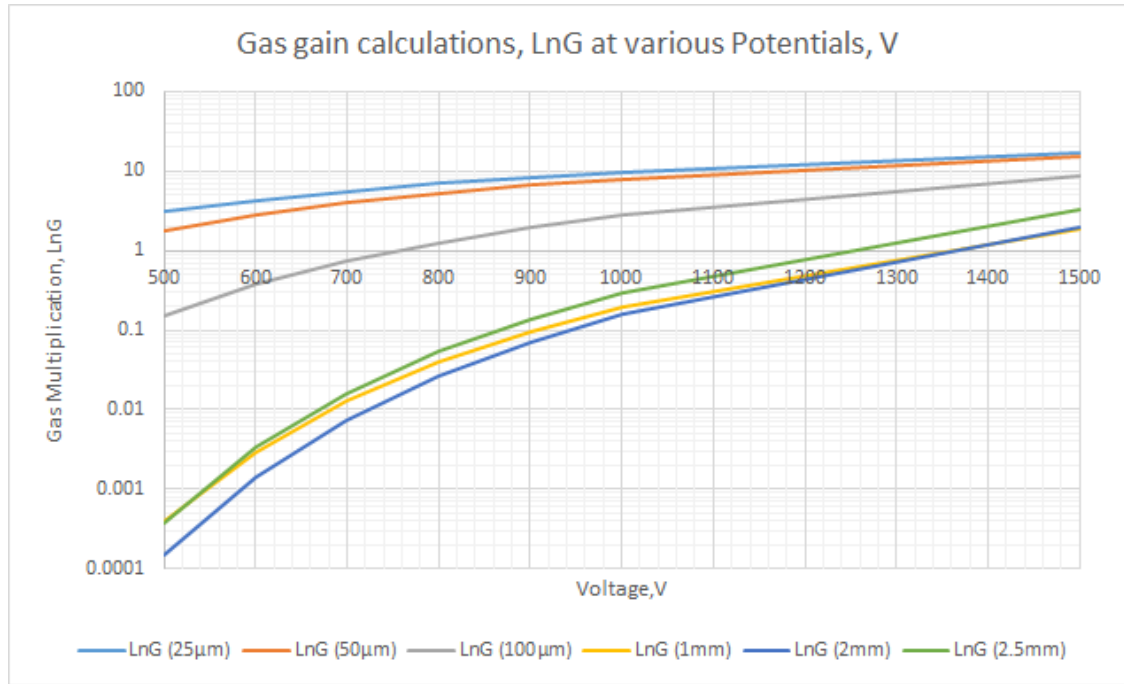


FIGURE 4.7: The calculated gas multiplication in a cylindrical type Wall-less TEPC at different potentials for a 5 mm cavity counter simulating  $2 \mu\text{m}$  at 165 torr

The effect of electrons and ions potentially recombining required an appropriate choice in the size of the anode wire and the applied potential to sustain the gas multiplication. Figure 4.7 illustrates that significant gas multiplication occurs above 500 V and continues as the voltage increases for wire sizes ranging from 25 to 100  $\mu\text{m}$ . Below 1200 V the gas multiplication on an anode wire of sizes ranging from 1 mm to 2.5 mm are not expected to be significant. Based on these findings, anode potential tubes of diameter 2 mm were chosen to shield a 50  $\mu\text{m}$  gold plated tungsten wire acting as the positive electrode. The graph indicates that the natural logarithm of the gas gain on a 2 mm anode potential tube at about 850 V would be around 0.04 and the gas gain on the 50  $\mu\text{m}$  anode wire would be significantly higher at the same potential. Based on these favorable findings the detector was designed and constructed for the 2 mm anode potential tubes to exist just outside the 5 mm sensitive volume, potentially restricting or limiting any



gas multiplication occurring outside of the 5 mm sensitive volume.

### Counter and Vacuum Chamber Assembly Parts

The parts for the detector and chamber were sourced from scientific part suppliers and from old detectors parts available locally in the laboratory. For the counter assembly, Figure 4.8 (a) and (b), illustrates two anode potential guide tubes with brass fittings and a 50  $\mu\text{m}$  gold plated tungsten wire (1.82 g), with 99.95% purity respectively, insulated by delrin plastic. The 30mm x 30mm copper mesh with 88% transparency, Figure 4.8 (c) was obtained through Delta Scientific a subsidiary of "Goodfellow". Further specifications of the electro-formed mesh used as the cathode are available in Appendix B.1. Figures 4.8 (d),(e), and (f) illustrate parts of the counter and a jig fabricated locally to hold the counter at a fixed position in the chamber. The vacuum fittings (silicone O-rings, KF50 bored and blank flanges, clamps and center rings) for the vacuum chamber, were procured from Kurt J. Lesker a leading high-quality vacuum equipment supplier. A cross-shaped stainless steel pipe, with KF50 openings of approximately 50 mm in diameter was attached to a 14 cm long full nipple stainless steel pipe, which made the total length of the chamber approximately 30.5 cm. The jig in Figure 4.8 (f) was inserted into one end of the chamber connecting to a ISO KF50 safe high voltage (SHV) flange connector and grounded at the other end onto the inlet outlet gas valve flange connector as shown earlier in the sketch in Figure 4.6. A schematic of the full chamber with counter is already presented in Figure 4.2, highlighting the plunger position controller (obtained from Huntington Mechanical Labs. Inc.), which has a graduated stroke length of 100 mm. So with a 5 mm cavity mimicking a movement of 2  $\mu\text{m}$  the chamber has a measurement range from the edge of the source beam to the anode wire of 41  $\mu\text{m}$ . When attached to a source, the plunger under vacuum can be moved incrementally back and forth from the counter. The jig in Figure 4.8 (g) holds the counter at a fixed position in the chamber at approximately 6.7 cm centrally from either side.



FIGURE 4.8: A montage of the assembly parts for use in the design and construction of a cylindrical type Wall-less TEPC: (a) Magnified image of 2 mm diameter anode potential guide tubes, with brass fittings; (b) magnified image 50 $\mu\text{m}$  gold plated tungsten anode wire; (c) 30 mm x 30 mm copper mesh with 88% transparency; (d) mesh attached to the body of the A150 plastic column to form the cathode, with a 5 mm opening; (e) partial assembly of the counter;(f) counter affixed to holder for insertion into the vacuum chamber;(g) partial assembly in vacuum chamber;(h) full assembly of chamber with detector positioned in side, and perpendicular to the plunger holding the source; (i)current architecture for collecting results.

The full architectural set up is displayed in Figure 4.8 (i). The counter is connected through a SHV connector to a pre-amplifier power connection with a integrated APTEC (AHV-2PC) universal high voltage auto-bias PC plug in card. The setup has two (2) series 5000 multi-channel analyzer (MCA)carrier cards (called MCArds) that measure each pulse height and processes it into its respective bin or channel. The height of the pulse is a factor of the time the built in capacitor takes to discharge the voltage, each discharge having a different height. Based on each height, the MCA sorts the data for display with the APTEC data acquisition software. A dual channel oscilloscope independently displays pulses generated by both MCAard 1 and MCArd 2.

With the counter components fully assembled to the electronic architecture a relative gain test was conducted to determine if the detector was operating in the proportional region. To conduct this test an  $^{241}\text{Am}$  (See Appendix B for image and specifications) source was installed into a collimator and source holder designed and 3D printed locally in lab on the Maker-bot Printer specifically for this experiment (see Appendix B.2.4 and B.2.5 for details). The high voltage was placed at 500V across the counter and an alpha peak collected at an amplifier gain of 75. The voltage was increased to 600V and the amplifier gain adjusted accordingly to a gain of 20. The alpha peaks measured 39 and 57 counts with a relative gain calculated to be 1 and 5.48 respectively. Figure 4.9 shows a chart and table of the relative gain findings for this WTEPC. To determine the relative gain,  $G$ , equation 4.2 was used to solve the logarithm of  $G$ .

$$G = \frac{P_{i=1} \text{Amp}_{i=1}}{P_{i=2} \text{Amp}_{i=2}} \quad (4.2)$$

Where  $P_{i=1}$  is the position of the alpha peak at position  $i=1$  and  $\text{Amp}_{i=1}$  is the corresponding Amplifier gain at the same position. The Figure 4.9, gives a table of increasing voltage and the values of the calculated relative gain. The test indicated that the WTEPC appears to be functioning in the proportional region Figure 4.9, a positive test for proportionality with the logarithm of the relative gain increasing linearly as the voltage increases.

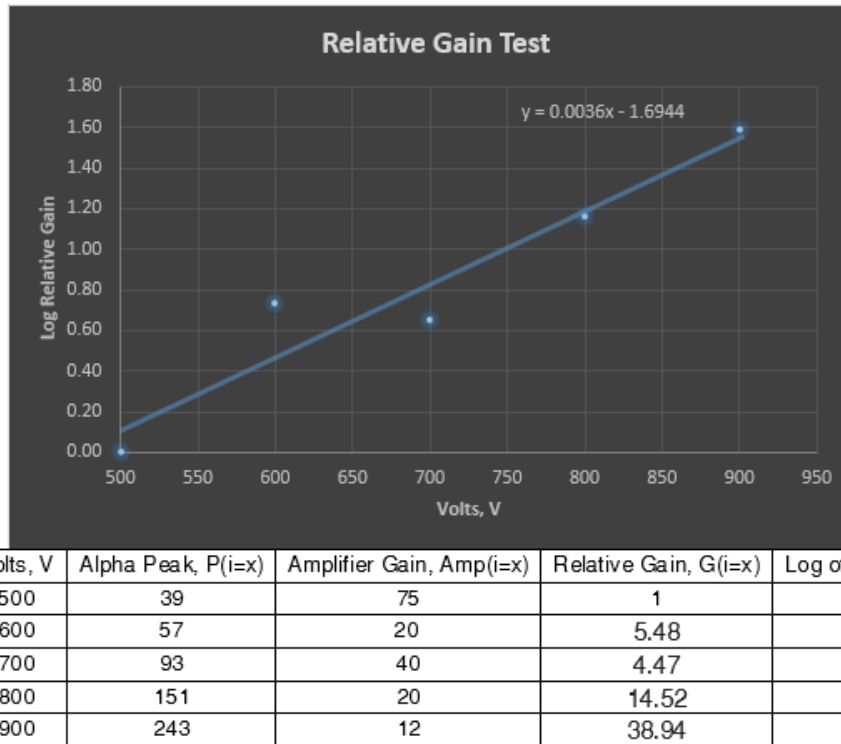


FIGURE 4.9: Relative Gain Test for the WTEPC in the Proportional Region

This was a good indication that the WTEPC constructed was a working counter having the potential to measure low energy short range particles.

## 4.2 Operation of the WTEPC Architecture

The WTEPC was assembled and irradiated by sources in two different modes, with the anode potential tubes installed and the other with the tubes removed. Figure 4.5 presented earlier shows a version of the counter used in investigations with the anode potential tubes installed around the 50  $\mu m$  gold plated tungsten positive electrode. For comparison, Figure 4.10 illustrates the counter being assembled with the 2 mm anode potential aluminum tubes uninstalled with the counter acting as a single wire counter. Investigations for near field dosimetry

were carried out to determine which method produced a better peak resolution. This involved operation of the WTEPC in anti-coincidence mode and coincidence mode.

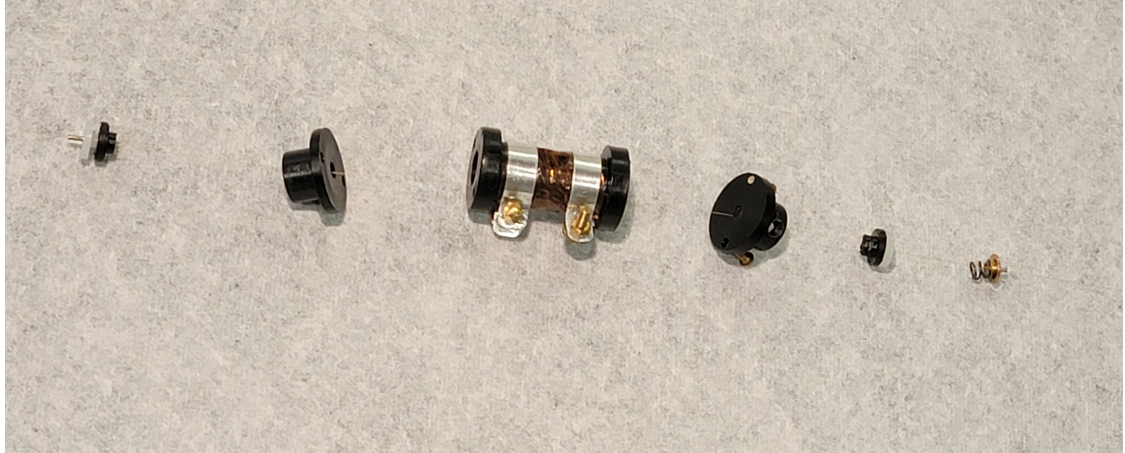


FIGURE 4.10: Wall-less TEPC with Anode Potential tubes uninstalled

### 4.2.1 Anti-Coincidence Mode

In anti-coincidence mode or "Normal mode" the collection set up for the MCARD is displayed in Figure 4.11. The "number of channels in spectrum", along with the 'ADC Gain' radio buttons were set to 16384 for the number of channels to digitize a full scale signal. The 'Lower Level Discriminator' (LLD) and 'Upper Level Discriminator' (ULD) vertical slider bars were set to 200 and 16383 respectively. The 'Offset' and 'Internal channel offset' features were not utilized for this investigation. The 'External Offset Input' feature was not used and pulse above the ULD were set to be ignored.

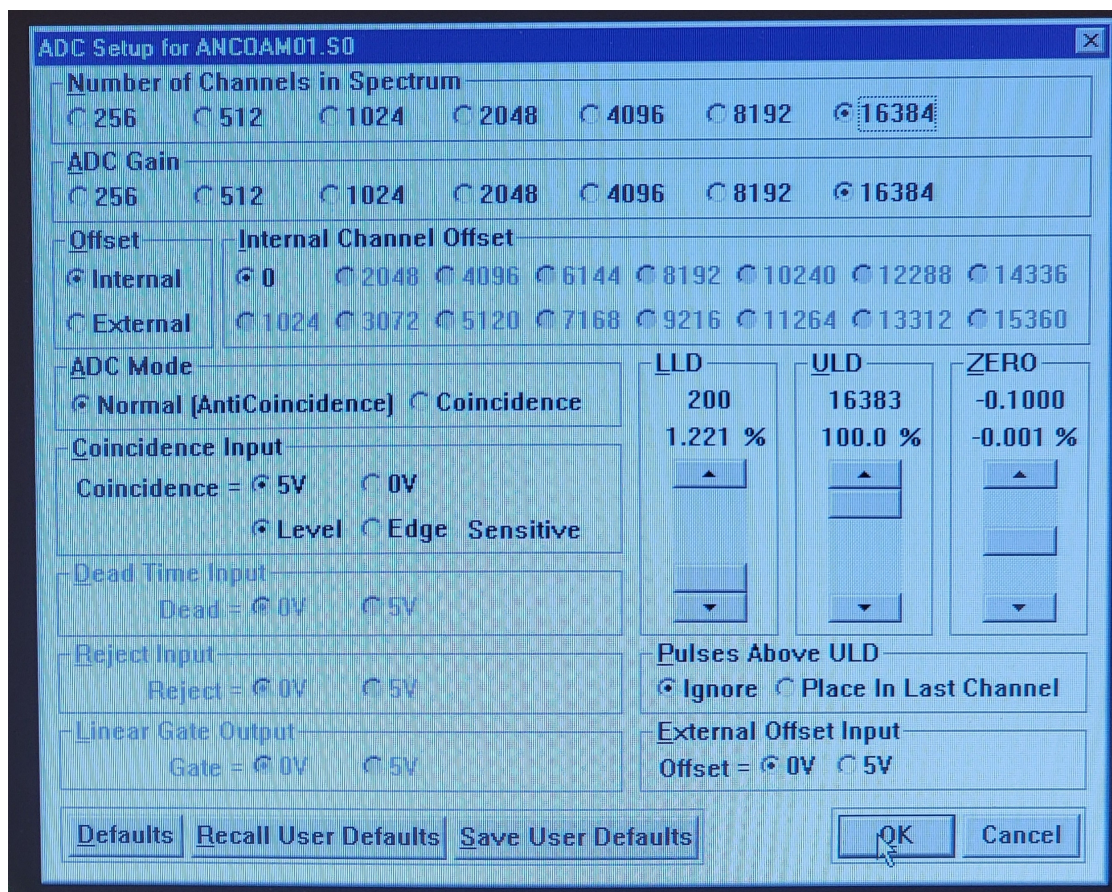


FIGURE 4.11: APTEC Data acquisition System with ADC set up for pulse height data collection on 'MCARD'#1

Figure 4.12 displays the pulse height collection of 5.6 MeV  $^{241}\text{Am}$  alpha particles in normal anti-coincidence mode with the anode potential tubes installed. After a true collection time of 76187 seconds. The APTEC data acquisition software collected a peak height at channel number 2434 with an average count rate of 10.31 counts per second, a dead time of 3.42% and gross counts of 758447.

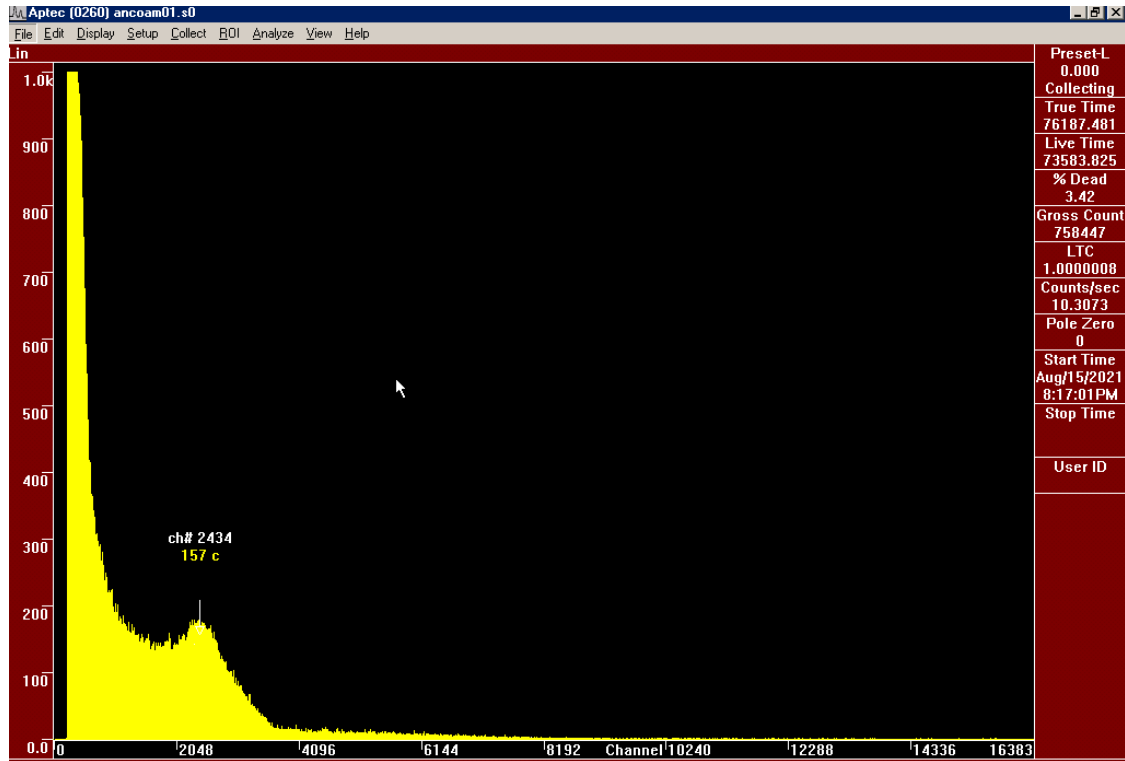


FIGURE 4.12: APTEC Data acquisition System with ADC set up in Anti-Coincidence Mode with Anode Potential Tubes Installed

For optimization of the counter the anode potential tubes were removed to investigate if the resolution of the counter would improve. The true collection time was around 6 times less than before, there was virtually no dead time and the resolution of the peak improved significantly round about the same channel number. Figure 4.13 illustrates the painted region of interest peak. The lower gross counts and count rates are factors of the counting time, but with the anode potentials tubes removed the resolution of the peak was much better.

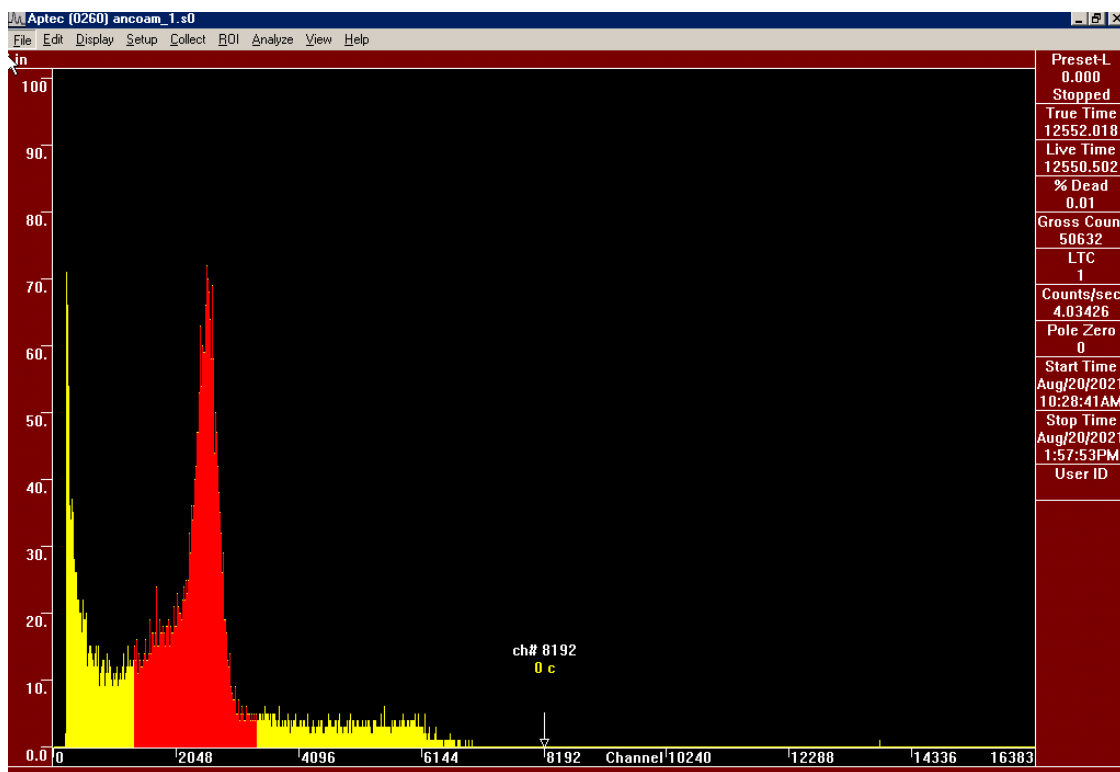


FIGURE 4.13: APTEC data acquisition system with ADC settings in anti-coincidence mode with anode potential tubes uninstalled. The area painted red represents majority of the 50632 gross counts.

This was an indication of the progress made in design and construction of the WTEPC to measure energy depositions over a simulated  $2\mu\text{m}$  tissue cavity. The pulse-height spectra generated by the counter exposed to a  $0.1\mu\text{Ci}$ ,  $^{241}\text{Am}$  source produced a prominent peak around channel number 2434 number and is believed to be from events generated by alpha particles passing through the counter. To produce this result, the high voltage across the counter was set at approximately 750V with the gain at 30 and the APTEC-ADC settings in anti-coincidence mode.



## 4.2.2 Coincidence Mode

The improvement of the shape and resolution of the peak collected for events produced from 5.5 MeV alphas are shown in Figure 4.12 and 4.13. It was also important to investigate if the resolution of the peak could be further optimized by eliminating those events that are produced by alpha particles potentially not crossing the counter along its diameter. To improve this the apparatus was upgraded with a surface barrier detector (SBD) illustrated in Figure 4.14 and installed in 4.15. The SBD is connected to a gate and delay generator as displayed by the circuit diagram in Figure 4.16. The collection and set up for MCARD #2 was arranged differently. This time the ADC mode was toggled to 'coincidence mode' and the coincidence input set to 'edge sensitive' settings with the other features left unchanged.

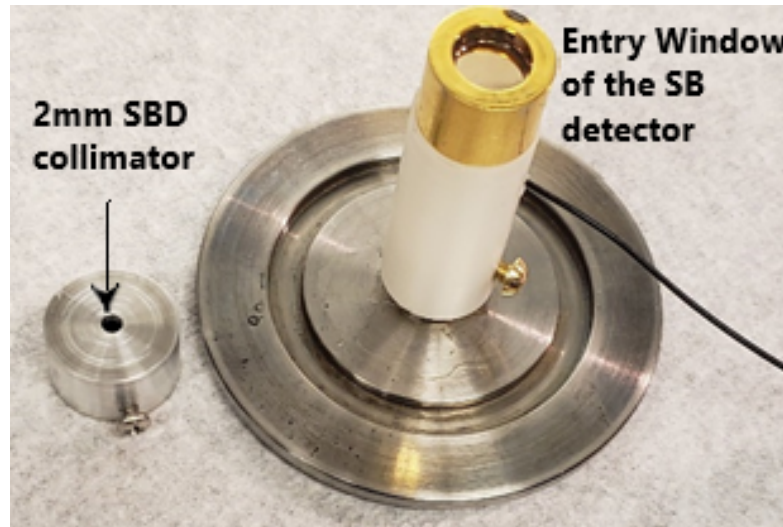


FIGURE 4.14: The Surface Barrier Detector fixed to a KF50 vacuum flange towards the back of the apparatus.

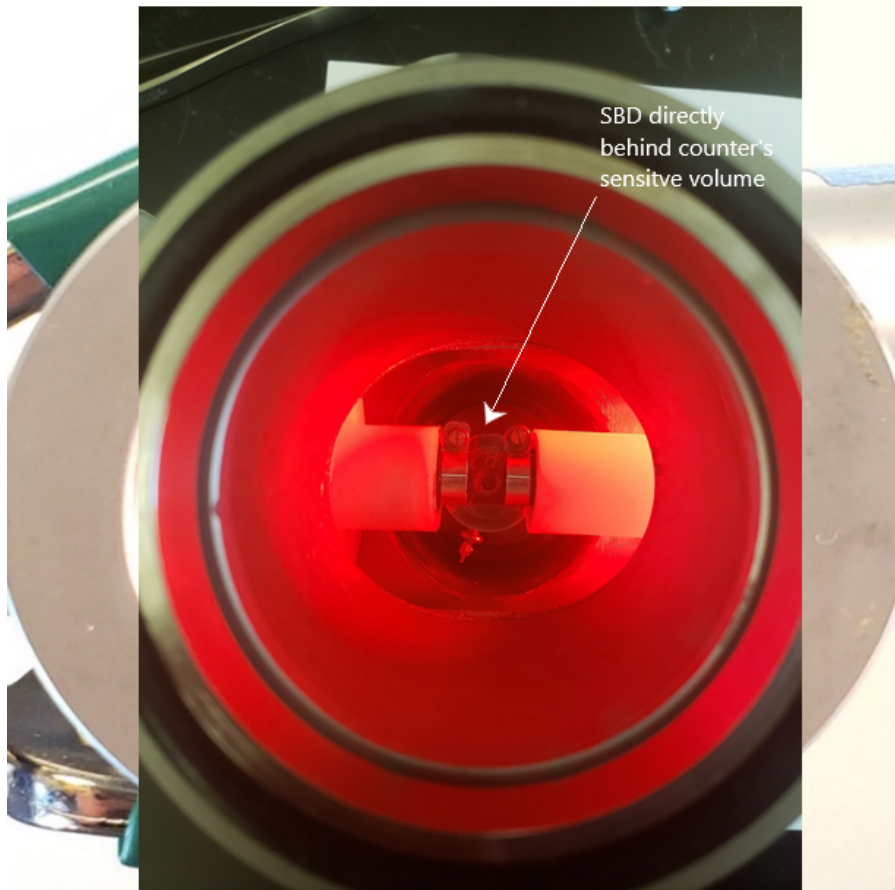


FIGURE 4.15: The Surface Barrier Detector (SBD) installed behind the counter's  $2 \mu s$  sensitive volume.

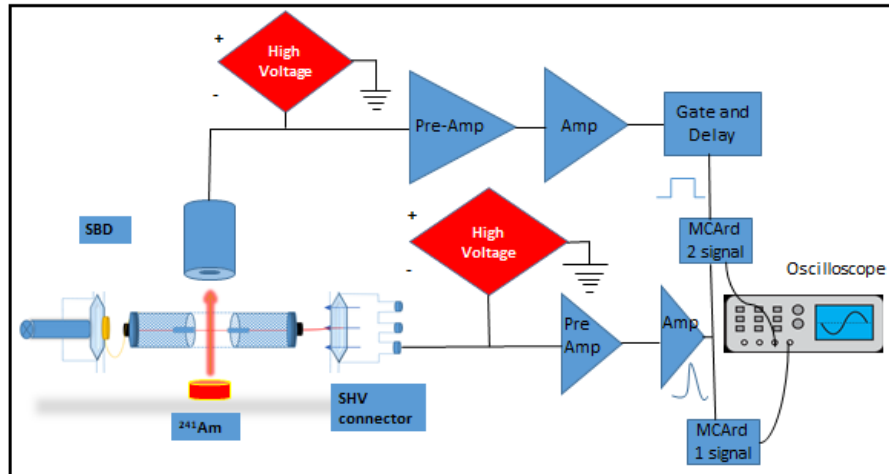


FIGURE 4.16: Circuit diagram with installed Surface Barrier Detector to Perform Coincidence experiments to improve the WTEPC Calibration

With the input set to pulse edge sensitive settings, the pulse edge had to occur before and about 100 ns beyond the analog pulse peak. In order to achieve this a module with a gate and delay (GD) generator, a pulser, an amplifier and an external pre-amplifier were assembled with the SB detector. The GD generator settings were set to a delay time of  $4 \mu\text{s}$  and the width to  $2 \mu\text{s}$ . As a result the signal overlap can be seen in Figure 4.17.

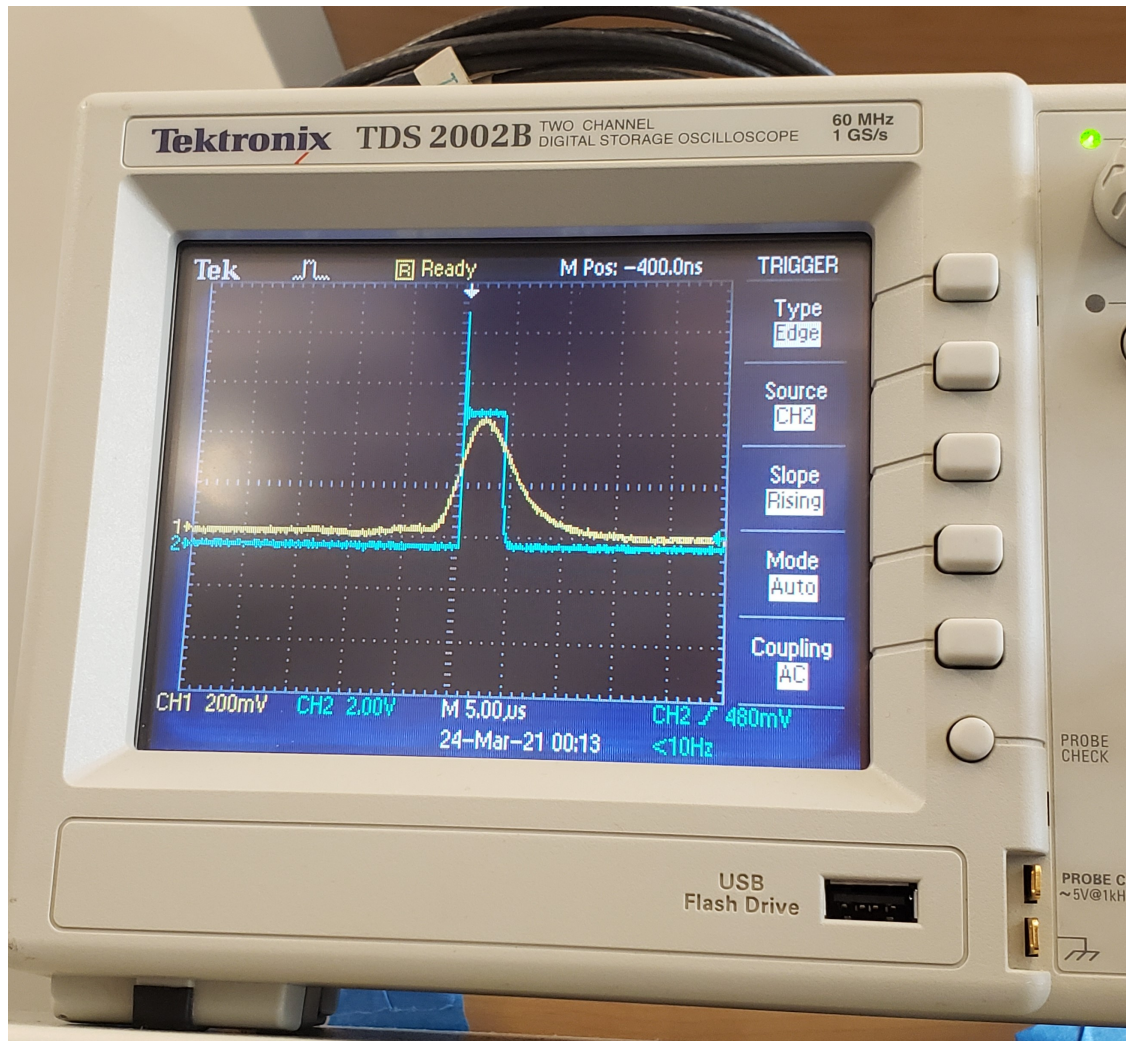


FIGURE 4.17: Oscilloscope Displays the overlap between the signals on the SBD and the WTEPC

Figure 4.18 shows the collected spectra for a  $^{241}\text{Am}$  alpha source in coincidence mode with the anode potential tubes installed and the peak height indistinguishable from the noise, indicating a poor peak resolution. The events were collected after 75258 seconds with dead time of 4.45% at a very low count rate of 0.39 counts per second.

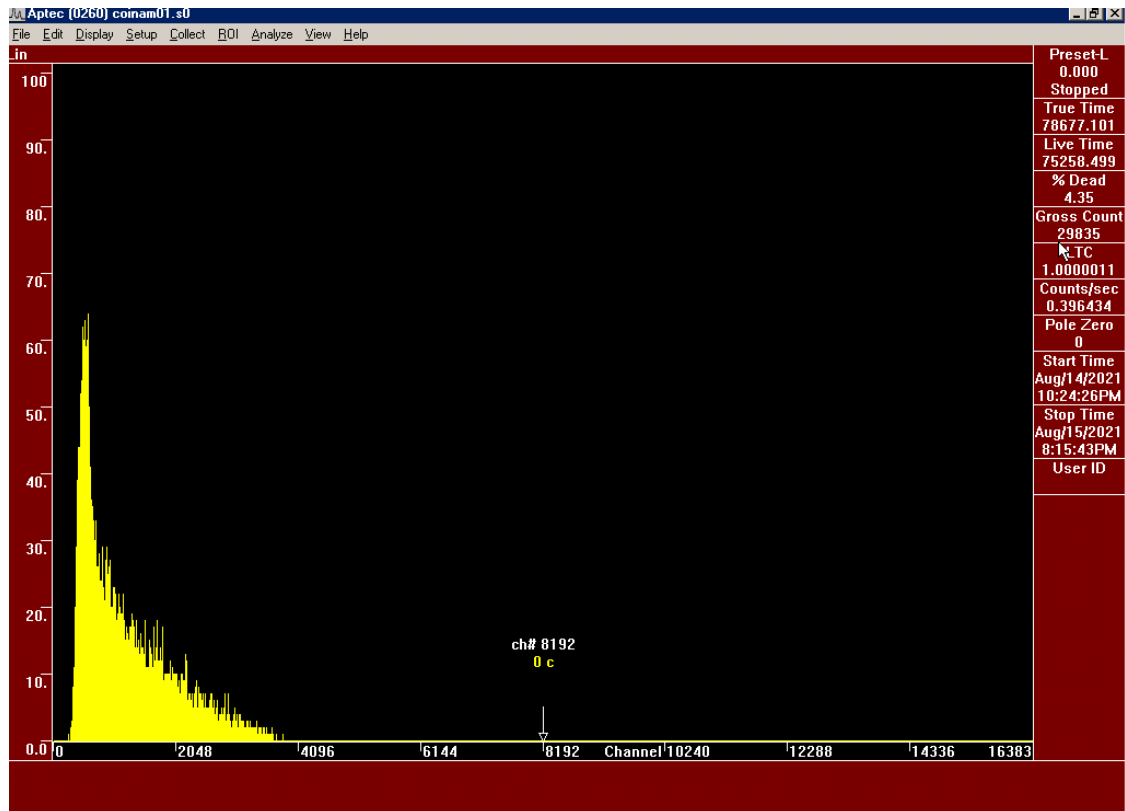


FIGURE 4.18: APTEC Data acquisition System with ADC set up in Coincidence Mode with anode potential tubes installed.

Just as before the counter was disassembled and the anode potential tubes removed to determine if the peak resolution would improve. The peak resolution improved considerably as illustrated in Figure 4.19. The dead time also improved with the count rate remaining about the same. The detector was allowed to collect for an even a longer time, Figure 4.20, collecting about twice the gross counts. The resolution continued to improve even though the count rate remained the same.

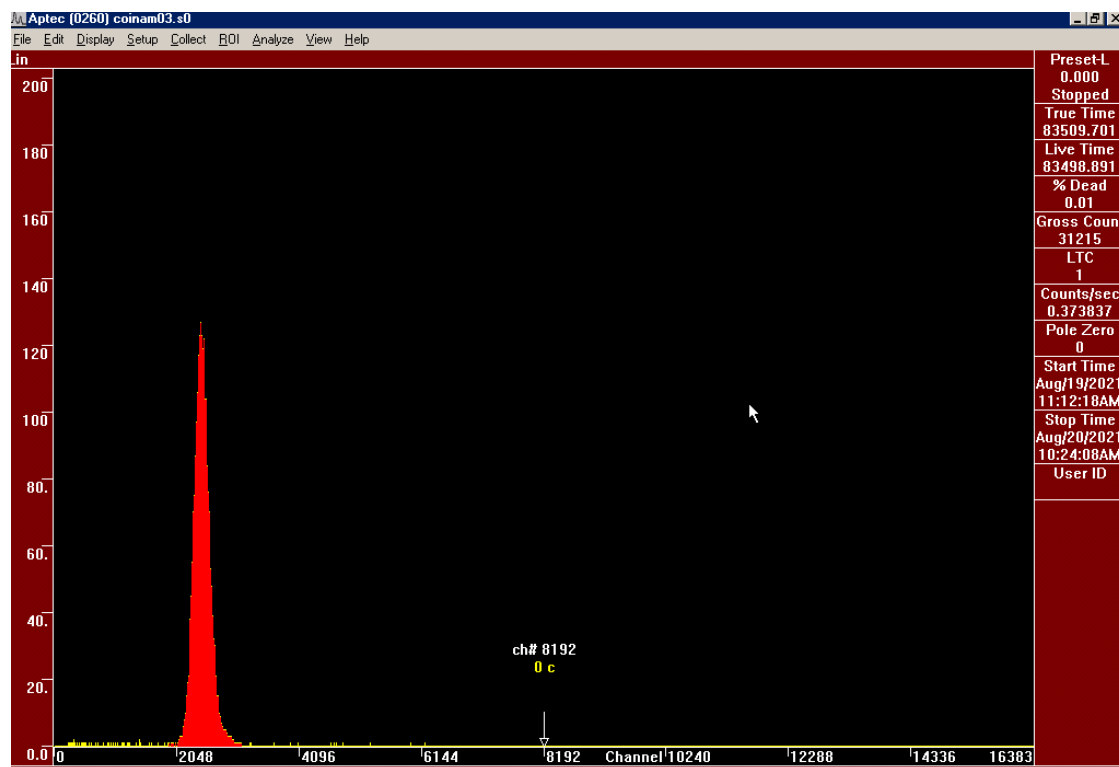


FIGURE 4.19: APTEC Data acquisition System with ADC set up in Coincidence Mode with Anode Potential Tubes Uninstalled

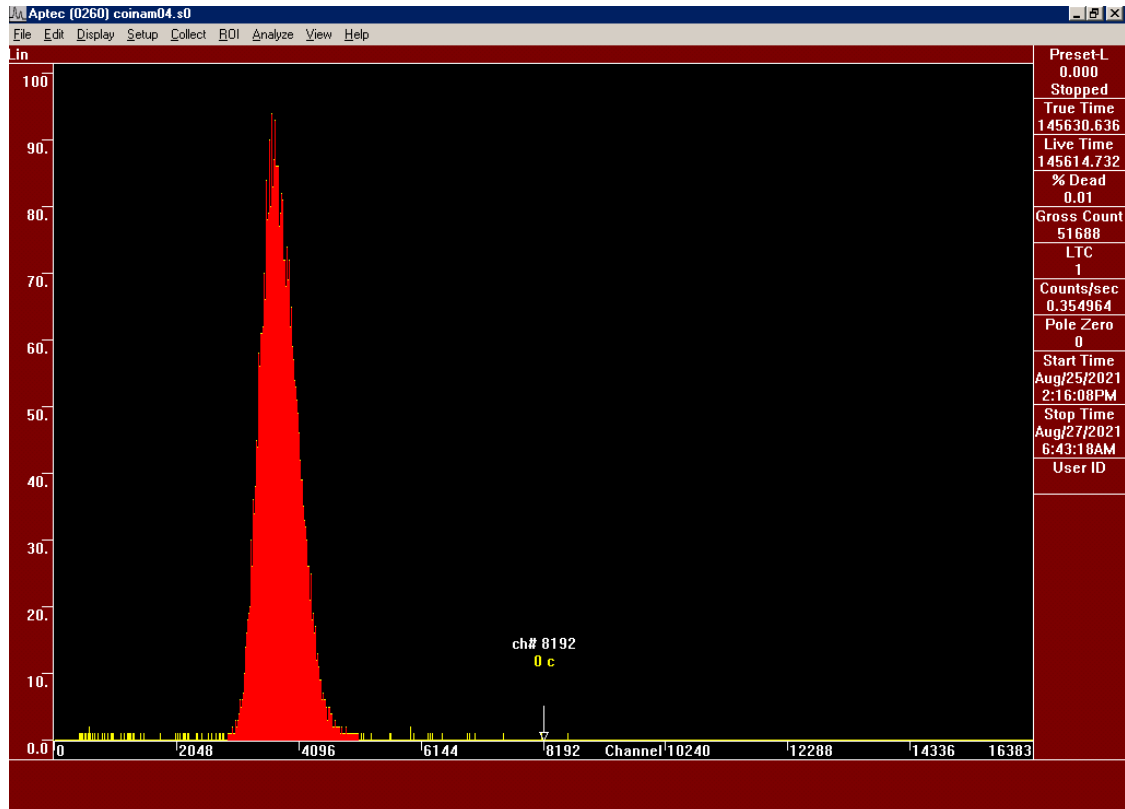


FIGURE 4.20: APTEC Data acquisition System with ADC set up in Coincidence Mode with Anode Potential Tubes Uninstalled over an Extended Counting Period

With these findings it was wise to calibrate the counter at its optimal condition to collect events with the electronics set to coincidence mode and the anode potential tubes removed. The section that follows presents the procedure used to calibrate the counter, Figure 4.21 illustrates the main components of the experimental set used to measure the energy depositions across the WTEPC.

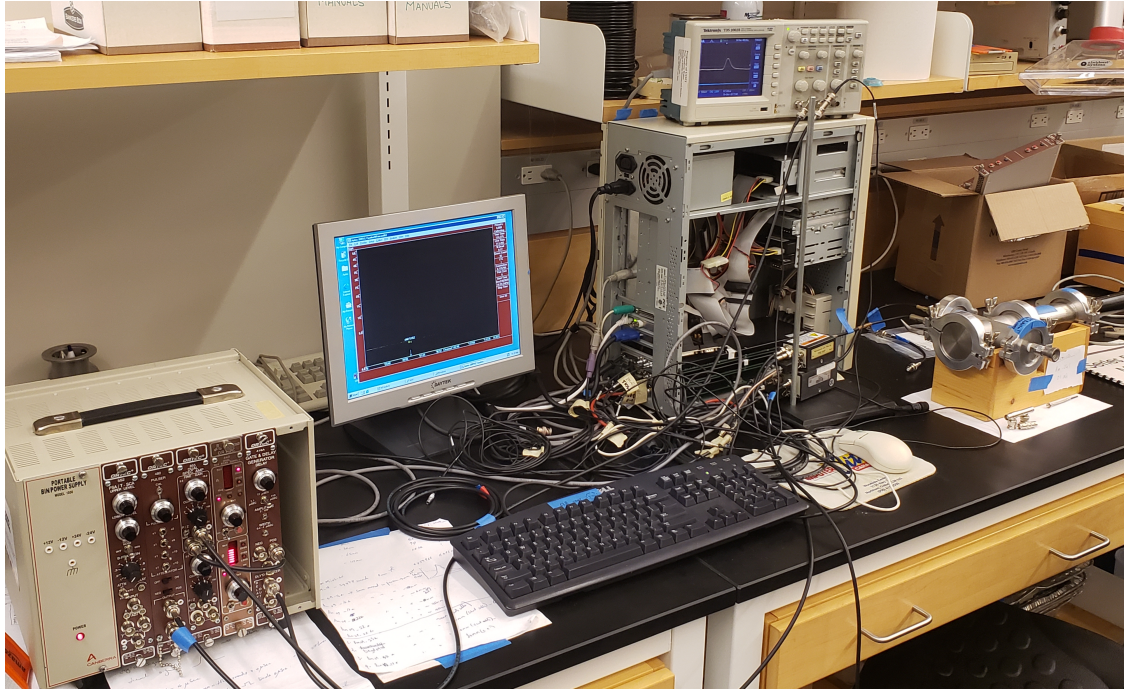


FIGURE 4.21: Experimental set up of the electronics to measure alphas crossing the WTEPC to the SBD in coincidence mode. A rear panel J5 pinout, DB-25 external connector along Pin# 11 carried the coincidence signal. A Gate and Delay generator which shapes the analog pulse, a pulser, an amplifier, a pre-amplifier, a SBD, a WTEPC installed inside chamber and a multi-channel analyzers made up the electronic architecture. The oscilloscope was used to display the signals for the SBD and WTEPC on both MCARD carriers.

### 4.2.3 Far West Technology Single Wire Counter Alpha Experiment

Before calibrating the counter, an experiment was conducted to determine if the main experimental set up was suitable to produce measurements of imparted energy to a microscopic cavity of similar volume and test material as the main microdosimetric investigation for HP dosimetry. It was important to determine if the current architectural set up was adequate to recover microdosimetric event



sizes with a commercial counter. A commercially designed and constructed counter, a Far West Technology (F.W.T.) TEPC illustrated in Figure 4.22 replaced the main experimental WTEPC apparatus presented earlier in Figure 4.21. The F.W.T. counter was connected to a separate high voltage source and charge sensitive pre-amplifier as indicated in Figure 4.16. As a quality control check of the experimental electronic architecture the 2 inch single wire F.W.T. counter was set up under the same operating conditions as the experimental Wall-less type TEPC. The F.W.T. counter has a built in 5.8 MeV  $^{244}\text{Cm}$  source emitting alpha particles across the sensitive volume of the counter through a small aperture simulating a  $2\ \mu\text{m}$  cavity at a TE gas pressure of 14.7 torr. Figure 4.23 illustrates the measured alpha spectrum. The alpha pulses recovered were well defined with over 18000 counts detected, at a rate of 13 counts per second for a counting time of approximately 25 minutes. Each pulse represents a single energy deposition event. After defining the region of interest around the extremities of the peak the channel number (ch#4759) corresponding to the center of the peak (18 counts) indicated the average energy lost by the alpha particle crossing the counter. This result indicated that the current architecture was adequate to measure pulse and calibrate a counter using range-energy data for the determination of microdosimetric event-size distributions in the main Wall-less type TPEC experiment.



FIGURE 4.22: Far West Technology (F.W.T.) Commercial TEPC Single Wire Counter

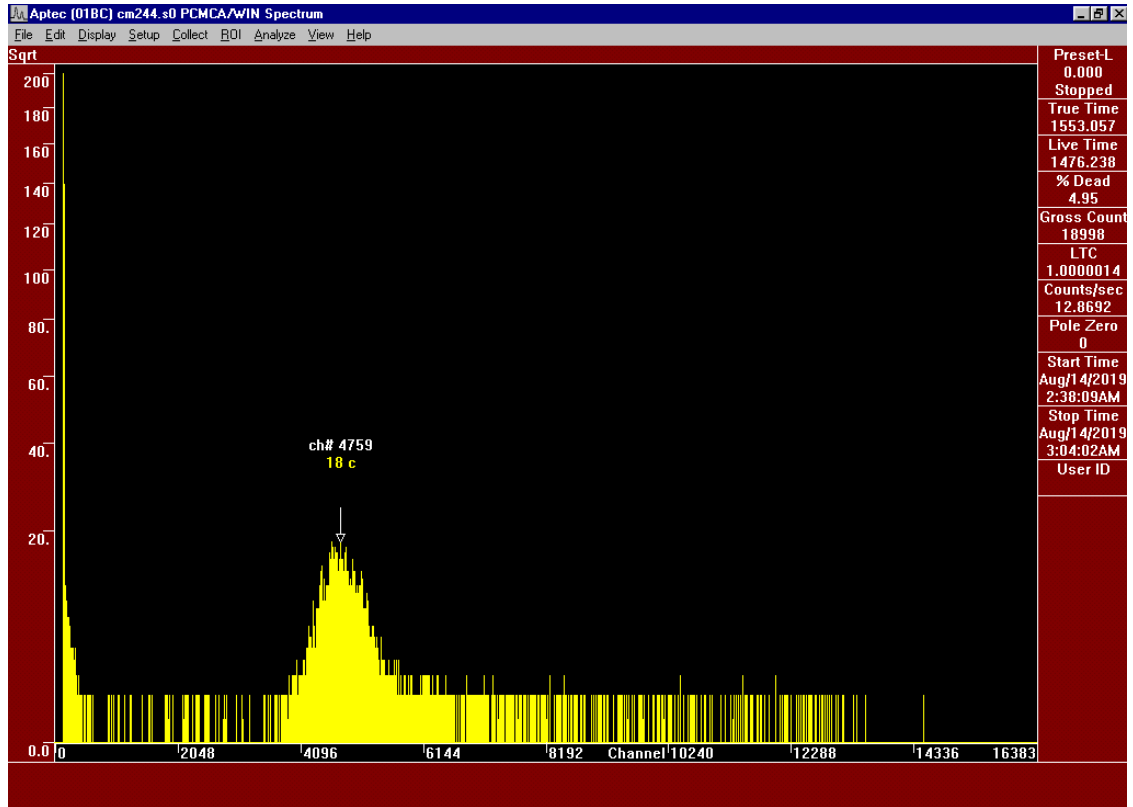


FIGURE 4.23: A measured Far West Technology (F.W.T.)  $^{244}\text{Cm}$  alpha source with a  $2\ \mu\text{m}$  single wire counter.

#### 4.2.4 Alpha Source Experiment and Calibration of the Wall-less TEPC

At this point in the investigation the testable question was whether the apparatus and electronic set up was capable of measuring event sizes using a laboratory available  $^{241}\text{Am}$  source. The pulse-height spectra generated by the wall-less type TEPC exposed to a  $0.1045\ \mu\text{Ci}$ ,  $^{241}\text{Am}$  in lab source, is displayed in Figure 4.24. In the figure, the smaller peak at channel number 549 indicating 431 counts was suspected to be from 60 keV photons typically associated with  $^{241}\text{Am}$ , while under the painted area, the larger peak is believed to be from events generated by the 5.5 MeV alpha particles depositing energy into the 5 mm spherical cavity, as

the beam crosses the counter. To arrive at these result, the high voltage across the counter was set at 750 V with the gain set at 30 and the APTEC-ADC settings in coincidence mode.

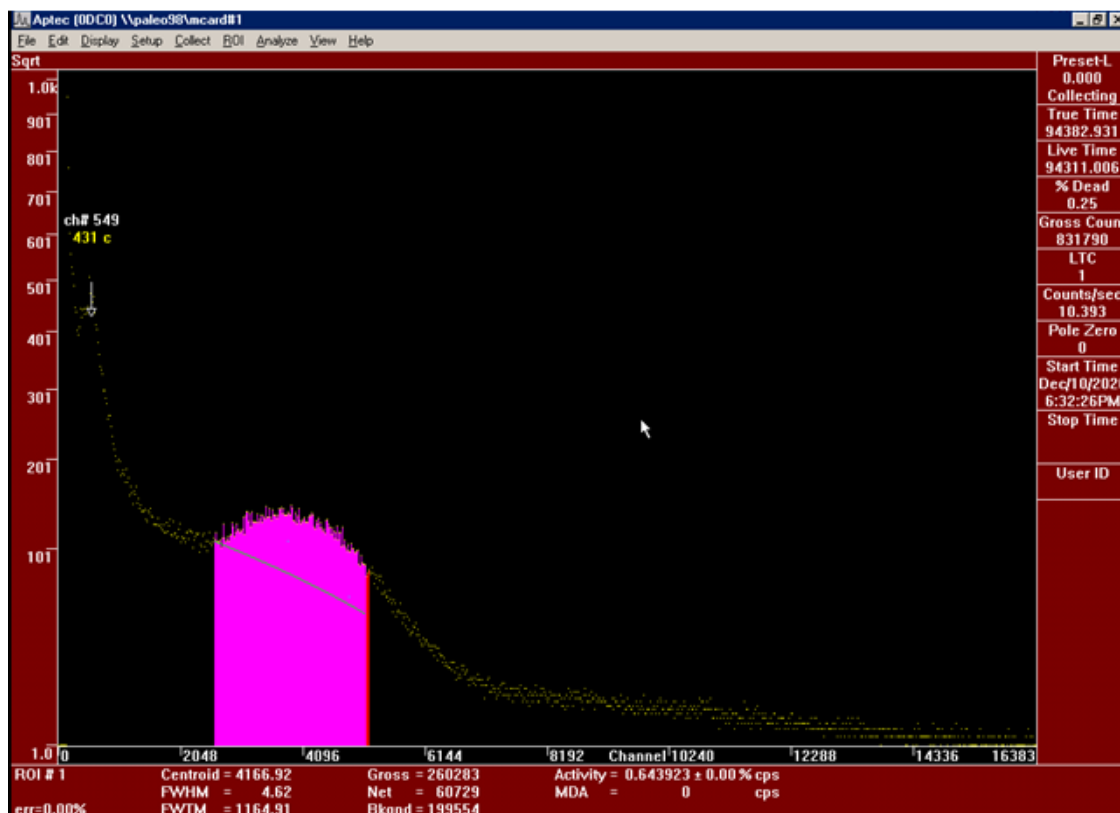


FIGURE 4.24: Pulse Height Spectra for a  $0.1 \mu\text{Ci } ^{241}\text{Am}$  Source, with 750 V across the Positive Electrode at an Amplifier Gain set at 30.

Repeat performance of these measurements at the same settings and observing the position of the main peak was a good diagnostic technique in tracking the performance of the wall-less counter. The unfavorable changes in performance allowed the investigator to detect faults within the electronics, and apparatus issues resulting from movement and agitation during set up, placing the chamber under vacuum, filling the chamber with TE gas and finally sliding the plunger in and out to achieve the appropriate source to counter distances. The typical

issues affecting the performance of the counter were chaffed or ruptured soldering on the ground wire connections, the field effect transistor (FET) going bad in the pre-amplifier and leakage of the gas from the vacuum chamber. However, with favorable results from both the F.W.T. experiment and the alpha source experiments the next appropriate step was calibrating the W-TEPC to achieve the main objectives of determining microdosimetric event sizes and any potential changes in radiation quality at simulated micro-metric distances away from the fixed counter position.

Historically, for microdosimetric investigations TEPC are calibrated using an internally mounted alpha source or by very soft x-rays [53] [54], of some known energy. For this investigation the apparatus was mounted with a  $5.5\text{MeV}$ ,  $0.1\mu\text{Ci}$   $^{241}\text{Am}$  source pictured in Appendix B.2.1. The source was placed inside a 3D printed collimator that was specifically designed to mount the source onto the sliding plunger directly in line with the center of the 5mm spherical cavity in the counter. A 3D sketch of the source collimator and source holder are illustrated in Appendix B.2.4 and B.2.5 respectively.

As previously discussed, a TEPC measures the charge produced in the counter which is proportional to the number of ion pairs created by the depositing energy. The mean energy required to produce one ion pair is called the  $\bar{W}$ -value. It was outside the scope of this work to identify the type and energy of each ionizing particle forming an event in the counter, hence the principle applied was to convert the number of measured ions formed by the imparted energy into a constant  $\bar{W}$ -value. To account for the difference between the  $\bar{W}$ -value from alpha particles used for calibration and those from electrons generated in this investigation, a calibration factor was determined. Figure 4.25 illustrates a range-energy relationship for alpha particles over a cavity range of  $15\ \mu\text{m}$  to  $50\ \mu\text{m}$  in unit density propane based TE-Gas. With the alpha energy from an  $^{241}\text{Am}$  source starting at around  $5.5\ \text{MeV}$  the energy lost over a  $1.2\ \mu\text{m}$  simulated tissue distance from the source to the counter (approximately 3 mm in actual distance) was calculated to be  $105.2\ \text{keV}$ . This leaves a remaining energy of approximately  $5.395\ \text{MeV}$  entering the  $2\ \mu\text{m}$  tissue simulated sensitive volume (5 mm in diameter). For a simulated site diameter of  $2\ \mu\text{m}$  a lineal energy calibration factor of

134.17  $keV\mu m$  was calculated. The calibration factor was derived from the equation:

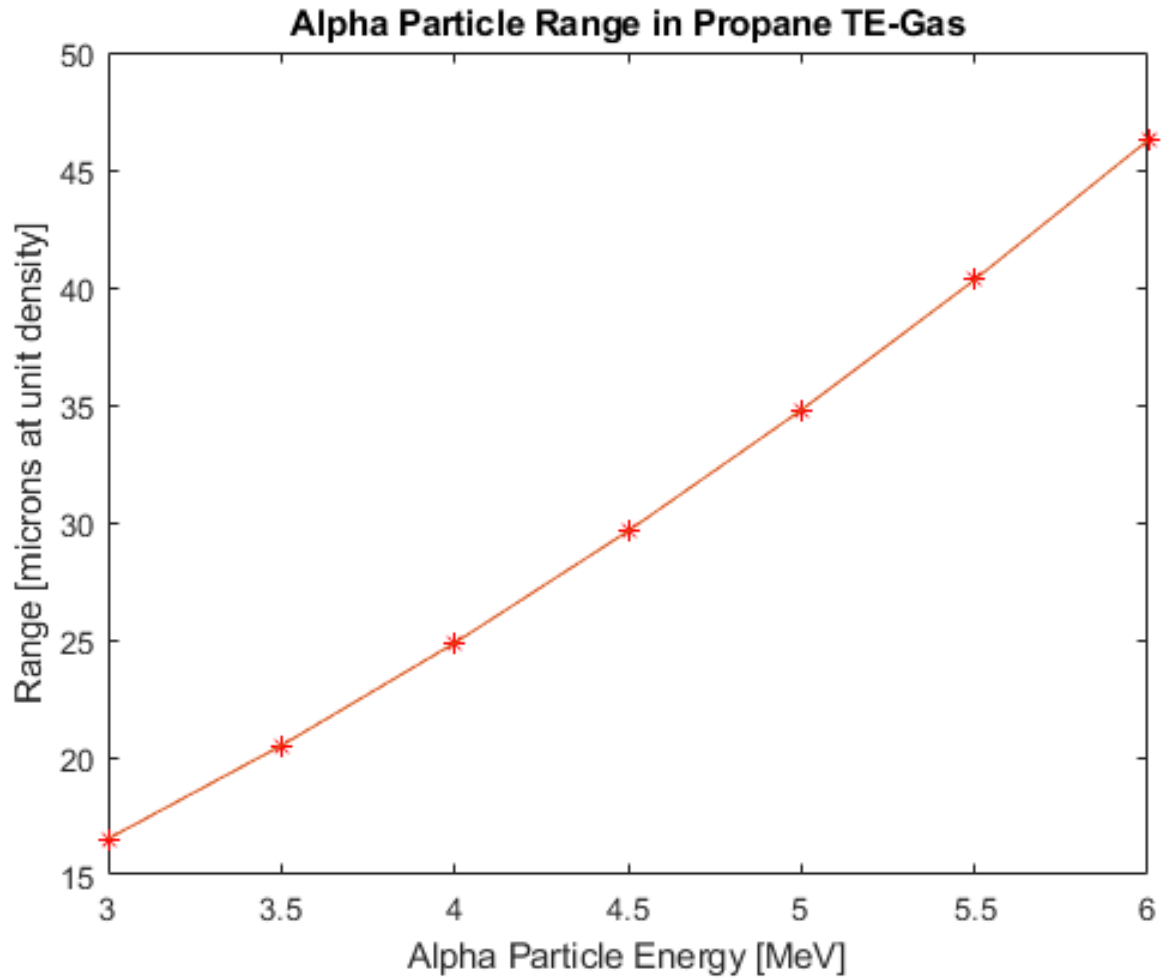


FIGURE 4.25: Alpha Particle Energy and its Range in Propane based Tissue Equivalent Gas

$$CF_y = \frac{\Delta E}{\bar{l}} \quad (4.3)$$

Where,  $\bar{l}$  is the mean chord length of the spherical counter, measured as two

thirds its simulated diameter and  $\Delta E$  is the mean energy lost by the alpha particles crossing a  $2 \mu m$  simulated path-length. This technique of using an internal alpha source of known energy was employed and discussed by other investigators [53][23]. For a chosen high voltage setting of 700V and an amplifier gain of 2 the alpha peak position on the APTEC MCA pulse height acquisition display was at channel number 3763. Therefore, the calibration factor (CF) given the amplifier gain and high voltage was determined by the equation:

$$CF_{gain=2} = \frac{CF_y}{Ch_{gain=2}}(keV/\mu m/chn) \quad (4.4)$$

The lowest event size (LES) was determined by the noise level of the whole electronic architecture at the amplifier gain being used. For example, at a gain of say 50, the calibration factor at that channel number ( $Ch_{\#}$ ) would be calculated as:

$$CF_{50} = \frac{CF_y}{Ch_{50}} \frac{2}{50}(keV/\mu m/chn) \quad (4.5)$$

Therefore with an inspection of the noise level at a gain of 50, if the noise was at a lower limit of detection (LLD) at channel number 200 then the LES would be calculated by the equation:

$$LES \approx CF_{50} * LLD(keV/\mu m) \quad (4.6)$$

Similarly, to determine the highest event sizes (HES), the upper limit of detection (ULD) around channel number 16383 is multiplied by the CF. Both measurements provide the range of event sizes one can expect for the counter at the desired amplifier gain. Both the  $^{63}Ni$  and  $^{14}C$  sources were measured at a gain of 50 with the CF calculated to be  $0.001426 \text{ keV}/\mu m/Chn$ .

### 4.2.5 Beta Source Experiments

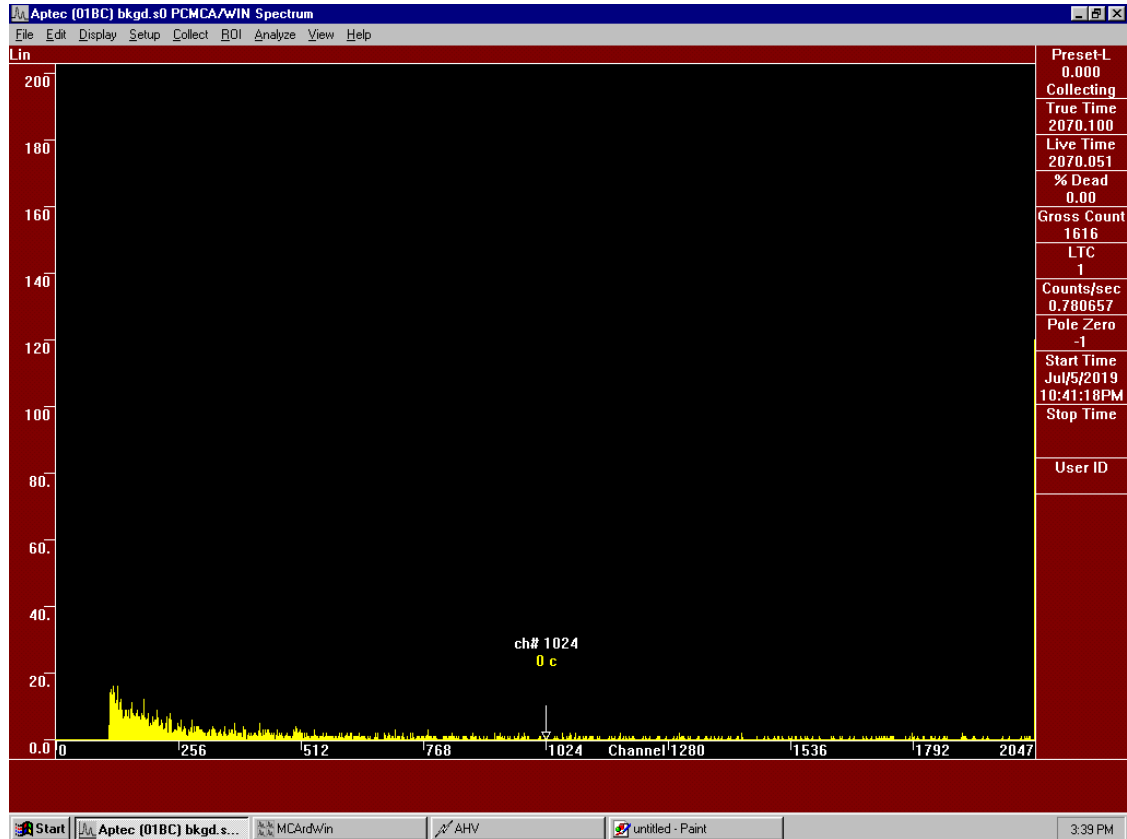


FIGURE 4.26: Background Spectrum of the Wall-less type TEPC

Before any data collection, a background measurement was taken for reference and used to subtract any unwanted residual pulses. Figure 4.26 illustrates the background measurement collected over a period of 2070 s. Within that time a gross count of 1616 counts was recorded at a rate of 0.8 counts per second (0.0% dead time). The gain on the "APTEC PC/MCA/win" acquisition software was set at 2 to reduce the noise pulses at the lower range, with the applied voltage set to 500 V. With the plunger position adjusted to 0 mm under same experimental conditions, a 17.4 keV ( $E_{avg}$ )  $^{63}\text{Ni}$  pure beta emitter was placed inside the counter. The pressure in the chamber was adjusted to 165 torr to simulate



a 2  $\mu\text{m}$  site size in the propane based TE gas. Figure 4.27 displays the acquired spectrum after approximately 21 hours.

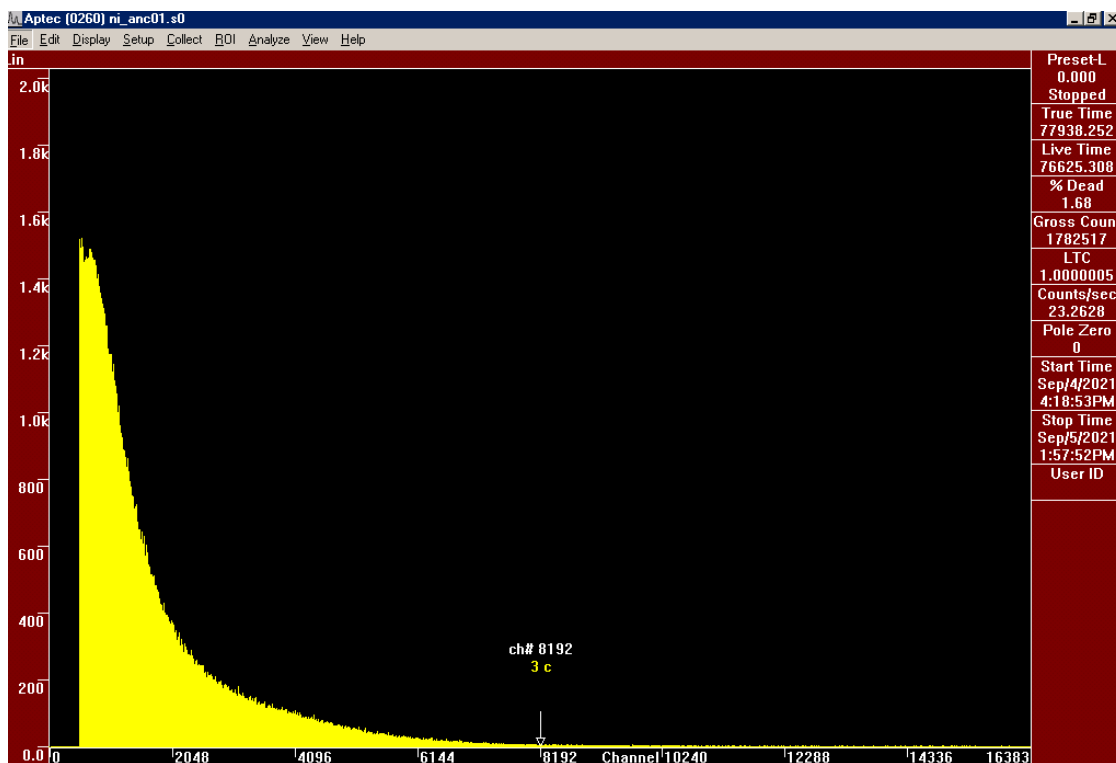


FIGURE 4.27: Spectrum Collected from 17.4 keV ( $E_{avg}$ )  $^{63}\text{Ni}$  Pure Beta Emitter at 0 mm Source to counter Distance, with the Counter Simulating a 2  $\mu\text{m}$  Site Size

It should be noted here that the properties of beta particles are unique, and a prominent beta peak is not expected as beta particles exist as a range of energies. The energy from an emitted electron or positron from a particular beta decay can have a range of values shared in accordance with the laws of energy conservation and momentum. The light mass of a beta particle allows rapid loss of energy through gas interactions resulting in their characteristic haphazard path and trajectories.

### 4.3 Experimental Determination of Lineal Energy and Dose Mean Lineal Energy

The definitions of the microdosimetric quantities used in this work are presented in Section 2.4.1. Each event or ionization across the chord length of the  $2 \mu m$  simulated cavity creates a pulse at the amplifier which is proportional to the energy deposited. The MCA outputs a delimited text file (\*.csv) tabulating each count registered per channel number over a range of 16383 channels. The experimental value for lineal energy,  $y$  ( $keV/\mu m$ ), was determined from the product of the derived CF ( $keV/\mu m/chn$ ) given above, and their respective channel number up to 16383 channels, indicating event sizes in the range of  $0.60keV/\mu m \leq y \leq 23.36keV/\mu m$ .

The dose mean lineal energy,  $\bar{y}_D$ , is the average event size according to the energy deposited, the equation presented in Equation 2.19 can be rearranged so that:

$$\bar{y}_D = \int_0^{\infty} y d(y) dy \quad (4.7)$$

Where  $d(y)$ , is the dose weighted probability density function of lineal energies, that indicate that higher lineal energies will result in higher doses.

$$d(y) = \frac{y f(y)}{\bar{y}_F} \quad (4.8)$$

The  $\bar{y}_F$  is the average event-size according to frequency, and determines how often the same event occurs

$$\bar{y}_F = \int_0^{\infty} y f(y) dy \quad (4.9)$$

The calculated  $\bar{y}_F$  values are not presented in this work, however, these values are important in determining the  $\bar{y}_D$  values. So for each channel, the experimental determination is given by:

$$\bar{y}_F = \frac{\sum_{k=0}^{16383} (Ch_{\#} * CF)(Counts)}{\sum_{k=0}^{16383} Counts} \quad (4.10)$$

Considering Equations 4.7 and 4.8, the dose mean lineal energy,  $\bar{y}_D$  is determined experimentally as follows:

$$\bar{y}_D = \frac{\sum_{k=0}^{16383} (Ch_{\#} * CF)^2 (Counts)}{\sum_{k=0}^{16383} (Ch_{\#} * CF) Counts} \quad (4.11)$$

### 4.3.1 Plotting the Microdosimetric Event-Size Spectra from Experiments

The raw output data from the experiment represented linearly, does not add any value to the microdosimetric interpretation of lineal energy as a function of event sizes. Therefore, for each measurement, 300 equal logarithmic bins were created with the MATLAB code illustrated in Appendix B.4 and B.5 for the alpha and beta sources respectively.

The code requests the lowest channel number ( $Ch_{\#} = 424$ ) or the lowest limit of detection (LLD) set by the APTEC MCA settings during measurements along with the calibration factor. Appendix B.3 illustrates a sample of the code which produces the fractional absorbed dose per logarithmic bin of lineal energy, that is, the  $y.d(y)$  as a function of  $y$  logarithmic bins, where 50 bins represents a decade of  $y$  in  $keV/\mu m$ . Al-Bayati (2013), describes in detail the mathematical principle behind creating these equal bins of lineal energy [55]. The desired relationship between the logarithmic value and the linear value is given by equation:

$$\frac{dLn(y)}{dy} = \frac{1}{y} \quad (4.12)$$

We can rearrange Equation 4.12 as  $dy = y_i \Delta lny$  which is represented geometrically in Figure 4.28.

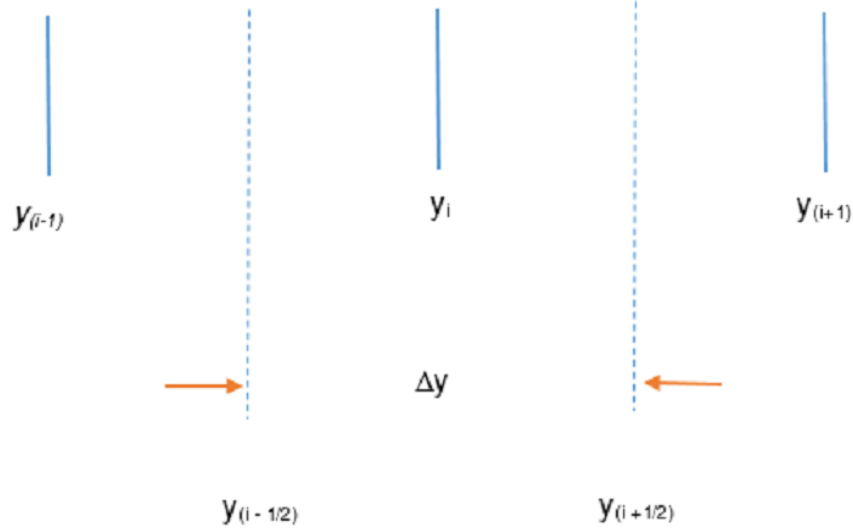


FIGURE 4.28: Intervals of linear energy,  $y$ , defined by two bins of equal logarithmic interval for 50 intervals per decade of linear energy

For 50 equal bins we can write:

$$dy = [(y_{i-\frac{1}{2}}) - (y_{i+\frac{1}{2}})] = [10^{\frac{(x+\frac{1}{2})}{50}} - 10^{\frac{(x-\frac{1}{2})}{50}}] = 10^{\frac{x}{50}} [10^{\frac{1}{100}} - 10^{-\frac{1}{100}}] \quad (4.13)$$

If we enter Equation 4.13 into Equation 4.12 we get:

$$dLn(y) = \frac{10^{\frac{x}{50}} [10^{\frac{1}{100}} - 10^{-\frac{1}{100}}]}{10^{\frac{x}{50}}} = 0.4605 \quad (4.14)$$

The term  $dLn(y) = 0.4605$  indicate the numerical value of the logarithmic intervals, which essentially are the number of logarithmic intervals used per decade of lineal energy.

If 50 intervals are required then,

$$dlogy = \frac{1}{50} \text{ and, } dlny = \frac{ln10}{50} = 0.04605 \quad (4.15)$$

In general, if  $X$  logarithmic bins are required per decade of lineal energy then,

$$d \ln y = \frac{\ln 10}{X} \quad (4.16)$$

### 4.3.2 Normalization

For an ideal visualization of the contribution of lineal energy,  $y$  over a wide range of values, the microdosimetric distributions are represented using logarithmic histogram plots of the probability density functions multiplied by the lineal energy ( $y$ ) values, and are shown as a function of the log values of  $y$ . The area under the curve  $yd(y)$  between two values of  $y$  is proportional to the fraction of dose by events with lineal energy in that range[56]. Correspondingly, the area under the curve  $yf(y)$  between two values of  $y$  is proportional to the fraction of events over the range. The  $f(y)$  term refers to the number of events occurring between event sizes  $y + d(y)$ , where  $d(y) = (y + dy) - y$ . The distributions  $f(y)$  and  $d(y)$  are independent of the dose absorbed, but are dependent on the size and shape of the volume in which the energy is deposited [23]. The frequency distribution explained by several authors [55] [56] is a probability density of  $y$ , and if the total area is made equal to 1 then equal areas under the curve represent equal dose fractions of the total dose[23]. This allows for the direct comparison of several spectra on a normalized chart, Figure ?? presented earlier, is an example of a normalized spectrum for single-event lineal energy dose distribution of different photon energies. This can be mathematically represented as:

$$Area = \int_{min}^{max} yd(y)d \ln y = 1 \quad (4.17)$$

For this experiment, the output values from the MATLAB code "logplot" generates the  $yd(y)$  values over the required 300 bins. To normalize the individual values of  $yd(y)$ , they are corrected after dividing by the sum of all  $yd(y)$  values and the magnitude of the logarithmic interval (0.04605). This can be represented mathematically as:

$$\sum_{i=1}^{300} yd(y) = 21.7155266; 1 \leq i \leq 300 \quad (4.18)$$

### 4.3.3 Experimental Determination of Dose and Dose Rate

The calibration factor, CF, was also used to determine the microdosimetric calculations for total dose and dose rate by the equation:

$$Dose, D(Gy) = \frac{Ch_{\#} * CF * Counts(keV/\mu m/chn) * 1.602 \times 10^{-16}(J/keV) * \bar{l}(\mu m)}{m_{gas}(kg)} \quad (4.19)$$

The Dose is calculated in J/kg which has the special unit the Gray(Gy), 1 Kilo-electron Volt is converted to 1 Joule (J) of energy by the factor  $1.602 \times 10^{-16}(J/keV)$ . The total dose from each deposition of energy recorded by the counter is a product of the number of pulse heights per 16383 channels ( $Chn\#$ ) by the total events given as counts, by the CF and the mean chord length  $\bar{l}$ , all taken as a ratio of the mass of the TE gas, measured in kg. The  $\bar{l}$  was calculated as 2/3 the diameter ( $2 \mu m$ ) of the simulated cavity,  $1.33 \mu m$ . The mass of the propane based TE was a product of the density of the gas and its volume ( $\pi r^2 h$ ). The density,  $\rho$ , of the gas was calculated to be  $0.396495 kg/m^3$  at a pressure of 165 torr and its volume  $9.81748E - 08 m^3$ .

The dose rate quantity (Gy/s) is a ratio of the Dose, D (Gy), and the time(s) for collecting a spectra and can be expressed by the equation:

$$DoseRate, \dot{D}(Gy/s) = \frac{\int y \cdot f(y) dy \cdot \bar{l}(\mu m)}{m_{gas}(kg) \cdot t(s)} (1.602 \times 10^{-16}(J/keV)) \quad (4.20)$$

### 4.3.4 Determination of the Uncertainties in Experimental Microdosimetry

The experimental uncertainties typically associated with microdosimetric quantities have been covered by several authors [57], [53], [55] and more recently [58]. The major sources of error are considered to be associated with the counting

statistics and the Alpha-source calibration procedure. To reduce the level of uncertainty in this work the detector was allowed to acquire data for roughly 24 hours which was determined as a sufficient counting time to improve the statistical accuracy of the results. Poisson error determined by  $\sqrt{N}$ , where  $N$  is the number of counts in a channel, was calculated to be  $< 0.1\%$ . According to Waker 1985, in the article "Experimental uncertainties in Microdosimetric measurements" indicate that  $\sqrt{N}$  and  $N$  depend on the total dose absorbed by the counter. Discrepancies in the experimental determination of the microdosimetric quantities for this work are attributed to geometry issues and alignment of the beams in the vacuum chamber.

To determine the random errors associated with the  $\bar{y}_D$  and dose rate ( $\dot{D}$ ) the fractional uncertainties associated with the propagation error in statistics was applied for different measured values according to [20]. As indicated by Knoll (2010), standard deviation analysis is required beyond the error in the number of counts, as the calculated quantities involve summations of the frequency of counts. Taking Equations 4.7 and 4.9 into account, the standard deviations in  $\bar{y}_D$  values was determined by the error propagation formula described by Broughton(2016) [58]:

$$\frac{\sigma_{\bar{y}_D}}{\bar{y}_D} = \sqrt{\frac{\sum_{i=1}^N y_i^4 f(y_i)}{[\sum_{i=1}^N y_i^2 f(y_i)]^2} + \frac{\sum_{i=1}^N y_i^2 f(y_i)}{[\sum_{i=1}^N y_i f(y_i)]^2}} \quad (4.21)$$

In terms of experimental quantities used in this work the  $\sigma_{\bar{y}_D}$  can be converted according to Equation 4.19 as:

$$\frac{\sigma_{\bar{y}_D}}{\bar{y}_D} = \sqrt{\frac{\sum_{i=1}^N (Ch_{\#} * CF)^4 * Counts}{[\sum_{i=1}^N (Ch_{\#} * CF)^2 * Counts]^2} + \frac{\sum_{i=1}^N (Ch_{\#} * CF)^2 * Counts}{[\sum_{i=1}^N (Ch_{\#} * CF) * Counts]^2}} \quad (4.22)$$

The standard deviation in the dose rate  $\dot{D}$ , was determined similarly by applying the same concept to equation 4.20, and is determined for  $\sigma_{\dot{D}}$  as follows:

$$\sigma_{\dot{D}} = \frac{1.602 \times 10^{-16} (J/keV) \cdot \bar{l}}{m_{gas}(kg) \cdot t(s)} \sqrt{\sum_{i=1}^N y_i^2 f(y_i)} \quad (4.23)$$

With the experimental quantities inserted into Equation 4.23, the  $\sigma_{\dot{D}}$  is converted to:

$$\sigma_{\dot{D}} = \frac{1.602 \times 10^{-16} (J/keV) \cdot \bar{l}}{m_{gas}(kg) \cdot t(s)} \sqrt{\sum_{i=1}^N (Ch_{\#} * CF)^2 * Counts} \quad (4.24)$$

Finally, the systematic errors in the determination of  $\bar{y}_D$  and dose for this Wall-less TEPC were estimated from the gas pressure, the path length, the  $W$ -value and the uncertainty on the energy depositions related to the calibration. The overall uncertainties are presented in Table 4.1, and were estimated by the square root of the individually determined squared percentage errors. For instance the internal diameter of the counter has an estimated error of roughly  $\pm 0.25mm$  per 5 mm diameter cavity. The resulting percentage error was estimated to be around 5%. The gas pressure and path length alone would have an overall error of approximately 3%.

TABLE 4.1: An Estimate of the Experimental Uncertainties for Measurements taken by the Wall-less TEPC for  $\bar{y}_D$  and Dose Rate ( $\dot{D}$ ) Determinations

	Error (%)
Gas pressure	2
Path length	2
Energy Calibration	5
Internal Diameter	5
W-value (Propane)	2
Overall uncertainty	8



## 4.4 Simulation and Modeling of Experiments with Monte Carlo Code PENELOPE

Another objective was the development of the Monte Carlo code PENELOPE to simulate the experimental conditions of this study. This has the importance of predicting through simulations other cases for HP exposures that potentially can not be measured experimentally. As a quality assurance, a benchmark experiment with an abundance of microdosimetric measurements was reproduced using PENELOPE to investigate its effectiveness for this current experiment.

### 4.4.1 Defining Geometry and Input Files

The first step in the process of running a PENELOPE simulation was defining a simple geometry of the WTEPC using constructive quadratic or quadric surfaces. Figure 4.29 illustrates a geometry( \*.geo) file being designed in PenGeomJar. A subroutine package creating a 10 cm TE gas (Material 1) outer-sphere with an inset 5 mm inner-sphere (Material 2) representing a  $2\mu\text{m}$  simulated site. In the editing tab 'Surface' a sphere is chosen by manipulating the indices for the X-scale, Y-Scale and Z-Scale. The X-Shift, Y-Shift and Z-Shift along the defined Z-plane for a radius of 5.25 cm around the angles Omega, Theta and Phi were defined based on the cavity dimensions of the experimental WTEPC. The editing tab 'Body' allows for selecting the materials and limiting surfaces in 'Body 1', 'Body 2' etc. The specific body number allows the simulation to provide energy deposition data relevant to that "Body".

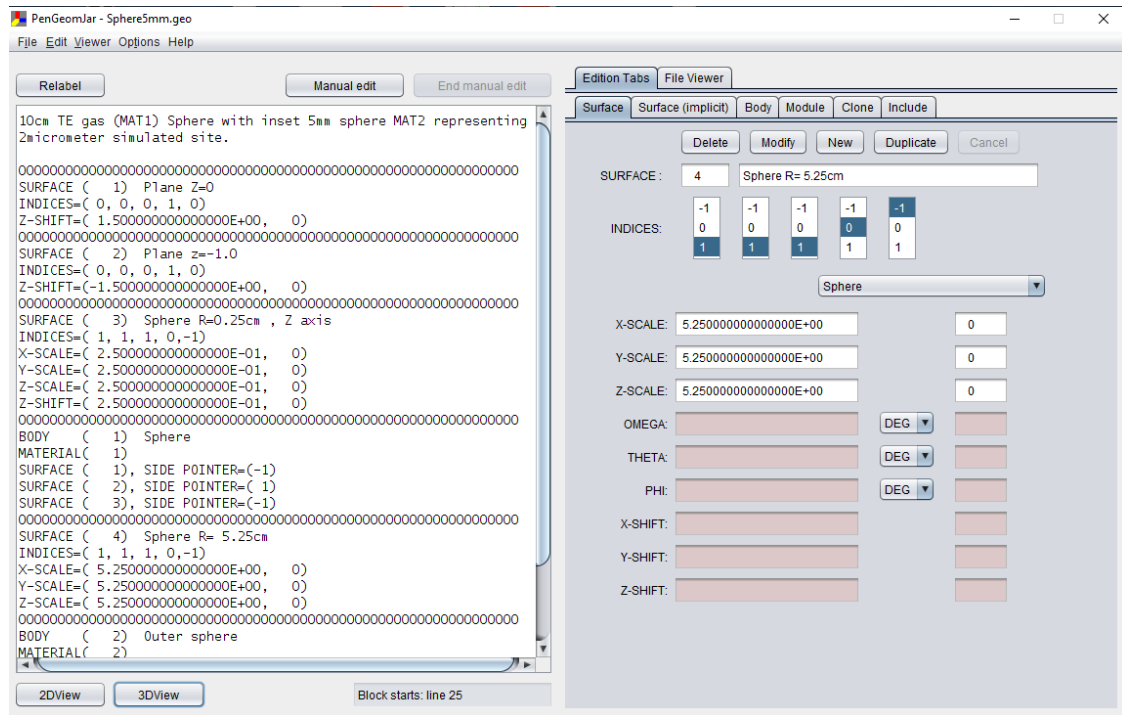


FIGURE 4.29: An Example of PenGeomJar Geometry Editing Tool.

Aside from editing, Pengeomjar has a built in JAVA supported graphical user interface, which was used to visualize the geometry definition files of the counter in 2D and 3D images presented in Figures 4.30 and 4.31 respectively.

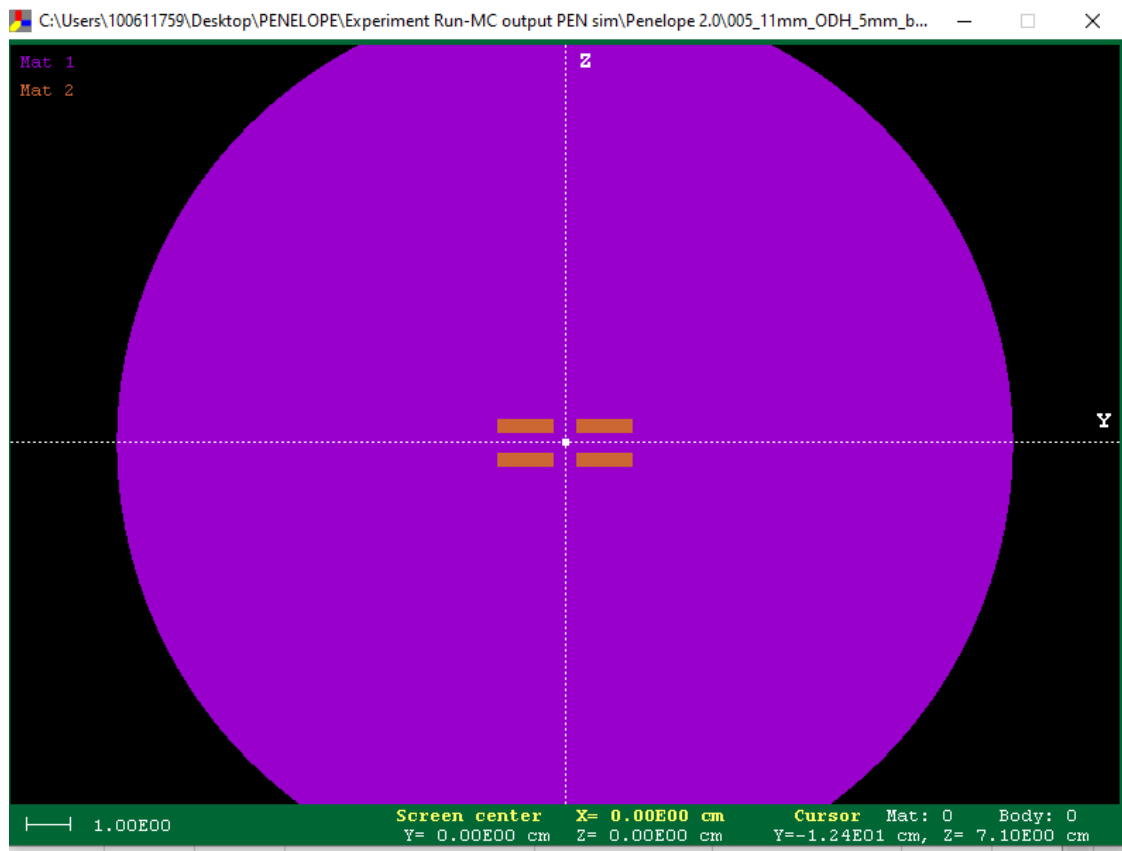


FIGURE 4.30: 2D View of the WTEPC geometry designed in PenGeomJar. The source is positioned just outside the 5 mm active site with the ability to move 10 cm away in the negative Z-direction

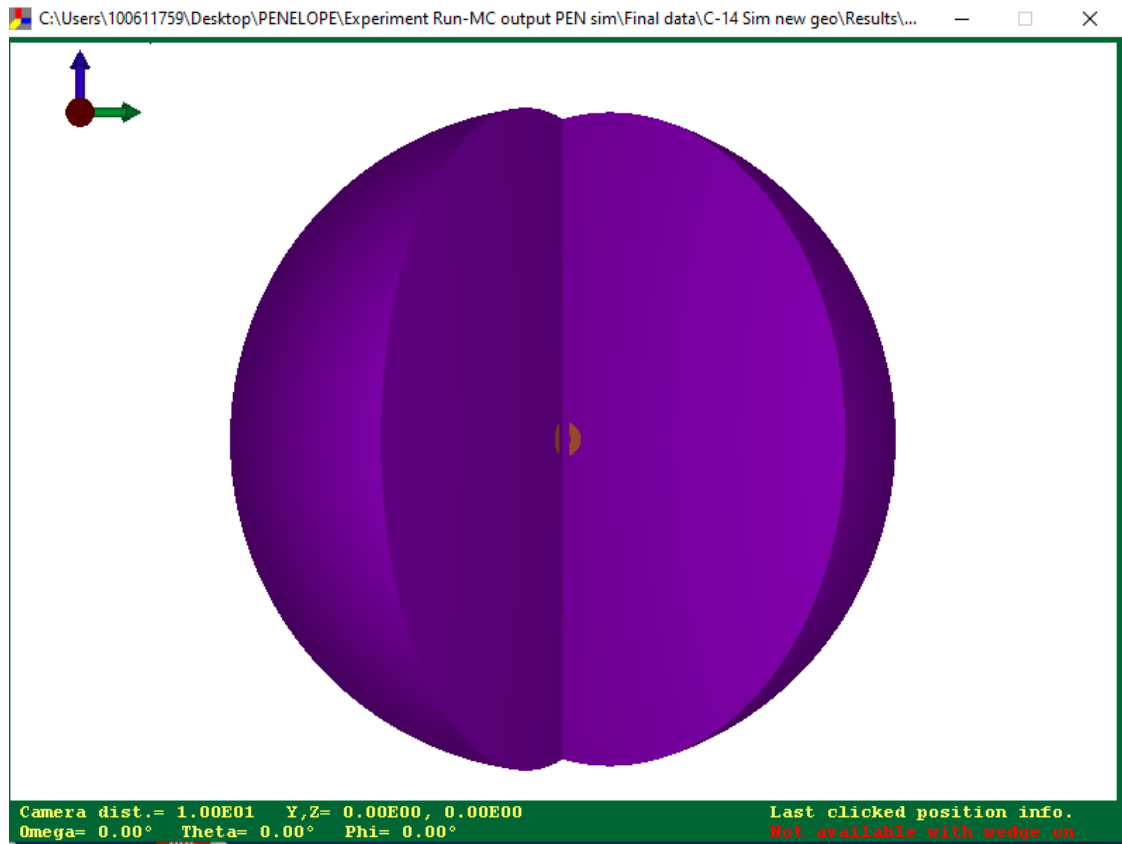


FIGURE 4.31: 3D View of the WTEPC geometry designed in Pen-GeomJar. The wedged out portion shows the sensitive 5 mm inner sphere of TE gas encapsulated by an outer 10 cm sphere of TE gas

Given a defined geometry for particle interactions, the next most important aspect for operating the code is the definition of the input file (*\*.in*). One experimental condition required simulating a  $2\ \mu\text{m}$  site sized counter exposed to a pure beta emitting  $^{63}\text{Ni}$  source decaying by beta minus emissions, with a mean energy of 17.42 keV and an end point energy of 66.95 keV. Instead of single energy entries for the mean and end point energies, PENELOPE allowed for the entire beta spectrum to be normalized and binned for sampling in Monte Carlo calculations, with the FORTRAN command "SPECTR". Using the Radiological Toolbox program, ICRP 107 data for  $^{63}\text{Ni}$  beta spectrum was normalized to

emission of a single beta particle over 100 uniform bins (see Appendix A.2 for an example of the Rad-toolbox Monte Carlo output bins appearing as a text file). Figure 4.32 illustrates some of the important sections of the input file required for a PENELOPE run.

```

1 TITLE Ni- 63 spectrum 100bins. A 5mm site size simulating 2um @165torr TE gas.
2     5.5cm away from the detector at subtended angle 2.5 degrees.
3     Note that interaction forcing distorts the detector output.
4
5     .
6     >>>>>>> Source definition.
7 SKPAR 1 [Primary particles: 1=electron, 2=photon, 3=positron]
8 SPECTR 0 2.80E-02
9 SPECTR 670 5.55E-02
10 SPECTR 1340 8.25E-02
11 SPECTR 2010 1.09E-01
12 SPECTR 2680 1.35E-01
13 SPECTR 3350 1.60E-01
14 SPECTR 4020 1.85E-01
15 SPECTR 4690 2.10E-01
16 SPECTR 5360 2.34E-01
17 SPECTR 6030 2.57E-01
18 SPECTR 6700 2.80E-01
19 SPECTR 7360 3.03E-01
20 SPECTR 8030 3.25E-01
21 SPECTR 8700 3.47E-01
22 SPECTR 9370 3.68E-01
23 SPECTR 10040 3.89E-01
24 SPECTR 10710 4.09E-01
25 SPECTR 11380 4.29E-01
26 SPECTR 12050 4.49E-01
27 SPECTR 12720 4.68E-01
28 SPECTR 13390 4.87E-01
29 SPECTR 14060 5.05E-01
30 SPECTR 14730 5.23E-01
31
32
33
34
35
36
37
38
39
40
41
42
43
44
45
46
47
48
49
50
51
52
53
54
55
56
57
58
59
60
61
62
63
64
65
66
67
68
69
70
71
72
73
74
75
76
77
78
79
80
81
82
83
84
85
86
87
88
89
90
91
92
93
94
95
96
97
98
99
100
101
102
103 SPECTR 64270 1.00E+00
104 SPECTR 64940 1.00E+00
105 SPECTR 65610 1.00E+00
106 SPECTR 66280 1.00E+00
107 SPECTR 66950 -1.00E+00
108 SPOSIT 0 0 -5.5 [Coordinates of the source]
109 SCONE 0 0 2.5 [Conical beam; angles in deg]
110
111 >>>>>>> Material data and simulation parameters.
112 MFNAME 265@2um.mat [Material file, up to 20 chars]
113 MSIMPA 1e3 1e3 1e3 0.02 0.02 2.5e2 2.5e2 [EABS(1:3), C1, C2, WCC, WCR]
114
115 >>>>>>> Geometry and local simulation parameters.
116 GEOMFN Sphere5mm.geo [Geometry file, up to 20 chars]
117 PARINP 1 0.005 thickness [Optional geometry parameters]
118 PARINP 2 0.01 radius [Optional geometry parameters]
119 DSMAX 1 1e-4 [KB, maximum step length in body KB]
120
121 >>>>>>> Interaction forcing.
122 IFORCE 1 1 4 2000 .1 2 [Interaction forcing]
123 IFORCE 1 1 5 200 .1 2 [Interaction forcing]
124
125 >>>>>>> Bremsstrahlung splitting.
126 IBRSPL 1 2 [KB, splitting factor]
127
128 >>>>>>> X-ray splitting.
129 IXRSPL 1 2 [KB, splitting factor, weight window]
130
131 >>>>>>> Emerging particles. Energy and angular distributions.
132
133
134
135
136
137
138
139
140
141
142
143
144
145
146
147
148
149
150
151
152
153
154
155
156
157
158
159
160
161
162
163
164
165
166
167
168
169
170
171
172
173
174
175
176
177
178
179
180
181
182
183
184
185
186
187
188
189
190
191
192
193
194
195
196
197
198
199
200

```

FIGURE 4.32: PENELOPE input file for a  $^{63}\text{Ni}$  beta particle spectrum hitting a 5 mm (simulating  $2\ \mu\text{m}$ ) inner-sphere TE gas in a 10 cm spherical TE gas shell.

The energy source 'SKPAR' is indicated as '1' for electrons, and the 'SPECTR' command is used to indicate the entire beta spectrum of  $^{63}\text{Ni}$  in 100 normalized bins. The 'SPOSIT' and 'SCONE' input the coordinates of the source position and angle of the conical beam from the source in the direction of Body 1, the area defined for modeling the energy depositions. In the example shown the source is positioned at "-5.5 cm" away from the  $2\ \mu\text{m}$  tissue site at angle subtended of "2.5" degrees, both along the negative z-axis. The Material file and simulation parameters are activated by the parameters 'MFNAME' and 'MSIMPA'. In the material file the ICRU report 49 numbered compounds are specified for the interacting materials in Body number 1 or 2. In this case "265" represents the numbered code for TE gas (propane based) and "266" for the material file for tissue equivalent plastic. The standard mass density of the gas was changed from 0.0018263 gram per cubic meter to 0.000396495 gram per cubic meter to represent the current pressure of the gas in the chamber at 165 torr. Critically important to enable condense history (CH) simulation in PENELOPE as opposed to track structure(TS) physics constructors are the selection of the step size limit and secondary production cut off parameters  $C_1 = C_2$ , and  $W_{cc} = W_{cr}$ . The values were chosen to be 0.2 and 250 eV respectively, within the range for PENELOPE optimization for microdosimetric applications as experienced by R D Stewart et. al (2001) and explained in section 3.2.1 of the literature review.

The geometry file was defined as indicated before in Figure 4.29, The 'TIME' allotted (in seconds) for each run, the number of simulated showers 'NSIMSH' and the name of the output dump files were all specified before each run. Figure 4.33 illustrates PENELOPE's subroutine package "shower.exe" that gives an indication of the trajectories of 50 electrons showers in a slab of 10 cm TE gas (propane based).

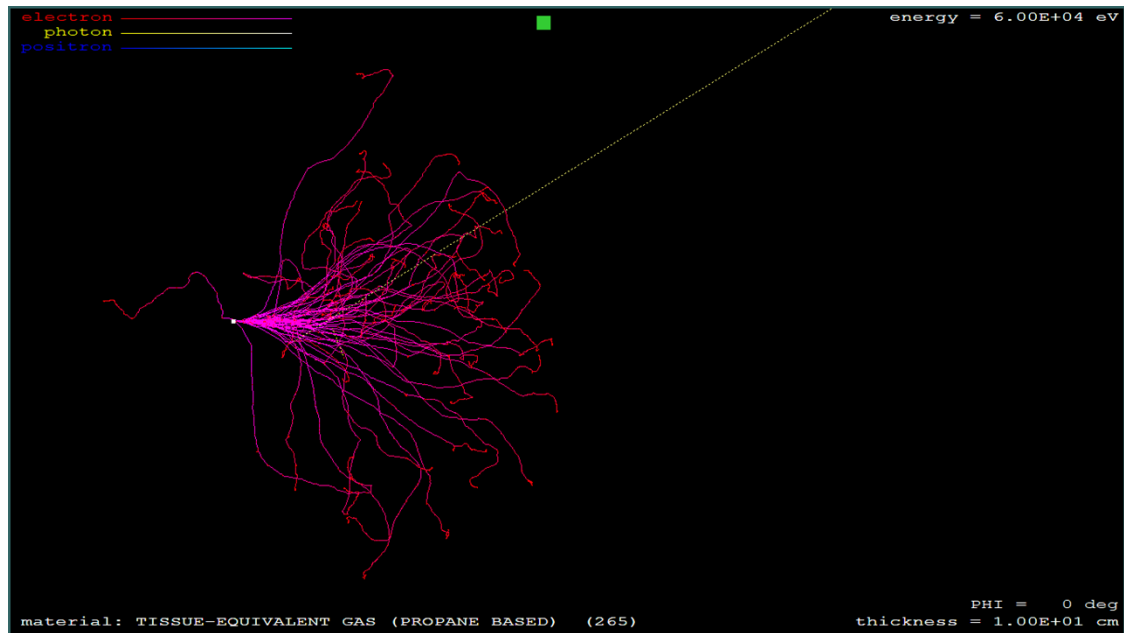


FIGURE 4.33: PENELOPE subroutine package "SHOWER.exe" displaying 50 electron showers in a 10 cm slab of TE gas (propane based)

#### 4.4.2 PENELOPE Output

PENELOPE produces three types of output files from a "Penmain.exe" run. Appendix A.3 gives examples of the Penmain output results after simulation. For the experimental conditions being investigated two Penmain output files are of importance, the energy-deposition detector # 1 simulation and the depth-dose distribution (data given in Appendix A.3). A graphical representation of the energy-deposition detector # 1 simulation is illustrated in Figure 4.34 by the Windows version of GNUplot program. The plot shows the energy distribution of the deposited energy on a simulated 'detector #1'. A steep gradient is observed at about 16.4 keV. These output files from PENELOPE however are not in a form to extract any microdosimetric data of significance to this study.



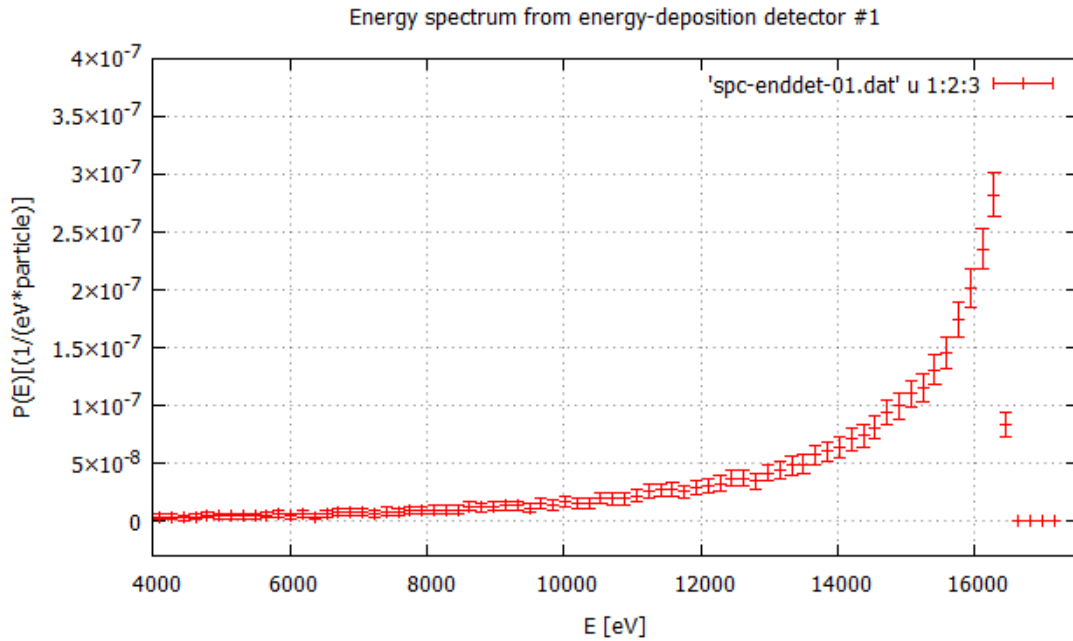


FIGURE 4.34: PENELOPE output results for a simulation of 17.42 keV electrons hitting the 5 mm sensitive volume around a 50  $\mu\text{m}$  gold plated tungsten wire.

Consequently, the challenge was to determine from these output files what are the single event doses deposited as a result of a single shower in the required volume defined as "Body 1", the counting area, having a 2  $\mu\text{m}$  simulated tissue volume. A single shower event was considered as the average energy deposition in the 2  $\mu\text{m}$  site or volume traversed, plus all its secondary electron tracks resulting from that single shower. In order to meet this requirement the code was modified to allow the lineal energy depositions in the defined 'Body' for each shower to be placed in electronic bins, with 50 bins representing a decade. This provided an average deposited energy per electron shower given in electron-volts(eV). With this modification microdosimetric data for the absorbed dose to tissue and the dose mean lineal energies were captured after each simulation.

### 4.4.3 Determination of Lineal Energy, $y$ , through Monte Carlo Simulations

The definitions of the microdosimetric quantities used in this work are presented in some detail in Section 2.4.1. The stochastic function lineal energy,  $y$ , after a PENELOPE simulation was determined by scoring all the frequency of energy depositions  $[f(y)]$  occurring in each individual bin over 250 bins. For each single event (tracks or incident particles and its secondaries) PENELOPE records the energy deposition on each energy level and distributes it into logarithmic bins of equal width using the formula given in equation 4.25.

$$\text{Energy, } \varepsilon = 10^{(f(y)/50)/1000} \quad (4.25)$$

Once the interactions of an incident particle along with its secondary tracks have been simulated all energy depositions corresponding to that bin are added to the frequency of events occurring in that energy bin. The lineal energy is then determined from the ratio of  $\varepsilon$  and the mean chord length,  $\bar{l}$ , given by the ratio  $y = \varepsilon/\bar{l}$ . For a  $2 \mu m$  simulated counter, a mean chord length of  $1.33 \mu m$  was used. The basic principle to scoring the lineal energy values from a single incident electron is illustrated in Figure 4.35, and discussed by Kyriakou et. al. (2017) in the work microdosimetry of electrons in liquid water using low-energy models of Geant4 [56].

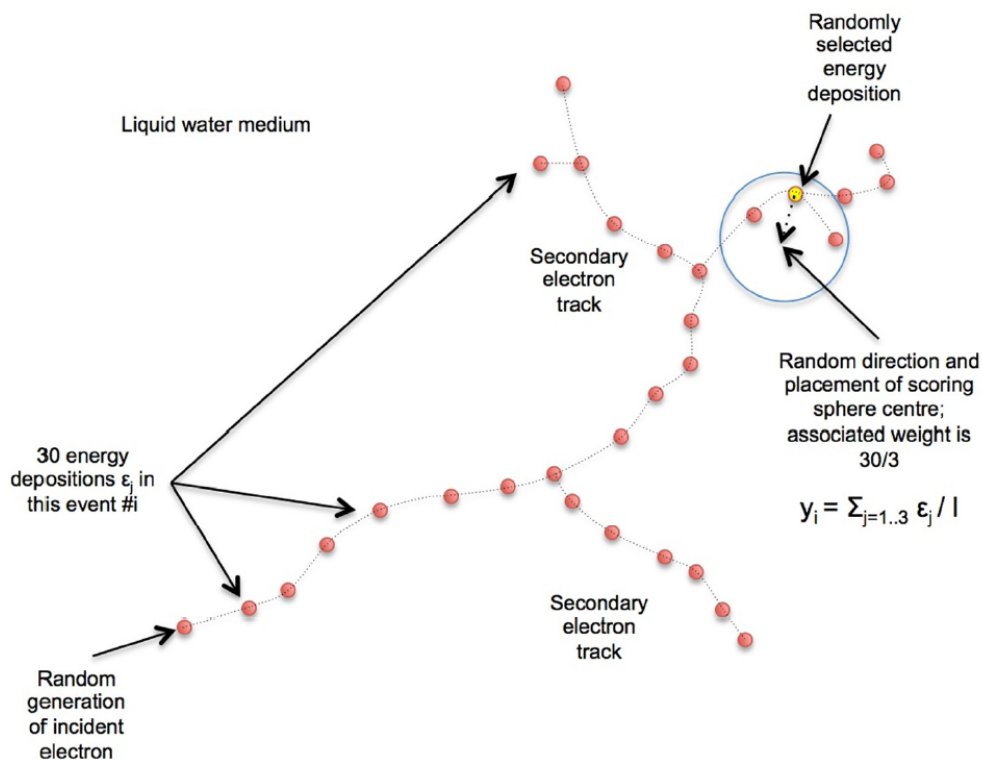


FIGURE 4.35: Principle of scoring of lineal energy values for a single incident electron. Depicted here are the three energy depositions in a randomly selected sphere and its associated statistical weight taken as 30/3 to determine the frequency of lineal energy occurring at that position or within that bin. The simulation illustrated here request 30 energy depositions events as opposed to the 2 billion electron showers requested for each run in PENELOPE to recover statistically accurate results.[56]

This method is repeated for many more single events and for any beta particle emitting radionuclides of interest. The output results recovered are from a constant selection by the user for any number of electron showers for a allotted time. In this work 2 billion electron showers over 86400 seconds were chosen for each run executed in PENELOPE, to determine if there are possible changes to the radiation quality and the dose over simulated tissue distances on a micro-metric scale. For each calculation the frequency-mean lineal energy,  $\bar{y}_F$  is determined,

which is the sum of the individual frequency of  $y$ ,  $f(y)$ , as a ratio of the sum of the  $yf(y)$  as described earlier in equation 4.9. The dose probability density function  $d(y)$  is obtained similarly to Equation 4.8.

#### 4.4.4 Determination of the Dose Mean Lineal Energy, $\bar{y}_D$ , Normalization and Dose Rate from Monte Carlo simulations

Given the extraction of the individual values for  $f(y)$  and  $\bar{y}_F$  the dose-mean lineal energy,  $\bar{y}_D$  was also determined. This from the ratio of the sum of  $yf(y)$  and the sum of  $y^2f(y)$ , a mathematical representation can be found in Equation 4.7. To ensure the area under the curve for the plot of  $yd(y)$  between two values of  $y$  is proportional to the fraction of dose by events with lineal energy, the results were normalized; similarly in in the manner discussed in Section 4.3.2.

The PENELOPE output file "penmain-res.dat" follows each simulation and is the most relevant result file for providing the average energy depositions in each simulated "Body" and provides a overall summary of the users experiment. The average energy deposition per electron shower for each simulation is given in electron volts with an uncertainty usually in the range of around 5% or less. The average deposited energy in Body 1, the sensitive cavity, also provides a simulation time in seconds. With these values a dose rate was determined for each source to counter movement.

### 4.5 A Low Energy Photon Irradiation Benchmark Simulation

A noteworthy experiment chosen for the availability of experimentally determined microdosimetric data was conducted by Kliauga and Dvorak and their findings presented in the peer reviewed journal, "Radiation Research Society". The article published in 1978, was entitled "Microdosimetric Measurements of

Ionization by Mono-energetic Photons". The objective of the study was to determine the microdosimetric event distributions of eight primary photon energies ranging from 11.9 keV to 1250 keV. The primary instrumentation was a 2.54 cm (1 inch) diameter wall-less tissue equivalent counter, encapsulated by a 10.2 cm spherical tissue equivalent plastic, 6.4 mm thick. Figure 4.36 illustrates the schematic of the WTEPC and the distribution of the microdosimetric results,  $y_d(y)$  as a function lineal energy,  $y$  for a  $1 \mu\text{m}$  simulated cavity at eight different photon energies.

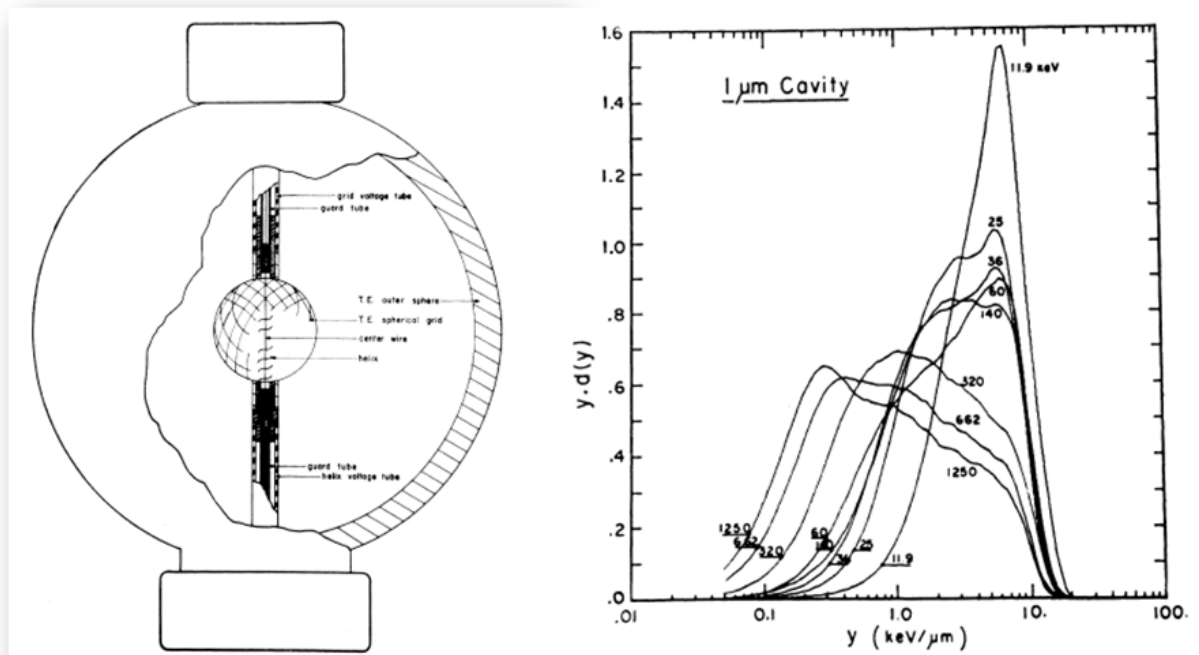


FIGURE 4.36: A schematic view of the wall-less counter and microdosimetric output results from the benchmark experiment by Kliauga and Dvorak (1978) used in a PENELOPE simulation to determine the microdosimetric event distributions of a range of monoenergetic photons.[18]

As described before, the first step in the procedure for a PENELOPE simulation was defining the geometry of the counter using constructive quadric surfaces.

Appendix A, Section A.1 displays a cropped copy of the design and editing tool used to define the geometry that is visualized in 2D and 3D images in Figures 4.37 and 4.38 respectively.

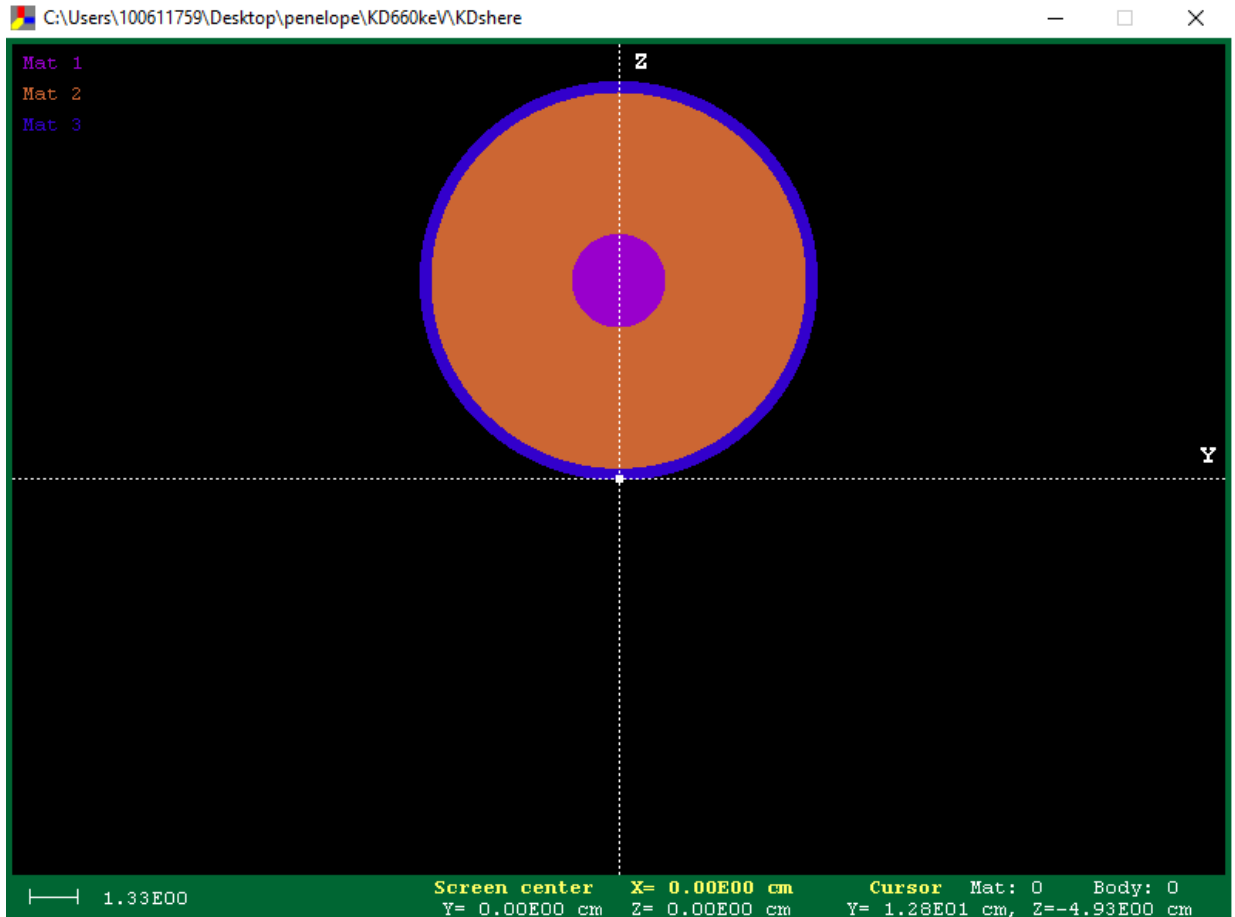


FIGURE 4.37: 2D View of the Wall-less counter geometry designed in PenGeomJar. Similar to the experiment the photon source is positioned just outside 6.4 mm thick TE plastic walls in the direction of the 2.54 cm counter at the centre of the chamber along the Z-direction

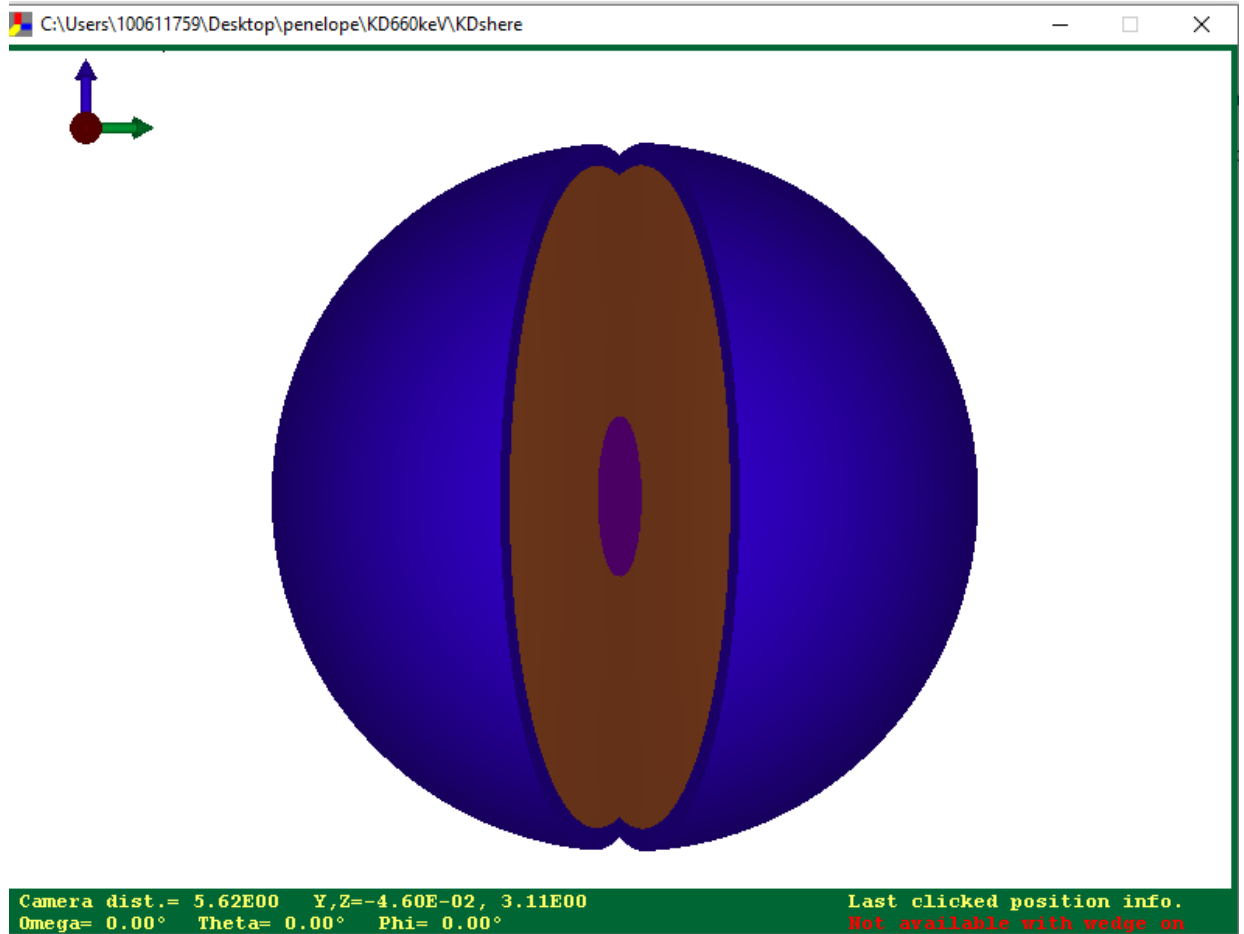


FIGURE 4.38: 3D View of the wall-less counter geometry designed in PenGeomJar. The wedged out portion shows the sensitive 2.54 cm inner sphere of TE gas (material 265) encapsulated by an outer 10 cm sphere of TE plastic (Material 266).

The next most important step in the procedure to operate PENELOPE is the definition of the input file (*\*.in*). Figure 4.39 illustrates an input file for one experimental run, for a 323 keV monoenergetic photon at some arbitrary distance away from a 2.54 cm spherical inset TE detector inside a 10.2 cm TE plastic spherical shell. The energy example was taken from the range of energies listed by Kliauga and Dvorak (1978) in *Table I* (Photon Sources) [18], for a  $^{51}\text{Cr}$

---

gamma ray. The input file required the energy 323 keV, 'SENRG', to be deposited in the specified Body 1. The 'SKPAR' was '2' for monoenergetic photons. The material file, in this case '265\_TEGas.mat', the name of the geometry file 'Xsphere.geo', the time allotted for the simulation (example 1200 seconds), and the name of the output file 'DUMPTO' and 'DUMPP', in this case 'Xrundump323'. For a closer look at an input file, a copy can be found in Appendix A.2.



```

1  TITLE Point source and a 10.2cm spherical shell with 2.54cm sphere inset
2  TE detector 323keV.
3  Note that interaction forcing distorts the detector output.
4  .
5  >>>>>> Source definition.
6  SKPAR 2 [Primary particles: 1=electron, 2=photon, 3=positron]
7  SENERG 323e3 [Initial energy (monoenergetic sources only)]
8  SPOS11 0 0 0.0001 [Coordinates of the source]
9  SCONE 0 0 5 [Conical beam; angles in deg]
10 .
11 >>>>>> Material data and simulation parameters.
12 MFNAME 265_TEGAS.mat [Material file, up to 20 chars]
13 MSIMPA le3 le3 le3 0.05 0.05 le3 le3 [EABS(1:3),C1,C2,WCC,WCR]
14 MFNAME 265_TEGAS.mat [Material file, up to 20 chars]
15 MSIMPA le3 le3 le3 0.05 0.05 le3 le3 [EABS(1:3),C1,C2,WCC,WCR]
16 .
17 >>>>>> Geometry and local simulation parameters.
18 GEOMFN xsphere.geo [Geometry file, up to 20 chars]
19 PARINP 1 0.005 thickness [Optional geometry parameters]
20 PARINP 2 0.01 radius [Optional geometry parameters]
21 DSMAX 1 le-4 [KB, maximum step length in body KB]
22 .
23 >>>>>> Interaction forcing.
24 IFORCE 1 1 4 2000 .1 2 [Interaction forcing]
25 IFORCE 1 1 5 200 .1 2 [Interaction forcing]
26 .
27 >>>>>> Bremsstrahlung splitting.
28 IBRSPL 1 2 [KB,splitting factor]
29 .
30 >>>>>> X-ray splitting.
31 IXRSPL 1 2 [KB,splitting factor, weight window]
32 .
33 >>>>>> Emerging particles. Energy and angular distributions.
34 NBE 0 0 100 [Energy window and no. of bins]
35 NBANGL 45 18 [No. of bins for the angles THETA and PHI]cd..
36 .

```

length: 3,325 lines: 64 Ln: 2 Col: 8 Sel: 0|0 Unix (LF) UTF-8 INS

FIGURE 4.39: PENELOPE input file for a 323keV photons hitting a 2.54 cm sphere inset TE detector in a 10.2 cm spherical shell.

## Chapter 5

# Results and Discussion

### 5.1 Experimental Investigation

The results of these investigations are divided into individual sections that give a summary of the experiments carried out to meet the objectives of this work. The resulting analysis of the data collected and a discussion relating to the dosimetry of hot particles using the microdosimetric technique both experimentally and with Monte Carlo simulations are presented in this chapter.

The investigations carried out in this work involved:

- Experimentation with a Far West Technology single wire counter to verify that the electronic architecture was functioning as required (Section 4.2.3).
- Examination of the wall-less type TEPC with a low range 5.5MeV alpha source for calibrating the device.
- Two beta source experiments for the microdosimetric determination of dose rate and the potential variations in radiation quality in lab with the WTEPC experimental device.
- Monte Carlo simulations of available beta sources measured with the experimental counter in lab, and several scenarios with other radionuclides associated with HPs that were not available for laboratory determinations.

Among the beta particle emitting sources of interest in hot particle dosimetry, six energies were examined including those associated with  $^{63}\text{Ni}$  and  $^{14}\text{C}$  for

their availability in lab. Table 5.1 illustrates the average energies and the end point energies associated with these and other radionuclides according to ICRP publication 107, for nuclear decay data required for dosimetric calculations [59]. The table also illustrates what the continuous slowing down approximation (CSDA) range,  $R_{\bar{E}}$  for each isotope, which is the distance ( $\mu m$ ) an electron is able to travel in propane based tissue equivalent gas at unit density. For the Monte Carlo experiments, a normalized beta spectrum, binned for sampling Monte Carlo calculations was generated for each radionuclide using the software "Radiological toolbox". Distribution of bins uniformed in beta energies between energies E1 and E2, and uniformed in probability, P(E1-E2) were used as the energy input data for PENELOPE's source parameter. An example of this Radtoolbox output file for input into PENELOPE can be found in Appendix A.2.

TABLE 5.1: Radionuclides listed in order of increasing average energies,  $\bar{E}$  along with their associated end point energies,  $E_{Max}$  in keV [59]. The approximate range in TE gas (Propane based) corresponding to the energy emitted from these beta particles,  $R_{\bar{E}}$ , are presented in ( $\mu m$ )[60]

Radionuclides	Average Energy, $\bar{E}$ (keV)	End Point, $E_{Max}$ (keV)	CSDA, $R_{\bar{E}}$ ( $\mu m$ )
$^3H$	5.6	18.51	1.0
$^{63}Ni$	17.4	66.9	6.5
$^{14}C$	49.4	156.4	42.0
$^{60}Co$	96.5	1491.3	139.5
$^{177}Lu$	133.3	497.8	275.2
$^{90}Sr$	195.9	546.0	439.0

## 5.2 Experimental Study of the Wall-less TEPC Response to Short Ranged Alpha and Beta particles

The energy deposition spectra for short ranged charged particles can only be investigated with wall-less counters. In this section the main findings are presented and discussed from investigations made with the wall-less TEPC. The microdosimetric quantities  $y$ , and  $\bar{y}_D$  were determined along with RBE values from short ranged particles emanating from  $^{63}\text{Ni}$  and  $^{14}\text{C}$  sources. An  $^{241}\text{Am}$  alpha particle source was used for internal calibration of the experimental apparatus and similar quantities determined to evaluate the response of the counter.

### 5.2.1 WTEPC's Response to $^{241}\text{Am}$ Alpha particles

In Table 5.2 a summary of the microdosimetric data generated after an  $^{241}\text{Am}$  source was moved incrementally away from the counter's sensitive volume at a physical distance tracked in millimeters equivalent to the simulated tissue distance given in micrometers ( $\mu\text{m}$ ). The table lists the experimentally measured absorbed dose rate ( $\mu\text{Gy}/\text{s}$ ) and the corresponding microdosimetric average, the dose mean lineal energy, given as  $\bar{y}_D$  for the alpha source. The dose mean lineal energy as discussed previously indicates the lineal energy with which on average the dose is delivered by the radiation in the site of interest. The  $\bar{y}_D$  value provides a measure of the potential for biological damage, and at very small absorbed dose values Lindborg and Waker (2017) suggests that the ratio of the dose mean lineal energies determined inside the sensitive volume with diameters in the micro-metric range are found to be close to observed relative biological effectiveness (RBE) values for several biological endpoints [23]. The RBE values were calculated using equation 2.16 presented in subsection 2.3.4. The RBE is that factor needed to quantify the change in absorbed dose from one radiation quality to another in a volume when going from a potentially high radiation quality to a low radiation quality for some chosen survival outcome. The Figure in 5.1 illustrates that the dose rate given in  $\text{Gy}/\text{s}$ , steadily decreases with the

simulated tissue depth ( $\mu m$ ), as the source of radiation moves incrementally away from the counter's collecting volume. Here a physical movement of 5 mm on the sliding plunger represents a simulated tissue movement of approximately  $2 \mu m$  and the resulting imparted energy at this point provided a dose rate of approximately  $3.2 \mu Gy/s$  and a dose mean lineal energy of  $193.38 keV/\mu m$ . The dose rate as a function of distance here does not appear to obey the inverse square law, however the dose rate decreases significantly as the source to simulated tissue distance increases. The  $\bar{y}_D$  values behaved as expected increasing gradually as the source is moved further away from the sensitive volume. The  $\bar{y}_D$  value or the radiation quality, is the stochastic microdosimetric version of the the non-stochastic LET, that will increase in value with decreasing energies. Similarly an increase was expected in the RBE or radiation weighting factor values given their dependence on the  $\bar{y}_D$  values.

TABLE 5.2:  $^{241}Am$  Microdosimetric measurements made with the WTEPC

Position,(mm)	Simulated Distance, $(\mu m)$	Dose Rate, $(\mu Gy/s)$	$\bar{y}_D,(keV/\mu m)$	RBE
2.5	1	4.68 (0.022)	176.74 (1.52)	1.00
5	3	3.18 (0.012)	193.38 (1.34)	1.09
10	5	2.61 (0.008)	208.23 (1.15)	1.18
15	7	1.69 (0.009)	214.77 (2.07)	1.22
20	9	1.17 (0.005)	217.99 (1.75)	1.23
25	11	0.87 (0.004)	219.61 (1.65)	1.24
30	13	0.66 (0.003)	224.15 (1.92)	1.27
35	15	0.52 (0.004)	229.33 (3.12)	1.30
40	17	0.42 (0.003)	235.68 (2.93)	1.33
45	19	0.36 (0.002)	242.91 (2.61)	1.37
50	21	0.32 (0.002)	253.32 (3.40)	1.43

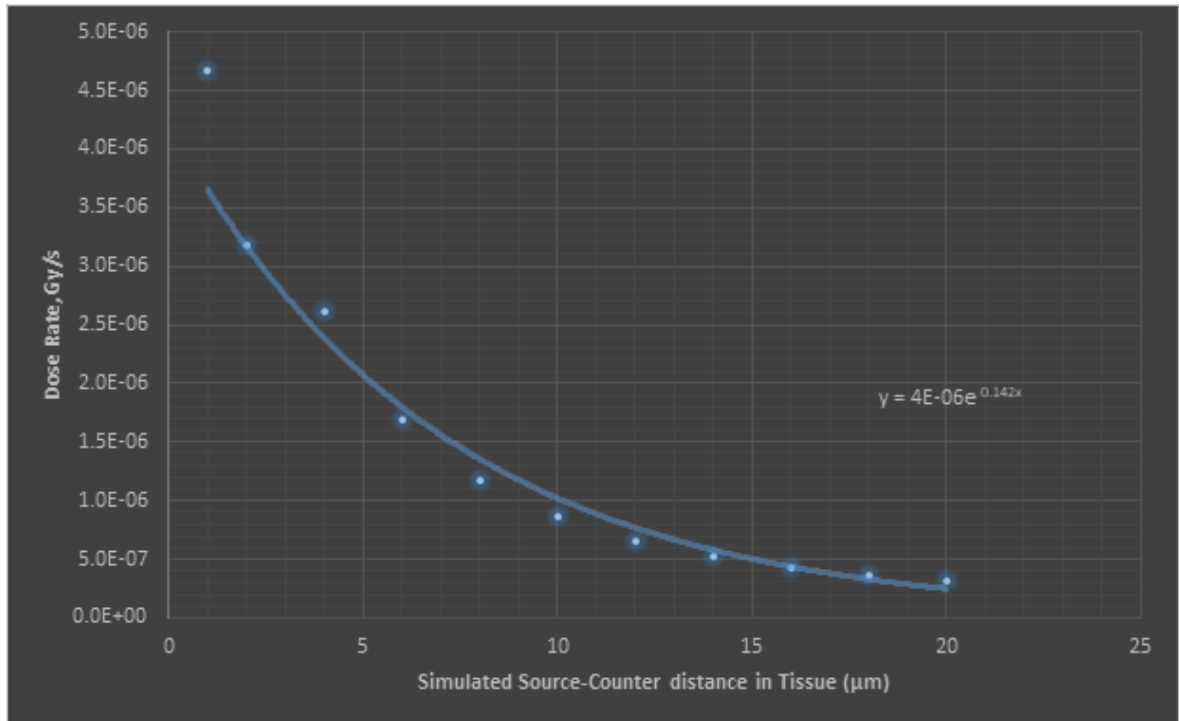


FIGURE 5.1: An  $^{241}\text{Am}$  Alpha Particle Dose Rate (Gy/s) variations in Simulated Source-Counter Distances in Tissue ( $\mu\text{m}$ ). The activity of the  $^{241}\text{Am}$  source at the time of measurement was approximately  $3.70 \text{ kBq}$

In Figure 5.2 the plots illustrate that as the source moves away from the detector the energy of the alpha particles arriving at the  $2 \mu\text{m}$  sensitive volume will be lower and their stopping power higher. This resulted in larger energy deposition events as shown by the shifting to the right of the event-size peaks to higher and higher event-sizes in the target volume.

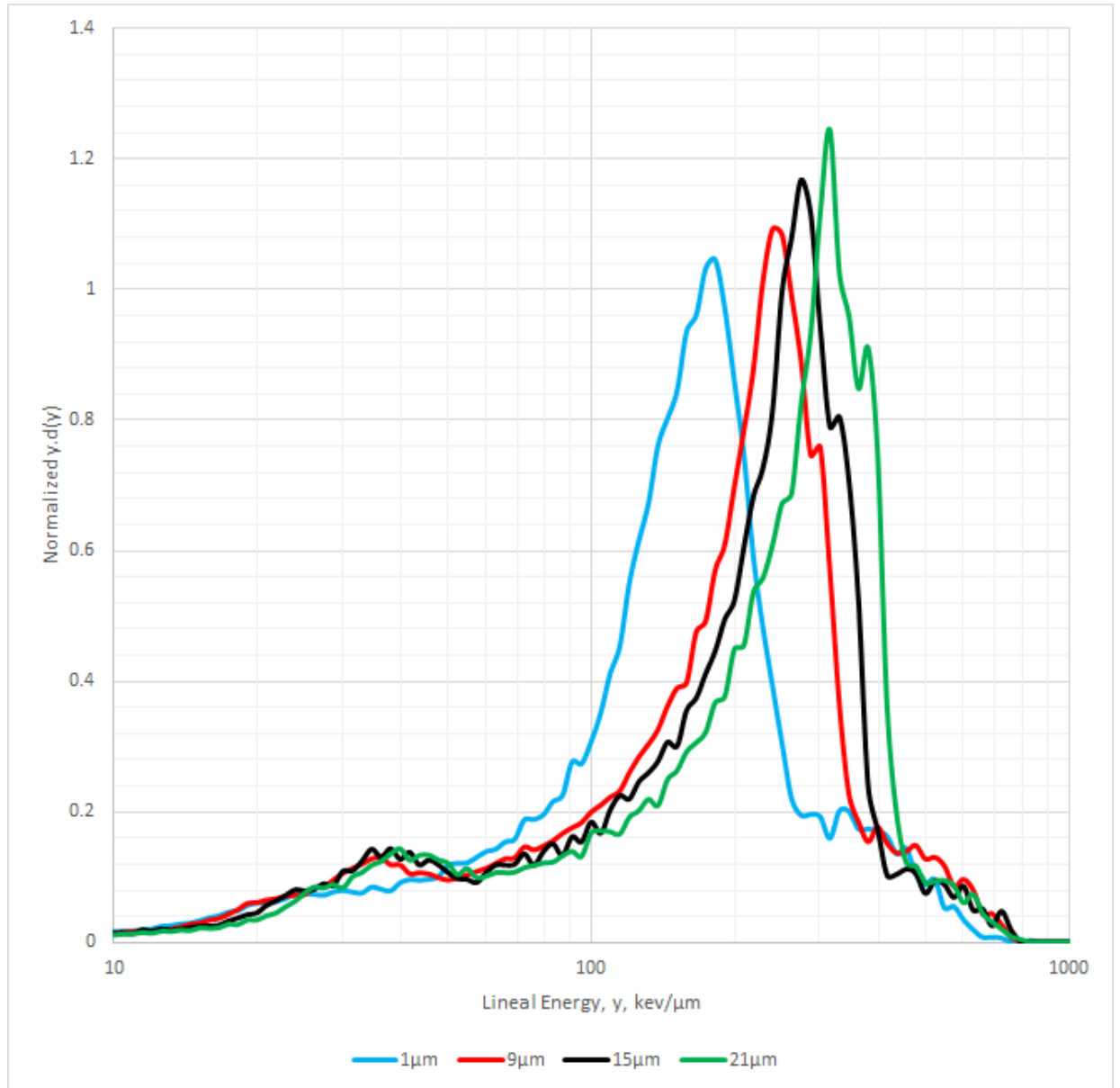


FIGURE 5.2: Fractional Absorbed Dose per Logarithmic Interval of Lineal Energy for Several Tissue Distances away from a 5.5  $MeV$   $^{241}Am$  Alpha Emitting Source Crossing a 2  $\mu m$  Simulated Cavity Site. The Spectrum is Normalized to Unit Density of Tissue Equivalent Gas (propane based)

The position of each individual peak on a microdosimetric spectrum, is an indication of the modal imparted energy of the charged particles, in this case  ${}^4\text{He}$  ions. At the height of this event the stopping power of the charged particles are believed to be at a maximum and the path of the particle across the simulated cavity size ( $2\ \mu\text{m}$ ) is also at its maximum. The peak position is also an indication that the range of the charged particle matches the simulated site's diameter. The logarithmic arrangement of the lineal energy,  $y$ , on the horizontal axis is a technique usually used by investigators presenting microdosimetric measurements and allow for the unique shoulder and edge of the charged particle to be readily identified. As expected the lineal energies at each simulated distance away from the  $2\ \mu\text{m}$  site during the apparatus calibration were all different. Each plot in Figure 5.2 displays a sharp increase at lower  $y$ -values, believed to be caused by very low energy alpha particles crossing the target site or became terminal there. Alpha decay energies associated with  ${}^{241}\text{Am}$  are  $5.486\ \text{MeV}$  (85%),  $5.443\ \text{MeV}$  (13%) and  $5.388\ \text{MeV}$  (2%), and a gamma ray energy of  $59.409\ \text{keV}$  for the resulting stable  ${}^{237}\text{Np}$ . The approximately  $60\ \text{keV}$  photons produce electrons with mean energy around  $10\ \text{keV}$  that have a slowing down approximation in tissue of roughly  $2\ \mu\text{m}$  identical to the cavity site's diameter. At simulated source to counter tissue distances of  $9\ \mu\text{m}$ ,  $15\ \mu\text{m}$  and  $21\ \mu\text{m}$ , Figure 5.2 (red, black, and green legends respectively), there is an appearance of smaller peaks around the  $40\ \text{keV}/\mu\text{m}$   $y$ -value, that is less pronounced for the  $1\ \mu\text{m}$  tissue distance. The electrons tracks from the  $60\ \text{keV}$  photons will have a longer range than the  $2\ \mu\text{m}$  sensitive cavity and are possibly crossing the cavity without electrons stopping there. The triangular shaped spectra with a prominent shoulder and edge agrees well with other microdosimetric spectra produced by other investigators of short ranged alpha particles at similar dimensions [61][62] and [63]. Referring to the Figure in 5.2, the plots were displayed on a logarithmic scale for ease of comparison among the different tissue distances and to identify a few of the important features of each spectra. The chart illustrates the dose weighted lineal energy spectra for evaluation of the fraction of absorbed dose delivered per unit logarithmic interval of  $y$ -values ( $\text{keV}/\mu\text{m}$ ) at each source to tissue simulated distance. The peak in the distributions indicate that most of the dose was deposited with



high lineal energies, mainly between  $100 \text{ keV}/\mu\text{m}$  and  $400 \text{ keV}/\mu\text{m}$ . Indicative of low alpha particle energies with increasing source to target distances are the higher stopping powers increasing in y-values with a shift to the right.

### 5.2.2 WTEPC's Response to $^{63}\text{Ni}$ Beta particles

Important to determining the response of beta particles in a wall-less TEPC are the range and energies of the particles interacting in the gas. According to Table 5.1,  $^{63}\text{Ni}$  has an average energy of 17 keV and an associated travel range of  $6.5 \mu\text{m}$  in propane based tissue equivalent gas at unit density. However,  $^{63}\text{Ni}$ , a pure beta minus emitter, exist as a spectrum of energies as displayed in Figure 5.3, and possesses an end point energy of approximately  $66 \text{ keV}$  which can only travel a maximum tissue distance of approximately  $58 \mu\text{m}$  [60]. The objectives at this point in the investigation were to determine the response of the WTEPC to the  $^{63}\text{Ni}$  spectrum, and produce calculations of the dose mean lineal energies,  $\bar{y}_D$ , and the RBE ratios.

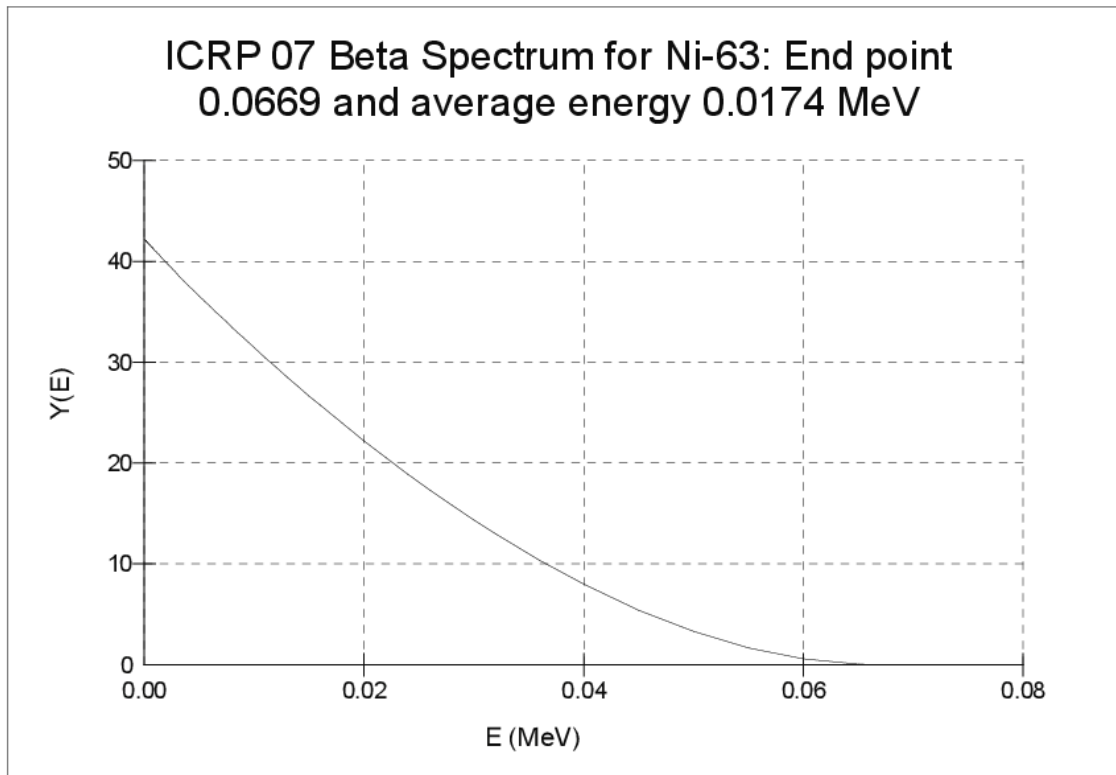


FIGURE 5.3:  $^{63}\text{Ni}$  Beta Spectrum. Source: Radtoolbox, ICRP 07

The findings of this investigation are summarized in Table 5.3. As indicated previously, the Poisson error associated with each event-size was calculated to be less than 0.1%, given that the total number of counts collected were in the range of  $10^6$  for each measurement. As expected low standard deviations values were recovered for the calculated dose rate, and  $\bar{y}_D$  values. The explanations for determining these random errors are provided in section 4.3.4, along with the equations used to calculate the error propagation. The overall experimental uncertainty (root mean square) attributed to calibration and geometry issues was estimated around 8% for  $\bar{y}_D$ . Overall estimated experimental uncertainties was also discussed by [23], for measurements in a  $^{60}\text{Co}$   $\gamma$  beam. The overall uncertainties in  $\bar{y}_D$  was measured to be 6% [23].

The measured dose rate as a function of the simulated source to counter distances in tissue are illustrated in the Figure 5.4. The dose rate sharply decreases from a maximum of  $0.3 \mu\text{Gy}/\text{s}$  at a source to target simulated tissue distances of  $X \mu\text{m}$  that agrees with the relationship:  $0.3997X^{-1.08}$ . The dose rates even though displaying a steep dose gradient does not strictly obey the inverse square law, the dose at each position however are potentially due to the finite range of beta particles at particular simulated tissue distances. As the spectrum of energies vary, all the low energy beta particles are expected to be absorbed over short distances, leaving the more energetic high energy ones. Consequently, a steep dose gradient would be anticipated, and is supported by these findings.

TABLE 5.3:  $^{63}\text{Ni}$  Microdosimetric measurements made with the Wall-less TEPC. The numbers in parenthesis are the standard deviations

Simulated Source-Counter Distances ( $\mu\text{m}$ )	Dose Rate, ( $\text{nGy/s}$ )	$\bar{y}_D$ , ( $\text{keV}/\mu\text{m}$ )	RBE
1	300.3 (0.28)	3.745 (0.01)	1.000
3	228.0 (0.23)	3.760 (0.01)	1.004
5	109.8 (0.17)	3.786 (0.01)	1.011
7	58.4 (0.10)	3.879 (0.02)	1.036
9	33.7 (0.09)	4.138 (0.03)	1.105
11	22.5 (0.12)	4.415 (0.06)	1.179
13	17.6 (0.05)	4.679 (0.04)	1.249
15	15.1 (0.08)	4.642 (0.07)	1.239
17	12.6 (0.15)	5.804 (0.16)	1.550
21	11.3 (0.08)	6.129 (0.10)	1.636
25	10.9 (0.16)	6.070 (0.20)	1.621
29	11.2 (0.17)	6.313 (0.22)	1.685
33	9.86 (0.22)	6.083 (0.31)	1.624
37	10.8 (0.06)	6.411 (0.08)	1.712
41	12.1 (0.09)	6.381 (0.10)	1.704

The microdosimetric quantity  $\bar{y}_D$ , was calculated for 15 incremental source to target simulated distance. Lower energy electrons have a higher stopping power than higher energy electrons and with these variations in mind some changes to radiation quality were expected. At the greatest simulated source to target tissue distance of 41  $\mu m$ , a dose mean lineal energy of 6.4  $keV/\mu m$  was calculated. This corresponded to a very low dose rate of 0.012  $\mu Gy/s$  and a RBE of 1.7. The results of the experiment suggest an increase in the biological effectiveness of electrons with increasing source to counter tissue distances as dose rates decreases. Generally an RBE value of 1 for electrons is accepted by the international bodies governing ALARA principles in radiation protection both for medical and industrial operations. In this work the results indicate that the RBE is closer to a rounded value of 2 than 1. These findings are supported by expert investigators such as Bellamy and Eckerman (2013) in published work on the RBE of low-energy electrons and photons [64] from the U.S Environmental Protection Agency (EPA). In Figure 5.5 a copy of their results illustrate the RBE values determined for various radionuclide emitting low energy beta particles. A cut off energy of 5  $keV$  was adopted for their investigations and the RBE for  $^3H$  determined to be 2. It should also be noted that the authors believed that the estimate of RBE for electrons was relatively insensitive to the choice of cutoff energy. Tritium has an average energy of 5.6  $keV$  and a range of approximately 1  $\mu m$  in tissue. In previous work by Nikjoo et. al. [65], [66], [67], it was also determined that RBE from low-LET radiations may be strongly influenced by the fraction of dose deposited by electrons at the end of their range, below 5  $keV$ . In this work it was determined that electrons at distances between 17  $\mu m$  to 41  $\mu m$  could produce RBE values rounded to 2.

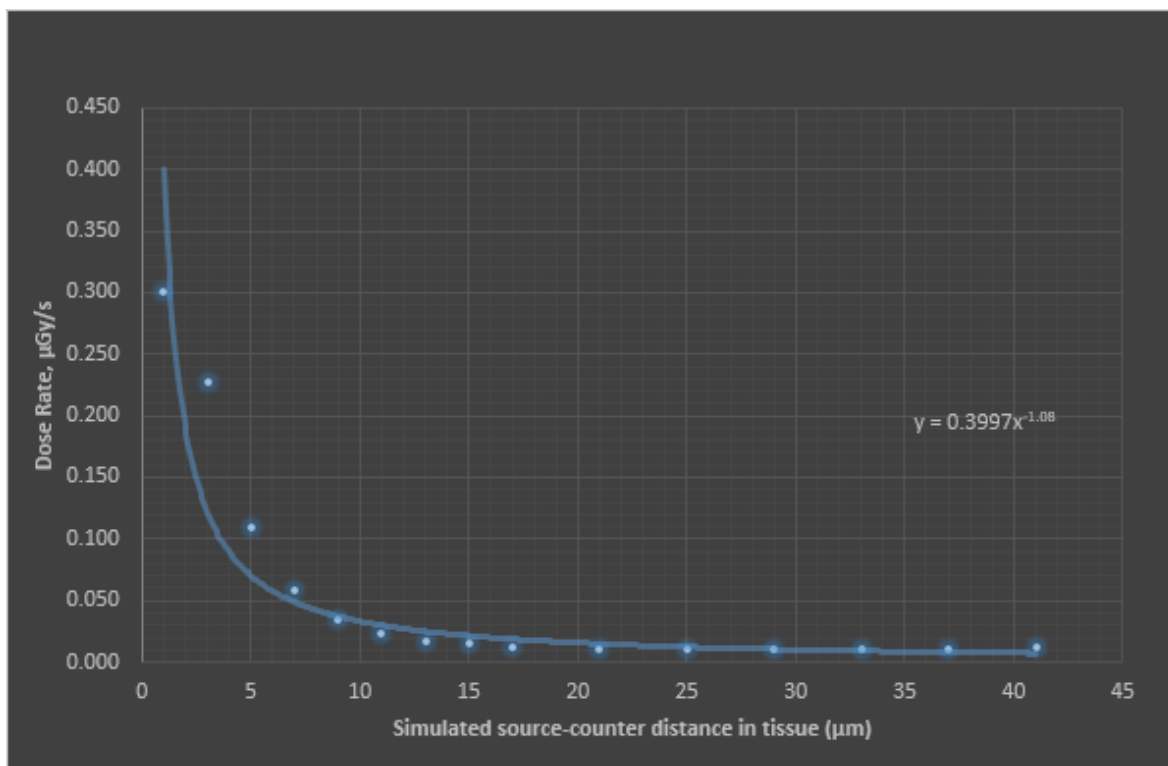


FIGURE 5.4: Dose Rate( $\mu Gy/s$ ) from  $^{63}Ni$  Beta Particles varied against Simulated Source-Counter Distances in Tissue ( $\mu m$ ). The activity of the  $^{63}Ni$  source at the time of measurement was approximately  $341 kBq$

<b>Nuclide</b>	<b>E<sub>c</sub> (keV)</b>					
	<b>1.5</b>	<b>2.0</b>	<b>3.0</b>	<b>4.0</b>	<b>5.0</b>	<b>6.0</b>
H-3	1.67	1.74	1.86	1.97	2.05	2.11
C-14	1.23	1.24	1.24	1.26	1.27	1.28
P-32	1.01	1.01	1.01	1.01	1.01	1.01
Sr-90	1.11	1.11	1.11	1.11	1.12	1.12
Y-90	1.01	1.01	1.01	1.01	1.01	1.01

FIGURE 5.5: RBE Values for Selected Beta Emitting Radionuclides Relative to 1 MeV Electrons. An energy cut off of 5 keV was adopted by the investigators. Retrieved from the US EPA report on the "Relative Biological Effectiveness of Low Energy Electrons and Photons" [64].

In order to properly evaluate the important features of the microdosimetric spectra a plot of 5 peaks at varying source to counter simulated tissue distance is illustrated in Figure 5.6. This comparison allowed for better identification of each peak given a logarithmic representation of the lineal energies on a normalized spectra, where equal areas under the curves represent equal dose fractions of the total dose. Even at optimal operating conditions high noise signals populated the counter at a gain of 50 with the counter expected to produce event sizes between  $0.364 \text{ keV}/\mu\text{m}$  to  $22.9 \text{ keV}/\mu\text{m}$ . Therefore, the sharp cut-offs at the extreme ends of the spectra were a product of the lower limit of detection set by the investigator and the upper limit of detection built into the multi-channel analyzer. Majority of the dose fractions occur between peak  $y$ -values in the range of  $2 \text{ keV}/\mu\text{m}$  and  $6 \text{ keV}/\mu\text{m}$  at simulated tissue distances up to  $13 \mu\text{m}$ . These peak formations are due to higher energy electrons with ranges greater than the simulated cavity sizes known as "crossers". The mean energy of these electrons that cross the target site have a range of approximately  $7 \mu\text{m}$  which is over

---

two to three times greater than the simulated target site of  $2 \mu m$ . The shoulder in the event size spectra is found where the average energy of the electron's range matches the simulated cavity size. The sharp drop above  $10 keV/\mu m$  is called the electron edge and is a result of the maximum energy that can be imparted by the electrons to the site being simulated. The spectra shares similar shapes up until  $13 \mu m$  simulated tissue distance. At further source to counter tissue distances around  $29 \mu m$  the dose is produced by higher energy beta particles traveling longer distances in tissue, the average energies and range of electrons decrease considerably and the stopping power of dose fractions increases with decreasing energies. The lack of smoothness of the curves at further tissue distances was as a result of lower statistics even after very long counting times (86400 s) as less beta particles get to the counter as the source is pulled further away.



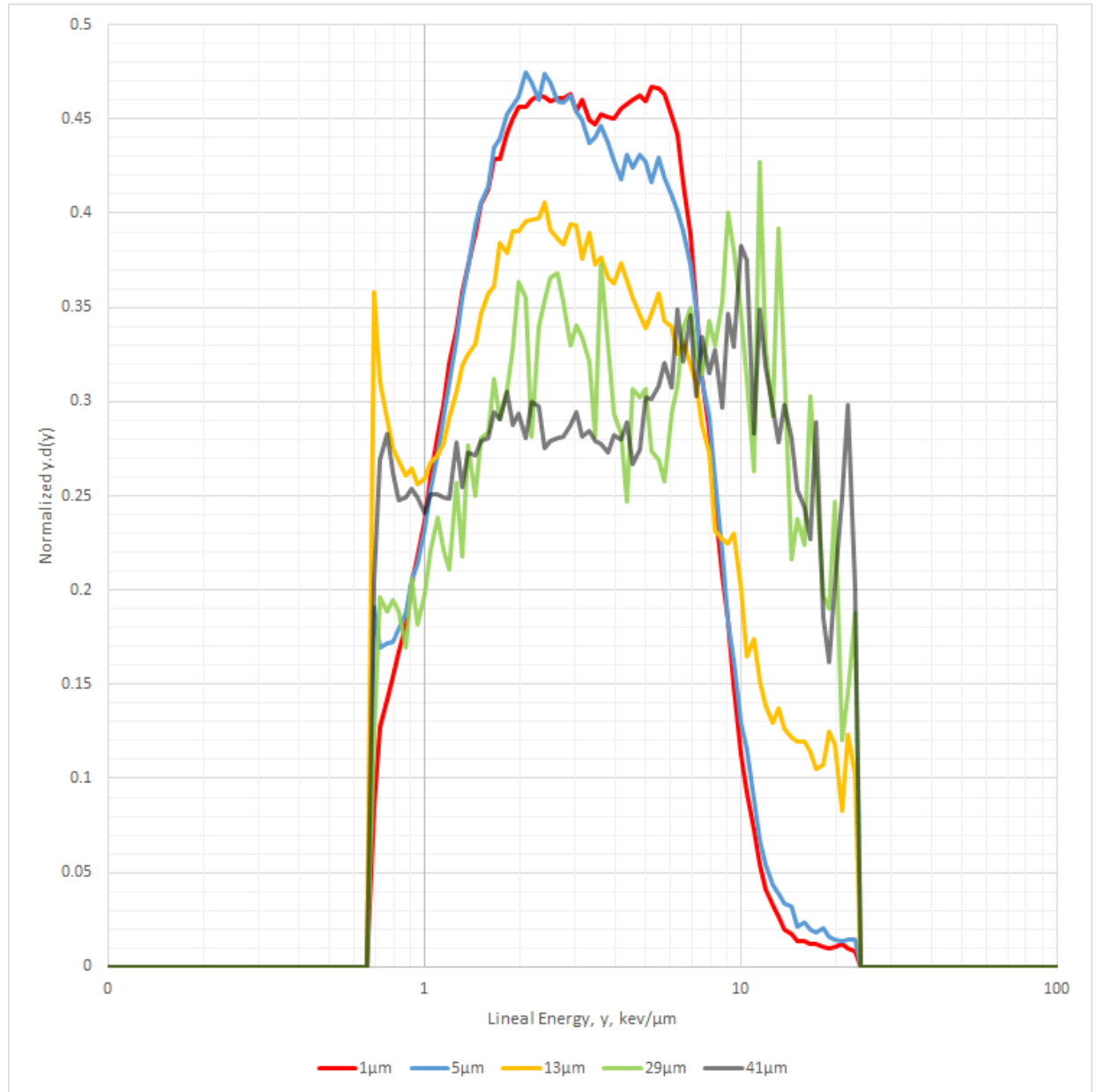


FIGURE 5.6: Fractional Absorbed Dose per Logarithmic Interval of Lineal Energy for Several Tissue Distances away from a 17.4 keV  $^{63}\text{Ni}$  Beta Emitting Source at its Average Energy Crossing a  $2 \mu\text{m}$  Simulated Cavity Site. The vertical axis is displayed in a normalized  $yd(y)$  format as a function of  $y$  on logarithmic scale.

### 5.2.3 WTEPC's Response to $^{14}\text{C}$ Beta particles

To further investigate the response of the counter a lab available  $^{14}\text{C}$  beta source with significantly lower activity (103.9 nCi) than the  $^{63}\text{Ni}$  source was measured. Figure 5.7 illustrates the energy spectrum for  $^{14}\text{C}$  which has an average energy of 49.4keV and a travel range in propane based tissue equivalent gas of  $42\mu\text{m}$ .

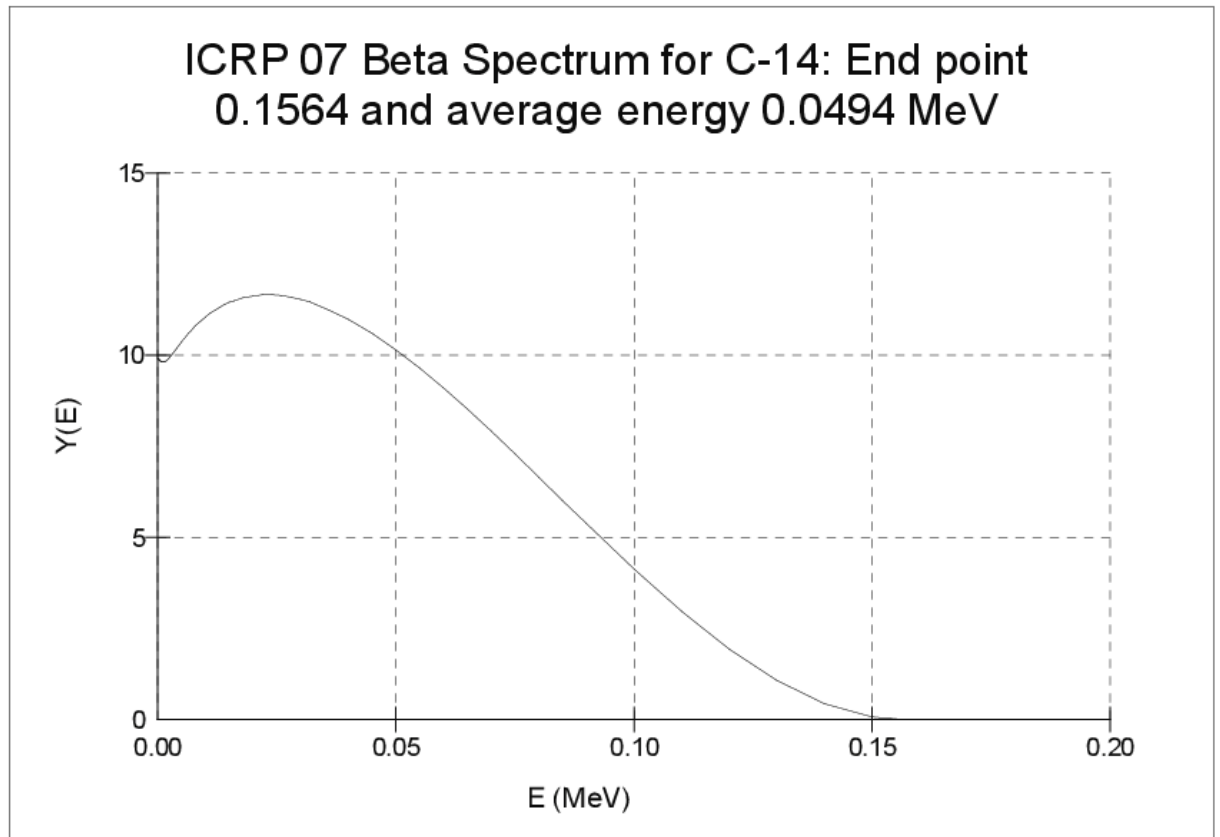


FIGURE 5.7:  $^{14}\text{C}$  Beta Spectrum. Source: Radtoolbox, ICRP 107

Table 5.4 gives a summary of the microdosimetric calculations and the ratios of RBE determined for various source to counter simulated tissue distances. Given the lower activity, significantly lower doses were calculated from the  $^{14}\text{C}$  beta particle interactions than previously observed for  $^{63}\text{Ni}$ . A moderate decrease in

dose rate activity was observed, and the relationship for dose rate as a function of simulated tissue movement or depth (in  $X\mu m$ ) in tissue followed the relationship:  $0.0311e^{-0.007X}$ , Figure 5.8. Similarly to the discussions made in the  $^{63}Ni$  investigation, the dose rate intensities do not obey the inverse square law, and a moderate dose gradient was observed in this investigation. The microdosimetric quantity,  $\bar{y}_D$ , as expected was highest when the source was pulled back to its maximum source to target tissue distance of  $41\mu m$ . The resulting dose mean lineal energy at this distance was  $4.91 keV/\mu m$ , lower in value to the findings of the  $^{63}Ni$  source at the same distance. An RBE value of 1.24 was calculated for electrons associated with  $^{14}C$  beta particles. These results have some agreement with the values presented in Figure 5.5 for  $^{14}C$  at a cutoff energy of  $5keV$  determined by experts at the US EPA, who investigated RBE values associated with low-energy electrons and photons [64].

TABLE 5.4:  $^{14}C$  Microdosimetric measurements made with the WTEPC in Anti-coincidence Mode. The numbers in parenthesis are the uncertainties.

Simulated Source-Counter Distance ( $\mu m$ )	Dose Rate, ( $nGy/s$ )	$\bar{y}_D$ , ( $keV/\mu m$ )	RBE
1	31.9 (0.05)	3.967 (0.02)	1.000
9	28.1 (0.08)	3.845 (0.04)	0.969
17	27.1 (0.11)	4.343 (0.05)	1.095
25	26.7 (0.10)	4.591 (0.05)	1.157
33	28.0 (0.17)	4.982 (0.08)	1.256
41	31.1 (0.12)	4.905 (0.05)	1.237

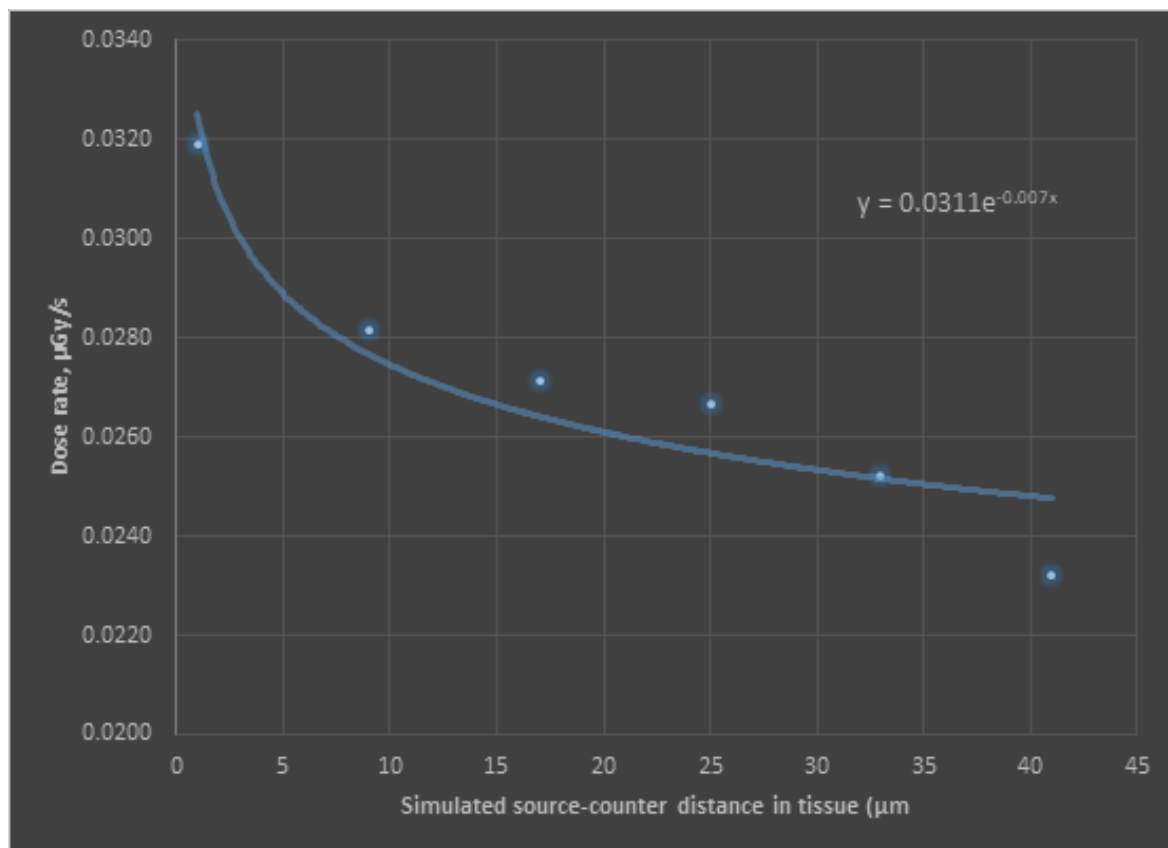


FIGURE 5.8:  $^{14}\text{C}$  Beta Particle Dose Rate ( $\mu\text{Gy/s}$ ) variations with Simulated Source-Counter Distances in Tissue ( $\mu\text{m}$ ). The activity of the  $^{14}\text{C}$  source at the time of measurement was approximately  $3.83 \text{ kBq}$

In Figure 5.9, at a simulated tissue distance of  $1 \mu\text{m}$  the plot indicates  $y$ -values below  $1 \text{ keV}/\mu\text{m}$  and  $10 \text{ keV}/\mu\text{m}$ . In order to accurately determine the peak locations, the shoulder and the electron edge data at each source to counter tissue distance were redistributed unto a normalized spectra. Figure 5.9 illustrates the spectra at varying simulated tissue distances, the peaks for distances above  $25 \mu\text{m}$  appear similar in shape with higher  $y$ -values due to lower energy electrons reaching the  $2 \mu\text{m}$  target site with the source pulled away. The peak at  $1 \mu\text{m}$  and  $9 \mu\text{m}$  have a lower  $y$ -value of approximately  $1 \text{ keV}/\mu\text{m}$  caused by higher

---

absorbed dose fractions resulting from these so called crossers with ranges far greater than the  $2 \mu m$  range of the simulated target site diameter. The shoulder indicates the region where electrons with ranges that do not match the simulated cavity size, and their average stopping power are at the maximum value of  $y$ . For the simulated distance above  $25 \mu m$  it appears around  $2 keV/\mu m$  and for lower distances at  $1 keV/\mu m$ . At the end of the plot the electron edge appears between  $10 keV/\mu m$  and  $20 keV/\mu m$ . This was also observed in  $^{63}Ni$  investigations and is believed to either be an artifact of this particular counter's design or from very very low energy beta particle reaching the counter. Electrons creating event sizes with  $y$ -values above the region of  $10$ - $12 keV/\mu m$  is unusual, and may be as a result of the preparative or investigative mechanism.

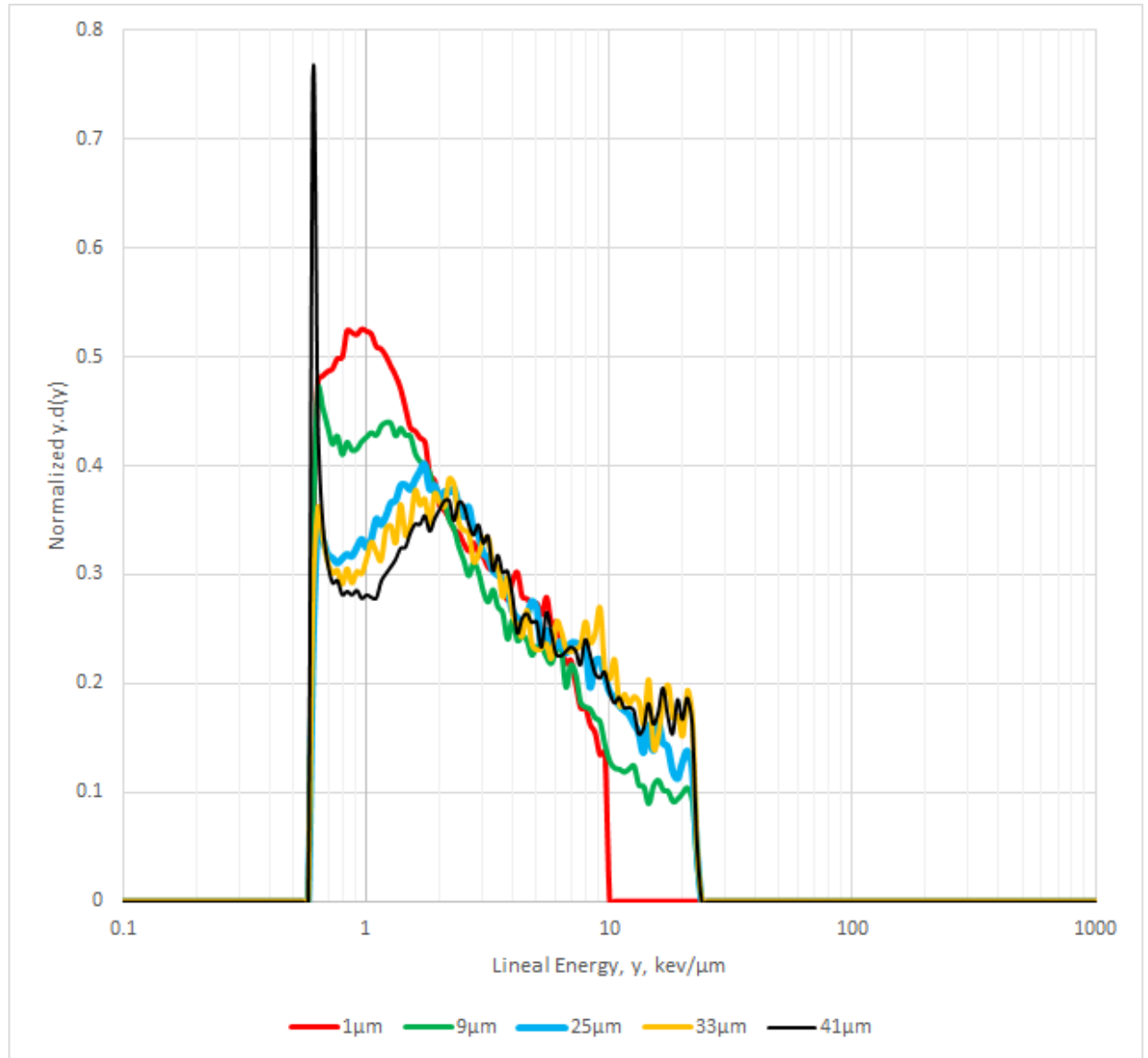


FIGURE 5.9: Fractional Absorbed Dose per Logarithmic Interval of Lineal Energy for Several Tissue Distances away from a 49.4 keV  $^{14}\text{C}$  Beta Emitting Source at its Average Energy Crossing a  $2 \mu\text{m}$  Simulated Cavity Site. The vertical axis is displayed in a normalized  $y.d(y)$  format as a function of  $y$  on logarithmic scale.

### 5.3 Monte-Carlo simulations of Photon Irradiations in a Wall-less TEPC. Results of the Transport Code PENELOPE for Kliauga and Dvorak's Benchmark Study.

Monte Carlo methods provide the ability to simulate physical experiments undertaken in lab and also those experiments that would not be possible given certain experimental limitations. As discussed earlier in Section 4.5, a benchmark study by Kliauga and Dvorak (1978), from Columbia University was chosen for its rich availability of experimentally determined microdosimetric data. The experimenters irradiated a 1 inch (2.54 cm) wall-less TEPC, Figure 4.36, with 8 different photon energies, and simulated 6 varieties of microscopic tissue site sizes with diameters ranging from  $0.5 \mu m$  to  $8 \mu m$  [18]. Figure 5.10 presents their results of the microdosimetric distributions over a range of cavities irradiated by 1250 keV  $^{60}Co$  photons as a function of lineal energy,  $y$ , plotted on a logarithmic scale. The low peak lineal energies are observed between  $0.2 keV/\mu m$  and  $0.6 keV/\mu m$  with the higher  $y$ -values associated with smaller cavity sizes. The shoulder regions appear at around  $1 keV/\mu m$  where the electrons with ranges matching the simulated cavity sites and has a maximum value of  $y$ . The electron edge extends up to around  $10 keV/\mu m$  where it sharply descends indicating the maximum energies that can be imparted as a result of the very low energy electrons interactions. The experiment concerning the  $2 \mu m$  simulated target size was modeled in PENELOPE for its potential similarities to this experimental work. Table 5.5 compares the dose mean lineal energies  $\bar{y}_D$  values calculated for several photon energies ranging from  $12 keV$  to  $1250 keV$ .

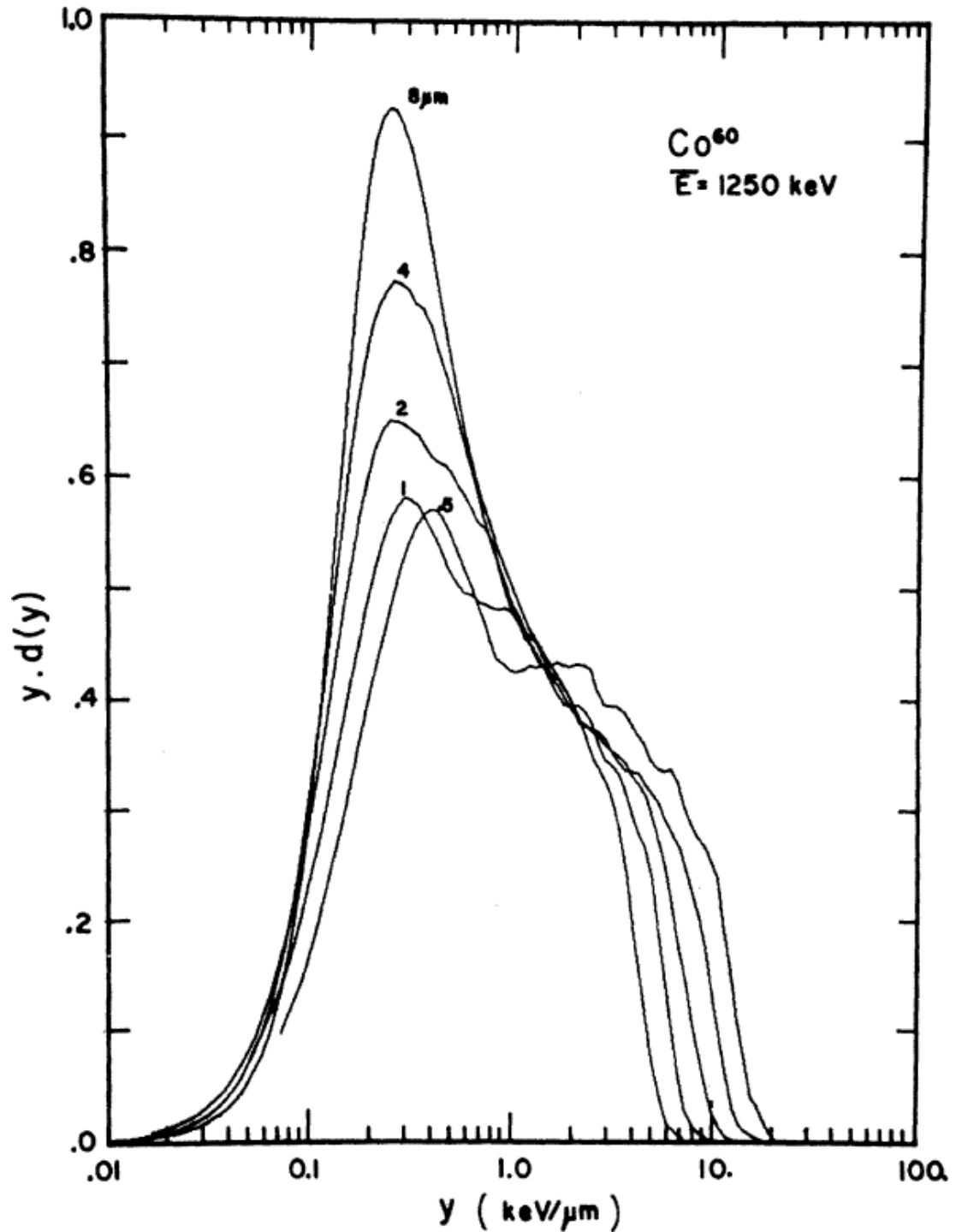


FIGURE 5.10: Kliauga and Dvorak Irradiated a 1 inch wall-less type TEPC with photons. These are the results of the distribution  $y d(y)$  as a function of  $y$ , for 1250keV  $^{60}\text{Co}$  photons at five simulated cavity sizes [18]. This investigation focused on the results around the 2  $\mu\text{m}$  simulated cavity size.



TABLE 5.5: A comparison of the values from Kliuaga and Dvorak's benchmark investigation and PENELOPE's simulation of an experiment at the  $2 \mu m$  simulated tissue site size, for eight monoenergetic photon beams. The random errors due to counting statistics are in parenthesis

Photon Energies, <i>keV</i>	KD Experiments, $2 \mu m$ site size $\bar{y}_D$	Penelope Simulation, $2 \mu m$ site size $\bar{y}_D$
1250	1.22	0.93 (0.14)
660	1.47	1.03 (0.02)
320	1.97	1.38 (0.08)
140	2.95	2.31 (0.04)
60	2.77	3.69 (0.11)
36	2.90	2.23 (0.07)
25	3.47	1.71 (0.10)
12	4.22	2.96 (0.05)

The results indicate that there is some agreement between the experimentally derived values for  $\bar{y}_D$  from Kliuaga and Dvorak (K-D) study and the simulated calculations by PENELOPE for each photon energy investigated. The standard errors calculated from the simulated  $\bar{y}_D$  values ranged from 2% to 14%, and there was no indication that lower or higher energies exhibited better confidence interval where values would overlap. PENELOPE in most of the simulated calculations for  $\bar{y}_D$  exhibited a lower value except for photons at 60 keV, having a random error of roughly 11%. The differences in Monte Carlo simulations and K-D determinations of  $\bar{y}_D$  at individual photon energies over a simulated cavity site of  $2 \mu m$  could be as a result of the simulation parameters chosen by the investigator. The materials and parameters of the K-D Wall-less TEPC experiment such as tissue equivalent gas, the counter materials and densities may not have been precisely modeled into PENELOPE. Stewart et. al.(2002) and Kyraiakou et. al.(2017) discussed in their work the careful considerations required to choose appropriate step length limits and parameters towards the energy losses occurring from hard and soft elastic and inelastic collisions within cell like volumes [49]

[56], and could account for some deviations. The accuracy of PENELOPE estimates can also be expected to decrease at smaller site sizes and at lower electron energy simulations [49]. A weighted dose distribution for 1250 keV photons in a 2  $\mu m$  simulated tissue site is illustrated in Figure 5.11 along with results for 60 keV and 660 keV photons. The microdosimetric quantity lineal energy,  $y$  ( $keV/\mu m$ ), for 1250 keV photons was calculated by PENELOPE to have a peak value of roughly 0.2  $keV/\mu m$ , with a similar peak value determined by K-D and illustrated in Figure 5.10. For 660 keV and 60 keV photons, similar  $y$ -values about 0.3  $keV/\mu m$  and 4.5  $keV/\mu m$  respectively were presented in the K-D study [18]. The normalized  $yd(y)$  curve in both the Monte Carlo simulation and the experimental K-D results appear to have similar shapes with the shoulder region and electron edge appearing around the same  $y$ -values. The dissimilarities in shape of the curves at 1250 keV for a 2  $\mu m$  cavity could be as a consequence of the simulation not including all the factors that lead to the resulting counter resolution (Figure 5.10) and therefore displays a more detailed (sharper) curve (Figure 5.11) than a measured spectrum. The results however indicated that the Monte Carlo code PENELOPE could produce reasonable and reproducible results towards predicting the responses of short ranged charged particle electrons from unknown sources that are potential hot particles, and would not be available for laboratory investigations.

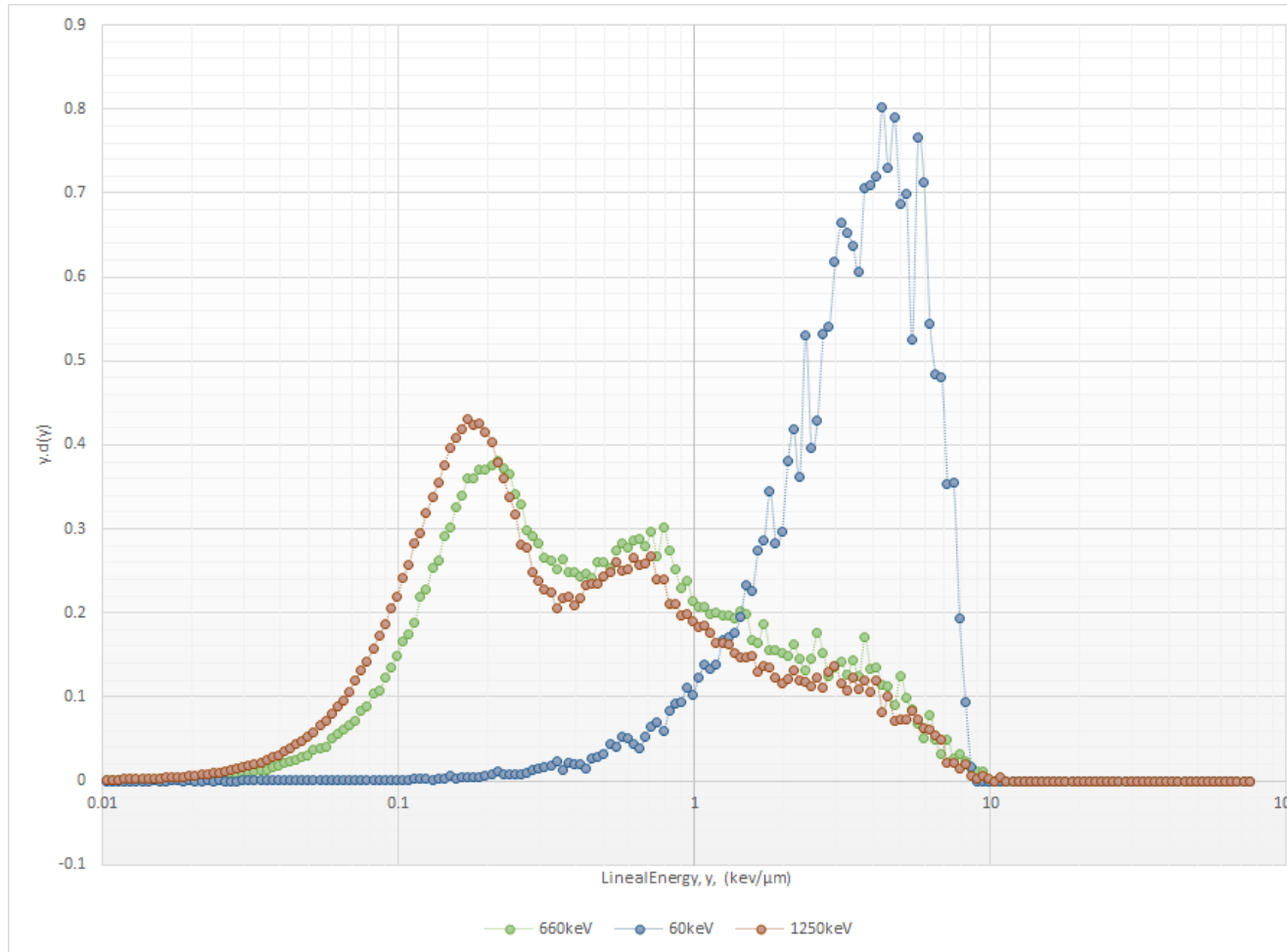


FIGURE 5.11: Monte Carlo calculations using PENELOPE resulting in the linear distribution  $yd(y)$  as a function of  $y$  (keV/ $\mu m$ ) on a logarithmic scale, for 1250, 660 and 60keV Photons in a 1 inch diameter wall-less TEPC benchmark experiment simulating a tissue cavity size of  $2 \mu m$ .

## 5.4 Monte Carlo Modeling for HP Dosimetry

In total six (6) beta particle emitting radionuclides were modeled using the Monte Carlo code PENELOPE:  ${}^3\text{H}$ ,  ${}^{14}\text{C}$ ,  ${}^{60}\text{Co}$ ,  ${}^{63}\text{Ni}$ ,  ${}^{177}\text{Lu}$  and  ${}^{90}\text{Sr}$ . The incident electrons in order of increasing average energies were 5.6, 17.4, 49.4, 96.5, 133.3 and 195.9  $\text{keV}$  respectively. Figure 5.12 illustrates the microdosimetric dose distribution  $yd(y)$  as a function of  $y$  on a logarithmic scale for six radionuclides at their varying energies. The simulated target tissue diameter is  $2\ \mu\text{m}$  and the source to counter or target simulated tissue distance is  $1\ \mu\text{m}$ . The chart shows clearly how the peak positions in the distribution are shifted depending on the electron energy of the beta particles. For low energy electrons below  $50\ \text{keV}$  PENELOPE calculations determined that peak  $y$ -values were greater than  $1\ \text{keV}/\mu\text{m}$  with electron edge values just above  $10\ \text{keV}/\mu\text{m}$ . For energies much greater than  $50\ \text{keV}$  peak  $y$ -values were at or below  $1\ \text{keV}/\mu\text{m}$ . These results are consistent with information presented by other investigators of dosimetric measurements of electrons using the microdosimetric method [18][53]. Monte Carlo calculations with PENELOPE for each individual radionuclide provided dose rate and quality variations over a fixed cavity diameter at different simulated tissue distance and are discussed in the sections that follow.

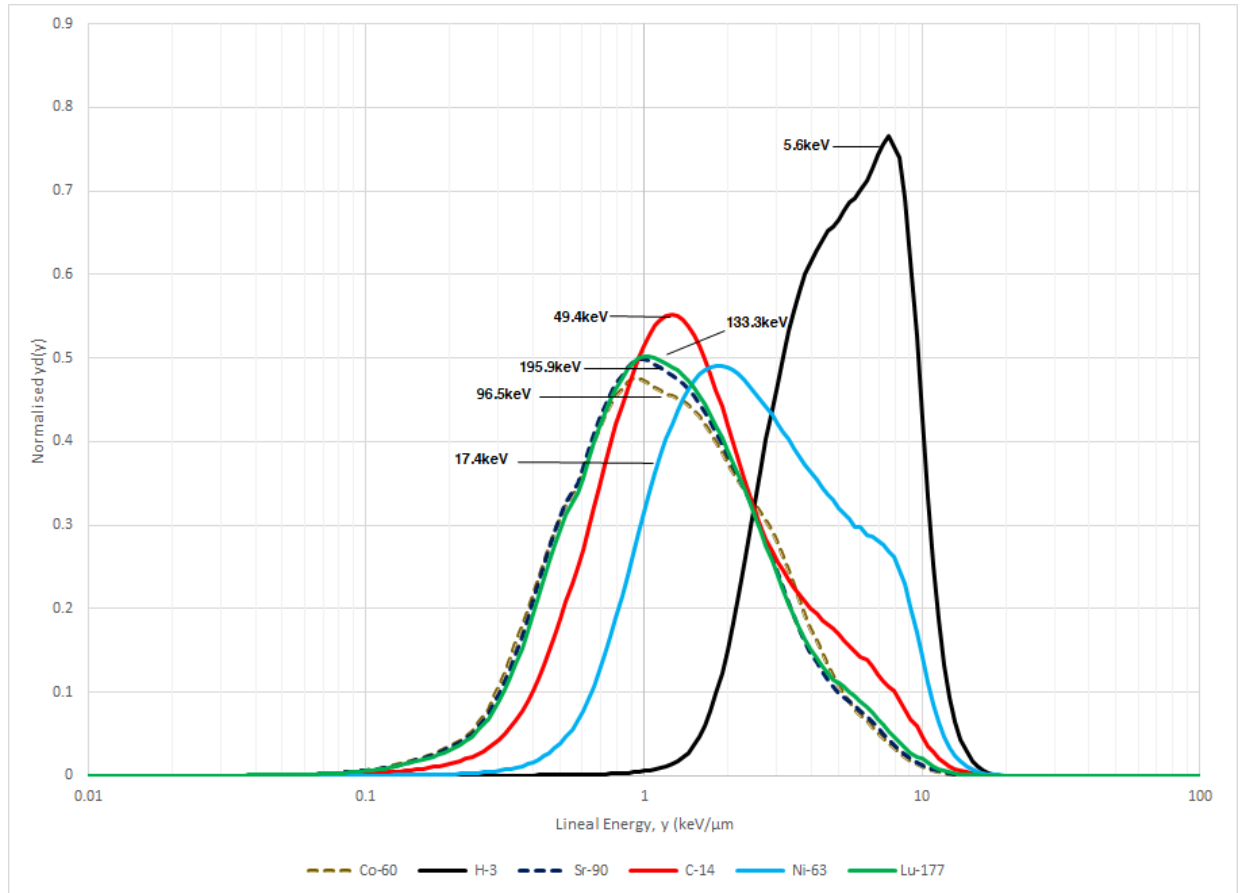


FIGURE 5.12: Fractional Absorbed Dose per Lineal Energy in a  $2 \mu\text{m}$  cavity site at a simulated Tissue Distance of  $1 \mu\text{m}$  away from Source, for 5 radionuclides simulating HPs, with average energies ranging from 5.6 keV to 196 keV. The microdosimetric distribution  $yd(y)$  is plotted as a function of  $y$  on a logarithmic scale.

Before this discussion however, it should be noted that the conical beam or SCONE parameter of the collimated beam for each radionuclide was taken into account with each simulated source to counter movement. Figure 5.13 is a schematic of the collimated beam at the outer edges of the simulated cavity with diameter  $2 \mu\text{m}$ , and illustrates the considerations made for the collimated source beam when it is pulled to a maximum distance away from the cavity's sensitive volume. At the edge of the cavity the beam is at a simulated tissue distance of 1

$\mu\text{m}$  away from the counter's anode wire and no angular determinations are necessary. When the source is pulled back a simulated tissue distance of  $3 \mu\text{m}$  the angle of the beam along the negative z-axis was calculated to be 18.4 degrees which PENELOPE recognizes as half the angle subtended for the electron beam falling inside the cavity. The investigator also examined an isotropic source geometry scenario. PENELOPE allows for the source parameter to be defined as an isotropic source, where the beam radiates in all directions. The SPOSIT parameter that gives the coordinates of the source was set to 90 degrees (half the angle subtended of  $\pi$  radians) and the SBOX parameter for the collimated source holder dimensions was defined for a 4 by 4 mm aperture. The beams in the opposite direction were not given any consideration, as they are angled away from the counter and are not expected to get the counter. This was an important discovery in the simulation process as the narrow angles provided reasonable information on  $\bar{y}_D$  and RBE variations, where as better results were determined for dose rate when the beam angle parameters was set for an isotropic source. The results presented are the microdosimetric quantities and RBE values calculated by PENELOPE for a step size limit of 0.02 and a secondary production cut of 250 eV for an isotropic source geometry with 180 degree angle beams in the direction of the negative z-axis.

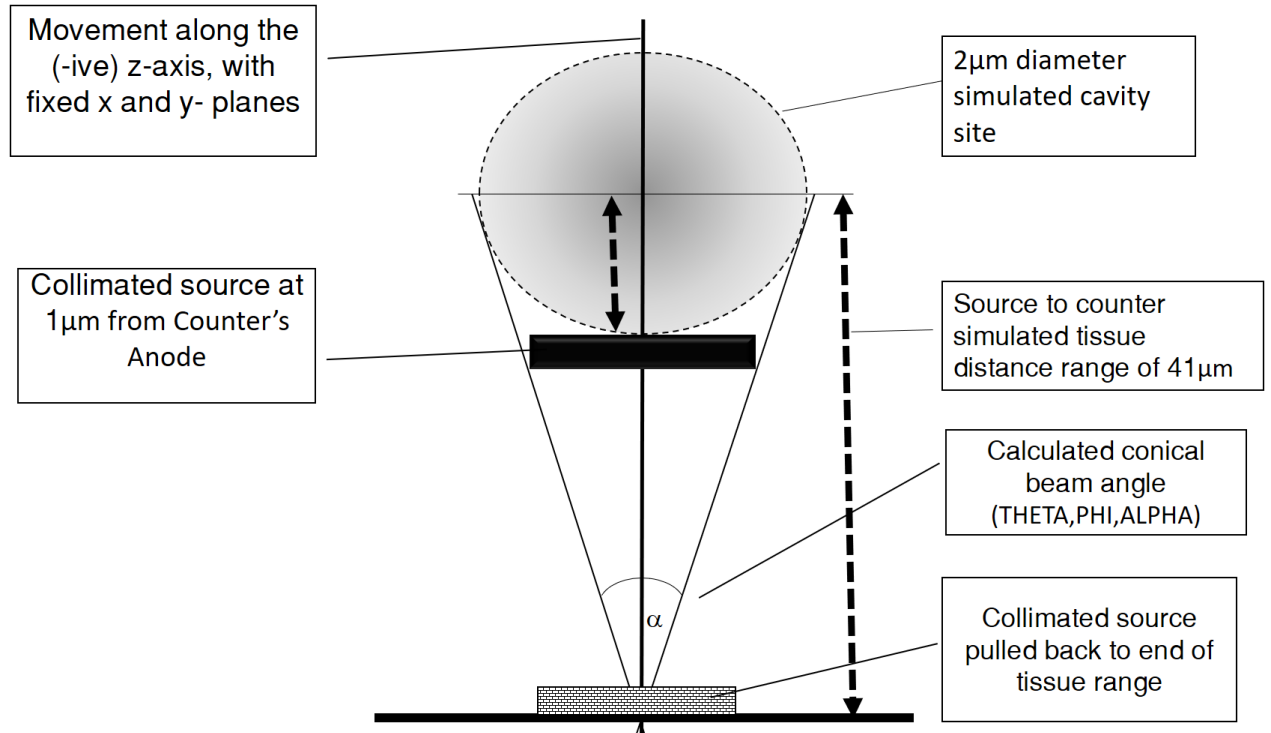


FIGURE 5.13: Schematic of the Source to Counter Simulated Tissue Distances for a  $2\mu\text{m}$  diameter simulated cavity size and the beam angle along the negative Z-axis

### 5.4.1 Monte Carlo Determination of $\bar{y}_D$ and RBE Values when Modeling the Wall-less TEPC with PENELOPE

The results presented in this section are the microdosimetric quantities and RBE values calculated by PENELOPE at a step size limit of 0.02 and a secondary production cut of 250 eV. These parameters were kept constant when defining the material simulation features in the transport code PENELOPE. As discussed earlier the step size limit value is the distance between hard elastic collisions and the production-cut specifies the cut off energies for the hard inelastic collisions and hard radiative transfer events specific to propane based tissue equivalent gas and tissue equivalent plastic. These values used were in the range of values recommended by Stewart et al. (PNNL, 2002) who investigated the properties of electrons in water when using PENELOPE for microdosimetry applications [49]. Table 5.6 summarizes the findings for electrons at various simulated tissue distances hitting a  $2 \mu m$  simulated tissue target with the source geometry parameter set for isotropic electron beams. In general the  $\bar{y}_D$  values increased with increasing simulated tissue distances away from the counter. The  $\bar{y}_D$  values for  $^3H$  overall were highest, and given that the range ( $1 \mu m$ ) of the average energies are less than the simulated target diameter, most of the energies are expected to deposit at higher stopping powers. Consequently, the RBE values were also slightly higher the further simulated electrons were away from the simulated counter. For all the radionuclide scenarios investigated with electron transport code PENELOPE, the average RBE values highlighted in red, Table 5.6, were calculated to be around 1, but less than 1.2. As observed in the previous experiment,  $\bar{y}_D$  and RBE values similarly increase as the source to target simulated tissue distances increase for each simulation.



TABLE 5.6: Microdosimetric values calculated by PENELOPE simulating isotropic sources emitting electrons at various tissue distances away from a 2  $\mu\text{m}$  diameter simulated target size model of the wall-less counter. The mean energy-range relationship for beta particles emitted from each radionuclide are in parentheses.

Simulated Source-Counter Distance ( $\mu\text{m}$ )	${}^3\text{H}$ (5.6keV, 1 $\mu\text{m}$ ) $\bar{y}_D$ , (keV/ $\mu\text{m}$ )	RBE	${}^{63}\text{Ni}$ (17.4keV, 6.5 $\mu\text{m}$ ) $\bar{y}_D$ , (keV/ $\mu\text{m}$ )	RBE	${}^{14}\text{C}$ (49.4keV, 42 $\mu\text{m}$ ) $\bar{y}_D$ , (keV/ $\mu\text{m}$ )	RBE	${}^{60}\text{Co}$ (96.5keV, 139.5 $\mu\text{m}$ ) $\bar{y}_D$ , (keV/ $\mu\text{m}$ )	RBE	${}^{177}\text{Lu}$ (113.3keV, 275.2 $\mu\text{m}$ ) $\bar{y}_D$ , (keV/ $\mu\text{m}$ )	RBE	${}^{90}\text{Sr}$ (195.9keV, 439 $\mu\text{m}$ ) $\bar{y}_D$ , (keV/ $\mu\text{m}$ )	RBE
1.00	4.47	1.00	3.07	1.00	2.15	1.00	1.57	1.00	1.69	1.00	1.61	1.00
2.20	4.50	1.01	3.13	1.02	-	-	-	-	-	-	-	-
2.40	4.52	1.01	3.17	1.03	-	-	-	-	-	-	-	-
2.60	4.53	1.01	3.21	1.05	-	-	-	-	-	-	-	-
2.80	4.51	1.01	3.23	1.05	-	-	-	-	-	-	-	-
3.00	4.49	1.00	3.23	1.05	2.29	1.06	1.62	1.03	1.76	1.04	1.67	1.03
3.20	4.58	1.02	-	-	-	-	-	-	-	-	-	-
3.40	4.73	1.06	3.46	1.13	-	-	-	-	-	-	-	-
3.60	4.82	1.08	3.56	1.16	-	-	-	-	-	-	-	-
4.40	5.03	1.12	-	-	-	-	-	-	-	-	-	-
5.00	5.10	1.14	3.74	1.22	2.69	1.25	1.90	1.21	2.10	1.24	1.93	1.20
7.00	4.89	1.09	3.70	1.20	2.61	1.22	-	-	2.11	1.25	-	-
9.00	4.04	0.90	3.63	1.18	2.59	1.21	1.96	1.25	2.07	1.23	2.00	1.24
11.00	-	-	-	-	2.51	1.17	-	-	1.76	1.04	-	-
13.00	-	-	3.69	1.20	-	-	1.96	1.26	2.14	1.26	2.03	1.26
15.00	-	-	3.65	1.19	-	-	-	-	2.10	1.24	-	-
17.00	-	-	3.61	1.18	2.50	1.16	1.98	1.27	2.12	1.26	1.99	1.24
19.00	-	-	-	-	-	-	-	-	2.08	1.23	-	-
21.00	-	-	3.72	1.21	2.53	1.18	1.95	1.25	2.10	1.24	1.99	1.23
23.00	-	-	-	-	-	-	-	-	2.06	1.22	-	-
25.00	-	-	2.96	0.96	2.53	1.18	1.95	1.24	2.06	1.22	2.00	1.24
27.00	-	-	-	-	-	-	-	-	2.01	1.19	-	-
29.00	-	-	4.30	1.40	2.49	1.16	1.64	1.05	1.60	0.95	2.06	1.28
31.00	-	-	-	-	-	-	-	-	2.07	1.23	-	-
33.00	-	-	3.54	1.15	2.63	1.23	1.94	1.24	2.17	1.28	1.77	1.10
35.00	-	-	-	-	-	-	-	-	1.79	1.06	-	-
37.00	-	-	3.81	1.24	1.95	0.91	1.94	1.24	1.62	0.96	1.90	1.18
39.00	-	-	-	-	-	-	-	-	2.19	1.30	-	-
41.00	-	-	4.54	1.48	2.75	1.28	1.88	1.20	2.32	1.37	1.47	0.91
Average	-	-	-	-	-	-	-	-	-	-	-	-

1.04      1.16      1.15      1.19      1.18      1.16

These findings compare well with RBE determinations from another Monte Carlo code NOREC (New Oak Ridge Electron transport Code). NOREC is an interaction by interaction simulator showing improvements to the Oak Ridge Electron transport Code (OREC) developed by Turner et al., (1998). RBE values similarly were around 1 for select beta emitting radionuclides with the exception of  $^3H$  which had an RBE determination of about 2 [64]. The values in both work show slight differences given PENELOPE simulated a spectrum of energies, which had non-monoenergetic particles at any given point, and a lower cut off energy of 250 eV. Conversely, the NOREC investigators declared a cut off energy of 5 keV for each radionuclide examined. The maximum range of electrons in propane based tissue equivalent gas is approximately 6.5  $\mu m$  for  $^3H$  electrons, so events beyond the maximum range were ignored. Observed  $\bar{y}_D$  and RBE values also appear to decrease beyond the maximum range as indicated by the values in Table 5.6.

Figures 5.14, 5.15, and 5.16 all illustrate dose rates per electron shower on the y-scale as a function of the simulated source to counter tissue distances on the x-scale for six scenarios of beta emitting radionuclides simulating a hot particle. With a cut off energy between hard inelastic collisions specified as 250 eV simulating low energy short ranged beta particles in each model the dose rates all appear to sharply decrease. As discussed earlier in Section 5.2.2 beta particles having limited ranges produce steep dose gradients, and these findings were also supported by the PENELOPE simulations in each scenario.

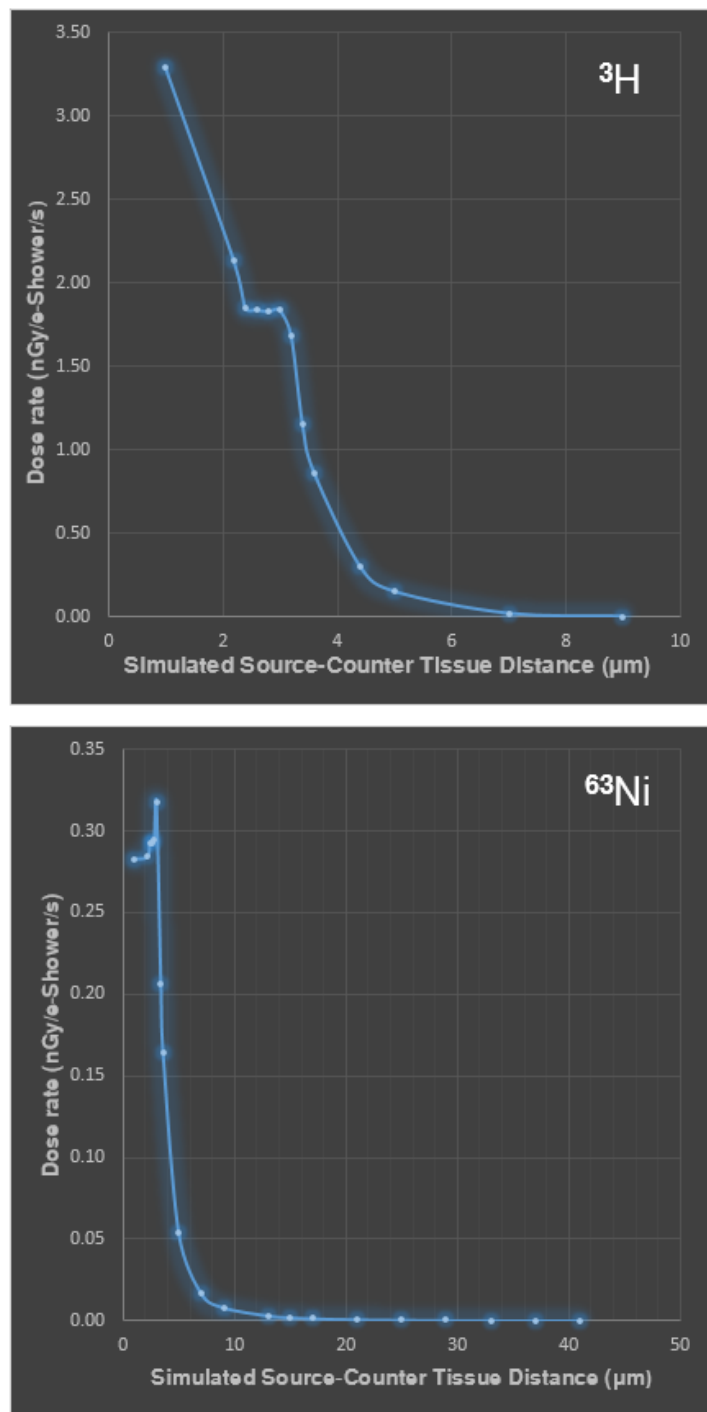


FIGURE 5.14: Dose Rates in nano-Grays per electron Shower per Second are modeled as a Variation of the Simulated Source to Counter Tissue distances for  $^3\text{H}$  and  $^{63}\text{Ni}$  in a  $2\mu\text{m}$  diameter tissue cavity for simulation parameters with a step length of 0.02 and a cut off energy of 250eV for 20 million electron showers.

In Figure 5.14, PENELOPE estimated dose rate values approach zero at a maximum range of  $7 \mu m$ , for beta particles associated with  ${}^3H$  and  $13 \mu m$  for particles from  ${}^{63}Ni$ , having relatively lower average electron energies between  $5 keV$  and  $17 keV$  respectively. For  ${}^{14}C$  the average energies are higher around  $50 keV$  and dose rate intensities approached zero at further distances away around  $25 \mu m$ , as displayed on the top of Figure 5.15. Below  $50 keV$  average electron energies, PENELOPE indicated beta particles have a finite range, and beyond a certain distance the dose rate per electron shower approaches zero. The curve at the bottom of Figure 5.15 for  ${}^{60}Co$  and also the curves in Figure 5.16 illustrate steep dose gradients, however the longer ranges associated with these electrons do not allow them to approach zero with PENELOPE not simulating distances beyond  $41 \mu m$  as instructed.

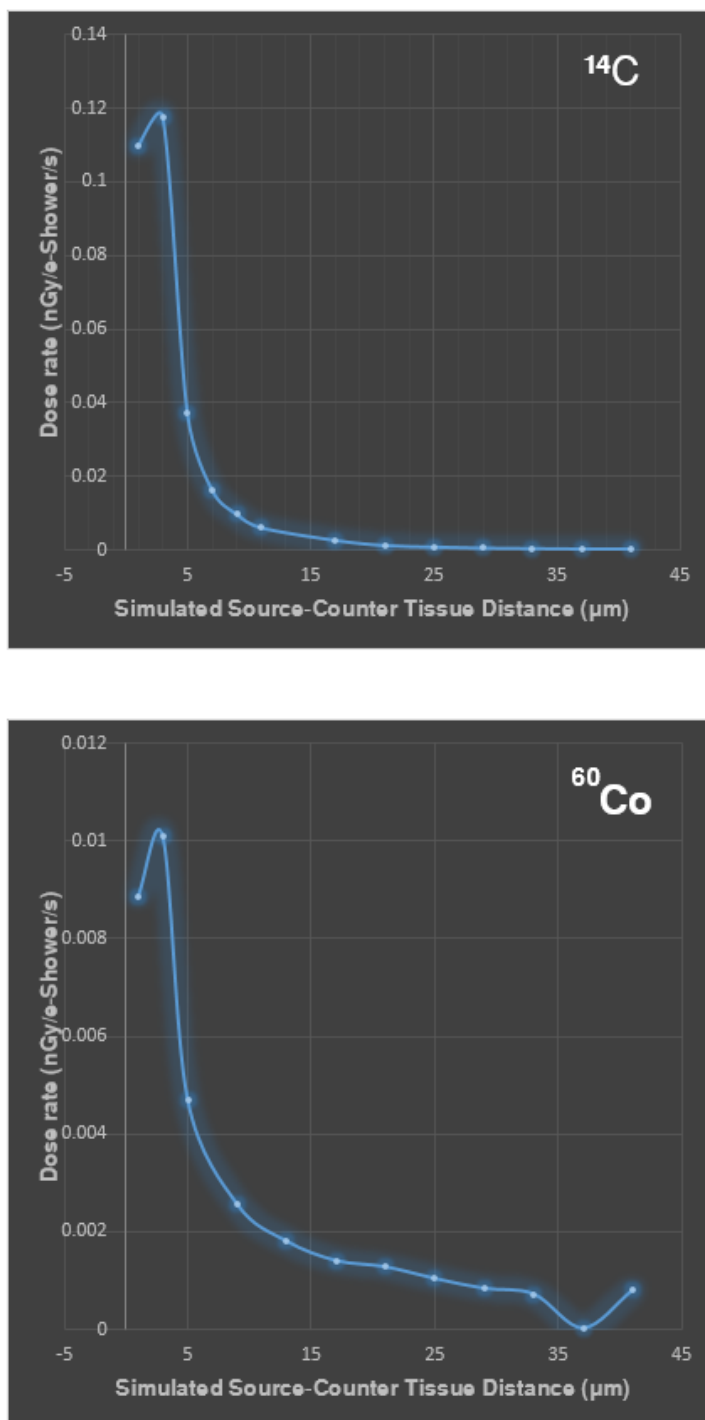


FIGURE 5.15: Same as Figure 5.14 but for  $^{14}\text{C}$  and  $^{60}\text{Co}$  in a  $2\ \mu\text{m}$  diameter tissue cavity for simulation parameters with a step length of 0.02 and a cut off energy of 250 eV for 20 million electron showers

---

With the exception of  $^3H$ , each dose rate chart as a function of simulated tissue distance clearly shows an increase in dose rate over a  $2 \mu m$  to  $3 \mu m$  tissue distance followed by a sharp decrease. This is explained by the average energy of the electron having a range matching the simulated cavity size and the stopping power is believed to be at a maximum at this range. Similar to the effect of the shoulder in a microdosimetric spectra. The plateauing effect observed for the  $^3H$  dose rate curve resulted from the associated beta particles having a lower range around one half of the diameter of the simulated cavity size, hence most of the lower energy particles are not able to cross  $2 \mu m$  as the simulated source to counter tissue distances increase.

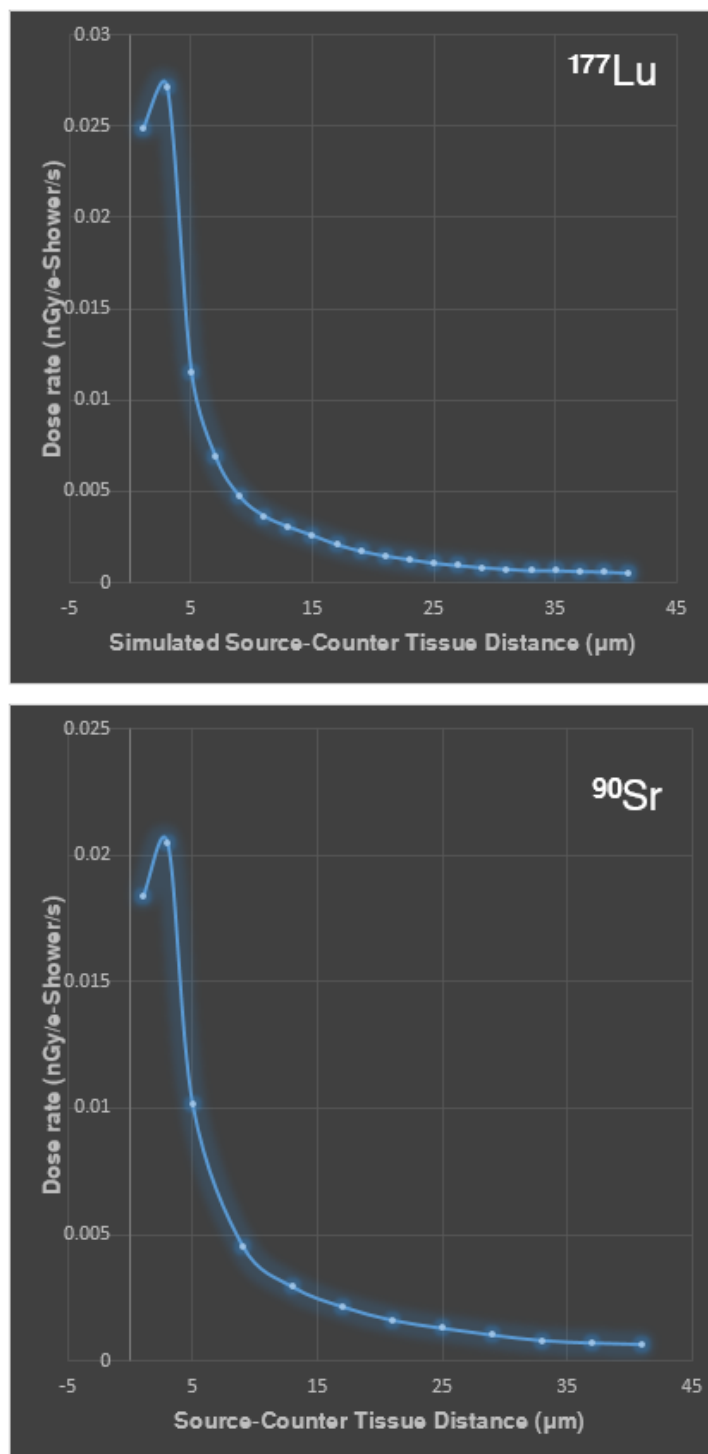


FIGURE 5.16: Same as Figure 5.14 but for  $^{177}\text{Lu}$  and  $^{90}\text{Sr}$  in a 2  $\mu\text{m}$  diameter tissue cavity for simulation parameters with a step length of 0.02 and a cut off energy of 250 eV for 20 million electron showers.

The corresponding microdosimetric distribution  $yd(y)$  of the dose-weighted lineal energy spectra for each hot particle source scenario was also investigated, comparing the fraction of absorbed dose delivered at various tissues distances away from the counter's cavity per logarithmic interval of lineal energy,  $y$ . The results are plotted on a linear y-scale and a logarithmic x-scale after normalization with individual average values each corresponding to  $\bar{y}_D$  a measurement of the radiation quality (Table 5.6). Regarding the microdosimetric spectra in Figures 5.17 and 5.18, sharp vertical peaks exist at lineal energies between  $2 \text{ keV}/\mu\text{m}$  and  $8 \text{ keV}/\mu\text{m}$ . Beta particles associated with  ${}^3\text{H}$  and  ${}^{63}\text{Ni}$  will have lower electron energies below 18 keV and their associated transit ranges are relatively short,  $< 7\mu\text{m}$ . If we compare these lower energy spectra with those in Figures 5.19 to 5.22 the higher peak  $y$ -values would suggest that  ${}^3\text{H}$  and  ${}^{63}\text{Ni}$  have relatively higher RBE values around this electron energy and below a certain range.



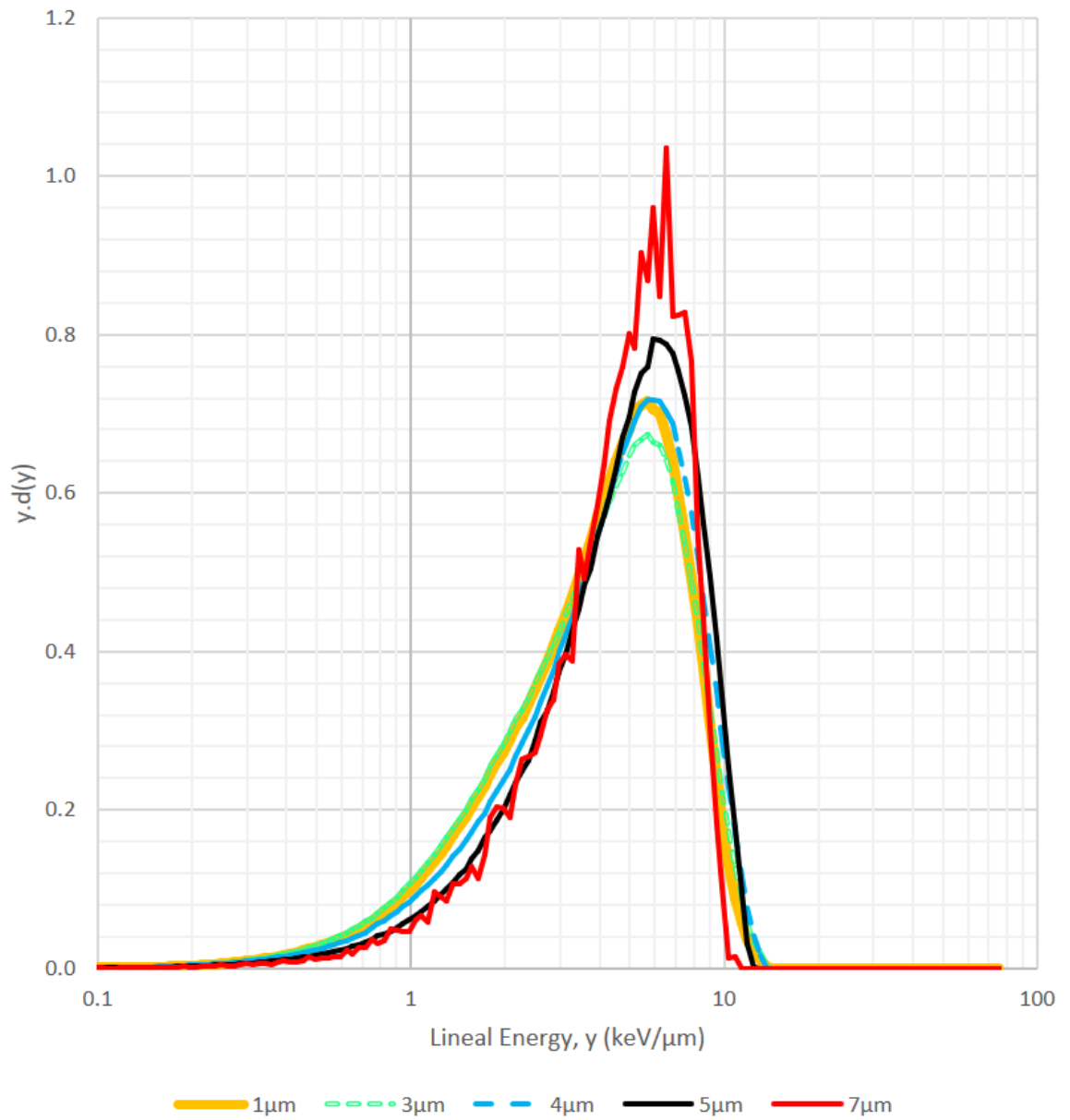


FIGURE 5.17: Microdosimetric dose distributions  $y d(y)$  as a function of lineal energy,  $y$ , calculated by PENELOPE for non-monoenergetic beta particles of  ${}^3\text{H}$  entering a simulated  $2 \mu\text{m}$  cavity site. Simulation parameters were set for a cut off energy of 250 eV for  $2 \times 10^7$  electron showers.

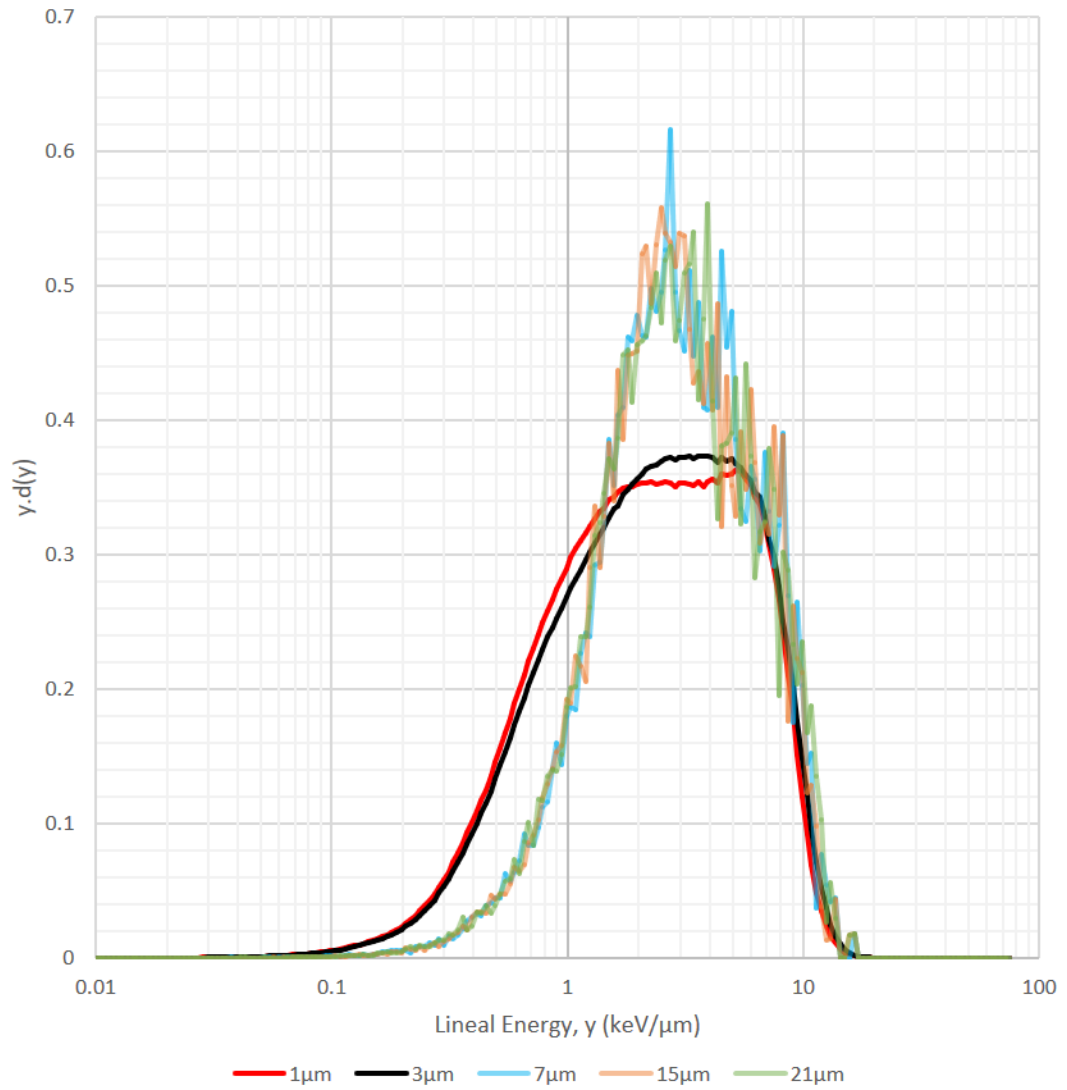


FIGURE 5.18: Microdosimetric dose distributions  $y d(y)$  as a function of lineal energy,  $y$ , calculated by PENELOPE for non-monoenergetic beta particles of  $^{63}\text{Ni}$  entering a simulated  $2 \mu\text{m}$  cavity site. Simulation parameters were set for a cut off energy of 250 eV for  $2 \times 10^7$  electron showers.

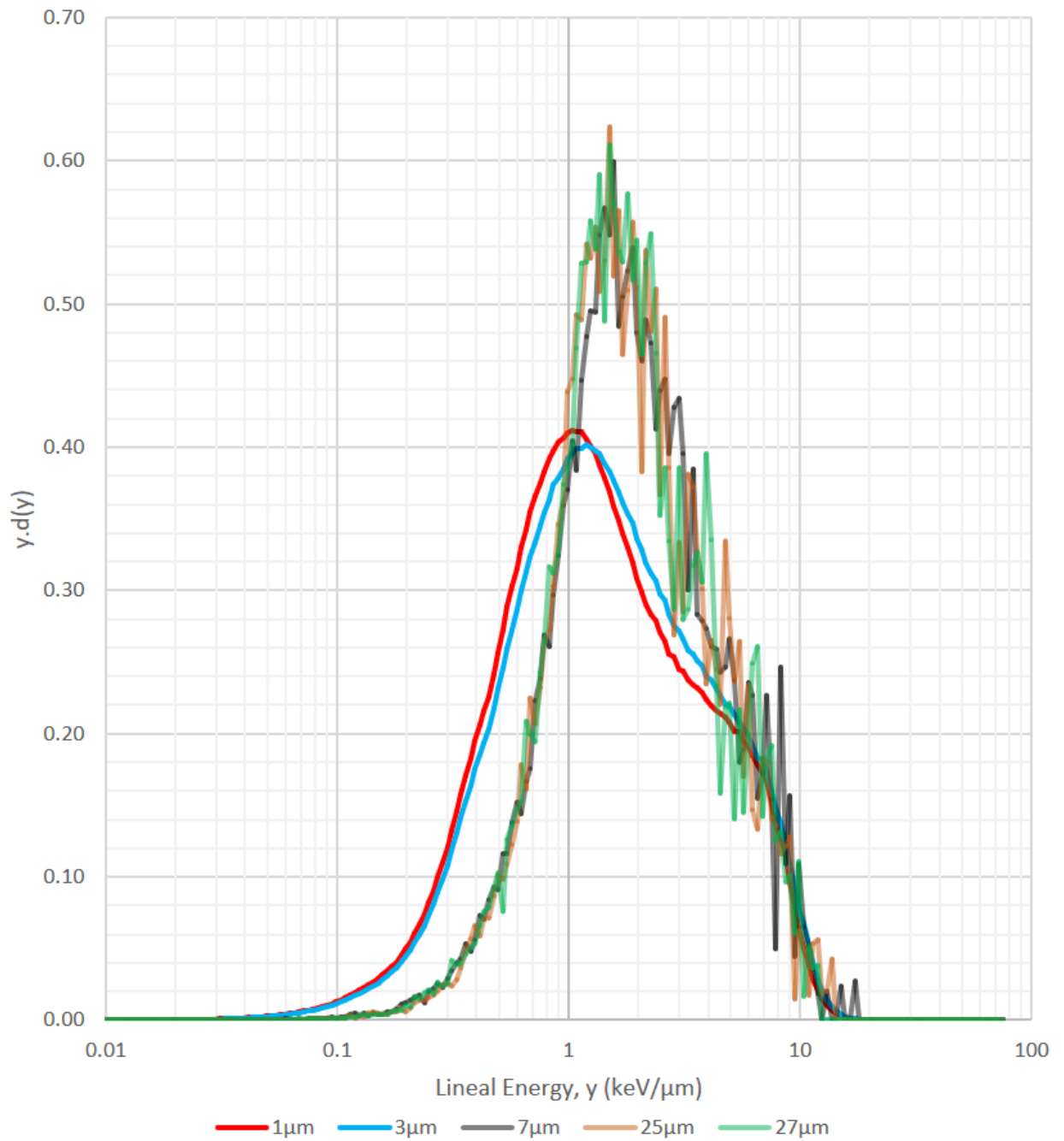


FIGURE 5.19: Microdosimetric dose distributions  $yd(y)$  as a function of lineal energy,  $y$  calculated by PENELOPE for non-monoenergetic beta particles of  $^{14}\text{C}$  entering a simulated  $2 \mu\text{m}$  cavity site. Simulation parameters were set for a cut off energy of 250 eV for  $2 \times 10^7$  electron showers.

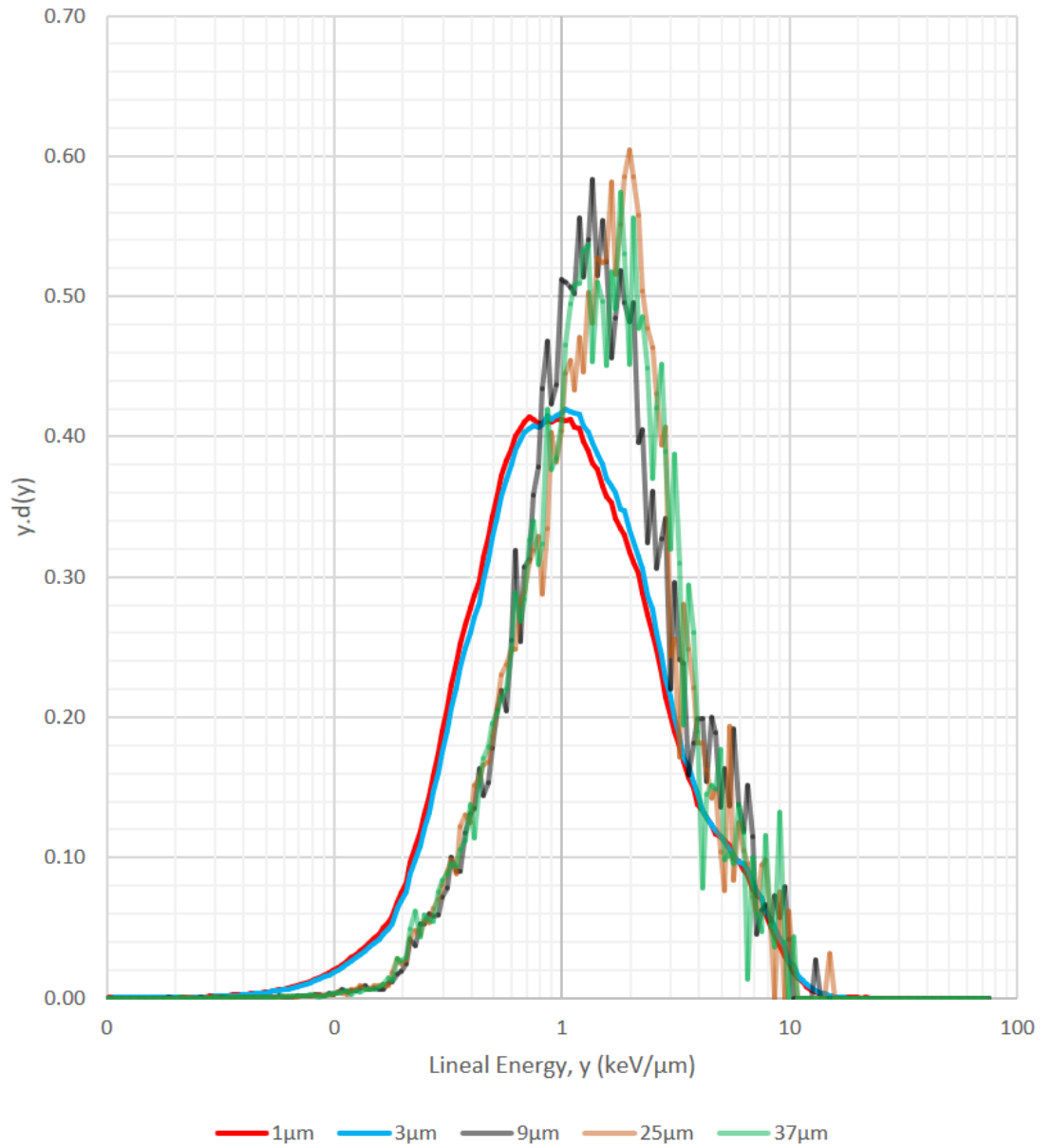


FIGURE 5.20: Microdosimetric dose distributions  $y d(y)$  as a function of lineal energy,  $y$  calculated by PENELOPE for non-monoenergetic beta particles of  $^{60}\text{Co}$  entering a simulated  $2\mu\text{m}$  cavity site. Simulation parameters were set for a cut off energy of  $250\text{eV}$  for  $2 \times 10^7$  electron showers.

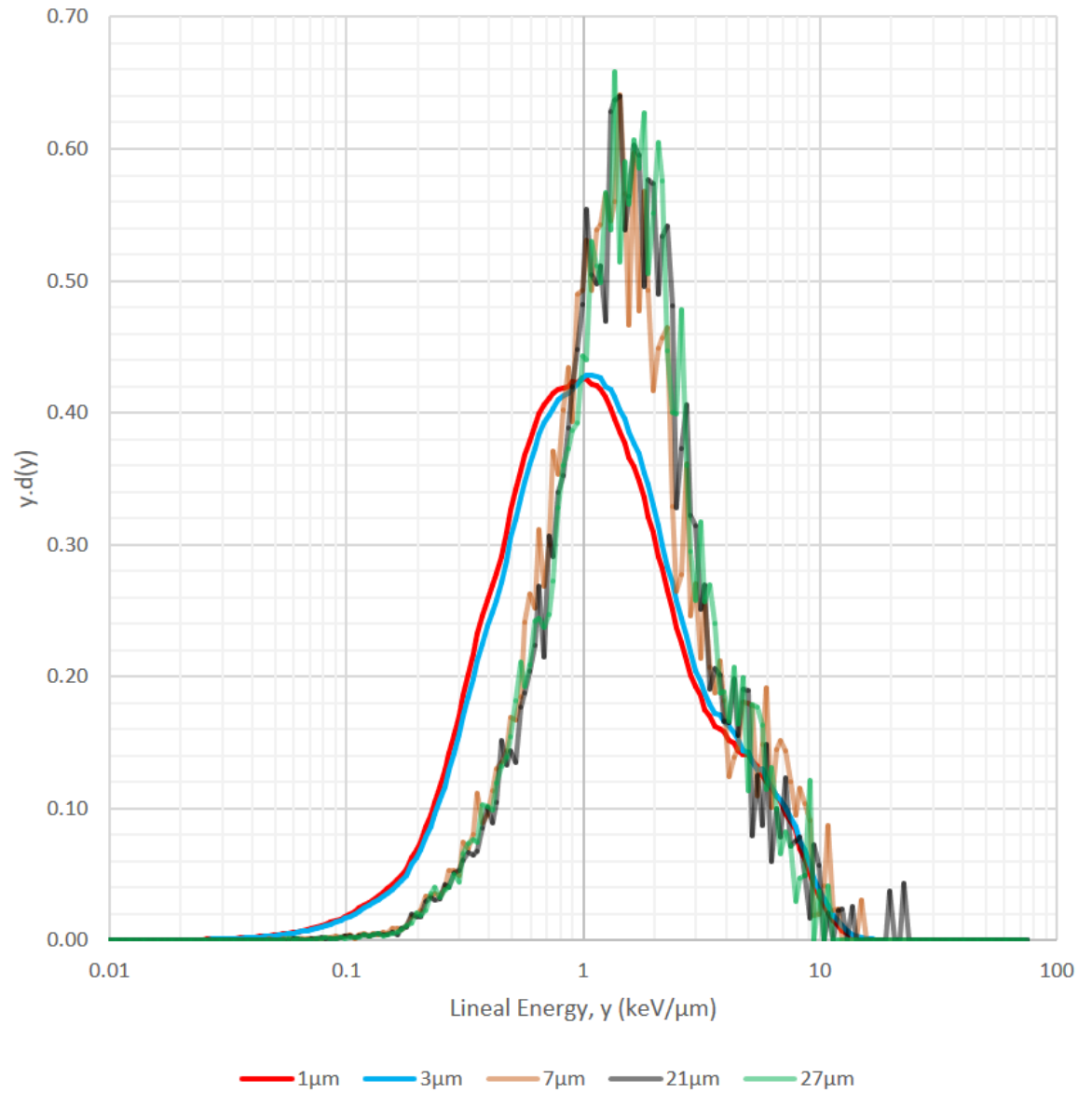


FIGURE 5.21: Microdosimetric dose distributions  $yd(y)$  as a function of lineal energy,  $y$  calculated by PENELOPE for non-monoenergetic beta particles of  $^{177}\text{Lu}$  entering a simulated  $2 \mu\text{m}$  cavity site. Simulation parameters were set for a cut off energy of 250 eV for  $2 \times 10^7$  electron showers.

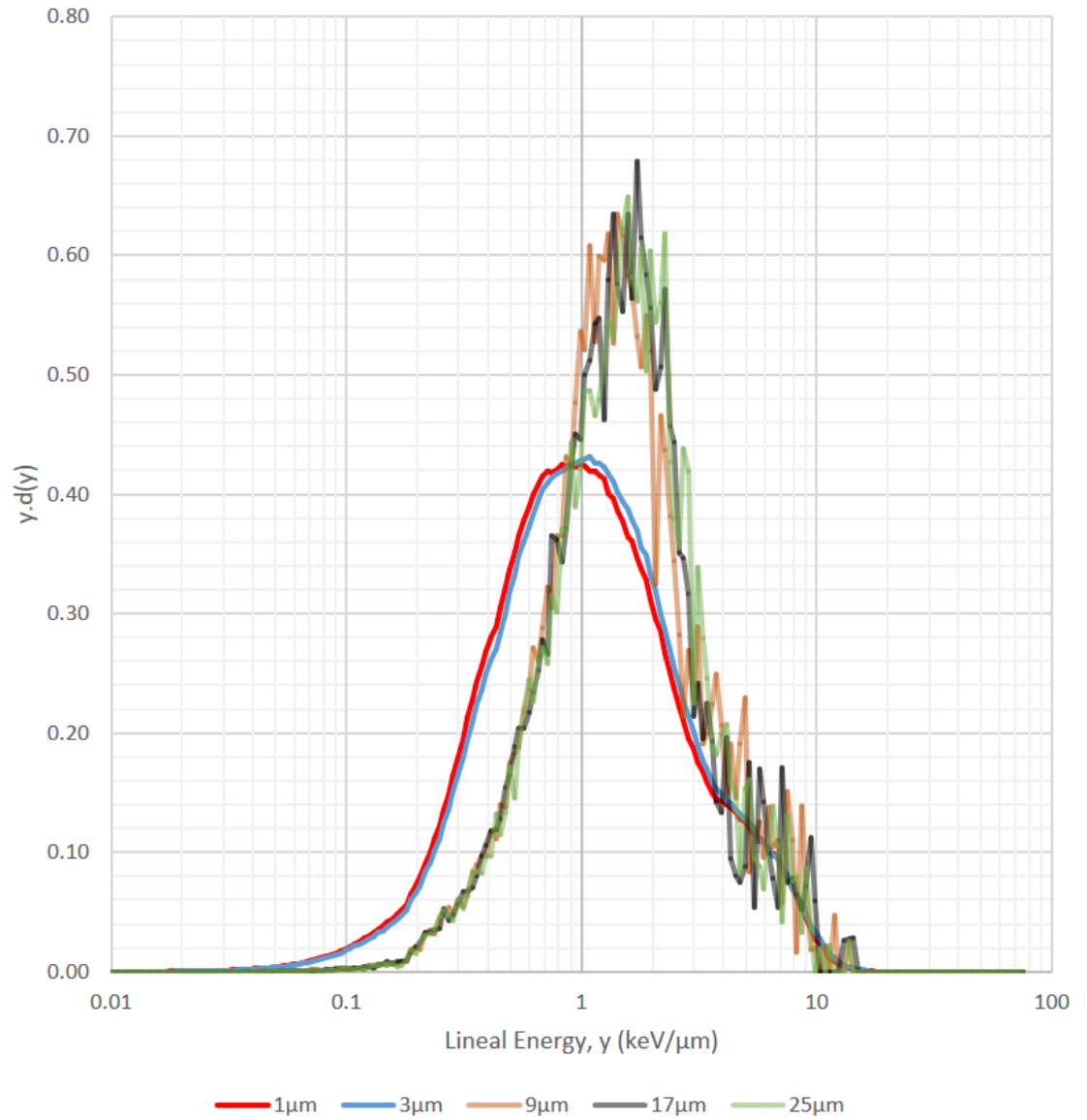


FIGURE 5.22: Microdosimetric dose distributions  $y d(y)$  as a function of lineal energy,  $y$  calculated by PENELOPE for non-monoenergetic beta particles of  $^{90}\text{Sr}$  entering a simulated  $2\mu\text{m}$  cavity site. Simulation parameters were set for a cut off energy of 250 eV for  $2 \times 10^7$  electron showers.

Peak shapes were relatively similar for  ${}^3H$  over several simulated tissue distances. For  ${}^{63}Ni$ , the peaks varied in dose weighted fractions over roughly the same peak lineal energy,  $3\text{ keV}/\mu\text{m}$ , but differed in shape as the simulated source to counter tissue distances were varied above  $7\mu\text{m}$ . As simulated source to counter tissue distances increased it was also observed that for higher energy electrons with relatively longer ranges a distinct separation in peak shape developed. For electrons at a simulated source to counter tissue distances of  $1\mu\text{m}$  to  $3\mu\text{m}$  the simulation indicated lower lineal energy values of about  $1\text{ keV}/\mu\text{m}$  for  ${}^{14}C$  (Figure: 5.19),  ${}^{60}Co$  (Figure: 5.20),  ${}^{177}Lu$  (Figure: 5.21) and  ${}^{90}Sr$  (Figure: 5.22). Slightly higher  $y$ -values,  $< 2\text{ keV}/\mu\text{m}$ , were noticed above simulated source to counter tissue distances in the range of  $7\mu\text{m}$  to  $37\mu\text{m}$ .

## 5.5 A Comparison of Experimental Measurements with Monte Carlo simulations

Investigation of the design and construction of the wall-less TEPC achieved the objective of allowing low energy short ranged beta particle interactions that otherwise would not be able to penetrate and enter the gas cavity of a regular walled TEPC. The results presented in Sections 5.2.1, 5.2.2 and 5.2.3 indicated that the current architecture was adequate to calibrate, and calculate microdosimetric quantities of  $\bar{y}_D$  and provide an estimate of the RBE. PENELOPE models for the transport of electrons within the parameters of this investigation also provided some useful information when source configurations were set to an isotropic geometry, and cut off parameters for hard inelastic and elastic collisions are placed at reasonable values. In this section a comparison of the findings from the experimental measurements and the Monte Carlo simulations generated by PENELOPE using the condense history approach for isotropic electron beams are presented.

### 5.5.1 $^{63}\text{Ni}$ and $^{14}\text{C}$ Experimental Results compared with PENELOPE Calculations

The sets of simulation and experimental measurement compared in Figures 5.23 and 5.24 overall illustrates good agreement between microdosimetric spectra. In Figure 5.23 (A)-(C) for the  $^{63}\text{Ni}$  scenario, the curves for the simulation skew more to the right having higher peak lineal energy values as source to counter tissue distances increase to around  $7\ \mu\text{m}$ . Experimental measurements exhibit lower  $y$ -values at  $1\ \text{keV}/\mu\text{m}$  around the same tissue distances, and indicate that more low energy particles are available in the simulation than the experiment shows. At distances around  $7\ \mu\text{m}$  however, which is the average range for beta particles in TE gas for  $17.4\ \text{keV}$   $^{63}\text{Ni}$  electrons, the behavior changes. In Figure 5.23 (D) both curves indicate spurious readings around the electron edge at



---

10  $keV/\mu m$  and indicate very low energy beta particles. In a realistic measurement situation more low energy particles are expected than in a simulated environment. However, in Figure 5.24 these very low energy electrons also appear at the electron edge above 10  $keV/\mu m$  in the scenario comparing  $^{14}C$  spectra. The sharp cut off experienced for each of the experimental curves was a result of the limits of detection set in the counter's MCA electronics, and indicate that larger pulses could also be available for detection outside these limits.

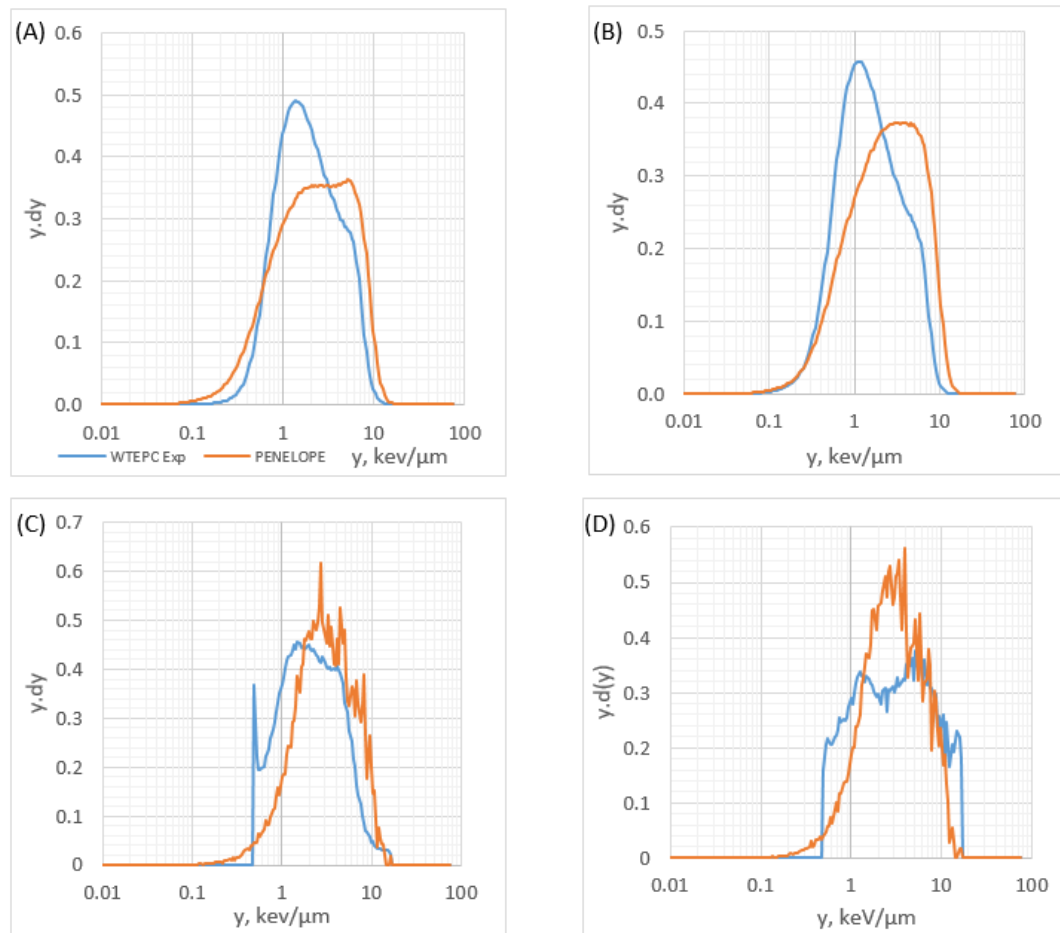


FIGURE 5.23: Comparison of the Monte Carlo Simulation with the WTEPC experiment for Fractional Absorbed Dose per Lineal Energy in a  $2 \mu\text{m}$  site at simulated tissue distances: (A)  $1 \mu\text{m}$ , (B)  $3 \mu\text{m}$ , (C)  $7 \mu\text{m}$  and (D)  $21 \mu\text{m}$  away from a  ${}^{63}\text{Ni}$  source. The curves with blue legend illustrates results generated from the WTEPC experiment, and the orange legend the Monte Carlo code PENELOPE output simulation results at the same source to counter tissue distances. The area under the curves delimited by values of lineal energies,  $y$ , corresponds to the fraction of absorbed dose presented as a distribution on a logarithmic horizontal axis for  $y$ , and linear  $yd(y)$  on the vertical axis.

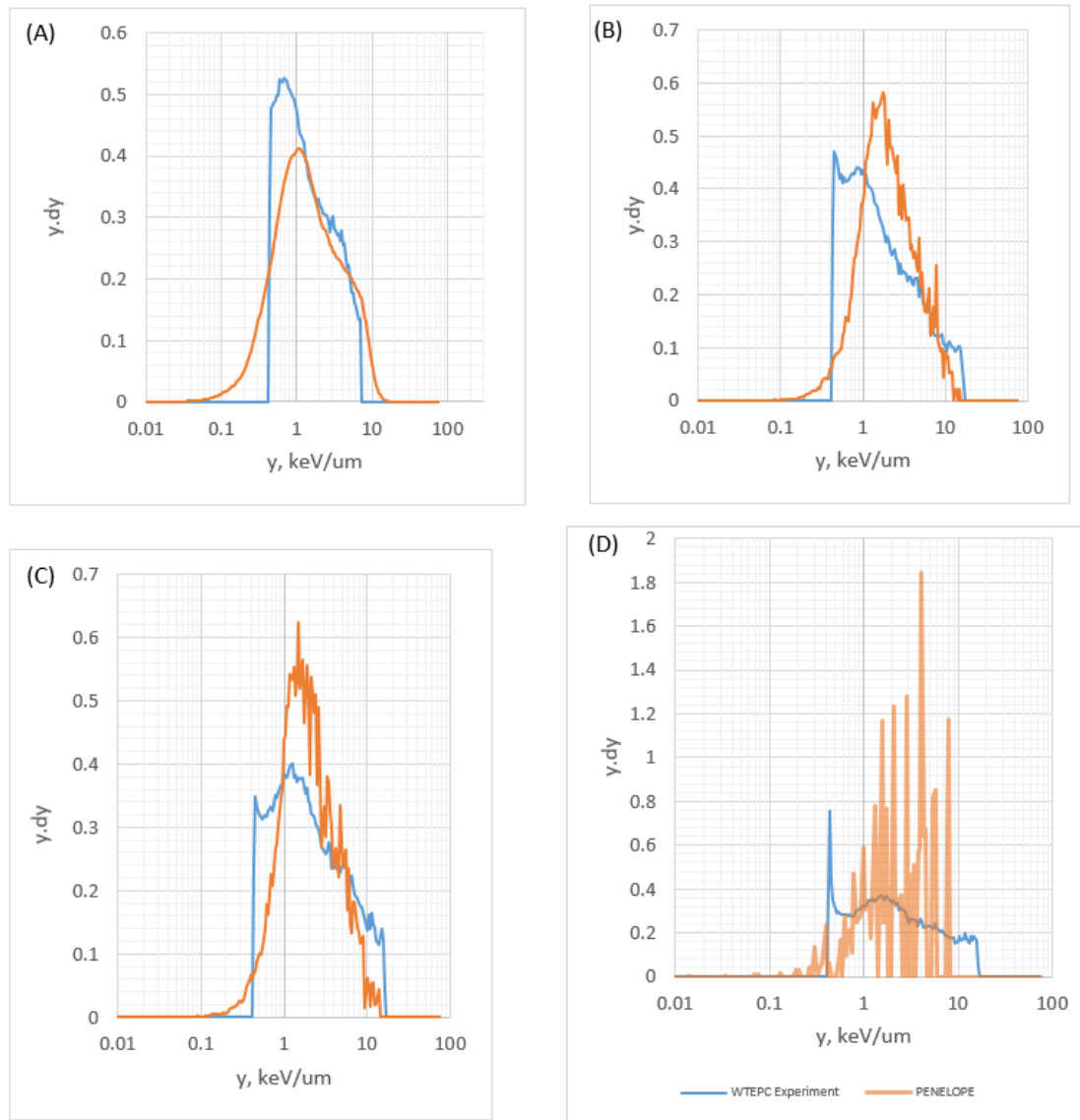


FIGURE 5.24: Comparison of the Monte Carlo Simulation with the WTEPC experiment for Fractional Absorbed Dose per Lineal Energy in a  $2 \mu\text{m}$  site at simulated tissue distances: (A)  $1 \mu\text{m}$ , (B)  $9 \mu\text{m}$ , (C)  $25 \mu\text{m}$  and (D)  $41 \mu\text{m}$  away from a  $^{14}\text{C}$  source. The curves with blue legend illustrates the results generated from the WTEPC experiment, and the orange legend the Monte Carlo code PENELOPE output simulation results at the same source to counter tissue distances. The area under the curves delimited by values of lineal energies,  $y$ , corresponds to the fraction of absorbed dose presented as a distribution on a logarithmic horizontal axis for  $y$ , and linear  $yd(y)$  on the vertical axis.

From this investigation the consistent difference between simulation and experiment was that the simulations saw more higher lineal energy event-sizes than the experimental measurements showed. This could be related to the actual source geometry, whereby the experimental sources were real with an actual structure that was not completely simulated by PENELOPE. The 4 mm collimated aperture and constructed source holder encapsulating the radioactive materials may have absorbed a portion of the low energy electron that ultimately would not get to the counter. Consequently, the effect becomes less of an issue indicating the overlap of simulation and experiment at longer source to counter simulated tissue distances. Both experiment and simulation presented similar results giving rise to some confidence in the use of PENELOPE to determine microdosimetric quantities in situations where the source cannot be measured using a classical dosimeter.

In summary, this chapter presented the Wall-less TEPC's response to the calibration source,  $^{241}\text{Am}$ , and the experimental sources  $^{63}\text{Ni}$  and  $^{14}\text{C}$ . Both experiment and simulation indicate an increase in biological effectiveness for low energy electrons, as source to target tissue distances are increased. Steep dose gradients were observed from low energy beta particles beams as dose rates decreased across tissue like distances. The Monte Carlo electron transport code PENELOPE proved to be a suitable computational tool for calculating microdosimetric quantities, and dose rate variations at microscopic sizes for low energy short ranged charged particles. Operated in the microdosimetric mode, the Wall-less TEPC showed the advantages in quantifying the impact of hot particles. Both absorbed dose rate and radiation quality measurements over tissue like dimensions were measured.

## Chapter 6

# Conclusions and Future Work

The objectives of this work were to investigate how absorbed dose rate and radiation quality varies with distance in tissue from a low-energy beta particle source, therefore contributing to our understanding of the potential biological impact of a hot particle (HP) contaminant. Through experimental measurements and calculations by means of Monte Carlo simulations several values for absorbed dose and dose mean lineal energies ( $\bar{y}_D$ ) at various source to target simulated tissue distances were determined, for various beta particle source scenarios simulating a HP. The experimental results demonstrated that the stochastic microdosimetric quantities lineal energy ( $y$ ) and  $\bar{y}_D$  for short ranged, low energy beta particles in microscopic regions increased with increasing source to counter simulated tissue distances. The  $\bar{y}_D$  values increased gradually as the source-target tissue distances increased, indicating a change in radiation quality and, based on microdosimetric analysis, an increase in biological effectiveness. As expected, dose rate values significantly decreased as source to target simulated tissue distances increased, unexpectedly the inverse square law was not obeyed with greater absorbed dose rate values observed over cell like distances.

Monte Carlo simulations using PENELOPE, generated microdosimetric probability distributions from which dose-mean lineal energy ( $\bar{y}_D$ ) values were derived and were in general similar to the experimental outcomes presented. Microdosimetric spectra and  $y$ -values measured in  $keV/\mu m$  were determined for six individual radionuclides representing potential hot particle scenarios. Sharp vertical overlapping peaks were observed at lineal energies between  $2 keV/\mu m$  and  $7 keV/\mu m$  for beta particles associated with  $^3H$  and  $^{63}Ni$ . For higher energy beta

particles above 50 keV, lineal energy peaks were observed around 1 keV/ $\mu\text{m}$ . At greater source to counter simulated tissue distances (above 3  $\mu\text{m}$ ) peak  $y$ -value distributions were skewed to the right indicating more low energy depositions. The higher peak  $y$ -values would suggest that relatively higher RBE values would be expected around certain electron energy and range. RBE results derived from PENELOPE simulations were consistent with previous determinations of RBE from other investigators using the Monte Carlo code NOREC [64].

## 6.1 Summary of Research Contributions

Hot particles (HP) are typically beta particle emitters that are expected during plant operations (refurbishment and decommissioning) and are expected emissions after severe nuclear accidents. The variations in the dose away from the HP is dependent upon the spectrum of the beta particles themselves as well as the inverse square law. This was shown to lead to steep dose gradients with implications in industry, medicine and the environment for surface and internal dosimetry.

The new knowledge contributed by this work addressing the radiation science and health physics complexities of hot particle dosimetry are as follows:

- The measurement of low energy beta particles for absorbed dose and radiation quality determinations, based on the principles of experimental microdosimetry, are only possible using a wall-less proportional counter. Such counters are not commercially available, consequently a wall-less TEPC with 88% transparency was designed and constructed and details of the design and signal processing electronics presented.
- A look into the implication of beta emitters potentially released into the environment and how to determine their microdosimetric characteristics is an important contribution of this work.
- Monte Carlo methods can be used in the development of experimental instrumentation as well as for computing dosimetric quantities in situations

where experimental methods are not easily applied. This work systematically investigated and developed the Monte Carlo code PENELOPE to take advantage of its low energy (as low as 50 eV) electron transport simulation capabilities in computing microdosimetric spectra. The developed code was benchmarked against published photon microdosimetric data and used to compute lineal energy spectra and microdosimetric quantities for a range of beta particle energies from 5 keV to 200 keV. Comparison of computational data with the wall-less counter experimental results across simulated tissue distance from 1  $\mu\text{m}$  to 41  $\mu\text{m}$  confirmed confidence in both the code and experimental technique to provide detailed dosimetric information for hot-particle beta emitters.

- The results of this investigation point to dose rates that decline by factors of the order of ten to twenty over distances that are comparable to two or three mammalian cell diameters for both alpha and beta emitters. Also, the microdosimetric parameters representative of biological effectiveness over similar distances increased by factors approaching 2. The implications of these findings are most significant in situations involving internal contamination where cells at risk, such as epithelial cells in lung and gut tissue, are in layers of a few cells or less. The significance of changes in radiation quality also comes into play in these situations. In radiation protection, for exposure situations where a regulatory limit has been exceeded, further investigation is required to assess the likely biological outcome of the exposure and this cannot be done without reference to a radiobiological understanding of radiation quality and not the simple invoking of radiation weighting factors. For therapeutic applications of beta or alpha emitters in medicine, consideration of dose-rate gradients and radiation quality are clearly essential as the margins between successful treatment and failure are thought to be of the order of ten percent.

## 6.2 Recommendations for Future Work

The results of this investigation indicate the need for further work and development of the methods adopted both in measurement and simulation:

- Direct hot particle dosimetry should be carried out in those situations where there is uncertainty concerning the nature of the hot particle in terms of its isotopic make up and physical structure and more so when an internal contamination has been detected. The apparatus described in this work was designed specifically for the low energy beta sources available in our laboratory and to prove the principle of measurement. An apparatus for operational hot particle dosimetry would have to be designed to take into account the longer ranges of the beta particles potentially encountered and a method engineered to enable easy introduction of the hot particle into the apparatus. Both these aspects require considerations of physical size for the whole apparatus and the counter itself, which in turn would require consideration of the optimum operating gas pressure and how quickly the apparatus could be prepared for measurement.
- Effort would also be required to simplify the data acquisition system, signal processing and presentation of results such that the measurement could be introduced as a quasi-routine procedure by health physics staff. In the expectation that higher energy beta sources may be involved in operational hot particle dosimetry the definition of the sensitive volume of the wallless proportional counter should be improved by the introduction of field tubes rather than relying on the geometry of the counter window alone as is the present case.
- Regarding simulation, the current code should be used to build a library of depth-dose curves and microdosimetric spectra for the complete range of isotopes expected in power plant operations so these simulations could be compared with measurements in the field from hot particles with likely poorly known characteristics and thereby decrease the uncertainty in identification of the HP and retrospective dosimetry for an exposed individual.



- On a more fundamental level, in this work the computational parameters WCC, WCR, C1, and C2 in PENELOPE were set to safe operating conditions recommended for propane based tissue equivalent gas. These safe operating limits were emphasized by several authors [56] [50] [49] for reliable microdosimetric results in materials other than water. An investigation into optimizing these parameters for the determination of nanodosimetric quantities for characterization of radiation induced damages at the DNA level should be carried out to contribute to a more comprehensive understanding of radiation quality and biological effectiveness.
- To supplement absorbed dose determination from current industry monitoring techniques with microdosimetric quantities that also quantify the radiobiological effectiveness in known or unknown short range charged particle fields.
- The above techniques in Monte Carlo simulations and the wall-less counter instrumentation were applied for determinations within micrometric cell like volumes at operational limits like  $H_p(0.07)$ . This research should be extended to determine nanodosimetric quantities for characterization of radiation induced damages at the DNA sizes.

In closing, both experiment and simulation indicate an increase in biological effectiveness for low energy electrons, as source to target tissue distances are increased. Steep dose gradients were observed from low energy beta particles beams as dose rates decreased across tissue like distances. The Monte Carlo electron transport code PENELOPE proved to be a suitable computational tool for calculating microdosimetric quantities, and dose rate variations at microscopic sizes for low energy short ranged charged particles. Operated in the microdosimetric mode, the Wall-less TEPC showed advantages in quantifying the impact of a hot particle. Both absorbed dose rate and radiation quality measurements over tissue like dimensions were quantified.









---

**Sample text for a "<sup>63</sup>Ni.in" PENELOPE Input File**

---

TITLE Ni- 63 spectrum 100bins. A 5mm site size simulating 2um @165torr TE  
gas.

0.0 cm(radius =1um simulated site size from the anode)away from  
the detector at 0deg subtended angle.

Note that interaction forcing distorts the detector output.

.

>>>>>> Source definition.

SKPAR 1 [Primary particles: 1=electron, 2=photon, 3=positron]

SPECTR 0 2.80E-02

SPECTR 670 5.55E-02

SPECTR 1340 8.25E-02

SPECTR 2010 1.09E-01

SPECTR 2680 1.35E-01

SPECTR 3350 1.60E-01

SPECTR 4020 1.85E-01

SPECTR 4690 2.10E-01

SPECTR 5360 2.34E-01

SPECTR 6030 2.57E-01

SPECTR 6700 2.80E-01

SPECTR 7360 3.03E-01

SPECTR 8030 3.25E-01

SPECTR 8700 3.47E-01

SPECTR 9370 3.68E-01

SPECTR 10040 3.89E-01

SPECTR 10710 4.09E-01

SPECTR 11380 4.29E-01

SPECTR 12050 4.49E-01

SPECTR 12720 4.68E-01

SPECTR 13390 4.87E-01

SPECTR 14060 5.05E-01

SPECTR 14730 5.23E-01

SPECTR 15400 5.40E-01

SPECTR 16070 5.57E-01

---

SPECTR 16740 5.74E-01  
SPECTR 17410 5.90E-01  
SPECTR 18080 6.06E-01  
SPECTR 18750 6.21E-01  
SPECTR 19420 6.36E-01  
SPECTR 20080 6.51E-01  
SPECTR 20750 6.65E-01  
SPECTR 21420 6.79E-01  
SPECTR 22090 6.92E-01  
SPECTR 22760 7.05E-01  
SPECTR 23430 7.18E-01  
SPECTR 24100 7.31E-01  
SPECTR 24770 7.43E-01  
SPECTR 25440 7.54E-01  
SPECTR 26110 7.66E-01  
SPECTR 26780 7.77E-01  
SPECTR 27450 7.87E-01  
SPECTR 28120 7.98E-01  
SPECTR 28790 8.08E-01  
SPECTR 29460 8.18E-01  
SPECTR 30130 8.27E-01  
SPECTR 30800 8.36E-01  
SPECTR 31470 8.45E-01  
SPECTR 32140 8.53E-01  
SPECTR 32810 8.61E-01  
SPECTR 33480 8.69E-01  
SPECTR 34140 8.77E-01  
SPECTR 34810 8.84E-01  
SPECTR 35480 8.91E-01  
SPECTR 36150 8.98E-01  
SPECTR 36820 9.04E-01  
SPECTR 37490 9.11E-01  
SPECTR 38160 9.16E-01  
SPECTR 38830 9.22E-01

---

SPECTR 39500 9.27E-01  
SPECTR 40170 9.33E-01  
SPECTR 40840 9.38E-01  
SPECTR 41510 9.42E-01  
SPECTR 42180 9.47E-01  
SPECTR 42850 9.51E-01  
SPECTR 43520 9.55E-01  
SPECTR 44190 9.59E-01  
SPECTR 44860 9.62E-01  
SPECTR 45530 9.66E-01  
SPECTR 46200 9.69E-01  
SPECTR 46860 9.72E-01  
SPECTR 47530 9.74E-01  
SPECTR 48200 9.77E-01  
SPECTR 48870 9.79E-01  
SPECTR 49540 9.82E-01  
SPECTR 50210 9.84E-01  
SPECTR 50880 9.86E-01  
SPECTR 51550 9.87E-01  
SPECTR 52220 9.89E-01  
SPECTR 52890 9.91E-01  
SPECTR 53560 9.92E-01  
SPECTR 54230 9.93E-01  
SPECTR 54900 9.94E-01  
SPECTR 55570 9.95E-01  
SPECTR 56240 9.96E-01  
SPECTR 56910 9.97E-01  
SPECTR 57580 9.97E-01  
SPECTR 58250 9.98E-01  
SPECTR 58920 9.98E-01  
SPECTR 59590 9.99E-01  
SPECTR 60260 9.99E-01  
SPECTR 60920 9.99E-01  
SPECTR 61590 1.00E+00



```

SPECTR 62260 1.00E+00
SPECTR 62930 1.00E+00
SPECTR 63600 1.00E+00
SPECTR 64270 1.00E+00
SPECTR 64940 1.00E+00
SPECTR 65610 1.00E+00
SPECTR 66280 1.00E+00
SPECTR 66950 -1.00E+00
SPOSIT 0 0 0 [Coordinates of the source]
SCONE 0 0 0 [Conical beam; angles in deg]
.
>>>>>> Material data and simulation parameters.
MFNAME 26502um.mat [Material file, up to 20 chars]
MSIMPA 1e3 1e3 1e3 0.02 0.02 2.5e2 2.5e2 [EABS(1:3),C1,C2,WCC,WCR]
MFNAME 266.mat [Material file, up to 20 chars]
MSIMPA 1e3 1e3 1e3 0.01 0.05 1e3 1e3 [EABS(1:3),C1,C2,WCC,WCR]
.
>>>>>> Geometry and local simulation parameters.
GEOMFN 005.geo [Geometry file, up to 20 chars]
PARINP 1 0.005 thickness [Optional geometry parameters]
PARINP 2 0.01 radius [Optional geometry parameters]
DSMAX 1 1e-4 [KB, maximum step length in body KB]
.
>>>>>> Interaction forcing.
IFORCE 1 1 4 2000 .1 2 [Interaction forcing]
IFORCE 1 1 5 200 .1 2 [Interaction forcing]
.
>>>>>> Bremsstrahlung splitting.
IBRSPL 1 2 [KB,splitting factor]
.
>>>>>> X-ray splitting.
IXRSPL 1 2 [KB,splitting factor, weight
window]
.

```

```
>>>>>>> Emerging particles. Energy and angular distributions.
NBE 0 0 100 [Energy window and no. of bins]
NBANGL 45 18 [No. of bins for the angles THETA and PHI]
.
>>>>>>> Impact detectors (up to 25 different detectors).
IPSF=0; no psf is created.
IPSF=1; a psf is created (for only one detector).
IDCUT=0; tracking is discontinued at the detector entrance.
IDCUT=1; the detector does not affect the tracking.
IDCUT=2; the detector does not affect tracking, the energy
distribution of particle fluence (integrated over the
volume of the detector) is calculated.
IMPDET 0 0 200 0 2 [E-window, no. of bins, IPSF, IDCUT]
IDBODY 1 [Active body]
.
>>>>>>> Energy-deposition detectors (up to 25).
ENDETC 0 0 200 [Energy window and no. of bins]
EDBODY 1 [Active body]
.
>>>>>>> Absorbed dose distribution.
GRIDZ 0 0.005 200 [Z coords of the box vertices, no. of
bins]
GRIDR 0.01 50 [Radius of the dose volume, no. of bins]
.
>>>>>>> Job properties
RESUME KD660dump660.dat [Resume from this dump file, 20 chars]
DUMPTO KD660dump660B.dat [Generate this dump file, 20 chars]
DUMPP 60 [Dumping period, in sec]
.
NSIMSH 2e7 [Desired number of simulated showers]
TIME 86400 [Allotted simulation time, in sec]
END [Ends the reading of input data]
```

---

---

**Sample of "Telemachus" - A code used to extract single event energy depositions from FORTRAN code in PENELOPE**

---

```
#include <stdio.h>
#include <math.h>

extern void cpenmain_(); // PENMAIN

int c_out;

#define P_ELECTRON  1
#define P_PHOTON    2
#define P_POSITRON  3

#define BDOI  4  // body of interest

long unsigned c1cnt, c1c2cnt, c2cnt;

double be[6]; // body energy
int    bd[6]; // body detect

#define CH_MAX 512
#define EMAX  5120.0
#define CH_ED  ( EMAX / (double)CH_MAX )

unsigned long mca[ CH_MAX ];
```

```
unsigned long lmca[ 251 ];
double      LE[ 251 ];

void append_mca( char * fn, long unsigned tcnt, long unsigned cnt ) {

    int i;
    FILE * f;

    f = fopen( fn, "a+" );

    fprintf( f, "\n,,Total showers, %lu\n", tcnt );
    fprintf( f, "\n,,Body 1 events, %lu\n", cnt );
    fprintf( f, "\n,,keV/chan, %10e\n", CH_ED );

    fprintf( f, "\nMCA begin\n" );
    for ( i = 0; i < CH_MAX; i++ ) {
        fprintf( f, "%3d,%6lu\n", i, mca[i] );
    }
    fprintf( f, "MCA end\n" );

    fprintf( f, "\nLOG MCA begin\n" );
    for ( i = 0; i < 251; i++ ) {
        fprintf( f, "%3d,%6lu, %12e\n", i, lmca[i], LE[i] );
    }
    fprintf( f, "LOG MCA end\n" );

    fclose( f );
}
```

```
static unsigned long tcnt = 0;
static unsigned long cnt = 0;

void tp_eos_(
    double * E1,
    double * E2,
    double * E3,
    double * E4,
    double * E5,
    double * E6 ) {

    static double max_energy = 0.0;
    static unsigned long ocnt = 10000;
    static double e_sum = 0;
    int i;
    static unsigned long pcnt = 0;

    tcnt++;

    if ( *E1 > 0.0 ) {
        cnt++;

        e_sum += *E1;

        if ( *E1 > max_energy ) {
            max_energy = *E1;
        }
    }
}
```

```
}

i = (int) ( *E1 / CH_ED );
if ( i >= CH_MAX ) {
    i = CH_MAX - 1;
}
mca[ i ]++;

{

double lix;
int    li;
lix = log( *E1 ) / log( 10 ) * 50;

li = (int) lix;

if ( li < 0 ) {
    li = 0;
} else if ( li > 250 ) {
    li = 250;
}
lmca[ li ]++;
LE[ li ] = *E1;
}

if ( ( cnt >= pcnt ) ) {
    printf( "\r EPB: %6lu %8lu %10e %10e %10e max: %10e ", cnt,
           tcnt, *E1, *E2, e_sum/cnt/(4/3), max_energy );
    pcnt += 10000;
}

if ( cnt >= ocnt ) {
    append_mca( "MCA_TEMP_INCR.CSV", tcnt, cnt );
}
```

```
        ocnt += 1000000;
        printf( "\n" );
    }

    if ( ( cnt == 100 ) || ( cnt == 10 ) ) {
        append_mca( "MCA_TEMP_INCR.CSV", tcnt, cnt );
    }

}

}

}

#if 0 // [[[

// This is hook from the PENELOPE2011 fortran code called at
// every interaction and the boundary crossing.
//

void track_point_(
    int * shower_number,
    int * kpar_idx,      // ???
    int * kpar,         // particle type
    int * IBODY,
    double * X,         // X, Y, Z cartesian coordinates of the
        interaction
    double * Y,
    double * Z,
    double * E          // Energy of the particle after the
        interaction
    )
```

```
{

    // NOT USED

}

#endif // ]]]]

int main()
{

    int i;

    printf( "program Telemachus (Son of the PENELOPE) ver 0.2.4
           201023.\n" );
    printf( " captures energy deposited in 6 bodies. LogMCA\n" );

    for ( i = 0; i < CH_MAX; i++ ) {
        mca[i] = 0;
    }
    for ( i = 0; i < 251; i++ ) {
        LE[i] = 0.0;
    }

    /// out_mca( 0, 0 );

    c_out = 0;

    cpenmain_(); // FORTRAM PENELOPE PENMAIN
```



---

```
    printf( "program Telemachus OK.\n" );  
  
    append_mca( "MCA.CSV", tcnt, cnt );  
  
    return 0;  
  
}
```

---

### A.3 PENMAIN(\*.dat) output files

#### Sample text $^{63}\text{Ni}$ PENELOPE output File

---

```

*****
**  Program PENMAIN. Results. **
*****

Date and time: 3rd Mar 2021. 00:33:30

Ni- 63 spectrum 100bins. A 5mm site size simulating 2um @165torr

Simulation time ..... 6.040850E+04 sec
Simulation speed ..... 3.310792E+04 showers/sec

Simulated primary showers ..... 2.000000E+09

Primary particles: electrons

Upbound primary particles ..... 1.893707E+09
Downbound primary particles ..... 3.831396E+07
Absorbed primary particles ..... 6.797897E+07

Upbound fraction ..... 9.557257E-01 +- 2.1E-05
Downbound fraction ..... 2.220648E-02 +- 1.3E-05
Absorption fraction ..... 3.398949E-02 +- 1.2E-05

Secondary-particle generation probabilities:
-----
|  electrons  |  photons  |  positrons  |
-----
|  upbound   | 8.872123E-03 | 5.668750E-05 | 0.000000E+00 |

```

---

		+ - 6.3E-06		+ - 5.1E-07		+ - 0.0E+00		
-----								
	downbound		3.049498E-03		2.983850E-05		0.000000E+00	
		+ - 3.7E-06		+ - 3.7E-07		+ - 0.0E+00		
-----								
	absorbed		1.165708E-01		2.790000E-06		0.000000E+00	
		+ - 2.4E-05		+ - 1.1E-07		+ - 0.0E+00		
-----								

Average deposited energies (bodies):

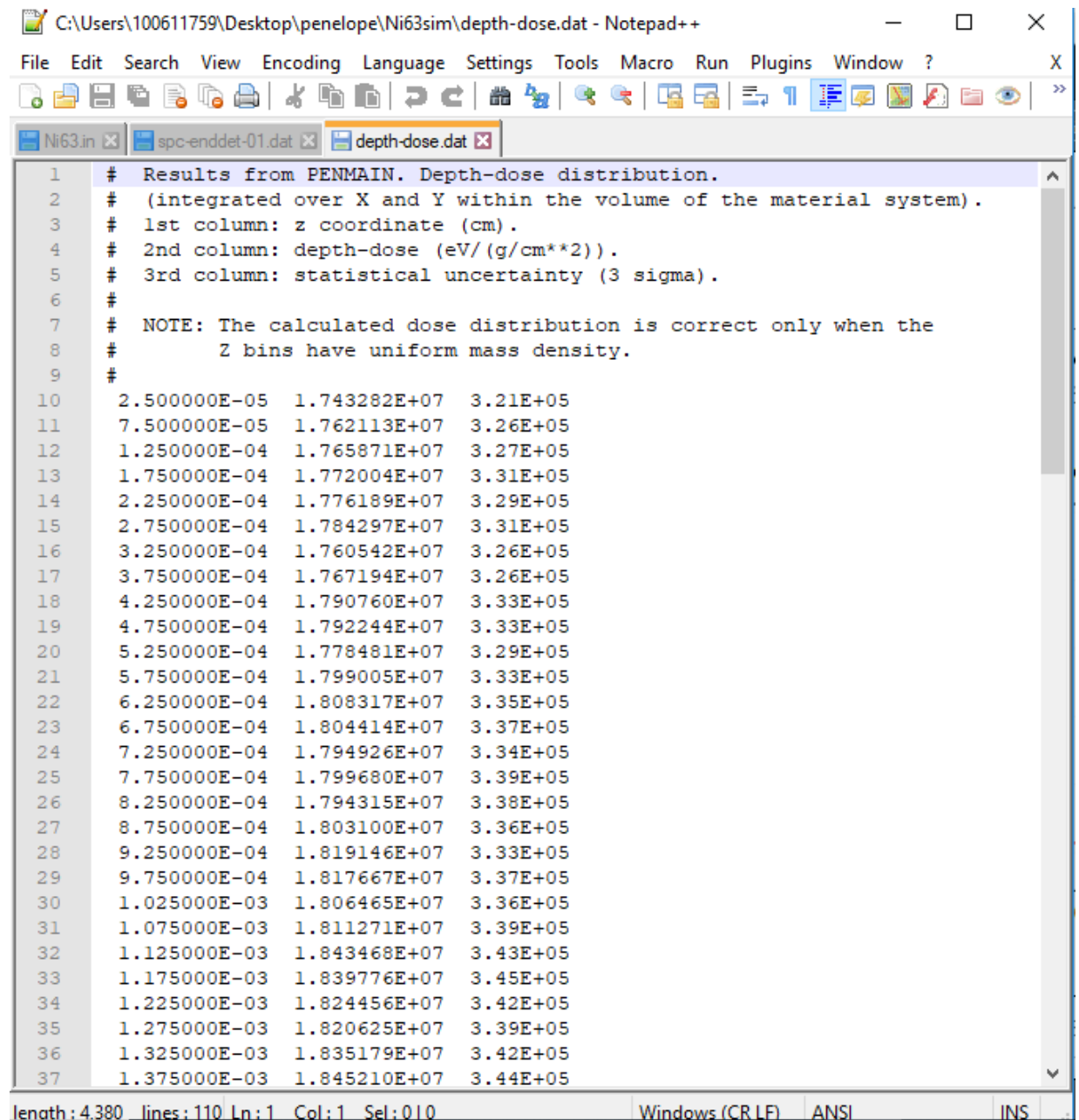
Body 1 ..... 1.883049E+03 +- 1.1E-01 eV (effic. = 4.29E+04)

Last random seeds = 915366750 , 1689681410

---

---

## Screen shots

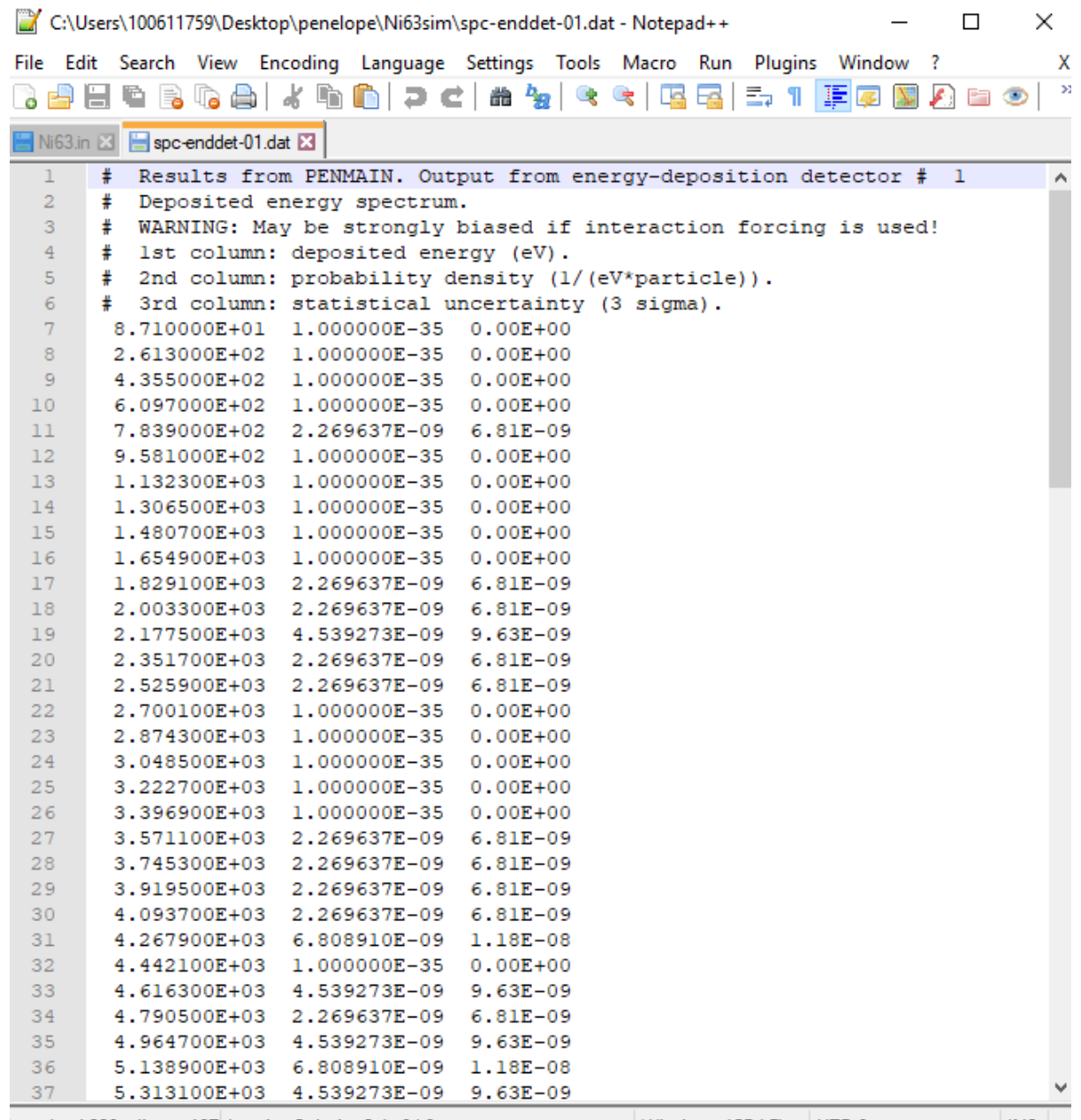


```
C:\Users\100611759\Desktop\penelope\ni63sim\depth-dose.dat - Notepad++
File Edit Search View Encoding Language Settings Tools Macro Run Plugins Window ? X
Ni63.in x spc-enddet-01.dat x depth-dose.dat x
1 # Results from PENMAIN. Depth-dose distribution.
2 # (integrated over X and Y within the volume of the material system).
3 # 1st column: z coordinate (cm).
4 # 2nd column: depth-dose (eV/(g/cm**2)).
5 # 3rd column: statistical uncertainty (3 sigma).
6 #
7 # NOTE: The calculated dose distribution is correct only when the
8 #       Z bins have uniform mass density.
9 #
10 2.500000E-05 1.743282E+07 3.21E+05
11 7.500000E-05 1.762113E+07 3.26E+05
12 1.250000E-04 1.765871E+07 3.27E+05
13 1.750000E-04 1.772004E+07 3.31E+05
14 2.250000E-04 1.776189E+07 3.29E+05
15 2.750000E-04 1.784297E+07 3.31E+05
16 3.250000E-04 1.760542E+07 3.26E+05
17 3.750000E-04 1.767194E+07 3.26E+05
18 4.250000E-04 1.790760E+07 3.33E+05
19 4.750000E-04 1.792244E+07 3.33E+05
20 5.250000E-04 1.778481E+07 3.29E+05
21 5.750000E-04 1.799005E+07 3.33E+05
22 6.250000E-04 1.808317E+07 3.35E+05
23 6.750000E-04 1.804414E+07 3.37E+05
24 7.250000E-04 1.794926E+07 3.34E+05
25 7.750000E-04 1.799680E+07 3.39E+05
26 8.250000E-04 1.794315E+07 3.38E+05
27 8.750000E-04 1.803100E+07 3.36E+05
28 9.250000E-04 1.819146E+07 3.33E+05
29 9.750000E-04 1.817667E+07 3.37E+05
30 1.025000E-03 1.806465E+07 3.36E+05
31 1.075000E-03 1.811271E+07 3.39E+05
32 1.125000E-03 1.843468E+07 3.43E+05
33 1.175000E-03 1.839776E+07 3.45E+05
34 1.225000E-03 1.824456E+07 3.42E+05
35 1.275000E-03 1.820625E+07 3.39E+05
36 1.325000E-03 1.835179E+07 3.42E+05
37 1.375000E-03 1.845210E+07 3.44E+05
length:4380 lines:110 Ln:1 Col:1 Sel:010 Windows (CR LF) ANSI INS
```

```

C:\Users\100611759\Desktop\PENELOPE\Experiment Run-MC output PEN sim\Ni-63 Simulation 100 MC bins (0,0,-5.5) (0,0,2.5)\p...
File Edit Search View Encoding Language Settings Tools Macro Run Plugins Window ?
penmain-res.dat
4  ** Program PENMAIN. Results. **
5  *****
6
7  Date and time: 16th Apr 2021. 15:04:51
8
9  Ni- 63 spectrum 100bins. A 5mm site size simulating 2um @16Storr
10
11 Simulation time ..... 6.305112E+04 sec
12 Simulation speed ..... 3.172029E+04 showers/sec
13
14
15 Simulated primary showers ..... 2.000000E+09
16
17 Primary particles: electrons
18
19 Upbound primary particles ..... 1.928334E+09
20 Downbound primary particles ..... 2.499845E+07
21 Absorbed primary particles ..... 4.666705E+07
22
23 Upbound fraction ..... 9.734611E-01 +- 1.9E-05
24 Downbound fraction ..... 1.554523E-02 +- 1.1E-05
25 Absorption fraction ..... 2.333353E-02 +- 1.0E-05
26
27 Secondary-particle generation probabilities:
28 -----
29 | | | | | electrons | photons | positrons |
30 -----
31 | upbound | 9.293846E-03 | 3.862600E-05 | 0.000000E+00 |
32 | | +- 6.5E-06 | +- 4.2E-07 | +- 0.0E+00 |
33 -----
34 | downbound | 3.046000E-03 | 2.003500E-05 | 0.000000E+00 |
35 | | +- 3.7E-06 | +- 3.0E-07 | +- 0.0E+00 |
36 -----
37 | absorbed | 7.440572E-02 | 1.691500E-06 | 0.000000E+00 |
38 | | +- 1.9E-05 | +- 8.7E-08 | +- 0.0E+00 |
39 -----
40
41 Average deposited energies (bodies):
42 | Body 1 ..... 1.263726E+03 +- 9.4E-02 eV (effic. = 2.57E+04)
43
44 Last random seeds = 850200119 , 1046353084
45
Normal text file length: 1,962 lines: 47 Ln: 1 Col: 1 Pos: 1 Windows (CR LF) UTF-8 INS

```



```
C:\Users\100611759\Desktop\penelope\Ni63sim\spc-enddet-01.dat - Notepad++
File Edit Search View Encoding Language Settings Tools Macro Run Plugins Window ?
Ni63.in x spc-enddet-01.dat x
1 # Results from PENMAIN. Output from energy-deposition detector # 1
2 # Deposited energy spectrum.
3 # WARNING: May be strongly biased if interaction forcing is used!
4 # 1st column: deposited energy (eV).
5 # 2nd column: probability density (1/(eV*particle)).
6 # 3rd column: statistical uncertainty (3 sigma).
7 8.710000E+01 1.000000E-35 0.00E+00
8 2.613000E+02 1.000000E-35 0.00E+00
9 4.355000E+02 1.000000E-35 0.00E+00
10 6.097000E+02 1.000000E-35 0.00E+00
11 7.839000E+02 2.269637E-09 6.81E-09
12 9.581000E+02 1.000000E-35 0.00E+00
13 1.132300E+03 1.000000E-35 0.00E+00
14 1.306500E+03 1.000000E-35 0.00E+00
15 1.480700E+03 1.000000E-35 0.00E+00
16 1.654900E+03 1.000000E-35 0.00E+00
17 1.829100E+03 2.269637E-09 6.81E-09
18 2.003300E+03 2.269637E-09 6.81E-09
19 2.177500E+03 4.539273E-09 9.63E-09
20 2.351700E+03 2.269637E-09 6.81E-09
21 2.525900E+03 2.269637E-09 6.81E-09
22 2.700100E+03 1.000000E-35 0.00E+00
23 2.874300E+03 1.000000E-35 0.00E+00
24 3.048500E+03 1.000000E-35 0.00E+00
25 3.222700E+03 1.000000E-35 0.00E+00
26 3.396900E+03 1.000000E-35 0.00E+00
27 3.571100E+03 2.269637E-09 6.81E-09
28 3.745300E+03 2.269637E-09 6.81E-09
29 3.919500E+03 2.269637E-09 6.81E-09
30 4.093700E+03 2.269637E-09 6.81E-09
31 4.267900E+03 6.808910E-09 1.18E-08
32 4.442100E+03 1.000000E-35 0.00E+00
33 4.616300E+03 4.539273E-09 9.63E-09
34 4.790500E+03 2.269637E-09 6.81E-09
35 4.964700E+03 4.539273E-09 9.63E-09
36 5.138900E+03 6.808910E-09 1.18E-08
37 5.313100E+03 4.539273E-09 9.63E-09
```

---

**PENELOPE Depth-Dose.dat txt**

---

```
# Results from PENMAIN. Depth-dose distribution.
# (integrated over X and Y within the volume of the material system).
# 1st column: z coordinate (cm).
# 2nd column: depth-dose (eV/(g/cm**2)).
# 3rd column: statistical uncertainty (3 sigma).
#
# NOTE: The calculated dose distribution is correct only when the
#       Z bins have uniform mass density.
#
1.250000E-05 1.000000E-35 1.00E-35
3.750000E-05 1.000000E-35 1.00E-35
6.250000E-05 1.000000E-35 1.00E-35
8.750000E-05 1.000000E-35 1.00E-35
1.125000E-04 1.000000E-35 1.00E-35
1.375000E-04 1.000000E-35 1.00E-35
1.625000E-04 1.000000E-35 1.00E-35
1.875000E-04 1.000000E-35 1.00E-35
2.125000E-04 1.000000E-35 1.00E-35
2.375000E-04 1.000000E-35 1.00E-35
2.625000E-04 1.000000E-35 1.00E-35
2.875000E-04 1.000000E-35 1.00E-35
3.125000E-04 1.000000E-35 1.00E-35
3.375000E-04 1.000000E-35 1.00E-35
3.625000E-04 1.000000E-35 1.00E-35
3.875000E-04 1.000000E-35 1.00E-35
4.125000E-04 1.000000E-35 1.00E-35
4.375000E-04 1.000000E-35 1.00E-35
4.625000E-04 1.000000E-35 1.00E-35
4.875000E-04 1.000000E-35 1.00E-35
5.125000E-04 1.000000E-35 1.00E-35
5.375000E-04 1.000000E-35 1.00E-35
5.625000E-04 1.000000E-35 1.00E-35
5.875000E-04 1.000000E-35 2.45E-10
```

---

6.125000E-04	1.000000E-35	1.00E-35
6.375000E-04	1.000000E-35	1.00E-35
6.625000E-04	1.000000E-35	1.00E-35
6.875000E-04	1.000000E-35	1.00E-35
7.125000E-04	1.000000E-35	1.00E-35
7.375000E-04	1.000000E-35	1.00E-35
7.625000E-04	1.000000E-35	1.00E-35
7.875000E-04	1.000000E-35	1.00E-35
8.125000E-04	1.000000E-35	1.00E-35
8.375000E-04	1.000000E-35	1.00E-35
8.625000E-04	1.000000E-35	1.00E-35
8.875000E-04	1.000000E-35	1.00E-35
9.125000E-04	1.000000E-35	1.00E-35
9.375000E-04	1.000000E-35	1.00E-35
9.625000E-04	1.000000E-35	1.00E-35
9.875000E-04	1.000000E-35	1.00E-35
1.012500E-03	1.000000E-35	1.00E-35
1.037500E-03	1.000000E-35	1.00E-35
1.062500E-03	1.000000E-35	1.00E-35
1.087500E-03	1.000000E-35	1.00E-35
1.112500E-03	1.000000E-35	1.00E-35
1.137500E-03	1.000000E-35	1.00E-35
1.162500E-03	1.000000E-35	1.00E-35
1.187500E-03	1.000000E-35	1.00E-35
1.212500E-03	1.000000E-35	1.00E-35
1.237500E-03	1.000000E-35	1.00E-35
1.262500E-03	1.000000E-35	1.00E-35
1.287500E-03	1.000000E-35	1.00E-35
1.312500E-03	1.000000E-35	1.00E-35
1.337500E-03	1.000000E-35	1.00E-35
1.362500E-03	1.000000E-35	1.00E-35
1.387500E-03	1.000000E-35	1.00E-35
1.412500E-03	1.000000E-35	1.00E-35
1.437500E-03	1.000000E-35	1.00E-35



---

1.462500E-03	1.000000E-35	1.00E-35
1.487500E-03	1.000000E-35	1.00E-35
1.512500E-03	1.000000E-35	1.00E-35
1.537500E-03	1.000000E-35	1.00E-35
1.562500E-03	1.000000E-35	1.00E-35
1.587500E-03	4.000356E-11	1.20E-10
1.612500E-03	3.198906E+03	9.60E+03
1.637500E-03	1.000000E-35	1.00E-35
1.662500E-03	1.000000E-35	1.00E-35
1.687500E-03	1.221897E+02	3.67E+02
1.712500E-03	2.349469E+03	7.05E+03
1.737500E-03	5.103275E+03	1.53E+04
1.762500E-03	1.903123E+04	5.71E+04
1.787500E-03	1.004697E+03	3.01E+03
1.812500E-03	2.905034E+04	8.52E+04
1.837500E-03	9.814117E+03	2.20E+04
1.862500E-03	3.593493E+03	1.08E+04
1.887500E-03	1.000000E-35	1.00E-35
1.912500E-03	4.846151E+03	1.45E+04
1.937500E-03	1.000000E-35	1.00E-35
1.962500E-03	7.619940E+03	1.73E+04
1.987500E-03	2.028746E+03	5.05E+03
2.012500E-03	1.000000E-35	1.00E-35
2.037500E-03	1.120026E+03	3.36E+03
2.062500E-03	8.660130E+03	2.27E+04
2.087500E-03	1.386002E+04	4.16E+04
2.112500E-03	1.210039E+04	3.63E+04
2.137500E-03	2.144592E+04	5.25E+04
2.162500E-03	1.564289E+04	3.47E+04
2.187500E-03	7.180393E+03	1.97E+04
2.212500E-03	1.509218E+04	3.40E+04
2.237500E-03	1.410431E+04	2.99E+04
2.262500E-03	9.002071E+03	2.70E+04
2.287500E-03	1.874604E+04	5.62E+04

---

2.312500E-03	8.355997E+03	2.51E+04
2.337500E-03	1.591073E+04	3.38E+04
2.362500E-03	1.430365E+04	4.29E+04
2.387500E-03	1.046552E+04	3.14E+04
2.412500E-03	2.048192E+04	6.14E+04
2.437500E-03	2.391913E+04	7.17E+04
2.462500E-03	3.004946E+04	9.01E+04
2.487500E-03	4.702305E+04	1.41E+05
2.512500E-03	2.952564E+04	8.86E+04
2.537500E-03	1.000000E-35	1.00E-35
2.562500E-03	1.000000E-35	1.00E-35
2.587500E-03	3.749257E+03	1.12E+04
2.612500E-03	1.000000E-35	1.00E-35
2.637500E-03	1.000000E-35	1.00E-35
2.662500E-03	1.000000E-35	1.00E-35
2.687500E-03	3.353520E+03	1.01E+04
2.712500E-03	1.000000E-35	1.00E-35
2.737500E-03	1.000000E-35	1.00E-35
2.762500E-03	1.000000E-35	1.00E-35
2.787500E-03	1.000000E-35	1.00E-35
2.812500E-03	1.000000E-35	1.00E-35
2.837500E-03	1.000000E-35	1.00E-35
2.862500E-03	1.000000E-35	1.00E-35
2.887500E-03	1.000000E-35	1.00E-35
2.912500E-03	1.000000E-35	1.00E-35
2.937500E-03	1.000000E-35	1.00E-35
2.962500E-03	1.101301E+04	3.30E+04
2.987500E-03	1.000000E-35	1.00E-35
3.012500E-03	1.000000E-35	1.00E-35
3.037500E-03	7.992719E+02	2.40E+03
3.062500E-03	1.000000E-35	1.00E-35
3.087500E-03	1.000000E-35	1.00E-35
3.112500E-03	5.334226E+03	1.60E+04
3.137500E-03	1.000000E-35	1.00E-35

---

3.162500E-03	1.373056E+04	4.12E+04
3.187500E-03	1.000000E-35	1.00E-35
3.212500E-03	1.000000E-35	1.00E-35
3.237500E-03	1.284990E+04	3.85E+04
3.262500E-03	4.748955E+03	1.42E+04
3.287500E-03	1.000000E-35	1.00E-35
3.312500E-03	4.859602E+03	1.46E+04
3.337500E-03	1.000000E-35	1.00E-35
3.362500E-03	1.000000E-35	1.00E-35
3.387500E-03	1.000000E-35	1.00E-35
3.412500E-03	1.000000E-35	1.00E-35
3.437500E-03	1.000000E-35	1.00E-35
3.462500E-03	1.000000E-35	1.00E-35
3.487500E-03	8.682811E+03	2.60E+04
3.512500E-03	1.000000E-35	2.15E-10
3.537500E-03	6.833255E+03	2.05E+04
3.562500E-03	5.820874E+03	1.75E+04
3.587500E-03	1.000000E-35	1.00E-35
3.612500E-03	1.549997E+04	3.38E+04
3.637500E-03	1.000000E-35	1.00E-35
3.662500E-03	1.000000E-35	1.00E-35
3.687500E-03	2.414028E+03	7.24E+03
3.712500E-03	1.000000E-35	1.00E-35
3.737500E-03	1.228205E+04	3.65E+04
3.762500E-03	8.638556E+02	2.59E+03
3.787500E-03	1.000000E-35	1.00E-35
3.812500E-03	1.000000E-35	1.00E-35
3.837500E-03	7.834845E+03	1.67E+04
3.862500E-03	1.234392E+03	3.70E+03
3.887500E-03	1.277194E+04	3.72E+04
3.912500E-03	2.640729E+04	7.92E+04
3.937500E-03	1.000000E-35	1.00E-35
3.962500E-03	1.000000E-35	1.00E-35
3.987500E-03	6.762940E+03	2.03E+04

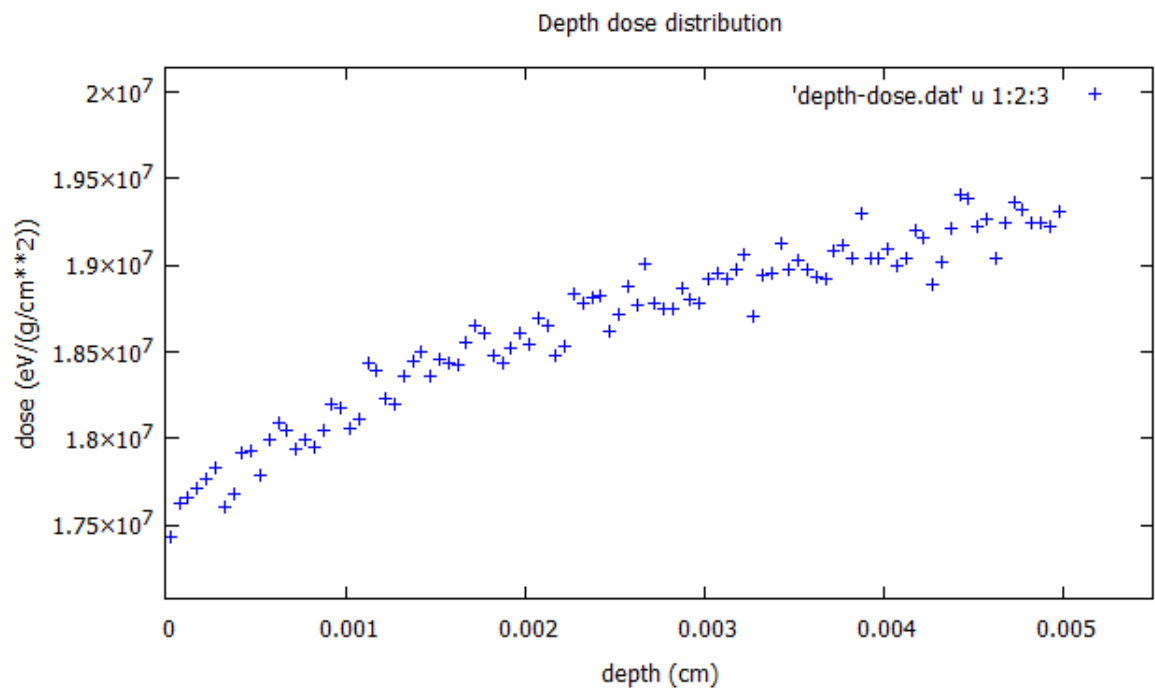
---

4.012500E-03	1.000000E-35	1.00E-35
4.037500E-03	1.000000E-35	1.00E-35
4.062500E-03	1.000000E-35	1.00E-35
4.087500E-03	4.850658E+03	1.46E+04
4.112500E-03	1.000000E-35	1.00E-35
4.137500E-03	1.000000E-35	1.00E-35
4.162500E-03	1.000000E-35	1.00E-35
4.187500E-03	2.086624E+03	6.26E+03
4.212500E-03	1.000000E-35	1.00E-35
4.237500E-03	1.000000E-35	1.00E-35
4.262500E-03	2.394412E+03	5.35E+03
4.287500E-03	1.000000E-35	1.00E-35
4.312500E-03	3.236299E+03	9.71E+03
4.337500E-03	8.489065E+03	2.55E+04
4.362500E-03	6.479863E+03	1.94E+04
4.387500E-03	1.000000E-35	1.00E-35
4.412500E-03	7.552074E+02	2.27E+03
4.437500E-03	7.260785E+03	2.18E+04
4.462500E-03	3.038637E+03	9.11E+03
4.487500E-03	1.000000E-35	2.39E-10
4.512500E-03	4.612983E+03	1.38E+04
4.537500E-03	1.743140E+03	4.85E+03
4.562500E-03	1.000000E-35	1.00E-35
4.587500E-03	1.625862E+04	2.90E+04
4.612500E-03	1.000000E-35	1.00E-35
4.637500E-03	1.000000E-35	1.00E-35
4.662500E-03	4.631155E+03	1.39E+04
4.687500E-03	2.072297E+03	6.22E+03
4.712500E-03	1.000000E-35	1.00E-35
4.737500E-03	3.501255E+04	7.46E+04
4.762500E-03	1.000000E-35	1.00E-35
4.787500E-03	1.105512E+03	3.32E+03
4.812500E-03	1.737931E+04	5.21E+04
4.837500E-03	1.000000E-35	1.00E-35

---

4.862500E-03	1.981702E+02	5.94E+02
4.887500E-03	1.000000E-35	1.00E-35
4.912500E-03	4.788130E+03	1.44E+04
4.937500E-03	1.000000E-35	1.00E-35
4.962500E-03	3.958865E+03	1.19E+04
4.987500E-03	1.000000E-35	1.00E-35

---



## Appendix B

# Experimental Wall-less TEPC

### B.1 Detector parts

30mm by 30mm Electro-formed Mesh procured from Delta Scientific a the Canadian subsidiary for Goodfellow.

Quote No 20620

<b>MANUFACTURER NAME</b>	<b>GOODFELLOW</b>				
<b>DESCRIPTION</b>	CU008720 Copper Mesh, Nominal Aperture: <b>0.2mm</b> , Thickness: <b>0.004mm</b> , Wire diameter: <b>0.0125mm</b> , Wires/inch: <b>118</b> , Open area: <b>88%</b> , Type: <b>Electro-formed mesh</b>				
<b>VOLUME PRICE (CAD)</b>	Order code	Size	1pc	2pcs	5pcs
	<b>182-875-90</b>	<b>30x30mm</b>	<b>C\$ 382.00</b>	<b>C\$ 486.00</b>	<b>C\$ 692.00</b>
	262-899-39	65x65mm	C\$ 654.00	C\$ 872.00	C\$ 1301.00
	862-420-91	130x130mm	C\$ 1160.00	C\$ 1751.00	
<b>TOLERANCES</b>	Thickness:		woven: $\pm 10\%$ electroformed: $\pm 20\%$		
	Wire diameter:		$\pm 10\%$		
	Size (linear dimension):		<100mm $\pm 1$ mm $\geq 100$ mm+2% / -1%		

## B.2 Radioactive Sources used in Experiments

### B.2.1 $^{241}\text{Am}$

Image and specifications of the  $^{241}\text{Am}$  source used experimentally.



**B.2.2**  $^{63}\text{Ni}$ 

Image and specifications of the  $^{63}\text{Ni}$  source used experimentally



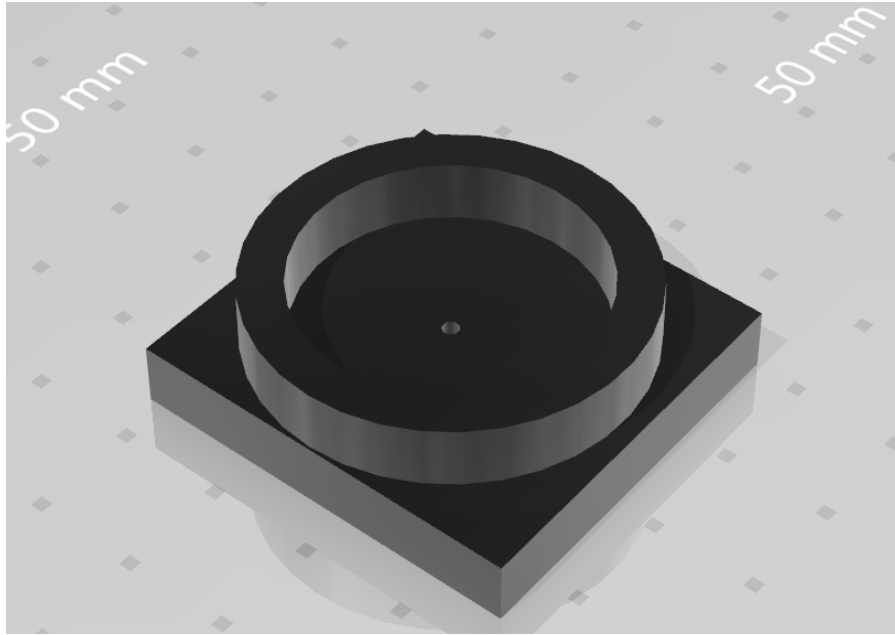


### B.2.3 $^{14}\text{C}$

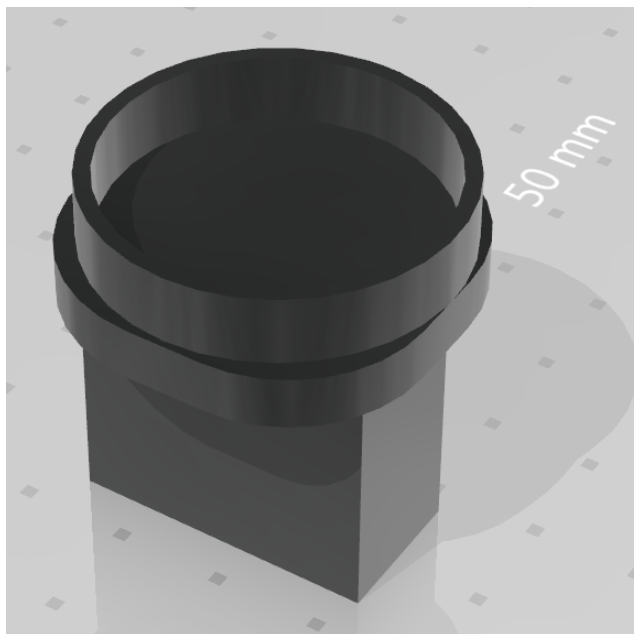
Image and specifications of the  $^{14}\text{C}$  source used experimentally.



### B.2.4 3D Printed Source Collimator



### B.2.5 3D Printed Source Holder



## B.3 Sample of Matlab Code

```

%This program redistributes linear mca (16383) data on an equal logarithmic
%interval basis (50 log bins per decade)

%Generating input PHS.....
filename = input('enter mca data spreadsheet name and extension....');
remca = xlsread(filename,-1);

%Entering required start information.....
lower_channel = input('Enter lowest channel from mca ');
calibration_factor = input('Enter calibration factor in keV/um/chn ');
starty = (lower_channel*calibration_factor);
endy = (calibration_factor * 16383);
start_log_chn = (log10(starty)*50+150);
end_log_chn = (log10(endy)*50 +150);
startlogchn = round(start_log_chn);
endlogchn = round(end_log_chn)

%Generating and initializing equal logarithmic interval array.....

log_plot = zeros(1,300);
eqlogplot = log_plot';

%Executing redistribution of linear data.....
%Setting initial conditions.....
factor = 10^(1/50);
logchncount = startlogchn;
startlinchn = (starty/calibration_factor);
endivy = (starty*factor);
endlinchn = (endivy/calibration_factor);
istartlinchn = round(startlinchn);
iendlinchn = round(endlinchn);

%redistributing linear PHS into equal logarithmic channels.....

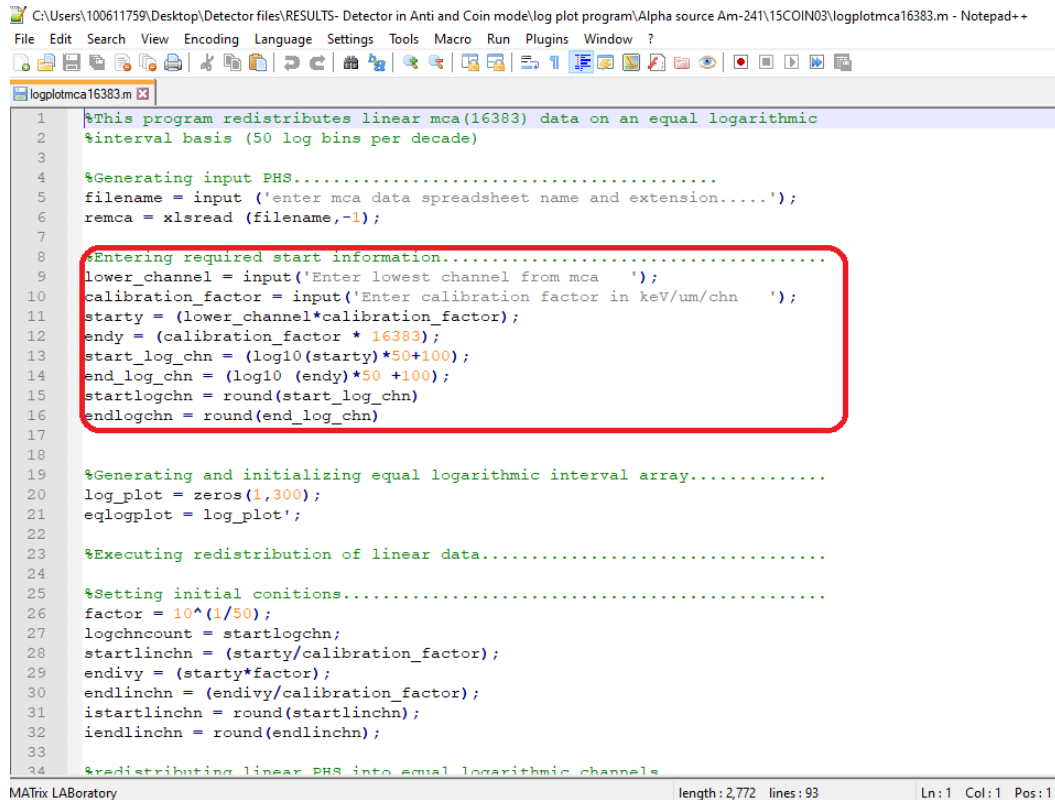
while(logchncount <= endlogchn)
    sum = 0;
    while (istartlinchn<=iendlinchn);
        sum = sum + remca (istartlinchn);
        istartlinchn = (istartlinchn +1);
    end
    eqlogplot (logchncount) = sum;
    logchncount = (logchncount +1);
    istartlinchn = iendlinchn;
    endivy = ((istartlinchn *
calibration_factor)*factor);
    endlinchn = (endivy/calibration_factor);
    iendlinchn = round(endlinchn);
    if iendlinchn > 16383;
        iendlinchn = 16383;
    end
end

xlswrite('logplot.xlsx',eqlogplot)
%sub program to plot results if
required.....
plot_request = input ('Enter "1" for plot "0"
for no plot');
if plot_request == 1;
    clf
    bar(eqlogplot,'r')
    %axis([50 300 0 4000])
    title ('Dose per Logarithmic Bin')
    xlabel ('Logarithmic Bins: 50 per Decade:
100 = 1keV/um')
    ylabel ('y.d(y)')
    %hold on
end

%Normalization.....
nsum=0;
ncount=1;
while ncount<=300
    nsum=nsum+eqlogplot(ncount);
    ncount=ncount+1;
end
nsum;
logint=0.04605;
figure
neqlogplot = eqlogplot./
(nsum*logint);
bar(neqlogplot)
axis([100 250 0 0.5])
title ('Fractional Dose per
Logarithmic Bin')
xlabel ('Logarithmic Bins:
50 per Decade: 100 =1keV/um')
ylabel('y.d(y)')

```

## B.4 Matlab Programme: *LogplotMCA16383* for Alpha particles



```

1  %This program redistributes linear mca(16383) data on an equal logarithmic
2  %interval basis (50 log bins per decade)
3
4  %Generating input PHS.....
5  filename = input('enter mca data spreadsheet name and extension....');
6  remca = xlsread(filename,-1);
7
8  %Entering required start information.....
9  lower_channel = input('Enter lowest channel from mca ');
10 calibration_factor = input('Enter calibration factor in keV/um/chn ');
11 starty = (lower_channel*calibration_factor);
12 endy = (calibration_factor * 16383);
13 start_log_chn = (log10(starty)*50+100);
14 end_log_chn = (log10(endy)*50 +100);
15 startlogchn = round(start_log_chn)
16 endlogchn = round(end_log_chn)
17
18
19 %Generating and initializing equal logarithmic interval array.....
20 log_plot = zeros(1,300);
21 eqlogplot = log_plot';
22
23 %Executing redistribution of linear data.....
24
25 %Setting initial conditions.....
26 factor = 10^(1/50);
27 logchncount = startlogchn;
28 startlinchn = (starty/calibration_factor);
29 endivy = (starty*factor);
30 endlinchn = (endivy/calibration_factor);
31 istartlinchn = round(startlinchn);
32 iendlinchn = round(endlinchn);
33
34 %redistributing linear PHS into equal logarithmic channels

```

MATrix LABoratory length: 2,772 lines: 93 Ln: 1 Col: 1 Pos: 1

## B.5 Matlab Programme: *Beta<sub>L</sub>LogplotMCA16383* for Beta particles

The original Matlab programme B.4 (*LogplotMCA16383*) was altered to accommodate the 300 bins produced from the PENELOPE simulation for various beta particle sources. The allowed for the creation of charts with both experimental and simulated results overlaid onto an equal logarithmic bin scale.

```

C:\Users\100611759\Desktop\Detector files\RESULTS- Detector in Anti and Coin mode\log plot program\Beta_logplotmca16383.m - Notepad++
File Edit Search View Encoding Language Settings Tools Macro Run Plugins Window ?
Beta_logplotmca16383.m
1 %This program redistributes linear mca(16383) data on an equal logarithmic
2 %interval basis (50 log bins per decade)
3
4 %Generating input PHS.....
5 filename = input ('enter mca data spreadsheet name and extension....');
6 remca = xlsread (filename,-1);
7
8 %Entering required start information.....
9 lower_channel = input ('Enter lowest channel from mca ');
10 calibration_factor = input ('Enter calibration factor in keV/um/chn ');
11 starty = (lower_channel*calibration_factor);
12 endy = (calibration_factor * 16383);
13 start_log_chn = (log10(starty)*50+150);
14 end_log_chn = (log10 (endy)*50 +150);
15 startlogchn = round(start_log_chn)
16 endlogchn = round(end_log_chn)
17
18
19 %Generating and initializing equal logarithmic interval array.....
20 log_plot = zeros(1,300);
21 eqlogplot = log_plot';
22
23 %Executing redistribution of linear data.....
24
25 %Setting initial conitions.....
26 factor = 10^(1/50);
27 logchncount = startlogchn;
28 startlinchn = (starty/calibration_factor);
29 endivy = (starty*factor);
30 endlinchn = (endivy/calibration_factor);
31 istartlinchn = round(startlinchn);
32 iendlinchn = round(endlinchn);
33
34 %redistributing linear PHS into equal logarithmic channels
MATrix LABoratory length: 2,772 lines: 93 Ln: 1 Col: 1 Po

```

## B.6 Matlab Code Interface

The screenshot displays the MATLAB R2020b environment. The main window is the Editor, showing a script named `Beta_logplotmca16383.m`. The script contains the following MATLAB code:

```

1 %This program redistributes linear mca(16383) data on an equal logarithmic
2 %interval basis (50 log bins per decade)
3
4 %Generating input PHS.....
5 filename = input ('enter mca data spreadsheet name and extension....');
6 remca = xlsread (filename,-1);
7
8 %Entering required start information.....
9 lower_channel = input('Enter lowest channel from mca ');
10 calibration_factor = input('Enter calibration factor in keV/um/chn ');
11 starty = (lower_channel*calibration_factor);
12 endy = (calibration_factor * 16383);
13 start_log_chn = (log10(starty)*50+150);
14 end_log_chn = (log10 (endy)*50 +150);
15 startlogchn = round(start_log_chn)
16 endlogchn = round(end_log_chn)
17

```

The Command Window shows the execution of the script:

```

>> logplotmca16383
enter mca data spreadsheet name and extension...."ANCOAM19.xlsx"
Enter lowest channel from mca 476
Enter calibration factor in keV/um/chn 0.0014262025

startlogchn =

```

The interface also shows the current folder containing files like `Am-241 @800V x40_a.xlsx`, `ANCOAM19.CSV`, `ANCOAM19.xlsx`, `ANCOAM19A.fig`, `ANCOAM19B.fig`, `logplot.xlsx`, and `logplotmca16383.m`. The workspace is currently empty.

## Bibliography

- [1] A. Sh. Aydarous. “Development of an ICCD-scintillator system for measurement of spatial dose distributions around ‘hot particles’”. en. In: *Radiation Protection Dosimetry* 108.4 (Apr. 2004), pp. 317–326. ISSN: 0144-8420, 1742-3406. DOI: [10.1093/rpd/nch044](https://doi.org/10.1093/rpd/nch044). URL: <https://academic.oup.com/rpd/article-lookup/doi/10.1093/rpd/nch044> (visited on 08/28/2019).
- [2] M W Charles and J D Harrison. “Hot particle dosimetry and radiobiology—past and present”. en. In: *J. Radiol. Prot.* 27.3A (Sept. 2007), A97–A109. ISSN: 0952-4746, 1361-6498. DOI: [10.1088/0952-4746/27/3A/S11](https://doi.org/10.1088/0952-4746/27/3A/S11). URL: <http://stacks.iop.org/0952-4746/27/i=3A/a=S11?key=crossref.323a376f1440b36575f2558700d3ca78> (visited on 08/19/2019).
- [3] A. Sh Aydarous. “Calculated effects of backscattering on skin dosimetry for nuclear fuel fragments”. eng. In: *Radiat Prot Dosimetry* 130.2 (2008), pp. 141–148. ISSN: 0144-8420. DOI: [10.1093/rpd/ncm494](https://doi.org/10.1093/rpd/ncm494).
- [4] Colby D. Mangini and David M. Hamby. “SCALING PARAMETERS FOR HOT-PARTICLE BETA DOSIMETRY”. en. In: *Radiat Prot Dosimetry* 172.4 (Dec. 2016), pp. 356–366. ISSN: 0144-8420, 1742-3406. DOI: [10.1093/rpd/ncv529](https://doi.org/10.1093/rpd/ncv529). URL: <https://academic.oup.com/rpd/article-lookup/doi/10.1093/rpd/ncv529> (visited on 08/21/2019).
- [5] *NRC: Information Notice No. 87-39: Control of Hot Particle Contamination at Nuclear Power Plants*. URL: <https://www.nrc.gov/reading-rm/doc-collections/gen-comm/info-notices/1987/in87039.html> (visited on 08/22/2019).
- [6] International Atomic Energy Agency. *Radioactive particles in the environment: sources, particle characterization and analytical techniques*. en. OCLC: 1039222705. 2011. ISBN: 978-92-0-119010-9.

- [7] Internationale Atomenergie-Organisation, ed. *The Fukushima Daiichi accident*. en. STI/PUB. Vienna, Austria: International Atomic Energy Agency, 2015. ISBN: 978-92-0-107015-9.
- [8] Marco Kaltofen and Arnie Gundersen. “Radioactively-hot particles detected in dusts and soils from Northern Japan by combination of gamma spectrometry, autoradiography, and SEM/EDS analysis and implications in radiation risk assessment”. en. In: *Science of The Total Environment* 607-608 (Dec. 2017), pp. 1065–1072. ISSN: 0048-9697. DOI: [10.1016/j.scitotenv.2017.07.091](https://doi.org/10.1016/j.scitotenv.2017.07.091). URL: <https://www.sciencedirect.com/science/article/pii/S0048969717317953> (visited on 05/12/2021).
- [9] Amanda J. Reynolds. “The Biological Basis for Dose Limitation in the Skin”. en. In: *Journal of Thermal Biology* 18.4 (Aug. 1993), pp. 283–284. ISSN: 03064565. DOI: [10.1016/0306-4565\(93\)90015-L](https://doi.org/10.1016/0306-4565(93)90015-L). URL: <https://linkinghub.elsevier.com/retrieve/pii/030645659390015L> (visited on 08/29/2019).
- [10] ICRP. *The 2007 Recommendations of the International Commission on Radiological Protection (ICRP) - Volume 37, Number 2-4, Apr 01, 2007*. 2007. URL: <https://journals-sagepub-com.uproxy.library.dc-uoit.ca/toc/anib/37/2-4> (visited on 09/24/2019).
- [11] CNSC. “Canadian Nuclear Safety Commission (CNSC) Expectations for Licensee Response During Skin Contamination Events.” en. In: *Directorate of Nuclear Substance Regulation’s (DNSR) Article* (2016), p. 5.
- [12] Bruce Alberts et al. *Essential Cell Biology*. en. Google-Books-ID: Cg4WAgAAQBAJ. Garland Science, Jan. 2015. ISBN: 978-1-317-80627-1.
- [13] Wynn A. Volkert and Timothy J. Hoffman. “Therapeutic Radiopharmaceuticals”. en. In: *Chem. Rev.* 99.9 (Sept. 1999), pp. 2269–2292. ISSN: 0009-2665, 1520-6890. DOI: [10.1021/cr9804386](https://doi.org/10.1021/cr9804386). URL: <https://pubs.acs.org/doi/10.1021/cr9804386> (visited on 09/08/2019).



- [14] International Commission on Radiation Units and Measurements. “DOSIMETRY OF BETA RAYS AND LOW-ENERGY PHOTONS FOR BRACHYTHERAPY WITH SEALED SOURCES”. In: *Journal of the International Commission on Radiation Units and Measurements* 4.2 (2004), pp. 2–2. ISSN: 1473-6691. DOI: [10.1093/jicru/ndh018](https://doi.org/10.1093/jicru/ndh018). URL: <https://doi.org/10.1093/jicru/ndh018>.
- [15] G. Massillon-JL et al. “Characteristics of a new polymer gel for high-dose gradient dosimetry using a micro optical CT scanner”. en. In: *Applied Radiation and Isotopes* 68.1 (Jan. 2010), pp. 144–154. ISSN: 09698043. DOI: [10.1016/j.apradiso.2009.08.016](https://linkinghub.elsevier.com/retrieve/pii/S096980430900534X). URL: <https://linkinghub.elsevier.com/retrieve/pii/S096980430900534X> (visited on 09/16/2019).
- [16] J. Atanackovic, A. R. Hanu, and S. H Byun. “Eye lens dosimetry in Canadian CANDU nuclear power plants based on operational dosimetric quantities Hp(10) and Hp(0.07)”. en. In: *Applied Radiation and Isotopes* 177 (Nov. 2021), p. 109902. ISSN: 0969-8043. DOI: [10.1016/j.apradiso.2021.109902](https://www.sciencedirect.com/science/article/pii/S0969804321003018). URL: <https://www.sciencedirect.com/science/article/pii/S0969804321003018> (visited on 10/19/2022).
- [17] F. Bohra et al. “Quantification of pure beta spectra in mixed beta gamma fields as part of eye lens dosimetry at CANDU power plants”. en. In: *Applied Radiation and Isotopes* 174 (Aug. 2021), p. 109746. ISSN: 0969-8043. DOI: [10.1016/j.apradiso.2021.109746](https://www.sciencedirect.com/science/article/pii/S0969804321001524). URL: <https://www.sciencedirect.com/science/article/pii/S0969804321001524> (visited on 10/19/2022).
- [18] P. Kliauga and R. Dvorak. “Microdosimetric Measurements of Ionization by Monoenergetic Photons”. en. In: *Radiation Research* 73.1 (Jan. 1978), p. 1. ISSN: 00337587. DOI: [10.2307/3574570](https://www.jstor.org/stable/3574570?origin=crossref). URL: <https://www.jstor.org/stable/3574570?origin=crossref> (visited on 11/02/2019).
- [19] “Dosimetry Fundamentals”. en. In: *Introduction to Radiological Physics and Radiation Dosimetry*. Weinheim, Germany: Wiley-VCH Verlag GmbH, Dec. 2007, pp. 264–291. ISBN: 978-3-527-61713-5 978-0-471-01146-0. DOI: [10.1002/9783527617135.ch11](http://doi.wiley.com/10.1002/9783527617135.ch11). URL: <http://doi.wiley.com/10.1002/9783527617135.ch11> (visited on 09/19/2019).

- [20] Glenn F. Knoll. *Radiation detection and measurement*. en. 4th ed. OCLC: ocn612350364. Hoboken, N.J: John Wiley, 2010. ISBN: 978-0-470-13148-0.
- [21] J. E. (James Edward) Turner. *Atoms, radiation, and radiation protection*. 2nd ed. New York: Wiley, 1995.
- [22] International Commission on Radiological Protection ICRP. “ICRP publication 103: The 2007 Recommendations of the International Commission on Radiological Protection”. In: *Annals of the ICRP* 37.2-4 (Mar. 2007). DOI: [10.1016/j.icrp.2007.11.001](https://doi.org/10.1016/j.icrp.2007.11.001). URL: <https://doi.org/10.1016/j.icrp.2007.11.001>.
- [23] Lennart Lindborg and Anthony Waker. *Microdosimetry: experimental methods and applications*. 2017.
- [24] International Commission on Radiation Units and Measurements. *ICRU Report 31, Average Energy Required To Produce An Ion Pair*. International Commission on Radiation Units and Measurements., 1979. ISBN: 0-913394-26-2.
- [25] William P Jesse and John Sadaukis. “Absolute Energy to Produce an Ion Pair by Beta Particles from S35”. en. In: *VOLUME 107, NUMBER 3* (1957), p. 6.
- [26] International Atomic Energy Agency. *Relative biological effectiveness in ion beam therapy*. International Atomic Energy Agency, 2008.
- [27] Hans-Georg Menzel. “The Complexity of Quantities in Radiation Dosimetry: The issue of Radiation Quality”. In: *Radiation Protection Dosimetry* 183.No. 1-2 (2019), pp. 3–10. ISSN: 0144-8420.
- [28] Eric J. Hall and Amato J. Giaccia. *Radiobiology for the radiologist*. en. Eighth edition. Philadelphia: Wolters Kluwer, 2019. ISBN: 978-1-4963-3541-8.
- [29] International Commission on Radiological Protection. “ICRP publication 60: 1990 recommendations of the international commission on radiological protection”. en. In: *Annals of Nuclear Energy* 19.1 (Jan. 1992), pp. 51–52. ISSN: 03064549. DOI: [10.1016/0306-4549\(92\)90053-E](https://doi.org/10.1016/0306-4549(92)90053-E). URL: [https :](https://doi.org/10.1016/0306-4549(92)90053-E)

- [//linkinghub.elsevier.com/retrieve/pii/030645499290053E](https://linkinghub.elsevier.com/retrieve/pii/030645499290053E) (visited on 08/29/2019).
- [30] D. E. Lea and D.G. Catcheside. “THE MECHANISM OF THE INDUC-TION BY RADIATION OF CHROMOSOME ABBERATIONS IN TRADES-CANTIA”. en. In: (1942).
- [31] Kellere A. M and H.H. Rossi. “The theory of dual radiation action, Cur-rent Topics”. In: *Radiat. Res. Quarterly* 8 (1972), pp. 85–158. URL: <https://cir.nii.ac.jp/crid/1570572699170445056> (visited on 04/20/2023).
- [32] ICRU. *International Commission on Radiation Units and Measurements (ICRU) Report 36, Microdosimetry*. 1983. URL: <https://icru.org/reports/reports/microdosimetry-report-36> (visited on 10/28/2019).
- [33] J. Booz. “Microdosimetric spectra and parameters of low LET-radiations. Proceedings: 5th Symposium on microdosimetry. Verbania Pallanza, Italy, 22-26 September 1975.” en. In: (1976). URL: [http://inis.iaea.org/Search/search.aspx?orig\\_q=RN:7277208](http://inis.iaea.org/Search/search.aspx?orig_q=RN:7277208) (visited on 12/11/2019).
- [34] A. J. Waker. “Principles of Experimental Microdosimetry”. en. In: *Radiat Prot Dosimetry* 61.4 (Sept. 1995), pp. 297–308. ISSN: 0144-8420. DOI: [10.1093/oxfordjournals.rpd.a082801](https://academic.oup.com/rpd/article/61/4/297/1640587). URL: <https://academic.oup.com/rpd/article/61/4/297/1640587> (visited on 10/29/2019).
- [35] TE Burlin. “A general theory of cavity ionisation”. In: *The British journal of radiology* 39.466 (1966), pp. 727–734. ISSN: 1748-880X.
- [36] Oak Ridge Associated Universities ORAU. *Rossi Tissue Equivalent Proportional Counter (ca. 1960). Health Physics Historical Instrumentation Museum Collection. Updated 03.Jan 2012. Web. 13. Nov. 2017*. URL: <https://www.ornl.gov/ptp/collection/proportional%20counters/rossi.htm> (visited on 10/29/2019).
- [37] Frank Herbert Attix. “Topics in Radiation Dosimetry (Radiation Dosime-try, Supplement 1).” en. In: *Nuclear Science and Engineering* 55.1 (Sept. 1974). ISSN: 0029-5639, 1943-748X. DOI: [10.13182/NSE74-A23976](https://doi.org/10.13182/NSE74-A23976). URL:

- <https://www.tandfonline.com/doi/full/10.13182/NSE74-A23976>  
(visited on 10/30/2019).
- [38] W A Glass and WA Gross. *Topics in Radiation Dosimetry: Radiation Dosimetry. Edited by Frank Attix. Wall-less Detectors in Microdosimetry*. Vol. 1. Supplement 1. Academic Press, Newyork and London, 1972. ISBN: 1-4832-1622-5.
- [39] Ugur Akbas et al. “Surface and Buildup Region Dose Measurements with Markus Parallel-Plate Ionization Chamber, GafChromic EBT3 Film, and MOSFET Detector for High-Energy Photon Beams”. en. In: *Advances in High Energy Physics* 2016 (2016), pp. 1–10. ISSN: 1687-7357, 1687-7365. DOI: [10.1155/2016/8361028](https://doi.org/10.1155/2016/8361028). URL: <http://www.hindawi.com/journals/ahep/2016/8361028/> (visited on 11/07/2019).
- [40] DM Hamby et al. “Varskin 4: A Computer Code for Skin Contamination Dosimetry. United States Nuclear Regulatory Commission”. en. In: NUREG/CR-6918, Rev 1 (June 2011), p. 94.
- [41] D. M. Hamby et al. “The new VARSKIN 4 photon skin dosimetry model”. en. In: *Radiation Protection Dosimetry* 154.3 (May 2013), pp. 356–363. ISSN: 0144-8420, 1742-3406. DOI: [10.1093/rpd/ncs247](https://doi.org/10.1093/rpd/ncs247). URL: <https://academic.oup.com/rpd/article-lookup/doi/10.1093/rpd/ncs247> (visited on 11/04/2019).
- [42] J. Dubeau, B.E. Heinmiller, and M. Corrigan. “Multiple Methods for Assessing the Dose to Skin Exposed to Radioactive Contamination”. en. In: *Radiat Prot Dosimetry* (July 2016), rpd;ncw220v1. ISSN: 0144-8420, 1742-3406. DOI: [10.1093/rpd/ncw220](https://doi.org/10.1093/rpd/ncw220). URL: <https://academic.oup.com/rpd/article-lookup/doi/10.1093/rpd/ncw220> (visited on 11/04/2019).
- [43] J Dubeau et al. “A COMPARISON OF BETA SKIN DOSES CALCULATED WITH VARSKIN 5.35.3 AND MCNP5”. en. In: *Radiation Protection Dosimetry* 182.4 (Dec. 2018), pp. 502–507. ISSN: 0144-8420, 1742-3406. DOI: [10.1093/rpd/ncy108](https://doi.org/10.1093/rpd/ncy108). URL: <https://academic.oup.com/rpd/article/182/4/502/5058986> (visited on 11/04/2019).

- [44] Detec. *Activity Calculator Software*. en. 2019. URL: <http://detecsciences.com/en/activity-calculator.html> (visited on 11/04/2019).
- [45] R Ravichandran et al. “Extrapolation chamber mounted on perspex for calibration of high energy photon and electron beams from a clinical linear accelerator”. en. In: *J Med Phys* 34.1 (2009), p. 31. ISSN: 0971-6203. DOI: [10.4103/0971-6203.48718](https://doi.org/10.4103/0971-6203.48718). URL: <http://www.jmp.org.in/text.asp?2009/34/1/31/48718> (visited on 11/15/2019).
- [46] J Böhm and U Schneider. “Review of extrapolation chamber measurements of beta rays and low energy x rays”. In: *Radiation Protection Dosimetry* 14.2 (1986), pp. 193–198. ISSN: 1742-3406.
- [47] Patrícia L. Antonio, Marcos Xavier, and Linda V.E. Caldas. “Böhm extrapolation chamber: Study of its behavior in beta radiation fields at the Calibration Laboratory of IPEN”. en. In: *Radiation Physics and Chemistry* 104 (Nov. 2014), pp. 310–315. ISSN: 0969806X. DOI: [10.1016/j.radphyschem.2014.04.035](https://doi.org/10.1016/j.radphyschem.2014.04.035). URL: <https://linkinghub.elsevier.com/retrieve/pii/S0969806X14001637> (visited on 11/15/2019).
- [48] Alireza Haghghat. *Monte Carlo Methods for Particle Transport*. Crc Press, 2016. ISBN: 1-4665-9254-0.
- [49] R D Stewart et al. “Microdosimetric properties of ionizing electrons in water: a test of the PENELOPE code system”. en. In: *Phys. Med. Biol.* 47.1 (Jan. 2002), pp. 79–88. ISSN: 0031-9155, 1361-6560. DOI: [10.1088/0031-9155/47/1/306](https://doi.org/10.1088/0031-9155/47/1/306). URL: <http://stacks.iop.org/0031-9155/47/i=1/a=306?key=crossref.30ed1bac176e811222d237652fddb053> (visited on 10/31/2019).
- [50] Francesc Salvat. “PENELOPE-2014: A Code System for Monte Carlo Simulation of Electron and Photon Transport”. en. In: (2015).
- [51] Fawaz Ali. “Design and Characterization of Next-Generation Tissue Equivalent Proportional Counters for use in Low Energy Neutron Fields”. en. PhD thesis. University of Ontario Institute of Technology, 2014.

- [52] A. J. Waker. “Gas gain characteristics of some walled proportional counters used in microdosimetry”. In: *Commission of the European Communities, Radiation Protection/Microdosimetry, Proceeding of the Eighth Symposium Germany*. 1982, pp. 1017–1030.
- [53] Mohammad Taghi Eivazi. “The application of experimental microdosimetric techniques to the dosimetry of X-rays in the diagnostic energy range.” eng. Accepted: 1990. Ph.D. University of Leeds, 1990. URL: <https://ethos.bl.uk/OrderDetails.do?uin=uk.bl.ethos.238708> (visited on 07/07/2022).
- [54] M. N. Varma. *Calibration of proportional counters in microdosimetry*. English. Tech. rep. BNL-31777; CONF-820931-5. Brookhaven National Lab., Upton, NY (USA), Jan. 1982. URL: <https://www.osti.gov/biblio/6926135> (visited on 07/15/2022).
- [55] Saad Najm Al-Bayati. “The application of experimental microdosimetry to mixed-field neutron-gamma dosimetry”. en. Accepted: 2013-01-08T20:54:51Z. Thesis. Dec. 2012. URL: <https://ir.library.ontariotechu.ca/handle/10155/294> (visited on 07/11/2022).
- [56] I. Kyriakou et al. “Microdosimetry of electrons in liquid water using the low-energy models of Geant4”. en. In: *Journal of Applied Physics* 122.2 (July 2017), p. 024303. ISSN: 0021-8979, 1089-7550. DOI: [10.1063/1.4992076](https://doi.org/10.1063/1.4992076). URL: <http://aip.scitation.org/doi/10.1063/1.4992076> (visited on 11/23/2021).
- [57] Anthony Waker. “Experimental uncertainties in microdosimetric measurements and an examination of the performance of three commercially produced proportional counters”. en. In: *Nuclear Instruments and Methods in Physics Research Section A: Accelerators, Spectrometers, Detectors and Associated Equipment* 234.2 (Feb. 1985). Publisher: North-Holland, pp. 354–360. ISSN: 0168-9002. DOI: [10.1016/0168-9002\(85\)90928-3](https://doi.org/10.1016/0168-9002(85)90928-3). URL: <http://www.sciencedirect.com/science/article/pii/0168900285909283> (visited on 07/08/2022).

- [58] David Broughton. “Theoretical performance analysis of a novel hemispherical tissue equivalent proportional counter for neutron monitoring and dosimetry”. en. Accepted: 2016-04-11T16:23:59Z. Thesis. Feb. 2016. URL: <https://ir.library.ontariotechu.ca/handle/10155/637> (visited on 09/15/2022).
- [59] Eckerman K and Endo A. “ICRP Publication 107. Nuclear decay data for dosimetric calculations.” English. In: *Ann ICRP* 38.3 (Jan. 2008), pp. 7–96. ISSN: 0146-6453, 1872-969X. DOI: [10.1016/j.icrp.2008.10.004](https://doi.org/10.1016/j.icrp.2008.10.004). URL: <https://europepmc.org/article/med/19285593> (visited on 02/10/2022).
- [60] ESTAR NIST. *Stopping Powers and Range Tables for Electrons*. URL: <https://physics.nist.gov/PhysRefData/Star/Text/ESTAR.html> (visited on 07/14/2022).
- [61] Randall S. Caswell, Lisa R. Karam, and J. J. Coyne. “Systematics of Alpha-Particle Energy Spectra and Lineal Energy (Y) Spectra for Radon Daughters”. en. In: *NIST* 52 (Jan. 1994). Last Modified: 2017-02-17T12:48-05:00 Publisher: Randall S. Caswell, Lisa R. Karam, J J. Coyne, pp. 377–380. URL: <https://www.nist.gov/publications/systematics-alpha-particle-energy-spectra-and-lineal-energy-y-spectra-radon-daughters> (visited on 07/28/2022).
- [62] H. Fakir et al. “Microdosimetry of inhomogeneous radon progeny distributions in bronchial airways”. In: *Radiation Protection Dosimetry* 113.2 (Apr. 2005), pp. 129–139. ISSN: 0144-8420. DOI: [10.1093/rpd/nch444](https://doi.org/10.1093/rpd/nch444). URL: <https://doi.org/10.1093/rpd/nch444> (visited on 07/27/2022).
- [63] D. Nikezic and K. N. Yu. “Alpha-particle lineal energy spectra for the human lung”. In: *International Journal of Radiation Biology* 78.7 (Jan. 2002). Publisher: Taylor & Francis \_eprint: <https://doi.org/10.1080/09553000210123694>, pp. 605–609. ISSN: 0955-3002. DOI: [10.1080/09553000210123694](https://doi.org/10.1080/09553000210123694). URL: <https://doi.org/10.1080/09553000210123694> (visited on 07/27/2022).
- [64] Michael Bellamy and Keith Eckerman. “RELATIVE BIOLOGICAL EFFECTIVENESS OF LOW-ENERGY ELECTRONS AND PHOTONS”. en. In: (2013), p. 25.

- 
- [65] H. Nikjoo et al. “Computational modelling of low-energy electron-induced DNA damage by early physical and chemical events”. eng. In: *Int J Radiat Biol* 71.5 (May 1997), pp. 467–483. ISSN: 0955-3002. DOI: [10.1080/095530097143798](https://doi.org/10.1080/095530097143798).
- [66] H. Nikjoo et al. “Computational approach for determining the spectrum of DNA damage induced by ionizing radiation”. eng. In: *Radiat Res* 156.5 Pt 2 (Nov. 2001), pp. 577–583. ISSN: 0033-7587. DOI: [10.1667/0033-7587\(2001\)156\[0577:cafdts\]2.0.co;2](https://doi.org/10.1667/0033-7587(2001)156[0577:cafdts]2.0.co;2).
- [67] H. Nikjoo et al. “Modelling of DNA damage induced by energetic electrons (100 eV to 100 keV)”. eng. In: *Radiat Prot Dosimetry* 99.1-4 (2002), pp. 77–80. ISSN: 0144-8420. DOI: [10.1093/oxfordjournals.rpd.a006843](https://doi.org/10.1093/oxfordjournals.rpd.a006843).